

Paramagnetism & Structural Biology

*Biochemical & Biophysical Analysis of
IMP-1 Metallo- β -Lactamase*

Thomas James Carruthers

Research School of Chemistry

College of Physical and Mathematical Sciences

First Submitted: May 2014

Revised: October 2014

*A thesis submitted for the degree of Doctor of Philosophy at
the Australian National University*



Australian
National
University

Declaration

This thesis is composed of my original work and does not contain material previously published or written by another person, except where due reference has been made in the text. The content of this thesis is the result of work that I have carried out since the commencement of my research degree candidature and has not been previously submitted for another degree or diploma in any university or tertiary institution.

The first version of this thesis was submitted in May 2014 for examination. This version, submitted in October 2014, incorporates minor revisions and corrections.

Thomas James Carruthers

October 2014

~ ~ ~

Nanna

Gwendolyn May O'Sullivan

1937 – 2012

~ ~ ~

Acknowledgements

To my supervisor, Professor Gottfried Otting, who challenged my understanding of science at a fundamental level and provided much appreciated guidance and support throughout, I owe gratitude and respect.

I would also like to acknowledge my ‘other supervisor’, Thomas Huber, for always making time to talk and inspiring me to expand my knowledge of scientific computation, and Colin Jackson and Paul Carr for their assistance and training in protein crystallography and X-ray diffraction techniques.

Thanks to Hiromasa Yagi for his mentorship and teaching, Livnat Jurnou for her friendship and advice on many aspects of my work, and Tony Herlt who was a big inspiration to me to ‘do science right’.

Past and present members of the Otting, Huber, Ollis and Jackson groups have given advice and feedback on the entire project and their support is much appreciated.

The RSC has strong technical support from a great team – in particular I would like to thank Hamish Macarthur-Onslow (IT) and Viki Withers (microanalysis).

My friends who formed the *Docco Sunday* crowd, the *Coffee Club* crew and the *Beer O’Clock* guys all kept me sane, well fed and watered. Scott, Marlene, Elena and Panda were immensely supportive, commiserating over failed experiments and celebrating successes.

A special thank you to Grant for keeping it real and letting me live my music vicariously through you; Dad for your unwavering support and patience; Mum for your critique, your trust, and your faith in me, and finally to Mel, for being my brave companion on this leg of the journey – thank you.

Financial support from the Australian Postgraduate Award, the Research School of Chemistry and the Alan Sargeson Scholarship is acknowledged.

Resistance to β -lactam antibiotics by pathogenic bacteria is a global concern. Typically arising between 2 and 3 years after the introduction of the antibiotic into clinical use, it is usually due to β -lactamase activity. The gene for IMP-1, a metallo- β -lactamase with two catalytic metal ions, is located on an extremely mobile integron element, enabling the rapid horizontal transfer of β -lactam resistance between bacterial species, including genera of pathogenically relevant bacteria. Along with the absence of any viable metallo- β -lactamase inhibitors, this gene mobility makes IMP-1 particularly problematic in the clinical environment. Chapter two of this thesis reports nuclear magnetic resonance (NMR) analysis of IMP-1. 90% of the backbone amide resonances of IMP-1 were assigned using conventional 3D NMR experiments along with selective isotope labelling using cell-free methods. IMP-1 was found to have a high affinity for iron through the course of this study. The iron form was structurally and biochemically characterised using several techniques. A 1.8 Å crystal structure of the iron variant was solved, showing a tertiary structure almost identical to the previously solved X-ray structures of the di-zinc form. NMR analysis suggested subtle differences in structure and/or mobility between the two species.

Observed paramagnetic NMR effects induced by the iron centre included paramagnetic relaxation enhancement (PRE), which located the metal centre in the active site. Pseudocontact shifts (PCS) were also evident and a magnetic susceptibility anisotropy ($\Delta\chi$) tensor was calculated. Paramagnetic NMR methods concurred with anomalous X-ray scattering experiments, locating the metal-binding site of the iron ion. A protocol for the use of paramagnetic effects from the iron centre in a high-throughput drug screening is proposed.

A novel method of generating perdeuterated proteins using cell-free protein synthesis with isotope-labelled amino acids is described in chapter three. Performing the cell-free reaction in H_2O -based buffers avoids the need for back-exchange of protons onto the backbone amides, which would be required following expressions in D_2O . This is particularly useful for cases where protein refolding is impossible, such as the IMP-1 metallo- β -lactamase. For proteins that can be expressed in good yields, the cost

difference compared to conventional isotope-labelling methods is minimal. This chapter includes a reproduction of the application note produced for Cambridge Isotope Laboratories.

The use of hyperpolarising agents such as para-hydrogen has recently engendered much interest in the NMR community. This methodology promises up to 350-fold signal-to-noise improvements over conventional experiments that start with a Boltzmann thermal population. Chapter four of this thesis briefly documents the establishment of an *in-house* built para-hydrogen producing rig in preparation for future studies into hyperpolarisation techniques. A standard operating procedure for obtaining optimal yields is also included.

Structure determination of chemical products isolated from natural sources is an essential part of the natural drug discovery process. Chapter five briefly documents how NMR was used in this step for a natural product with pro-angiogenic biological properties extracted from soybean extracellular fluids that proved difficult to identify via other methods.

List of Abbreviations

- [FeZn]IMP-1 – IMP-1 with one iron ion and one zinc ion cofactor
- [ZnZn]IMP-1 – IMP-1 with two zinc ion cofactors
- [GaZn]IMP-1 – IMP-1 with one gallium and one zinc ion cofactor
- ALTADENA – adiabatic longitudinal transport after dissociation engenders net alignment
- ANU – Australian National University
- bFGF – basic fibroblast growth factor
- *bla*_{IMP-1} – β -lactamase gene for IMP-1
- BMRB – Biological Magnetic Resonance Data Bank
- CCR – cross correlated relaxation
- CD – circular dichroism
- CHES – 2-(cyclohexylamino)ethanesulfonic acid
- CSA – chemical shift anisotropy
- CSR – Currie-spin relaxation
- DD – dipole-dipole
- DMSO – dimethyl sulfoxide
- DTT – dithiothreitol
- *E. coli* – *Escherichia coli*
- EDTA – ethylene diamine tetraacetic acid
- EGTA – ethylene glycol tetraacetic acid
- EPR – electron paramagnetic resonance
- ES β L – extended spectrum β -lactamase
- ESI-MS – electro-spray ionisation – mass spectrometry
- FCS – Fermi-contact shifts
- FDA – Food and Drug Administration (USA)
- HEPES – 2-[4-(2-hydroxyethyl)piperazin-1-yl]ethanesulfonic acid
- HSQC – heteronuclear single quantum coherence
- HUVEC – human umbilical vein endothelial cells
- ICP-OES – inductively coupled plasma – optical emission spectroscopy
- ICP-MS – inductively coupled plasma – mass spectrometry
- IMP – metallo- β -lactamase active on imipenem
- IPTG – isopropyl β -D-1-thiogalactopyranoside
- JCSMR – John Curtin School of Medical Research (ANU)
- LB – lysogeny broth
- MES – 2-(*N*-morpholino)ethanesulfonic acid
- MIC – minimum inhibitory concentration
- MOPS - 3-morpholinopropane-1-sulfonic acid
- MS – mass spectrometry
- M β L – metallo- β -lactamase
- NDM – New Delhi metallo- β -lactamase
- NMR – nuclear magnetic resonance
- NOE – nuclear Overhauser effect

- OD₆₀₀ – optical density at 600 nm
- *o*H₂ – *ortho*-hydrogen
- *P. aeruginosa* – *Pseudomonas aeruginosa*
- PASDNA – parahydrogen and synthesis allow dramatic enhancement of nuclear alignment
- PBP – penicillin binding protein
- PCS – pseudocontact shift
- PDB – Protein Data Bank
- PEGMME 2K – polyethylene glycol monomethyl ether, average mass 2,000 g/mol
- *p*H₂ – *para*-hydrogen
- PHIP – parahydrogen induced hyperpolarisation
- ppm – parts per million
- PRE – paramagnetic relaxation enhancement
- RDC – residual dipolar coupling
- *R*_{free} – crystallographic *R* factor calculated on only 5% of reflection data left out of structure calculation
- RMSD – root-mean-square deviation
- RSB – Research School of Biology (ANU)
- RSC – Research School of Chemistry (ANU)
- SDS-PAGE – sodium dodecyl sulfate – polyacrylamide gel electrophoresis
- spp. – *species pluralis* – multiple species
- TCEP – tris(2-carboxyethyl)phosphine
- TCI cryoprobe – proton optimised triple resonance NMR ‘inverse’ cryoprobe (Bruker)
- TGA – Therapeutic Goods Administration (Aus)
- Tris - tris(hydroxymethyl)aminomethane
- TROSY – transvers relaxation-optimised spectroscopy
- UNSW – University of New South Wales
- UV – ultraviolet
- RMSD – root-mean-square deviation
- VIM – Verona integron-encoded metallo-β-lactamase
- Zn₁ – the 3HIS metal-binding site of IMP-1
- Zn₂ – the ASP/CYS/HIS metal-binding site of IMP-1

Table of Contents

Declaration	III
Acknowledgements	VII
Abstract	IX
List of Abbreviations	XI
Table of Contents	XIII
1 Introduction to Paramagnetic NMR and Outline of Thesis	1
1.1 Paramagnetism in Structural NMR	1
1.2 Outline of Thesis	13
2 Biomolecular and Biophysical Analysis of IMP-1 Metallo-β-Lactamase	15
2.1 Introduction	15
2.2 Results: Initial System Optimisations	36
2.3 Results: Identification of an Iron-Binding IMP-1 Species	41
2.4 Results: Biochemical Comparison of [FeZn]IMP-1 and [ZnZn]IMP-1	54
2.5 Results: X-Ray Diffraction Structure Determination of [FeZn]IMP-1 and Anomalous Scattering	65
2.6 Results: NMR Analysis of IMP-1	76
2.7 Discussion	101
2.8 Conclusion	123
2.9 Experimental Methods	124
3 Cell-free protein synthesis with $^2\text{H}/^{15}\text{N}/^{13}\text{C}$-labelled amino acids in H_2O for the production of perdeuterated proteins with ^1H in the exchangeable positions	137
3.1 Introduction	137
3.2 Results	139
3.3 Discussion	147
3.4 Conclusions	153
3.5 Methodology	154
	XIII

3.6	Reproduction of the Submitted Application Note	155
4	The Set-Up, Optimisation and Operation of an In-House Built Para-Hydrogen Producing Rig	161
4.1	Introduction	161
4.2	Results	165
4.3	Discussion	175
4.4	Conclusions and Future Work	178
4.5	Experimental Methodology	178
5	Promotion of Mammalian Angiogenesis by Neolignans Derived from Soybean Extracellular Fluids – NMR Elucidation of Natural Products	179
5.1	Introduction	179
5.2	Results	179
5.3	Publication	184
5.4	Experimental Methodology	184
6	Cited Literature	187

1 Introduction to Paramagnetic NMR and Outline of Thesis

Paramagnetic NMR is of particular interest to the author and has constituted a large portion of this body of work both theoretically and practically. The following introduction reviews paramagnetism in NMR, contextualising the major component of this work, documented in chapter two.

1.1 Paramagnetism in Structural NMR

The magnetic moment of an electron is 658 times larger than that of a proton.* Consequently, interactions between the nucleus and an unpaired electron can cause much larger effects in the NMR experiment than bi-nuclear interactions. Paramagnetic species can generate four long-range effects that provide structural information about the system: paramagnetic relaxation enhancement (PRE), residual dipolar couplings (RDCs), paramagnetic shifts (Fermi contact shifts (FCSs) and pseudocontact shifts (PCSs)), and cross-correlation between the Curie-spin and dipole-dipole relaxation (CCR).³⁻⁶ These four effects can be conveniently measured in a ¹⁵N-HSQC experiment by comparison of a diamagnetic state to the paramagnetic state.³ They depend on the magnetic susceptibility tensor (χ tensor), which is related to the electron g -factor by⁷

$$\chi = g^2 \cdot \frac{\mu_0 N_A \mu_B^2 S(S+1)}{3kT} \quad (1.1)$$

where μ_0 is the permeability of free space, N_A is Avogadro's number, μ_B is the magnetic moment of the free electron, S is the electron spin quantum number, k is the Boltzmann constant and T is the temperature. This equation assumes that the zero-field splitting is negligible compared to the electron spin Zeeman energy.⁴⁻⁷

* The proton magnetic moment (μ_p) is equal to $1.410606743 \times 10^{-26} \text{ JT}^{-1}$, where the electron magnetic moment (μ_B) is equal to $-928.476430 \times 10^{-26} \text{ JT}^{-1}$.^{1,2}

The relationship between the χ tensor and the g -factor means that, in general, systems with an anisotropic g -factor will have an anisotropic χ tensor. The anisotropy of the χ tensor can be described by the $\Delta\chi$ tensor with axial and rhombic components:^{3,4}

$$\Delta\chi_{\text{ax}} = \chi_z - \frac{\chi_x + \chi_y}{2} \quad (1.2)$$

$$\Delta\chi_{\text{rh}} = \chi_x - \chi_y \quad (1.3)$$

For systems with isotropic χ tensors, only the PRE effect is significant, whereas all four effects occur in systems with anisotropic χ tensors.^{3,4} The four effects are described in the following sections.

1.1.1 Paramagnetic Relaxation Enhancement

Paramagnetic centres generally cause line broadening due to paramagnetic relaxation enhancement (PRE). Two mechanisms contribute to this relaxation – Solomon-Bloembergen-type dipole-dipole relaxation and Curie-spin magnetic moment relaxation – as reviewed below.

PRE due to Dipole-Dipole Interactions (Solomon-Bloembergen Type Relaxation)

The first description of PRE relaxation is based on dipole-dipole interactions between the nucleus and the unpaired electron. Modified Solomon-Bloembergen equations can describe longitudinal (Γ_1) and transverse (Γ_2) PRE rates, and are described in terms of the probability of nuclear spin-flipping involving ω_I or ω_S (single-quantum transition frequencies of the nucleus or electron), or the sum or difference of ω_I and ω_S (double- and zero-quantum transitions):^{4,6-11}

$$\Gamma_1 = \frac{2}{15} \left(\frac{\mu_0}{4\pi} \right)^2 \frac{\gamma_I^2 g_e^2 \mu_B^2 S(S+1)}{r^6} \times \left[\frac{\tau_c}{1 + (\omega_I - \omega_S)^2 \tau_c^2} + \frac{3\tau_c}{1 + \omega_I^2 \tau_c^2} + \frac{6\tau_c}{1 + (\omega_I + \omega_S)^2 \tau_c^2} \right] + \frac{2}{3} S(S+1) \left(\frac{A}{\hbar} \right)^2 \left[\frac{\tau_f}{1 + \omega_S^2 \tau_f^2} \right] \quad (1.4)$$

$$\Gamma_2 = \frac{1}{15} \left(\frac{\mu_0}{4\pi} \right)^2 \frac{\gamma_I^2 g_e^2 \mu_B^2 S(S+1)}{r^6} \times \left[4\tau_c + \frac{\tau_c}{1 + (\omega_I - \omega_S)^2 \tau_c^2} + \frac{3\tau_c}{1 + \omega_I^2 \tau_c^2} + \frac{6\tau_c}{1 + (\omega_I + \omega_S)^2 \tau_c^2} + \frac{6\tau_c}{1 + \omega_S^2 \tau_c^2} \right] + \frac{1}{3} S(S+1) \left(\frac{A}{\hbar} \right)^2 \left[\tau_f + \frac{\tau_f}{1 + \omega_S^2 \tau_f^2} \right] \quad (1.5)$$

where γ_I is the gyromagnetic ratio of the nucleus, ω_I and ω_S are the Larmor frequencies of the nucleus and electron respectively and A/\hbar is the contact coupling constant, which is non-zero only for nuclei coordinated with the metal ion. τ_c and τ_f in the above equations are composed of the correlation times of the mechanisms of relaxation, namely the electron relaxation time (τ_s), the rotational correlation time (τ_r) and the exchange time (τ_M):⁴

$$\begin{aligned} \tau_f^{-1} &= \tau_s^{-1} + \tau_M^{-1} \\ \tau_c^{-1} &= \tau_s^{-1} + \tau_r^{-1} + \tau_M^{-1} \\ \text{where } \tau_s^{-1} &\gg \tau_r^{-1} \\ \text{and } \tau_M^{-1} &\simeq 0 \\ \therefore \tau_f^{-1} &\simeq \tau_c^{-1} \simeq \tau_s^{-1} \end{aligned} \quad (1.6)$$

The electron relaxation time is much faster than the rotational correlation time for most metal ions, and the exchange time is generally negligible for metallo-enzymes. τ_M may be small for non-covalent PRE inducing tags, however, it is usually much longer than the electron relaxation time.

From these equations, it can be seen that both Γ_1 and Γ_2 have an r^{-6} distance dependence. For most metal ions, there is little dependence on the rotational correlation time (τ_r) due to the short electron relaxation time (τ_s), but significant dependence on the gyromagnetic ratio of the nucleus particularly for transverse relaxation, where nuclei with lower gyromagnetic ratio such as ^{15}N and ^{13}C will suffer less from PRE than ^1H or ^{19}F . It follows that longer distances can be measured on ^1H than on heteronuclei. These equations rely on the assumption that electron relaxation arises from molecular motions

other than rotational tumbling.^{7,11} Notably, however, molecular reorientation significantly contributes to electron relaxation.^{12,13}

PRE due to Magnetic Susceptibility (Curie-Spin Relaxation)

The second mechanism for the PRE effect is described by magnetic susceptibility, or Curie-spin relaxation, where longitudinal PRE (Γ_1) and transverse PRE (Γ_2) relaxation rates are described by^{4,6-11}

$$\Gamma_1 = \frac{2}{5} \left(\frac{\mu_0}{4\pi} \right)^2 \left(\frac{B_0 \gamma_I g_e^2 \mu_B^2 S(S+1)}{3kTr^3} \right)^2 \times \left(\frac{3\tau_r}{1 + \omega_I^2 \tau_r^2} \right) \quad (1.7)$$

$$\Gamma_2 = \frac{1}{5} \left(\frac{\mu_0}{4\pi} \right)^2 \left(\frac{B_0 \gamma_I g_e^2 \mu_B^2 S(S+1)}{3kTr^3} \right)^2 \times \left(4\tau_r + \frac{3\tau_r}{1 + \omega_I^2 \tau_r^2} \right) \quad (1.8)$$

τ_c in the above equations is determined by the sum of the inverse correlation times of different mechanisms of relaxation. In contrast to dipole-dipole relaxation, τ_s does not appear in the equations because the notion of a Curie-spin assumes extremely fast electron relaxation:⁴

$$\begin{aligned} \tau_c^{-1} &= \tau_r^{-1} + \tau_M^{-1} \\ \text{where } \tau_M^{-1} &\simeq 0 \\ \therefore \tau_c^{-1} &\simeq \tau_r^{-1} \end{aligned} \quad (1.9)$$

This leaves the exchange time (τ_M), which is generally negligible for metallo-enzymes, so that τ_c is often equivalent to τ_r . τ_M is not zero for non-covalent PRE inducing tags and is not necessarily insignificant compared to the contribution from the rotational correlation time. It is interesting to note that paramagnetic labelling is also useful in solid-state NMR, particularly as it has been shown that the Curie-spin contribution to PRE is absent in solids due to the absence of molecular tumbling.¹⁴

From the above equations, the same r^{-6} distance dependence is evident as for dipole-dipole relaxation. In contrast, however, there is a B_0^2 dependence. There is also an inverse dependence on temperature T . This is compounded by the fact that τ_r increases with decreasing temperature. As in the case of dipole-dipole relaxation, there is a quadratic dependence on the gyromagnetic ratio of the nucleus.

PRE for Structural Measurements

As the Curie-spin relaxation mechanism of PRE depends largely on τ_r and not τ_s , the Curie-spin relaxation mechanism becomes particularly important for samples with large τ_r , such as proteins. Conversely, the Solomon-Bloembergen-type dipole-dipole relaxation relies heavily on τ_s . Therefore, where τ_r is much greater than τ_s , as is the case for all lanthanide(III) ions other than Gd(III), the Curie-spin predominates the transverse relaxation mechanism.^{6,13} For electrons where the electron spin-state is longer-lived than the rotational correlation time, the Solomon-Bloembergen-type dipole-dipole relaxation mechanism predominates the PRE relaxation. Bertini *et al.* described the cross-correlation between the Curie-spin relaxation mechanism to dipole-dipole interactions that causes errors in PRE calculations (section 1.1.3).² In the extreme case, this error can even cause the paramagnetic state to have a slower relaxation than the diamagnetic state. For this reason, PRE measurements are usually applied using unpaired electrons with long spin-state life times to make the dipole-dipole relaxation PRE mechanism predominant (such as for Mn(II), Gd(III) or the nitroxide radical).³

Regardless of the mechanism of relaxation enhancement, the r^{-6} distance dependence is the basis of structural information gained from PRE measurements, somewhat akin to distance restraints from NOE measurements. Unfortunately, additional effects complicate practical experimental work with biomolecules ligated with paramagnetic metal-binding tags. The importance of taking tag flexibility into account when calculating structures via PRE measurements has been pointed out in the literature.⁴⁻⁷ Bertini *et al.* discuss the point dipole approximation,⁴ where it is assumed that the unpaired electron is localised exactly on the metal ion. They advise that the assumption is suitable only for distances greater than 3 – 4 Å from a 4f electron, and 7 Å in the case of a 3d electron. However, this guideline was only valid in the case of a metal immobilized in a rigid metal-binding site on a metallo-protein. In the situation of a metal-binding tag attached to a protein via some flexible linker or a non-covalent tag in fast exchange between a binding site on the biomolecule and the unbound state, tag flexibility and uncertainty in electron position must be taken into account in structure calculations. Ma *et al.*¹¹ approximated the distance from the unpaired electron (Δ_r) as the sum of the distance from the metal centre (r_M) and the distance from the p_z orbitals of the carbon or nitrogen in the metal ligands (r_L), along with a correlation factor between the metal-centred and the delocalised unpaired electron spin.¹¹

$$\Delta_r = r_M^{-6} + ar_L^{-6}(\rho^\pi)^2 + br_M^{-3}r_L^{-3}\rho^\pi \quad (1.10)$$

where ρ^π is the normalized unpaired electron spin density in the p_z orbital, and a and b approximate to 0.16 and -0.4 for heteronuclei, and approximately 0.116 and $0.59\cos(2\varphi)^*$ for protons. They conclude that the value for Δ_r is dominated by the ligand-centred term for PREs measured for heteronuclei in a copper(II) protein and note that PREs measured for protons depend less on the ligand terms, claiming that ^1H -metal distances less than 10 Å can be accurately estimated. It is important to note that the lone electrons of lanthanide ions reside in the 4f orbitals, which largely isolates them from the ligand field, and they do not delocalise as readily as unpaired 3d electrons do.^{12,13} This factor improves the accuracy of PRE measurements using paramagnetic centres such as Gd^{3+} .

It is difficult to measure any other paramagnetic effects for nuclear spins close to the paramagnetic metal centre due to the significant line broadening caused by PRE. This can be overcome by measuring heteronuclear spins, which are less susceptible to PRE broadening. To regain some of the proton sensitivity, methods have been established to measure paramagnetic effects close to a binding site by using a tag with fast metal exchange between a paramagnetic and diamagnetic species¹⁵ or by using exchange spectroscopy with mixing times before and after the nitrogen evolution time.¹⁶

While it is straightforward to measure PREs by quantifying the increased T_2 relaxation rates and comparing with an appropriate diamagnetic reference, issues can arise if the paramagnetic tagging is incomplete and the chemical shift of the nuclear spin is the same in the diamagnetic and paramagnetic state, as any residual diamagnetic signal will affect the accuracy of peak line fitting of the paramagnetic species.

Another difficulty with PRE distance calculations in proteins is with locating dynamic loops or residues. Due to the r^{-6} distance dependence of the PRE, the distance r calculated from the average PREs will always be closer to the unpaired electron than the actual average position of the nucleus.

With the above considerations, distance restraints based solely on PREs need to be carefully assessed prior to assuming a simple r^{-6} relationship for any relaxation enhancement measured.

* φ is the angle between the metal-proton vector and the carbon/nitrogen-proton bond

1.1.2 Residual Dipolar Couplings

Molecules containing a paramagnetic centre with an anisotropic g -tensor will display weak molecular alignment in the presence of a high magnetic field. A result of this partial alignment is that residual dipolar couplings (RDCs), which give distance-independent information on the orientation of scalar-coupled spin pairs with respect to the principal axes of the molecular alignment tensor, become observable. The direct relationship between the alignment tensor A and the χ tensor is given by

$$A_{\text{ax, rh}} = \Delta\chi_{\text{ax, rh}} \frac{B_0^2}{15\mu_0 kT} \quad (1.11)$$

This can be used to describe the RDCs as a function of the $\Delta\chi$ tensor:^{3,4}

$$D_{\text{AK}} = \frac{hB_0^2\gamma_A\gamma_K}{240\pi^3r_{\text{AK}}^3kT} \left(\Delta\chi_{\text{ax}}(3\cos^2\theta - 1) + \frac{3}{2}\Delta\chi_{\text{rh}}\sin^2\theta\cos 2\phi \right) \quad (1.12)$$

where γ_A and γ_K are the gyromagnetic ratios of nuclei A and K, r_{AK} is the distance between nuclei A and K, χ_{ax} and χ_{rh} are the axial and rhombic components of the alignment tensor, θ is the angle between the A-B internuclear vector and the z -axis of the χ tensor, and ϕ is the angle between the projection of the A-B internuclear vector on the xy -plane and the x -axis of the χ tensor.

Interpretation of the equation highlights magnetic field and temperature dependence. The magnetic field dependence is a strong argument for measuring other paramagnetic parameters at lower magnetic fields as the decreased spectral resolution due to RDCs at high field increases the measurement error.^{6,13} This effect is not a special case for paramagnetic samples, but a property of partial molecular alignment with respect to the magnetic field.

As the use of RDCs was not specifically explored in this thesis, the reader is directed to the large body of literature available on the topic.¹⁷⁻²⁰

1.1.3 Cross-Correlated Relaxation

Curie-spin relaxation (CSR) is mathematically similar to chemical shift anisotropy (CSA) and the similarity extends to cross-correlated relaxation (CCR). Analogous to the TROSY²¹ effect, cross-correlation between CSR and dipole-dipole (DD) relaxation is manifested in differential line broadening of doublets. The difference in line width at half height in Hz for a spin A coupled to spin K depends on the orientation and position of the inter-spin vector with respect to the χ tensor:^{3,22}

$$\Delta\nu = \left(\frac{\mu_0}{4\pi}\right) \frac{B_0\gamma_A^2\gamma_K h}{10\pi^3 r_{AK}^3} \chi_{\text{iso}} \times \tau_r (3 \cos^2 \theta_{AK} - 1) \quad (1.13)$$

where θ_{AK} is defined as the angle between the AK vector and the vector connecting the paramagnetic centre and spin A . The measurement of the CCR effect due to paramagnetism is restricted to nuclear spins far enough from the metal ion that the line width is not dominated by the PRE effect, and close enough to the metal for the paramagnetic CSR/DD CCR to remain significant with respect to diamagnetic CSA/DD CCR. Importantly, paramagnetic CCR relies on the Curie-spin relaxation mechanism, which is only significant for paramagnetic centres with anisotropic χ tensors as described above (section 1.1.1). As with RDC measurements, CCR was not measured directly in this project and the reader is referred to the appropriate literature.^{2-4,22-24}

1.1.4 Paramagnetic Shifts

Metals with anisotropic χ tensors also cause changes to chemical shifts termed hyperfine shifts. The measured chemical shift is a linear combination of the diamagnetic shift, the Fermi contact shift and the pseudocontact shift.

Fermi Contact Shifts

Fermi contact shifts (FCSs) are due to the delocalisation of the unpaired electron through covalent bonds.²⁴⁻²⁶ FCSs are similar to scalar couplings in as much as they depend on bond and dihedral orientation, and they decay rapidly as the number of bonds between the paramagnetic metal and the nucleus observed increases.³ FCSs due to metals with highly anisotropic χ tensors are also orientation dependent and are more difficult to calculate. In general, for paramagnetic lanthanide centres and ^1H detection, few FCSs are observable, as the signals would be broadened beyond detection by the PRE effect.

Pseudocontact Shifts due to Magnetic Susceptibility

The more interesting form of paramagnetic shift is the pseudocontact shift (PCS). This effect arises from the magnetic dipole field generated at the site of the nucleus by rapidly relaxing unpaired electrons (Curie-spin). It is a through-space effect that can be observed at distances as great as 60 Å from the metal centre.²⁷

Due to the fast electron relaxation time, it can be assumed that the electron magnetic moment is always aligned with the magnetic field. This causes an increased magnetic field along the B_0 z -axis and a reduced field in the xy -plane. If the χ tensor is isotropic, the magnetic dipole moment associated with the unpaired electron is constant and any change in magnetic field experienced by surrounding nuclei averages to zero upon molecular rotation. However, if the χ tensor is anisotropic, the magnitude of the magnetic dipole field depends on the orientation of the $\Delta\chi$ tensor, so that molecular tumbling leaves behind a net dipole field.^{4,28} This is depicted in cartoon form in Figure 1-1.

Based on the molecular tumbling argument above, the PCS effect is independent of the isotropic χ tensor. Therefore, it is typically defined with respect to the $\Delta\chi$ tensor components in an equation that bears strong resemblance to equation (1.12).^{3,4}

$$\Delta\delta^{\text{PCS}} = \frac{1}{12\pi r^3} \left(\Delta\chi_{\text{ax}}(3\cos^2\theta - 1) + \frac{3}{2}\Delta\chi_{\text{rh}}\sin^2\theta\cos 2\phi \right) \quad (1.14)$$

where r is the distance between the unpaired electron and the nuclear spin, $\Delta\chi_{\text{ax}}$ is the axial component and $\Delta\chi_{\text{rh}}$ is the rhombic component of the $\Delta\chi$ tensor and θ and ϕ are, similar to equation (1.12), the spherical polar angles of the nuclear spin with respect to the principal axis. Measured in ppm, there is no magnetic field dependence or dependence on gyromagnetic ratio. PCSs give rise to approximately diagonal shifts in the ^{15}N -HSQC experiments typically performed in biological NMR, as the nitrogen of a NH group is close in space to the observed proton so that, at large distances from the paramagnetic centre, both nuclei experience very similar PCSs (Figure 1-2).

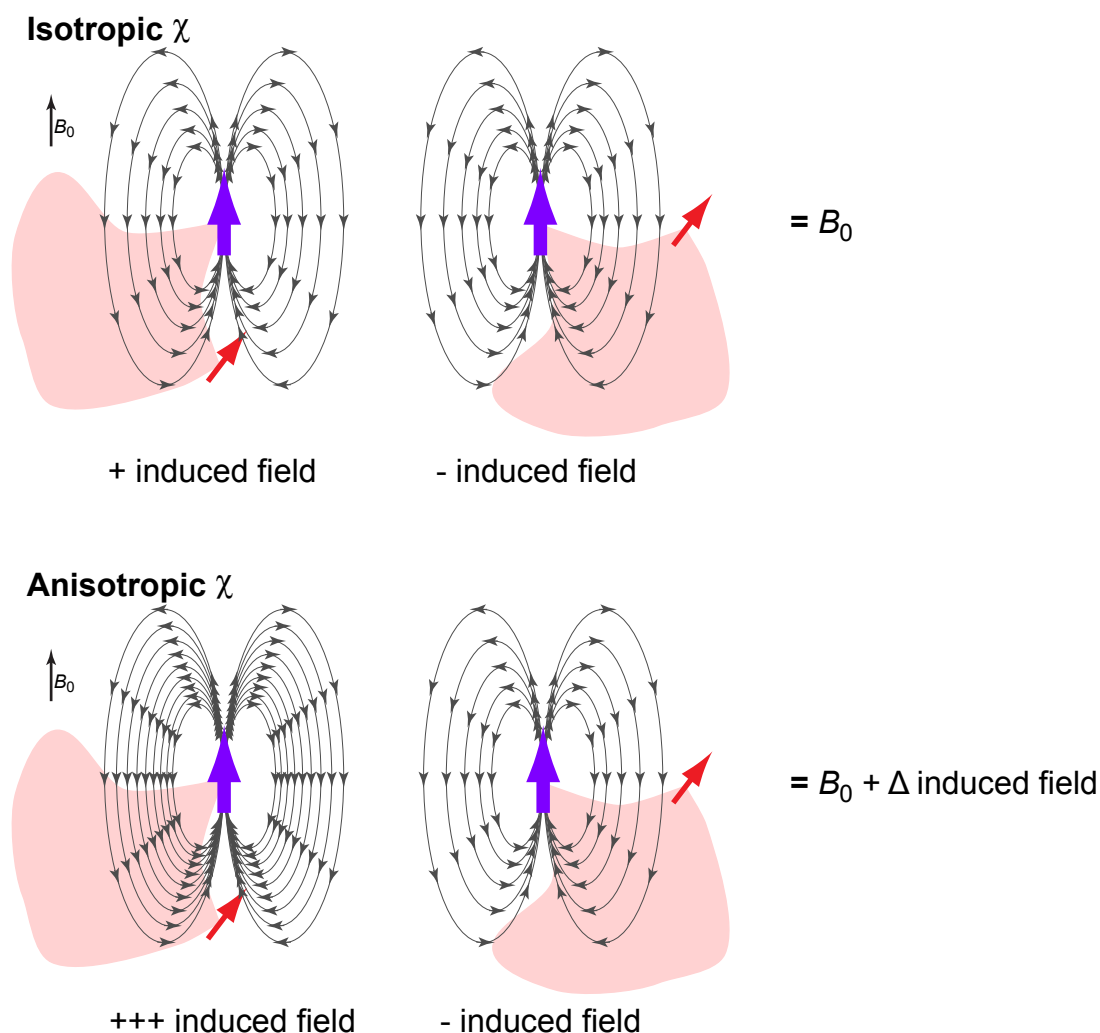


Figure 1-1 The electron magnetic moment (purple arrow) is always aligned with the B_0 field, and generates a magnetic dipole field. **Top**) The effect of the magnetic dipole field at the site of the proton spin (red arrow) averages to zero upon molecular tumbling if the χ tensor is isotropic. **Bottom**) If the χ tensor is anisotropic the magnetic dipole field changes in magnitude as the χ tensor axes reorientate with respect to B_0 , generating a net change in overall magnetic field strength at the site of the nuclear spin.

Slight deviations from diagonal shifts can arise from residual anisotropic chemical shifts (RACS),^{29,30} which are dependent on the chemical shielding anisotropy tensor (CSA tensor). This correction is small for backbone proton shifts, but can be significant for the nitrogen shift of backbone amides. Software applications such as Numbat³⁰ attempt to correct for RACS using pre-defined CSA-tensors,³¹ but typically PCSs are simply measured on proton shifts to remove the need for this correction.

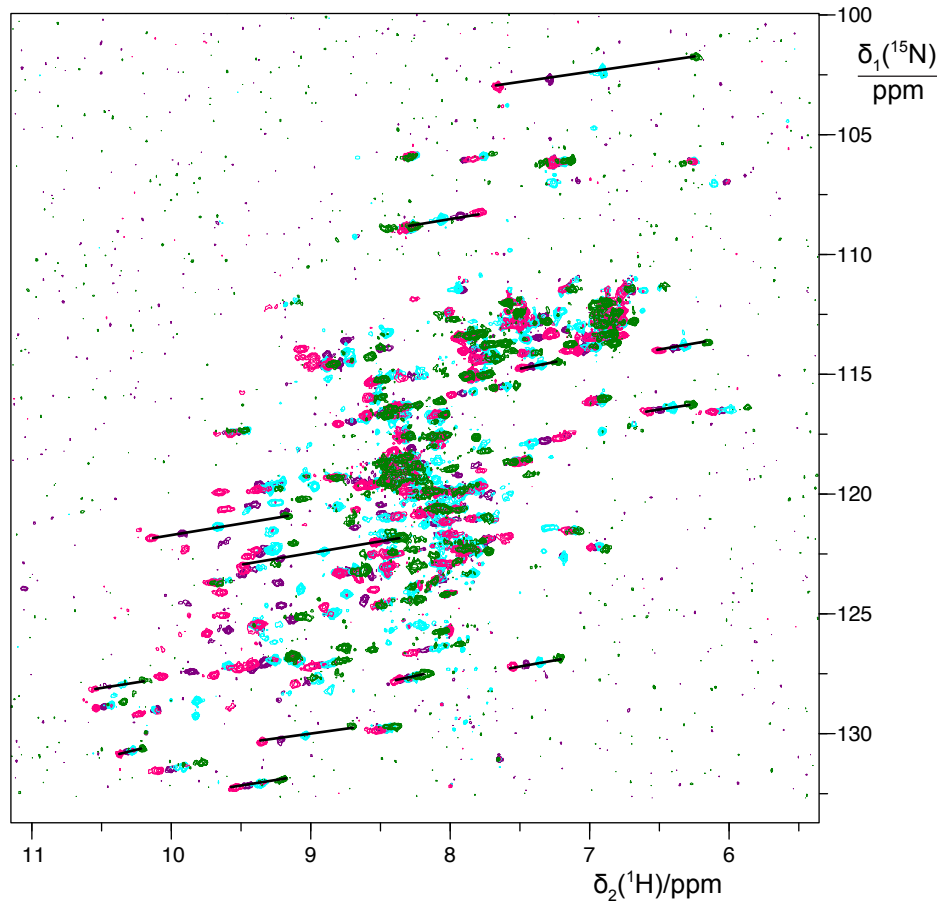


Figure 1-2 PCS can be easily measured as the change in chemical shift using ^{15}N -HSQC spectra of a paramagnetic sample (Tb^{3+} : green, Tm^{3+} : pink, Yb^{3+} : purple) and a diamagnetic reference (Y^{3+} : cyan). IMP-1 ligated with a 4-vinyl-DPA lanthanide binding tag³² to the cysteine mutant A69C. A selection of PCSs is highlighted with black bars. The samples were measured in 20 mM MES buffer, pH 6.5, 100 mM NaCl at 310 K on a Bruker 800 MHz NMR spectrometer with a TCI cryoprobe.

PCSs also display a pronounced temperature dependence arising from the definition of the $\Delta\chi$ tensor,³³ due to the temperature dependence of the spin state of the unpaired electron (equations (1.7) and (1.8)). The temperature dependence becomes apparent if the PCS is written as follows:

$$\Delta\delta^{\text{PCS}} = \frac{1}{12\pi r^3} \left(\frac{\mu_0 N_A \mu_B^2 S(S+1)}{3kT} \right) \times \left(\Delta g_{\text{ax}}^2 (3 \cos^2 \theta - 1) + \frac{3}{2} \Delta g_{\text{rh}}^2 \sin^2 \theta \cos 2\phi \right) \quad (1.15)$$

where the $\Delta\chi$ components have been substituted with Δg components, and the terms from equation (1.1) are substituted.

PCSs can be predicted accurately once the $\Delta\chi$ tensor is known. For a given molecular structure, this requires computational fitting of a minimum of eight parameters including the axial and rhombic components of the $\Delta\chi$ tensor, three Euler

angles to define the orientation of the $\Delta\chi$ tensor with respect to the molecular frame, and the three coordinates x , y and z to define the location of the metal centre. Fitting algorithms are available in software such as Numbat³⁰ or PyParaTools³⁴.

Paramagnetic Shifts for Structural Measurements

There are few cases where significant structural data have been obtained from FCSs, as they decay rapidly over few chemical bonds.^{4,28,35,36} Aside from the difficulty of measuring NMR signals of nuclei very close to the paramagnetic metal due to PRE line broadening, FCSs and PCSs occur together. It has been shown that the separation of FCSs and PCSs is possible, however, if a series of very chemically similar paramagnetic metals can be incorporated into a metal complex that is axially symmetric.³⁵ More recently, the separation has also been achieved for lower symmetry systems.³⁶ The separation is possible for lanthanide ions because of their similar coordination chemistry and ionic radii (La^{3+} - 1.04 Å to Lu^{3+} - 1.00 Å).

Measurements of PCSs have the potential to provide long-range structural information that can be obtained up to 40 Å³³ or, more recently, 60 Å²⁷ from the paramagnetic centre. The main difficulty with structure determination from PCSs is that often the $\Delta\chi$ tensor needs to be determined, which requires prior knowledge of the structure. The problem is currently approached in the PCS-ROSETTA³⁷ or GPS-ROSETTA³⁸ schemes by first predicting a structure using ROSETTA structure prediction methodology,³⁹ using the predicted structure to calculate the $\Delta\chi$ tensor and then utilising PCSs to rank the results to determine the best fitting structure. There has also been a series of attempts to use PCSs to assist NMR residue and backbone assignment,^{15,40-43} however, these methods require prior knowledge of a high-resolution structure and sometimes involve complex labelling schemes.

PCS measurements are quite sensitive to flexibility of tags or nuclear spins and will yield average PCSs if the mobility is fast on the NMR time scale. If the metal moves with respect to the protein, inaccuracies in the $\Delta\chi$ tensor fit occur, as a single tensor cannot describe PCS effects arising from different metal positions. Shishmarev and Otting investigated the implications of tag mobility in a modelling study and found that tag mobility can still be approximated by a single tensor if the largest PCS measurements are ignored or if fitting is performed on small local areas of interest such as a protein active site, rather than performing a global fit.⁴⁴

PCSs can be used to assist protein structure determinations determined by different methods. For example, PCS measurements have been used to correct crystal packing artefacts,⁴⁵ assess differences between NMR and X-ray diffraction structures³⁸ and verify homology models of ‘open’ and ‘closed’ forms of a protein that proved difficult to crystallise.⁴⁶ PCS measurements have also be used to determine structures of protein-ligand complexes,⁴⁷ small-molecule binding sites on protein surfaces,⁴⁸ protein-protein complexes⁴⁹ and as a method for fragment-based ligand screening.⁵⁰

1.2 Outline of Thesis

An application note resulting from this thesis is reproduced in chapter three, while the rest of the text describes unpublished work. Chapters two and three relate to the main body of work contained by this thesis on the IMP-1 metallo- β -lactamase. Chapter four documents the optimisation of a para-hydrogen-producing apparatus developed at the Research School of Chemistry at the ANU. It also includes a general protocol developed specifically for this apparatus. Chapter five documents the NMR work performed for a publication currently in the late stages of drafting describing a natural product identified with pro-angiogenesis properties. This work derives from a collaboration of the Research School of Biology, the Research School of Chemistry and the John Curtin School of Medical Research, all at the ANU.

- Chapter 1.** Introduction to Paramagnetic NMR and Outline of Thesis
- Chapter 2.** Biomolecular and Biophysical Analysis of IMP-1 Metallo- β -Lactamase
- Chapter 3.** Cell-Free Protein Synthesis with $^2\text{H}/^{15}\text{N}/^{13}\text{C}$ -Labelled Amino Acids in H_2O for the Production of Perdeuterated Proteins with ^1H in the Exchangeable Positions
- Chapter 4.** The Set-Up, Optimisation and Operation of an In-House Built Para-Hydrogen Producing Rig
- Chapter 5.** Promotion of Mammalian Angiogenesis by Neolignans Derived from Soybean Extracellular Fluids – NMR Elucidation of Natural Products

2 Biomolecular and Biophysical Analysis of IMP-1 Metallo- β -Lactamase

2.1 Introduction

2.1.1 β -Lactam Antibiotics

The largest group of antibacterials used in the clinic contain the β -lactam ring.⁵¹ This class of antibiotics has bactericidal properties based on the inhibition of enzymes responsible for the formation of peptidoglycan cross-linking required for cell wall biosynthesis in both Gram-negative and Gram-positive bacteria. The cell wall is essential for the survival of most bacteria to maintain osmotic stability and cell shape. The inhibition of these penicillin-binding proteins (PBPs) causes the equilibrium of cell wall biosynthesis and autolysis to become unbalanced, resulting in cell lysis.^{52,53}

There are six main structural subtypes of β -lactam antibiotics that are clinically relevant – penams (or penicillins), penems, cephalosporins, cephamycins, monobactams and carbapenems (Figure 2-1). Of these, the penams, penems, cephalosporins and cephamycins have a wide range of activity against Gram-positive and Gram-negative bacteria, whereas the monobactams are only active against aerobic Gram-negative bacteria. Finally, the carbapenems have potent and broad activity against Gram-positive and Gram-negative bacteria and are important for the treatment of multi-drug resistant bacteria. Carbapenems are currently the ‘last line of defence’ against many multi-drug resistant pathogens.⁵²

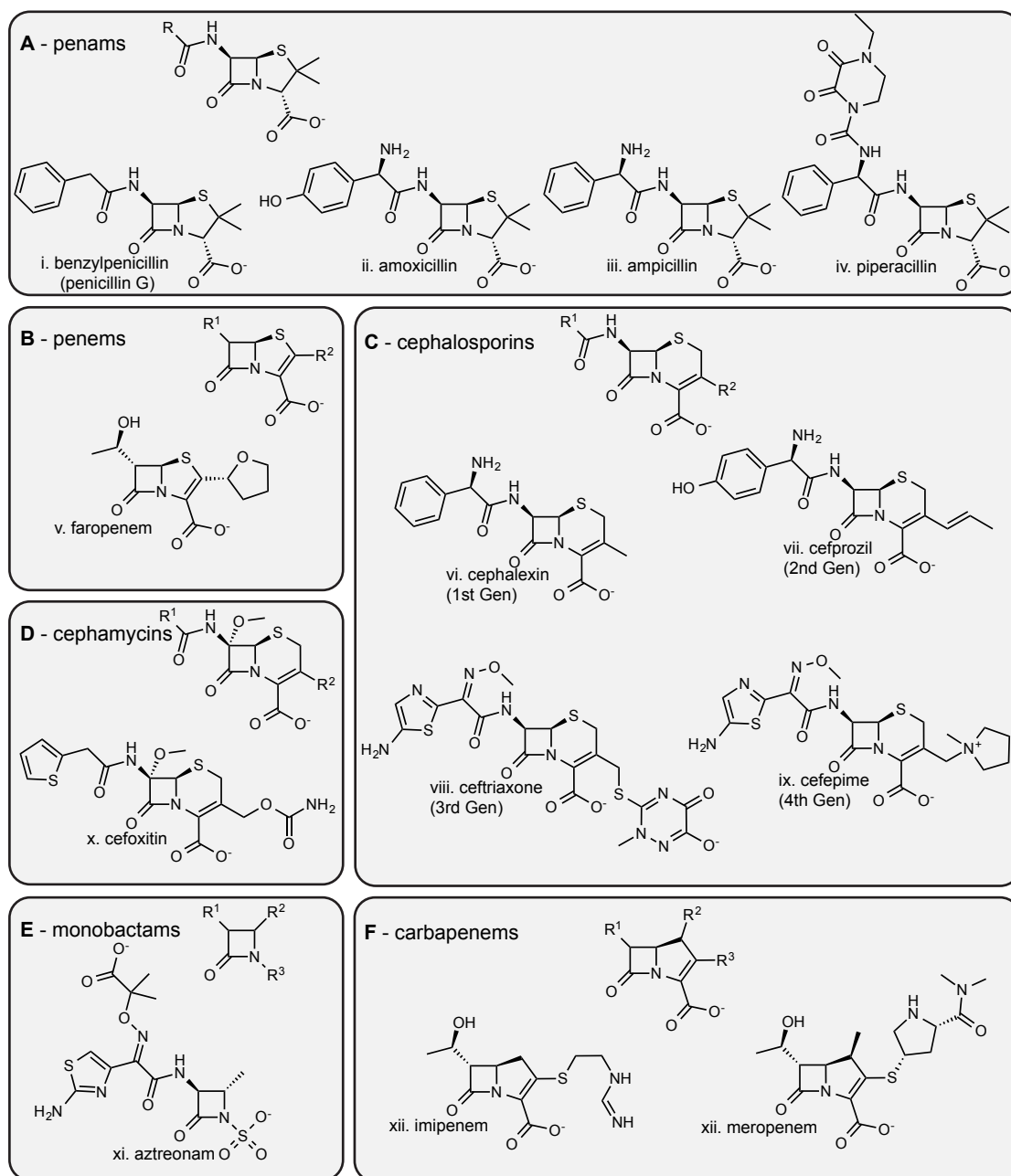


Figure 2-1 The chemical structures of clinical β -lactam drugs. **A)** The penams consist of the β -lactam ring fused with a 5-membered thiazolidine ring. The ring further destabilises the strained C-N amide bond of the β -lactam. Benzylpenicillin (i) was the first β -lactam discovered but is poor at passing through bacterial membranes. Extended spectrum penams include amoxicillin (ii), ampicillin (iii) and piperacillin (iv) and all have improved membrane penetration properties. **B)** The penems differ from the penams only by unsaturation of the fused ring. No naturally occurring penems exist and faropenem (v) is yet to attain FDA (USA) or TGA (Aus) approval. **C)** Cephalosporins have a fused 6-membered desaturated ring. They are typically classed into generations. Cephalexin (vi) is an example of the first-generation cephalosporins and is active against Gram-positive and Gram-negative bacteria. Cefprozil (vii) and other second-generation cephalosporins have extended activity against Gram-negative bacteria. Third-generation cephalosporins, including ceftriaxone (viii), have increased activity against Gram-negative bacteria, can penetrate the central nervous system and are useful in treating many hospital-acquired infections. Cefepime (ix) and other fourth-generation cephalosporins are zwitterions and have better penetration of outer membranes of bacteria. They can also cross the blood-brain barrier and so are useful in meningitis treatment. **D)** Cephamycins such as cefoxitin (x) are often classed as cephalosporins but differ by the presence of the methoxy group on the β -lactam ring. **E)** The monobactams are unique as they do not have a fused ring to the β -lactam core. Aztreonam (xi) is the only clinically available monobactam to date. **F)** Carbapenems are similar to the penams but with a carbon instead of a sulfur in the fused ring. Their structures make them resistant to most β -lactamase activity, and are often the antibiotics of last resort for many infections. Imipenem (xii) and meropenem (xiii) are both examples of ultra-broad spectrum injectable antibiotics. Chemical structures sourced from commercial supplier websites.⁵⁴

2.1.2 β -Lactam Antibiotic Resistance

Resistance to β -lactam antibiotics typically appears within 2 – 3 years after the introduction of a new antibiotic into clinical use.⁵¹ This resistance can be conferred through at least four distinct mechanisms.

Evolution of Penicillin Binding Proteins

Changing active site residues of PBPs can lower the affinity of β -lactam antibiotics without losing essential cell-wall biosynthesis activity. This subsequently increases resistance to β -lactam compounds, as is the case with the PBP2x, PBP2b and PBP2a genes in organisms such as *Streptococcus* spp., *Neisseria* spp. and *Staphylococcus* spp.^{52,53}

Downregulation of Outer Membrane Proteins

By reducing the number of outer membrane proteins, there are fewer porin channels by which the β -lactam antibiotic can enter the periplasm to inhibit the PBPs. This means that they must now diffuse directly through the outer membrane, which limits the concentration of drug at the target site. This is the case with some *Klebsiella pneumoniae*, *Escherichia coli* and *Enterobacter* spp. where the loss of the OprD gene is associated with imipenem resistance. Usually, however, this mechanism alone is not enough to confer clinically relevant antibiotic resistance and is usually found in combination with β -lactamase expression.^{52,55,56}

Evolution of Efflux Pumps

The evolution of efflux pumps to recognise and actively excrete β -lactams out of the periplasm also limits the concentration of the drug at the target site. These pumps are not only important in β -lactam resistance but other antibacterials also. This is a major component of the resistance in organisms such as *Pseudomonas aeruginosa* where the upregulation of the MexA-MexB-OprD system, along with the organism's low outer membrane permeability, attains penicillin, cephalosporins, quinolone, tetracycline and chloramphenicol resistance.^{52,53,55}

β-Lactamase Production

By far the most common mechanism of β-lactam resistance is the synthesis of a β-lactamase, an enzyme capable of hydrolysing the β-lactam antibiotic into an inactive compound.^{52,57}

2.1.3 β-Lactamases

The first β-lactamase was discovered in 1940 in *Escherichia coli* before the clinical use of benzylpenicillin.⁵⁸ It was originally thought that the enzyme was not clinically relevant as benzylpenicillin was targeted to treat staphylococcal and streptococcal infections. Now there are over 1350 identified β-lactamases,^{52,59} with many of these being clinically relevant.

The two types of β-lactamase enzymes hydrolyse the β-lactam substrate either by forming an acyl-enzyme intermediate through an active-site serine, or by utilising one or two catalytic metal ions, usually Zn^{2+} , to stabilise a reactive hydroxide molecule. Both groups of enzymes are ancient, with the serine group estimated from sequence diversity studies to have evolved with bacteria over the past 2 billion years.⁵¹ Some of the serine β-lactamases are estimated to have been encoded on mobile genetic elements for at least millions of years.⁵¹

Classification

Classification of these β-lactamases has traditionally been based on either the functional characteristics, or the amino-acid sequence of the enzymes. The most prevalent classification system based on amino-acid sequence is that described by Ambler *et al.* and defines four molecular classes based on conserved and distinguished amino-acid motifs.⁶⁰⁻⁶² Of these classes, A, C and D consist of serine β-lactamases, whereas the metallo-β-lactamases make up class B (Table 2-1).

Table 2-1 Sequence classification scheme for bacterial β-lactamasesⁱ

Main Type	Class	Distinct Conserved Amino Acids		
Metal	B	116H/N-x-H-x-D, 196H, 221C/S, 263H		
		Locus I ⁱⁱ	Locus II ⁱⁱⁱ	Locus III ^{iv}
Serine	A	70S-x-x-K	130S-D-N	234K-T/S-G
	C	64S-x-x-K	150Y-A/S-N	315K-T/S-G
	D	70S-x-x-K	144Y-G-N/H	216K-T/S-G

ⁱ data from references^{63,64}, numbering as per references⁶⁵⁻⁶⁸. An x signifies any amino acid.

ⁱⁱ locus I includes the catalytic serine and a lysine three residues away

ⁱⁱⁱ locus II corresponds to 130Ser in class A, 150Tyr in class C and 114Tyr in class D

^{iv} locus III corresponds to 234Lys in class A, 315Lys in class C and 216Lys in class D

Despite large sequence diversity in class B, the catalytic scaffold is relatively conserved and enables simple classification into three subclasses. B1 and B3 subclasses coordinate the Zn₁ site using three histidines, whereas subclass B2 utilises two histidines and an asparagine residue. Also, B1 and B2 coordinate the Zn₂ site with an aspartate, cysteine and histidine residue, whereas B3 has an aspartate and two histidines (Table 2-2). There has been some argument that B3 should form a completely distinct class due to its significant sequence difference to the B1 and B2 subclasses.⁶⁹⁻⁷¹

Table 2-2 Subclasses of class B β -lactamases and metal coordinating residuesⁱ

	B1	B2	B3
Zn₁	116H, 118H, 196H	116N, 118H, 196H	116H, 118H, 196H
Zn₂	120D, 221C, 263H	120D, 221C, 263H	120D, 121H, 263H

ⁱ numbering as per reference⁶⁷

While the sequence based system of classification is straightforward for biochemists to apply, an alternative classification system was suggested in 1989⁷²⁻⁷⁴ then updated in 1995⁷⁵ and 2010⁷⁶ by Bush *et al.* This system relates the varied enzymes by their function and defining analytical characteristics, which is perhaps more relevant given the clinical importance of the enzymes. Both the Bush and Ambler systems are used in current literature.

Table 2-3 Functional classification scheme for bacterial β -lactamasesⁱ

Group	Class	Distinctive substrate	Inhibited by CA or TZB ⁱⁱ EDTA ⁱⁱ		Defining characteristics	Representative enzymes
1	C	cephalosporins	No	No	Greater hydrolysis of cephalosporins than benzylpenicillin; hydrolyses cephamycins	AmpC, P99, ACT-1, FOX-1
1e	C	cephalosporins	No	No	Increased hydrolysis of ceftazidime and often other oxyimino- β -lactams	GC1, CMY-37
2a	A	penicillins	Yes	No	Greater hydrolysis of benzylpenicillin than cephalosporins	PC1
2b	A	penicillins, early cephalosporins	Yes	No	Similar hydrolysis of benzylpenicillin and cephalosporins	TEM-1, TEM-2, SHV-1
2be	A	extended-spectrum cephalosporins, monobactams	Yes	No	Increased hydrolysis of oxyimino- β -lactams (cefotaxime, ceftazidime, ceftriaxone, cefepime, aztreonam)	TEM-3, SHV-2,
2br	A	penicillins	No	No	Resistance to clavulanic acid, sulbactam, and tazobactam	TEM-30
2ber	A	extended-spectrum cephalosporins, monobactams	No	No	Increased hydrolysis of oxyimino- β -lactams combined with resistance to clavulanic acid, sulbactam, and tazobactam	TEM-50
2c	A	carbenicillin	Yes	No	Increased hydrolysis of carbenicillin	PSE-1, CARB-3
2ce	A	carbenicillin, cefepime	Yes	No	Increased hydrolysis of carbenicillin, cefepime, and ceftiofame	RTG-4
2d	D	cloxacillin	Variable	No	Increased hydrolysis of cloxacillin or oxacillin	OXA-1, OXA-10
2de	D	extended-spectrum cephalosporins	Variable	No	Hydrolyses cloxacillin or oxacillin and oxyimino- β -lactams	OXA-11, OXA-15
2df	D	carbapenems	Variable	No	Hydrolyses cloxacillin or oxacillin and carbapenems	OXA-23, OXA-48
2e	A	extended-spectrum cephalosporins	Yes	No	Hydrolyses cephalosporins. Inhibited by clavulanic acid but not aztreonam	CcpA
2f	A	carbapenems	Variable	No	Increased hydrolysis of carbapenems, oxyimino- β -lactams, cephamycins	KPC-2, IMI-1
3a	B (B1) (B3)	carbapenems	No	Yes	Broad-spectrum hydrolysis including carbapenems but not monobactams	IMP-1, VIM-1, CcrA L1, GOB-1
3b	B (B2)	carbapenems	No	Yes	Preferential hydrolysis of carbapenems	CphA, Sfh-1

ⁱ adapted from Table 1 in Bush *et al.*⁷⁶ⁱⁱ CA: clavulanic acid; TZB: tazobactam; EDTA: ethylenediaminetetraacetic acid

Group 1 – AmpC β -lactamases

Group 1 enzymes (class C) have been termed AmpC β -lactamases and are distinct in that they hydrolyse cephalosporins more efficiently than benzylpenicillin. They are not usually inhibited by clavulanic acid and are encoded on the chromosomes of many *Enterobacteriaceae* and a few other organisms.⁶⁸ In many organisms the expression of group 1 enzymes is low but inducible in the presence of certain β -lactams. Subgroup 1e enzymes are variants of group 1 with greater activity against ceftazidime and have been termed extended-spectrum AmpC (ESAC) β -lactamases. Group 1 enzymes are particularly significant in the clinic when the producing organism also has reduced outer-membrane permeability due to porin mutations.⁵⁶

Group 2 – Serine β -Lactamases

Group 2 enzymes include the enzymes from molecular classes A and D and make up the largest group of β -lactamases. Like group 1 enzymes, group 2 enzymes have an active site serine residue responsible for activity. The group has been subdivided into 12 subgroups. Subgroup 2a (class A) can hydrolyse penicillins but are usually inhibited by clavulanic acid. This subgroup is largely insignificant clinically as they do not hydrolyse current generation β -lactams. Subgroup 2b (class A) can also hydrolyse early cephalosporins but are also easily inhibited by clavulanic acid. Subgroup 2be comprises the extended-spectrum β -lactamases (ESBLs) and retain their activity against penicillins and cephalosporins but, in addition, can hydrolyse one or more oxyimino- β -lactams. They are still susceptible to clavulanic acid inhibition. Subgroups 2br and 2ber are similar to subgroups 2b and 2be, respectively, but have also acquired at least partial resistance to clavulanic acid. Subgroup 2c (class A) enzymes can hydrolyse carbenicillin or ticarcillin and subgroup 2ce also has expanded activity against cefepime and cefpirome. Both can be inhibited with clavulanic acid. Subgroup 2d (class D) enzymes can hydrolyse cloxacillin or oxacillin and have been referred to as OXA enzymes. Many of these enzymes have varied susceptibility to clavulanic acid inhibition, but are inhibited by the presence of NaCl.⁶⁴ Subgroup 2de and 2df also have extended activity against oxyimino- β -lactams or carbapenems, respectively. Subgroup 2e (class A) enzymes have the ability to hydrolyse extended-spectrum cephalosporins and can be inhibited by clavulanic acid. They are often confused for either group 1 or subgroup 2be, however, they are distinguished by their poor affinity for aztreonam. Subgroup 2f (class A) can hydrolyse carbapenems and can be inhibited better by

tazobactam than by clavulanic acid. Some plasmid-encoded subgroup 2f β -lactamases have been responsible for significant outbreaks of multi-drug resistant Gram-negative infections in USA⁷⁷ and Israeli⁷⁸ hospitals.

Group 3 – Metallo- β -Lactamases

Group 3 comprises the metallo- β -lactamases (class B) and all require at least one metal cation cofactor, usually zinc, for activity. They differ structurally and functionally from the other groups and are usually produced in combination with one or two other β -lactamases in clinical isolates. Prior to the discovery of groups 2df and 2f, they were functionally distinguished by their ability to hydrolyse carbapenems. They are now identifiable by their poor hydrolysis of monobactams and that they are not inhibited by clavulanic acid but are inhibited by ion chelators such as EDTA, dipicolinic acid or 1,10-phenanthroline.^{79,80} Subgroup 3a (subclasses B1 and B3) include the clinically relevant metallo- β -lactamase families such as IMP,^{*} VIM[†] and NDM[‡] that have spread globally. They require two zinc ions for maximal enzymatic activity and have a broad range of substrates. Subgroup 3b (subclass B2) enzymes are distinct in that they preferentially hydrolyse carbapenems in contrast to penicillins or cephalosporins. This subgroup differs from subgroup 3a as, mechanistically, the enzyme is most effective in hydrolysing carbapenems if only one zinc-binding active site is populated. In fact, the presence of the second zinc ion is actually inhibitory to the enzyme.^{81,82}

Clinically Available β -Lactamase Inhibitors

A naturally-occurring β -lactamase inhibitor, clavulanic acid (Figure 2-2A), was discovered in the late 1970's.⁸³⁻⁸⁵ This β -lactam is naturally synthesised by *Streptomyces clavuligerus* and shows little antimicrobial activity alone, but when combined with amoxicillin significantly lowers the MIC[§] against numerous bacteria.^{83,86} Shortly after the discovery of clavulanic acid, sulbactam (CP-45,899),^{87,88} and later tazobactam (YTR 830)^{52,89} were described (Figure 2-2B/C). Both of these compounds are penicillic acid sulfones developed by the pharmaceutical industry as synthetic compounds. These inhibitors are useful in the clinic in combinatorial drug therapy with

* IMP: metallo- β -lactamase active on imipenem

† VIM: Verona integron-encoded metallo- β -lactamase

‡ NDM: New Dehli metallo- β -lactamase

§ MIC: minimum inhibitory concentration

penam antibiotics. They are commonly administered as amoxicillin-clavulanate as Augmentin[®] (GlaxoSmithKline) and Clavamox[®] (Pfizer), ampicillin-sulbactam as Unasyn[®] (Pfizer) and Ampictam[®] (ELSaad), piperacillin-tazobactam as Tazocin[®] (Pfizer) and Piptaz[®] (Willow).

While these inhibitors are usually quite effective for the treatment of most of the serine β -lactamases (most of group 2 - class A and some class D), they are completely ineffective for group 3 (class B) β -lactamases.

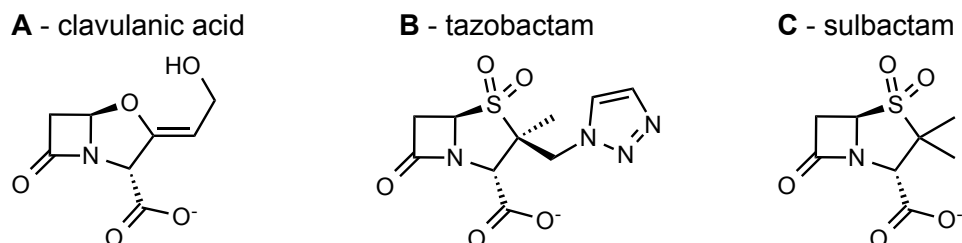


Figure 2-2 The chemical structures of **A)** clavulanic acid, **B)** tazobactam and **C)** sulbactam. The three β -lactamase inhibitors all contain the β -lactam ring, but are poor inhibitors of PBPs. Chemical structures sourced from commercial supplier websites.⁵⁴

2.1.4 Metallo- β -lactamases

Metallo- β -lactamases (M β LS) were discovered over 40 years ago, but were not initially considered a serious issue for antibiotic therapy because they were only found chromosomally encoded in nonpathogenic organisms.^{53,90-92} That view was abruptly altered by the appearance of the first acquired M β LS,⁹² encoded by mobile genetic elements that enable rapid and vast horizontal gene transfer between species and even genera of bacteria. These mobile M β LS were then able to transfer from clinically irrelevant bacteria to important human pathogens.⁹³ The most frequent M β LS present in clinically relevant Gram-negative bacterial pathogens are of the IMP and VIM type.^{92,94} Interestingly, significantly different IMP and VIM subtypes have appeared in distinct geographical areas, suggesting that the corresponding genes have been captured independently from natural reservoirs, rather than always being due to patient transfer.⁹⁴

It was also originally thought that M β L resistance was simply correlated to carbapenem use. However, studies analysing patient histories found that most had not received carbapenem therapy prior to isolation of M β L-positive strains.⁹⁵⁻⁹⁸ In a 2003 study in a Japanese hospital, only 15% of patients were identified as having been treated with carbapenems prior to *bla*_{IMP}-positive infections.⁹⁶ In fact, 22% were identified as not having been treated with any antibiotics at all.⁹⁶ As M β LS often co-exist on mobile

integrans with one or two other β -lactamases or antibiotic resistance genes, it is possible that they can be co-selected by unrelated classes of antibiotics.⁹⁷ This emphasises the complex relationship between antibiotic use and antibiotic resistance, and clearly demonstrates that limiting carbapenem consumption cannot be the only strategy for controlling M β Ls in clinical practice.

At least two new acquired M β L families have been discovered in the last 5 years. The first of the NDM family was reported in 2009,⁹⁹ and since then 10 variants have been assigned.¹⁰⁰⁻¹⁰⁴ This family of enzymes is particularly worrying as virtually all currently described isolates harbouring *bla*_{NDM} are also resistant to all commonly used non- β -lactam drugs.¹⁰⁵ NDM-1, NDM-3 and NDM-4 have been sporadically identified in Australia and New Zealand since 2009.^{106,107} At this stage, all isolates were from patients recently returning from the Indian subcontinent. Most recently, in 2013, a new enzyme named FIM-1 was reported as being identified in a *Pseudomonas aeruginosa* clinical infection in a hospital in Florence, Italy.¹⁰⁸

Activity

Unlike the serine β -lactamases, M β Ls have a wide, plastic active-site groove, which makes the group of enzymes able to accommodate most β -lactam substrates.^{109,110} Also unlike the serine β -lactamases, M β Ls are thought to not form a covalent substrate-enzyme intermediate, but rather to stabilise a catalytic water molecule or hydroxide ion to perform the hydrolysis.⁵³

Recent crystallographic works have structurally characterised bound intermediates of ampicillin, methicillin, benzylpenicillin, oxacillin and meropenem to NDM-1.^{111,112} These works have supported the hypothesised mechanism of β -lactam hydrolysis, indicated schematically in Figure 2-3, with the anionic intermediate stabilised in both group 3a and 3b enzymes by coordination with the zinc ions.¹⁰⁰

Computation docking studies have also been performed and identified two distinct substrate docking modes (Figure 2-4).¹¹³ ‘S’ conformers position the carbonyl oxygen of the β -lactam ring in coordination with Zn₁ and the negatively charged oxygen from the carboxylate in coordination with Zn₂. This positions the C-N amide bond of the β -lactam ring appropriately for hydrolysis by the bridging water/hydroxide ion. For ‘I’ conformers, the carboxylate oxygen either displaces the bridging hydroxide ion/water or simultaneously coordinates both Zn₁ and Zn₂ ions. These simulations seem

to match experimental evidence, with all ‘good’ substrates binding predominantly in the ‘S’ conformer, and ‘poor’ substrates (such as aztreonam and clavulanic acid) binding in the ‘I’ conformer.¹¹³

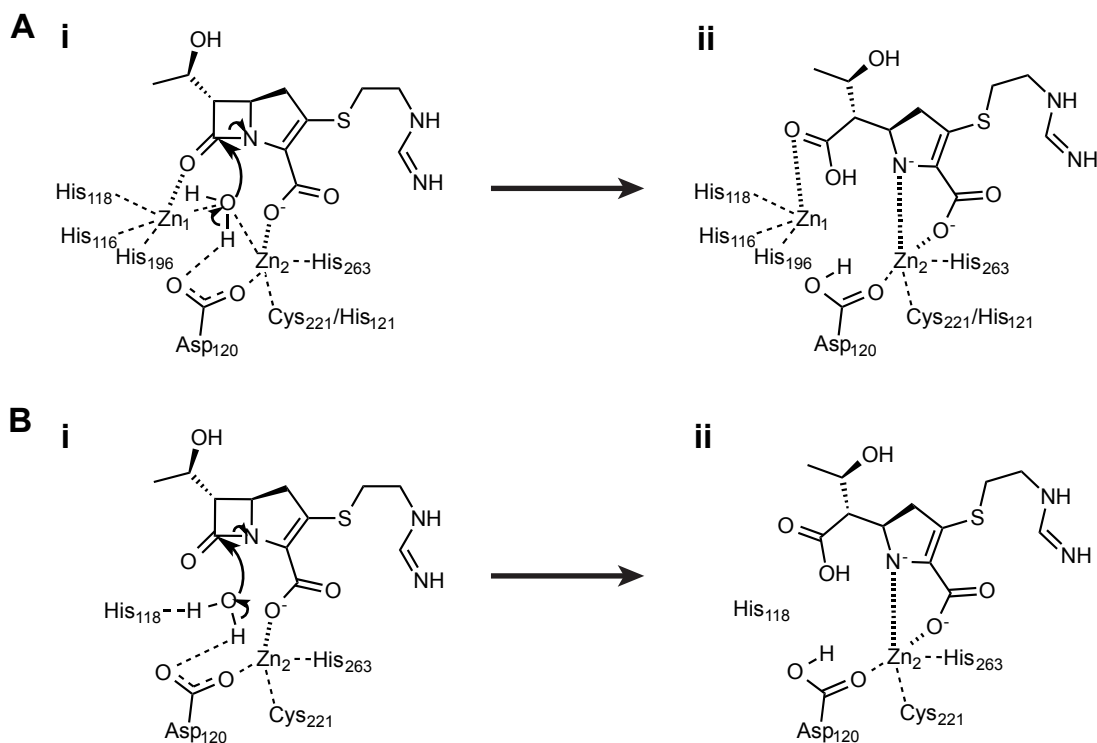


Figure 2-3 Schematic illustration of imipenem binding to a metallo-β-lactamase. **A**) In group 3a (class B1 and B3), the two zinc ions of the enzyme stabilise a bridging water/hydroxide ion and position the substrate so that nucleophilic attack on the C-N bond of the β-lactam ring can be performed. **B**) In group 3b (class B2) enzymes, a histidine and an aspartate residue position the water/hydroxide ion and the zinc ion positions the substrate. The enzyme i) positions the substrate then ii) stabilises the nitrogen anion intermediate. Figure constructed from data in reference⁵³

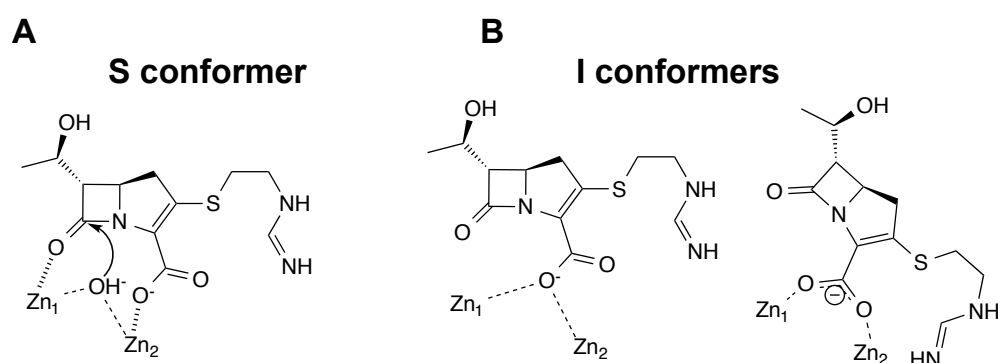


Figure 2-4 Different conformers of β-lactam binding predicted through computational docking simulations to NDM-1.¹¹³ **A**) In the ‘S’ conformer, the bridging water/hydroxide ion is positioned to perform nucleophilic attack on the C-N bond of the β-lactam ring. **B**) However, in the ‘I’ conformers the bridging water/hydroxide ion is displaced and the β-lactam is no longer positioned at the catalytic site. Figure constructed from data in reference¹¹³

While all MβLs are inhibited *in vitro* by metal chelators such as EDTA, EGTA, dipicolinic acid or 1,10-phenanthroline, these agents have no clinical significance.⁵⁷ However, at least for the IMP family, EDTA and EGTA are poor inhibitors, whereas 1,10-phenanthroline and dipicolinic acid are strongly inhibitory.^{79,114} This has ramifications for current phenotypic detection assays used in the clinic to identify MβLs, which typically rely on *in vitro* return of imipenem bactericidal activity in the presence of EDTA.¹¹⁴ The mechanism of inhibition by these polydentate chelators is argued to be not due to scavenging of the free metal but to the formation of a transient enzyme-metal-chelator ternary complex,⁷⁹ presumably in analogous way to the 'I' conformer (Figure 2-4B).

With the hope of finding novel inhibitors for metallo-β-lactamases, carbapenem derivatives,¹¹⁵ simple thiol containing molecules,¹¹⁶⁻¹¹⁸ thioester derivatives,¹¹⁹ succinic acid derivatives,¹²⁰ *N*-arylsulfonyl hydrazones,¹²¹ a series of tricyclic natural products¹²² and captopril¹²³⁻¹²⁵ have all been assayed as potential inhibitors with only partial success. No clinically available inhibitor yet exists for bacterial infections with resistance due to MβLs.^{82,126}

Expression and Cellular Location

As β-lactam inhibition of PBPs occurs at the site of cell-wall biosynthesis, the MβLs must be shuttled through the inner membrane to the periplasm of Gram-negative bacteria. They achieve this by means of an N-terminal signal peptide, which is cleaved upon transport through the inner membrane. Two potential shuttling pathways are available, either prior to or following enzyme folding. In 2009 it was determined that they are shuttled in a metal-free, unfolded form to the periplasmic space via interaction with the DnaK and Sec systems.¹²⁷ It has been reported that MβLs are also secreted, after active transport to the periplasm, into the local environment.¹²⁸

Metallo- β -Lactamase Superfamily

While M β LS share less than 25% amino-acid sequence identity,⁶⁷ structural studies of multiple M β LS indicate that they all share a unique $\alpha\beta/\beta\alpha$ sandwich fold,¹¹⁰ with the active site located at the interface between the two domains. This M β L $\alpha\beta/\beta\alpha$ sandwich fold type gave rise to the naming of the metallo- β -lactamase superfamily of 6000 metallo-enzymes defined in 1997 (Table 2-4).¹²⁹ Most of the members of the superfamily display a dinuclear metal active site, have diverse biological function⁵⁷ and are known to bind a wide range of metals including Zn(II), Fe(II), Fe(III), and Mn(II).¹³⁰ The superfamily consists of 16 families, of which only 10 have representative structures experimentally determined.^{57,131} The M β L fold is the most abundant metal-binding domain found in archaea and bacteria, and widely spread in eukaryotes.¹³⁰ The prevalence of the metal- β -lactamase superfamily has hampered drug development as any potential drug that inhibits the broad family of β -lactamases needs to avoid inhibiting the wide range of human proteins based on this fold.^{57,126,131}

The broad substrate specificity, poor inhibition by clinically available β -lactamase inhibitors and fast horizontal genetic spread make M β LS a more particularly potent threat to the existing arsenal of β -lactam antibiotics than other classes of β -lactamases.⁸²

Table 2-4 Enzymes of the metallo- β -lactamase superfamilyⁱ

Group	Enzyme family (representative enzyme)	Metal cofactors ⁱⁱⁱ	Function
1 ⁱⁱ	metallo- β -lactamases (IMP-1)	1 or 2 zinc ions	β -lactam hydrolysis
2 ⁱⁱ	glyoxalases II	2 ions – mix of zinc, iron or manganese	S-D-lactoglutathione hydrolysis
3 ⁱⁱ	flavoproteins (rubredoxin:oxygen oxydoreductase)	2 iron ions	Reduction of dioxygen
4 ⁱⁱ	arylsulfatase (tRNaseZ)	2 zinc ions	Phosphodiesterase, pre-tRNA processing
5	type II polyketide synthetases	ND	Production of actinorhodin, granaticin, griseusin, monensin, mithramycin, etc.
6 ⁱⁱ	β -CASP – RNA (CPSF-73)	2 zinc ions	Processing mRNA 3'-ends
7 ⁱⁱ	β -CASP – DNA (SNM1)	2 zinc ions	Repair of DNA interstrand crosslinks
8	comE	ND	DNA uptake
9 ⁱⁱ	choline binding protein E (Pce)	2 iron ions	Hydrolyses choline-phosphoester bonds
10	PhnP protein	ND	Alkylphosphonate uptake
11	CMP-N-acetylneuraminate monooxygenase	2 iron ions	Synthesis of N-glycolylneuraminic acid
12 ⁱⁱ	N-acyl homoserine lactone hydrolase (AiiA)	2 zinc ions	Quorum-quenching lactonase
13 ⁱⁱ	alkylsulfatase (SdsA1)	2 zinc ions	Degradation and metabolism of the biocide SDS
14	carbofuran hydrolase	ND	Hydrolysis of the insecticide carbofuran
15 ⁱⁱ	methyl parathion hydrolase (MPH)	2 zinc ions	Hydrolysis of the insecticide methyl parathion
16	class II 3', 5'-cyclic nucleotide phosphodiesterases	ND	Control of cAMP in yeast

ⁱ data from references^{57,131}ⁱⁱ groups that have at least one representative structurally characterisedⁱⁱⁱ ND: Not yet determined.

2.1.5 IMP Metallo- β -Lactamases

IMP-1 (so named as it is active on imipenem¹³²) was first discovered in a *Pseudomonas aeruginosa* strain collected in 1988 in Japan¹³³ and was the first mobile M β L identified as a source of acquired resistance to carbapenems in clinically relevant Gram-negative pathogenic bacteria. Since then, 48 members of the IMP family have been assigned in the Lahey Clinic,⁵⁹ however, citations and sequences are currently withheld for seven of these (Table 2-5).

Classification and Family

The IMP family belongs to group 3a (class B1) and its members coordinate two catalytic zinc ions. Zhao *et al.* reviewed the IMP family in mid 2011 and analysed the relation between the variants.¹³⁴ Six subgroups were defined with at least 88% sequence identity between members of the subgroups. Since then, sequences for IMP-27, IMP-28 and IMP-29 have been released and 14 new IMP variants have been reported.¹³⁵⁻¹³⁷ Figure 2-5 contains an updated phylogenetic tree including the released sequences and members of the family newly reported since 2011. Using the same method of subdivision, the previously defined six subgroups can logically be extended to eight, where IMP-27 makes up subgroup 7 and IMP-31 and IMP-35 constitute subgroup 8 (see Figure 2-5).

Table 2-5 IMP family of metallo- β -lactamases

ID	GenBank Ref.	Identity ⁱ	Ref.	ID	GenBank Ref.	Identity ⁱ	Ref.
IMP-1	S71932	100	138	IMP-25	EU541448	99.1	139
IMP-2	AJ243491	89.0	140	IMP-26	GU045307	95.2	141
IMP-3	AB010417	99.1	142	IMP-27	JF894248	81.6	135
IMP-4	AF244145	95.6	143	IMP-28	JQ407409	93.4	136
IMP-5	AF290912	94.3	144	IMP-29	HQ438058	89.4	137
IMP-6	AB040994	99.6	145	IMP-30	DQ522237	99.6	146
IMP-7	AF318077	92.5	147	IMP-31	KF148593	81.5	148
IMP-8	AF322577	89.8	149	IMP-32	JQ002629	83.3	150
IMP-9	AY033653	86.3	151	IMP-33	JN848782	86.0	152
IMP-10	AB074433	99.6	153	IMP-34	AB715422	99.6	154
IMP-11	AB074436	87.2	155	IMP-35	JF816544	83.8	156
IMP-12	AJ420864	85.0	157	IMP-36	ⁱⁱ		
IMP-13	AJ550807	85.8	158	IMP-37	JX131372	85.0	159
IMP-14	AY553332	83.3	160	IMP-38	HQ875573	95.2	161
IMP-15	AY553333	91.6	162	IMP-39	ⁱⁱ		
IMP-16	AJ584652	86.4	163	IMP-40	AB753457	99.1	164
IMP-17	ⁱⁱ			IMP-41	AB753458	86.7	164
IMP-18	AY780674	82.9	165	IMP-42	AB753456	99.6	164
IMP-19	EF118171	89.4	166	IMP-43	AB777500	92.1	167
IMP-20	AB196988	88.9	168	IMP-44	AB777501	86.3	167
IMP-21	AB204557	86.7	169	IMP-45	KJ510410	85.9	170
IMP-22	DQ361087	87.3	171	IMP-46	ⁱⁱ		
IMP-23	ⁱⁱ			IMP-47	ⁱⁱ		
IMP-24	EF192154	89.4	172	IMP-48	ⁱⁱ		

ⁱ Percentage identity to IMP-1 after sequence alignment. Signal peptides were predicted using the SignalP 4.1 Server¹⁷³ and removed prior to alignment using Clustal Omega^{174,175} on the EBI web server.¹⁷⁶

ⁱⁱ Members of the family that have been assigned an ID without sequence information or a citation yet available.⁵⁹

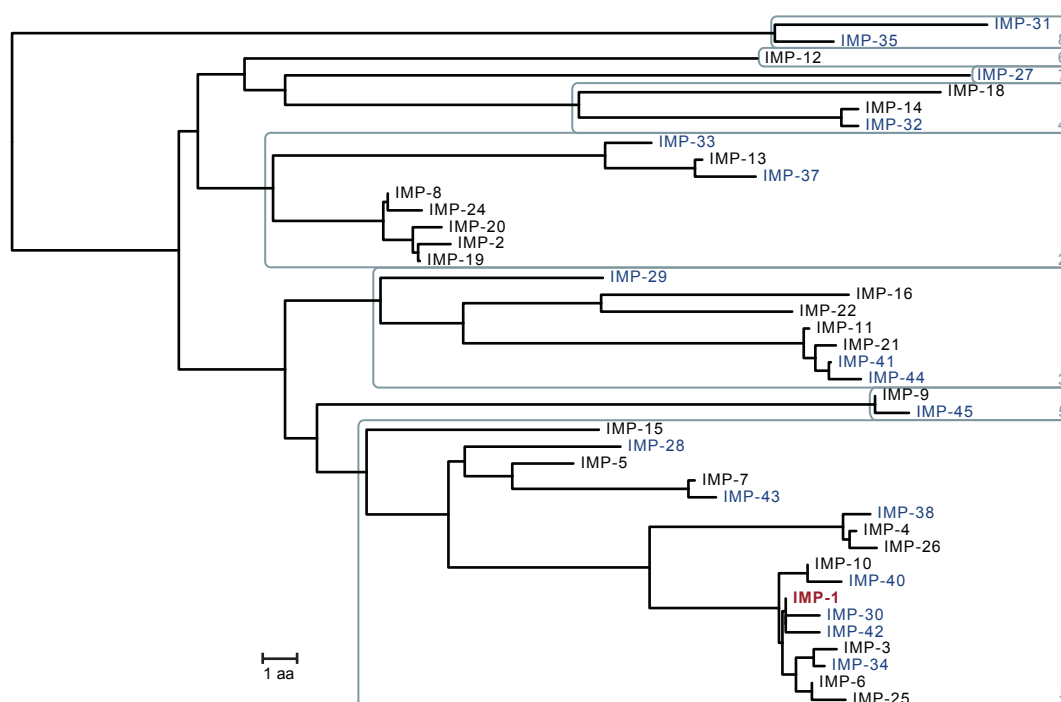


Figure 2-5 Updated unrooted phylogenetic tree of the IMP family based on amino-acid sequences. IMP-1 is highlighted in red, and IMP family members with sequences made available since the review by Zhao *et al.* in mid 2011¹³⁴ are highlighted in blue. Grey boxes indicate the subgroups – subgroups 7 and 8 are newly defined in this work. Horizontal branch lengths are drawn to scale and are proportional to the number of different amino-acid residues. The distance along the vertical axis is of no significance. The amino-acid sequences were downloaded from GenBank under the accession numbers listed in **Table 2-5**. Signal peptides were predicted using the SignalP 4.1 Server¹⁷³ and removed prior to alignment using Clustal Omega^{174,175} on the EBI web server.¹⁷⁶ The phylogenetic tree was calculated using ClustalW2-Phylogeny,^{177,178} also on the EBI web server.¹⁷⁹ Figure generated using FigTree v1.4.0.¹⁸⁰

Genetic Context

The IMP family of MβLs are typically encoded on class 1 mobile integrons and occasionally on class 3 mobile integrons. These are extremely mobile genetic elements and provide a mechanism for efficient horizontal transfer of the *bla*_{IMP} gene between bacteria. The *bla*_{IMP} gene cassette generally includes aminoglycoside resistance genes (such as *aacA4*), class D β-lactamase genes (*bla*_{OXA}) and chloramphenicol resistance genes (*catBs*).¹³⁴ This means that patient treatment with β-lactam, aminoglycoside and chloramphenicol medications results in selective pressure, favouring bacteria harbouring these multi-resistant gene cassettes and further compromising these antibiotic regimes.

Structure

To date, only IMP-1 has been crystallised while the other members of the family are yet to be structurally characterised. IMP-1 is a 228 amino-acid protein not including the additional N-terminal 18 amino-acid signal peptide that is cleaved during transport

to the periplasm (Figure 2-6). It has a molecular weight of 25.2 kDa and a pI of about 9.^{79,181}

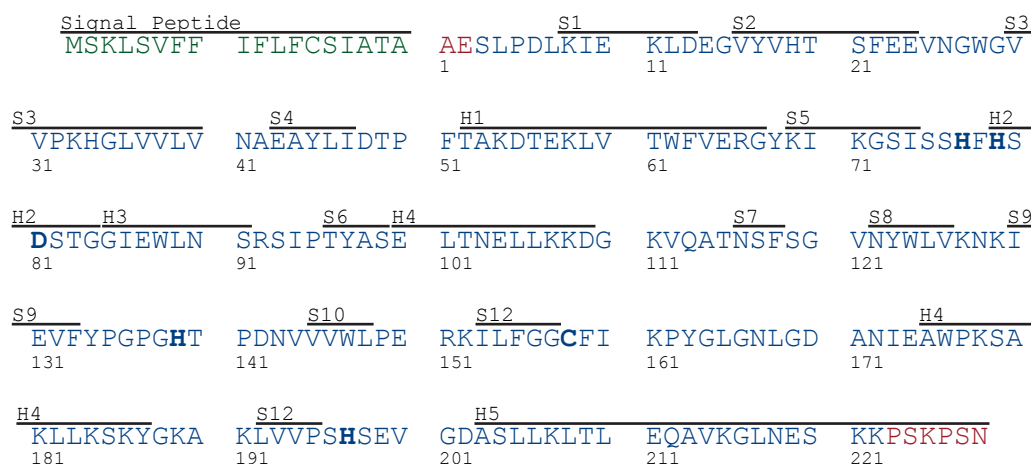


Figure 2-6 Amino-acid sequence for IMP-1 metallo- β -lactamase. The signal peptide is included at the N-terminus and highlighted in green. Residues involved with metal ligation are in bold. Secondary structure elements are also indicated (as per crystal structure 1JJE¹²⁰). Residues in red are disordered and not observed in crystal structures 1DDK¹⁸² or 1JJE¹²⁰.

Six structures for the wild type^{118,120,182,183} and four structures of single amino-acid mutants^{109,184} are listed in the PDB. The wild type structure solved to 3.1 Å resolution without any inhibitors present (1DDK) is shown in Figure 2-7. The structure shows the typical MBL $\alpha\beta/\beta\alpha$ fold with the two metal ions residing between the two β -sheets. The two zinc ions have a distance separation of 3.3 Å^{*} while for the structures of wild type IMP-1 with reversible inhibitors, the distance between the two zinc ions is 3.6 – 3.7 Å. The authors argue the difference is due to the poor resolution of the 1DDK structure (3.1 Å).¹⁸² However, it is noted that the *B*-factor of Zn₂ and its coordinating ligands are much higher than that of Zn₁ (Table 2-6). This suggests that the occupancy of the zinc ions could be lower than 100% for the Zn₂ site, which could account for the discrepancy in measured inter-metal distance.

Table 2-6 *B*-factors of the active-site zinc ions and their coordinating ligands in 1DDK¹⁸²

Residue ⁱ	Atom	<i>B</i> -factor	Residue ⁱ	Atom	<i>B</i> -factor
Zn ₁	Zn	3.13	Zn ₂	Zn	11.16
77His	N ^{δ1}	5.17	81Asp	O ^{δ2}	18.23
79His	N ^{ε2}	5.20	158Cys	S ^γ	2.10
139His	N ^{ε2}	4.44	197His	N ^{ε2}	9.49

ⁱ numbering as per Figure 2-6.

* The authors report a distance of 3.5 Å between the two zinc ions in 1DDK, however, this measurement could not be replicated.¹⁸² Measurement of this distance using the coordinate file of 1DDK currently listed in the PDB gives a distance of 3.28 Å.

The bridging water/hydroxide ion was not observed in this structure and this was also originally attributed to the low resolution,¹⁸² however, an acetate ion was cocrystallised into the active site with one of the oxygens bound to both zinc ions. This binding of acetate to the active site is echoed in another structure at 3.0 Å resolution (1WUP).¹⁸⁴ It is more likely that the acetate ligand has replaced the bridging water/hydroxide ion in both of these cases, rather than the water/hydroxide ion not being observable.

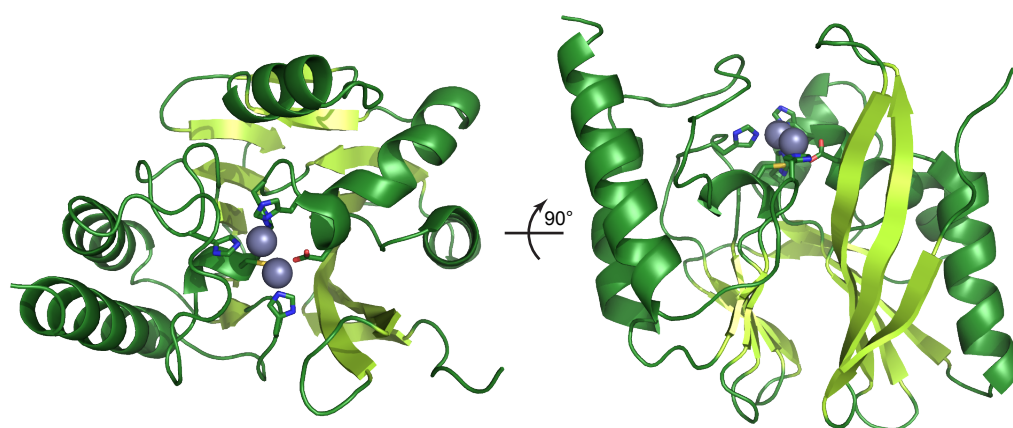


Figure 2-7 Structure of IMP-1 metallo-β-lactamase (1DDK).¹⁸² Grey spheres indicate zinc ions. Side chains are depicted for residues involved in metal ligation. α-helices and loops are depicted in dark green, and β-sheets are highlighted in light green. The αβ/βα fold is particularly evident in the orientation of the structure on the right.

The highest resolution structures of the wild-type enzyme were solved to 1.8 Å with biaryl succinic acid inhibitors (1JJE and 1JJT).¹²⁰ These structures, along with all the other structures of inhibitor bound IMP-1, have a sulfur or oxygen atom from the inhibitor replacing the coordination site of the bridging water/hydroxide ion, ligating to both zinc ions similar to the ‘I’ conformer mentioned earlier (Figure 2-4). This adds weight to the previously proposed mechanism of inhibition of group 3a MβLs.¹¹³ Following this logic, it could be conceived that the acetate ion, found in 1DDK and 1WUP, acts as an inhibitor, albeit a poor one.⁷⁹

Relevance of IMP-Type MβLs in Australia

In Australia, the predominant type of carbapenem resistance detected is due to IMP-4,¹⁸⁵ identified at the Alfred Hospital (Melbourne, Australia) in 2002¹⁸⁶ and then linked to a large clinical outbreak at the same hospital in 2004 and 2005.^{98,187} In this outbreak, 62 patients were identified as carrying MβL-producing organisms, of which 40 were either inpatients or recently discharged (within 48 hours) from the Intensive Care Unit (ICU), and the other 12 had a prior ICU stay within 2 months. 72 isolates of

MβL-producing organisms belonging to 8 different genera of pathogenic bacteria were collected during the outbreak. Genotypic characterisation determined all the isolates to contain an IMP-type MβL gene and all sequenced isolates identified the presence of *bla*_{IMP-4}. It is proposed that the presence of MβL-producing organisms contributed to 15 (65%) of the 23 deaths in this group. A further 6 new cases were identified in the 8 months following the study.⁹⁸

In September 2006, a patient known to be *bla*_{IMP-4} positive was transferred from another Sydney hospital to the Burns Unit (BU) at the Concord Repatriation General Hospital (CRGH) (Sydney, Australia).¹⁸⁵ A clinical outbreak of *bla*_{IMP-4} followed, lasting at least until August 2012. 92 MβL-producing isolates were detected in 63 patients at the CRGH during the study, of which 55% were related to the BU. All isolates were *bla*_{IMP-4} positive except for a single non-BU case of *bla*_{VIM-1}. During the 6-year study, 1.5% of BU patient admissions were deemed to acquire an MβL-producing infection during their stay. Fortunately, most cases consisted of asymptomatic colonisations rather than clinical infections, and no deaths were attributed to IMP-4 producing bacteria during the study. 71 environmental isolates, predominantly from shared patient shower facilities, were confirmed to be MβL positive. The persistence of multi-drug resistant Gram-negative bacteria in mostly wet areas, despite heightened hospital disinfection protocols, highlights the need to pursue more effective cleaning and sterilisation techniques, especially for areas such as plumbing and drains that are susceptible to biofilm formation.¹⁸⁵

Subject of Study

Protein NMR analysis can provide valuable structural and dynamic information that is unavailable through other analyses such as X-ray crystallography. However, NMR analysis of β-lactamases has been limited to date, with BMRB assignment entries for only TEM-1 (class A – group 2b, BMRB: 6042, 6357, 7236-7239), and CcrA (class B1 – group 3a, BMRB: 4102). IMP-1 is the subject of the present study as a representative of the IMP family and group 3a metallo-β-lactamases. To the best of my knowledge, no protein NMR studies have been performed on IMP-1 or any IMP-type metallo-β-lactamase to date.

2.1.6 Anomalous X-Ray Scattering

Anomalous X-ray scattering experiments were used in this project and are briefly introduced here.

Normal X-ray scattering applies only for X-radiation that is far removed from any resonant frequency of the atom. However, if the X-ray source is close to the resonant frequency of the atom, scattering is damped due to absorption of the X-radiation energy. This leads to resonant-scattering terms:¹⁸⁸

$$f = f_o + f' + if'' \quad (2.1)$$

where f is the total scattering, f_o is the normal scattering and the real and imaginary terms f' and f'' are the change in amplitude and phase of the scattering between two X-ray energies, respectively. The f' and f'' terms are often small in respect to f_o and so were initially only investigated in early X-ray scattering experiments for the purpose of applying a wavelength dependent correction for the ‘anomalous scattering’. The wavelength dependence is element specific and can be derived by theoretical approximation¹⁸⁹ using accessible tools such as the online interface implemented at the Biomolecular Structure Center.¹⁸⁸ The values of f' and f'' change most drastically at the ion absorption edge, as depicted in Figure 2-8.

After the adaptation of tuneable X-ray sources at synchrotrons, anomalous scattering, which is now sometimes referred to as resonant scattering, can be useful for the identification of element type. By tuning the X-radiation source to the ion edge, large anomalous scattering coefficients can be observed and identification of metal ion type can be assigned.¹⁹⁰ This is particularly useful in determining metal ion type in multinuclear binding sites.

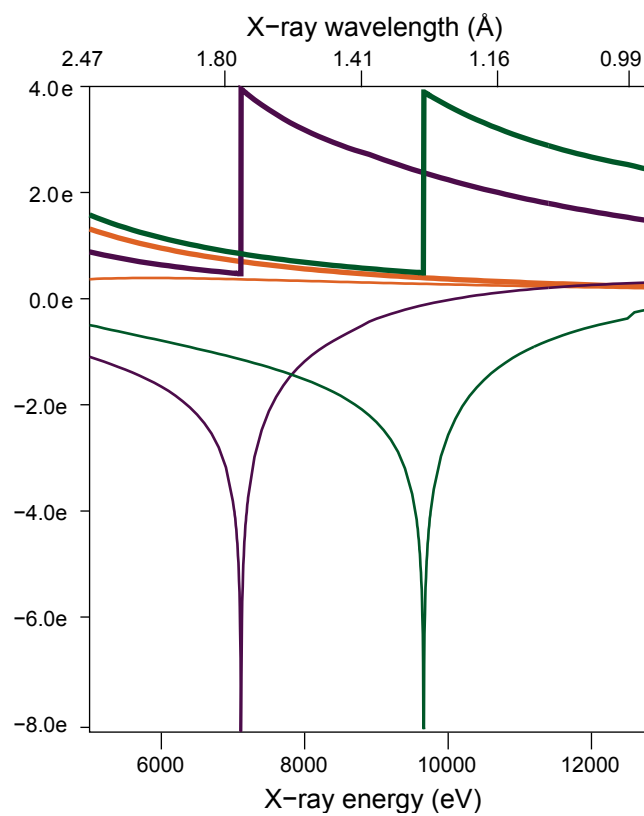


Figure 2-8 Plot of the theoretical anomalous absorption and dispersion coefficients, f' (light line) and f'' (heavy line), for sulfur (orange), iron (purple) and zinc (green).^{188,191} The sulfur, iron and zinc κ absorption edges are at 2472.0, 7112.0 and 9658.6 eV respectively.¹⁸⁸

2.2 Results: Initial System Optimisations

Expression, purification and NMR protocols were optimised prior to dedicated analysis of the IMP-1 enzyme.

2.2.1 *In vivo* Expression of IMP-1

The recombinant expression of IMP-1 from *E. coli* was optimised based on the protocol by Sivashanmugam *et al.*¹⁹² Two rounds of colony selection were performed to find highly expressing colonies. Further selection for triple-labelled protein was also performed using 70% D₂O rich media plates as recommended.¹⁹² Expression yields were found to be optimal for cultures expressing at 25 °C for 20 to 22 hours. This is consistent with literature reports for IMP-1 and other metallo- β -lactamases.¹²⁸

Starter culture conditions were found to have a significant impact on expression yield. Much higher yields were obtained by using a two-step starter culture that was then concentrated for expression. Optimal and reproducible yields were obtained by using a 50 mL starter culture, grown for 8 hours, to inoculate a 1 L culture grown for 16 hours. The cells from this culture were then spun down and resuspended into 200 mL of defined media (section 2.9.2).

It was also discovered that, after resuspension of the cells in minimal media, the pH of the culture had dropped to a level close to the limit of the buffering capability of the phosphate buffer, and would drop to below pH 4.1 in less than 5 hours after induction (Figure 2-9), and as low as pH 3.5 after 22 hours. Adjusting the pH of the culture directly after resuspension to between 8.0 and 8.4 with dilute NaOH or KOH regained control of the pH for the duration of the expression. It was noted that increasing the phosphate buffer concentration also improved pH stability, however, this alternative was abandoned as large amounts of precipitant, presumably insoluble metal phosphate salts, formed in the media prior to resuspending the bacterial cells.

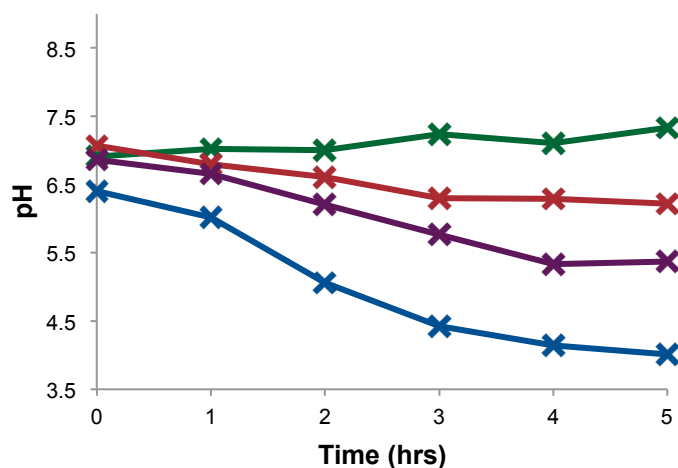


Figure 2-9 pH of the high cell density defined media after induction with 1 mM IPTG. The pH of the media dropped to less than 4.1 in under 5 hours after induction (blue). Even adjusting to pH 7.5 one hour prior to induction (purple) still allowed the media to drop outside the buffering capability of the phosphate buffer by 3 hours, whereas ‘overshooting’ to pH 8.0 to 8.4 one hour prior to induction (red) maintained a suitable pH range for the entire expression time course of 22 hours (data not shown). Adjusting the pH to 7.2 hourly (green) also maintained pH stability, but gave no increase of protein yield.

Finally, it was noted that, due to the high cell density protocol, a large amount of genomic DNA was present in the lysate prepared for purification and the lysate was still viscous even after long centrifuge runs at 32,000 g. While protein was obtainable from the thick lysate after filtration, a significant increase in the yield of purified protein was obtained if the lysate was treated with DNase I prior to the centrifugation step. This also reduced the viscosity of the lysate and facilitated filtering prior to chromatography.

Using the method described in section 2.9.2, the typical yield of isotope-labelled, purified protein was approximately 220 mg/L of labelled media, or 45 mg/L of initial rich media growth culture.

2.2.2 Purification of IMP-1

The initial purification protocol from *P. aeruginosa* expressions described by Watanabe *et al.* used an ammonium-sulfate precipitation followed by ion exchange chromatography and, finally, two size exclusion columns.¹³³ Laraki *et al.* and Goto *et al.* later improved the purification method of the enzyme from *E. coli* overexpression to a cation exchange separation followed by either anion exchange or size exclusion chromatography.^{79,193} This was simplified to a single cation exchange column in the present work (section 2.9.6). After binding the crude protein sample onto the SP Sepharose column using 50 mM HEPES at pH 7.5, a wash step with 100 mM NaCl was applied for 1 column volume, followed by a linear gradient from 100 to 500 mM NaCl

over 5 column volumes. Fractions were collected and pooled for a single peak evident in the UV₂₈₀ trace. This shortened the protocol down to a single column, dramatically reducing both the purification time and buffer use. Employing this method, purity of greater than 95% (estimated from SDS-PAGE) was easily obtained (Figure 2-10). This purification method, followed by rapid desalting via gravity-flow gel filtration and concentration via ultrafiltration, enabled completion of the entire process, from harvesting the cells from the expression media to a prepared NMR sample, in less than 4 hours.*

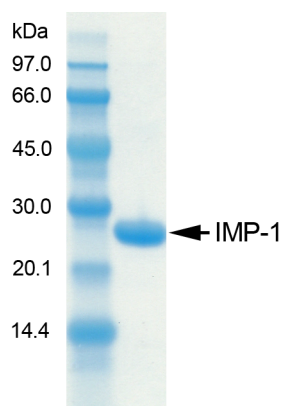


Figure 2-10 15% SDS-PAGE showing the typical high purity obtained for IMP-1 (highlighted by black arrow) after only SP Sepharose cation exchange chromatography with a shallow NaCl gradient.

It was noted early in the project that cell-free samples gave very little signal in the NMR experiment, however, a coarse purification through a short SP cation exchange column resulted in the expected signals (Figure 2-11).[†] This prompted the development of a rapid parallel method of rough purification using Amicon Pro Affinity Concentrators (Millipore) (section 2.9.6).

* It is noted that a somewhat similar single-column purification protocol was developed concurrently elsewhere,¹⁹⁴ however, the method described here avoids lengthy dialysis steps and is more specific to the high yields obtained from the high-cell-density protein production method used in this work.

[†] The initial observation and suggestion to purify cell-free products was by A/Prof. X.-C. Su prior to the commencement of this PhD project. This observation was confirmed by the author, as demonstrated in Figure 2-11.

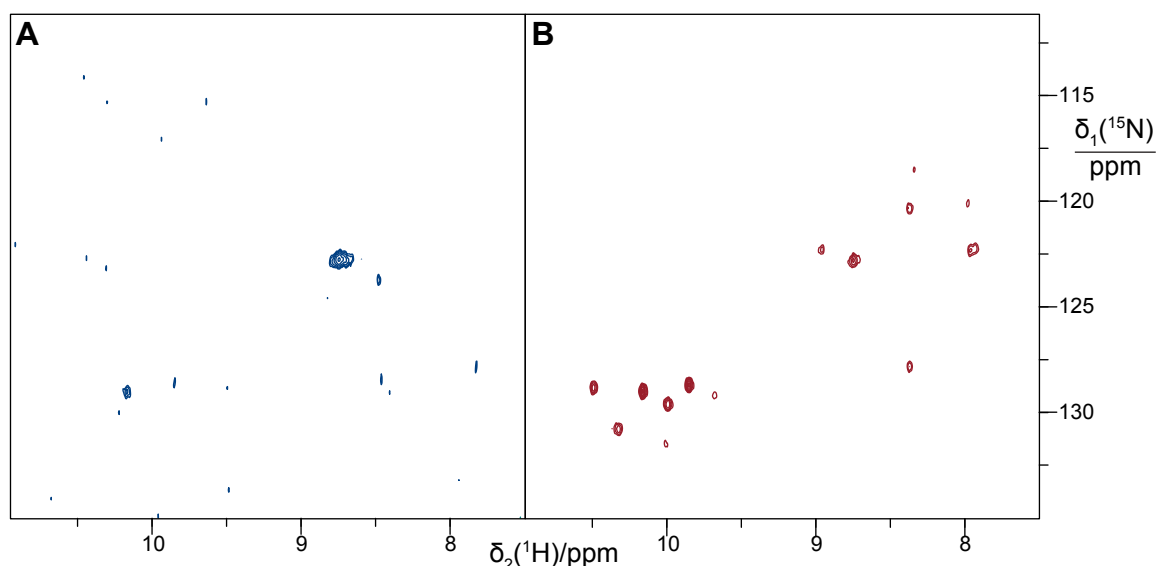


Figure 2-11 ^{15}N -HSQC spectrum of IMP-1 labelled with ^{15}N -Trp, Cys, Met and Gln either **A)** after 2.5×10^8 -fold dilution of unbound small molecules using an ultrafiltration device or **B)** following rapid purification through a short SP cation exchange column. Purification of cell-free products is essential to observe NMR signals. Samples measured in 20 mM MES pH 6.5 at 298 K.

2.2.3 NMR Conditions

NMR experiments formed the foundation of the project, and the early optimisation of NMR conditions was essential. Initial NMR spectra recorded were noted to have large variations in signal intensity, specifically with the more dispersed signals where many cross-peaks in a 3D HNCA experiment were missing. Therefore, the NMR conditions for the enzyme were optimised using the 1-1 echo experiment¹⁹⁵ (Figure 2-12) in the manner described by Anglister *et al.*¹⁹⁶

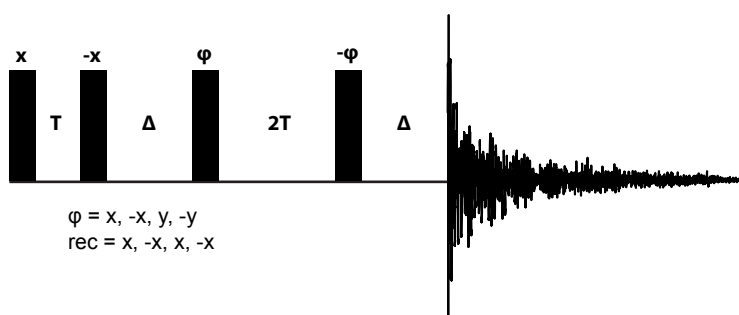


Figure 2-12 1-1 echo NMR experiment. Black bars indicate $\pi/2$ hard pulses. Delay $T = (1/4\delta)$ (85 μsec at 600 MHz), where δ is the frequency difference between the water resonance and the amide protons. The relaxation delay Δ is varied to obtain an estimate of the transverse relaxation time T_2 .

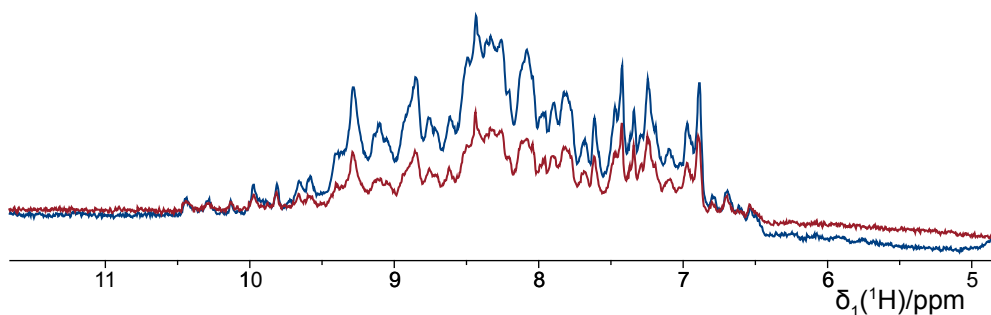


Figure 2-13 1-1 echo NMR experiment result, where $\Delta_{\text{red}} = 8$ ms and $\Delta_{\text{blue}} = 2.4$ ms. Intensity ratio of amide signals estimated by scaling the 1D spectrum in overlay display in TopSpin software (in this case: $I_{\text{red}}/I_{\text{blue}} \approx 0.5$).

Using different Δ delays, a rough estimate for τ_c can be made by comparing the intensities of 1D spectra (Figure 2-13) applying the relationships in (2.2),¹⁹⁶

$$\begin{aligned} T_2 &\approx \frac{2(\Delta_A - \Delta_B)}{\ln \frac{I_A}{I_B}} \\ \tau_{c(\text{ns})} &\approx \frac{1}{5T_{2(\text{s})}} \end{aligned} \quad (2.2)$$

where Δ is the variable delay and I is the average peak height of the amide region.

Initial results in 50 mM HEPES, pH 7.0 at 298 K, gave τ_c estimates of approximately 19 ns, consistent with a protein size of about 48 kDa. This suggested that dimerisation may be occurring under these conditions so a series of temperatures, buffers and salt additives was tested to find conditions consistent with the monomeric form. Final conditions of 20 mM MES buffer (pH 6.5) with 100 mM NaCl at 310 K yielded a τ_c estimate of 11 ns, which correlates with the monomeric mass of 25 kDa. The protein was found to be very stable under these conditions and NMR spectra could be recorded for several weeks with minimal product degradation observed.

2.3 Results: Identification of an Iron-Binding IMP-1 Species

2.3.1 Identification of Purple Pigment in IMP-1 Protein Preparations

It was noted that several high expression trials of the enzyme had a purple colouration after purification, which was unexpected for a zinc-binding enzyme (Figure 2-14). To the best of my knowledge, this purple colouration of IMP-1 had not been described previously apart from a brief comment by Moali *et al.*,¹⁹⁷ noting a dark violet pigment for a highly expressing single mutant of another metallo- β -lactamase, BcII, which included a loop from IMP-1 (EVNGWGV). The reported removal of the pigment by dialysis against 100 mM citrate, followed by dialysis against 50 mM HEPES (pH 7.5) with 1 mM ZnSO₄ implies the possibility of the colouration being due to a contaminating metal ion, as the citrate potentially acted as a chelating agent. Initial NMR spectra of the violet IMP-1 samples in this study showed many examples of peak doubling, which would also be consistent with the notion that a contaminating metal was coordinating the enzyme (Figure 2-15).

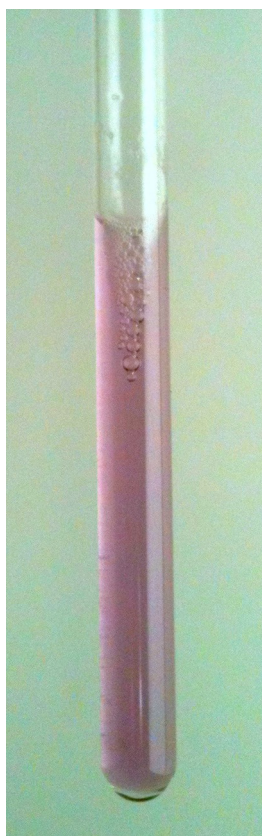


Figure 2-14 Purple coloured sample of IMP-1 in a 5 mm NMR tube.

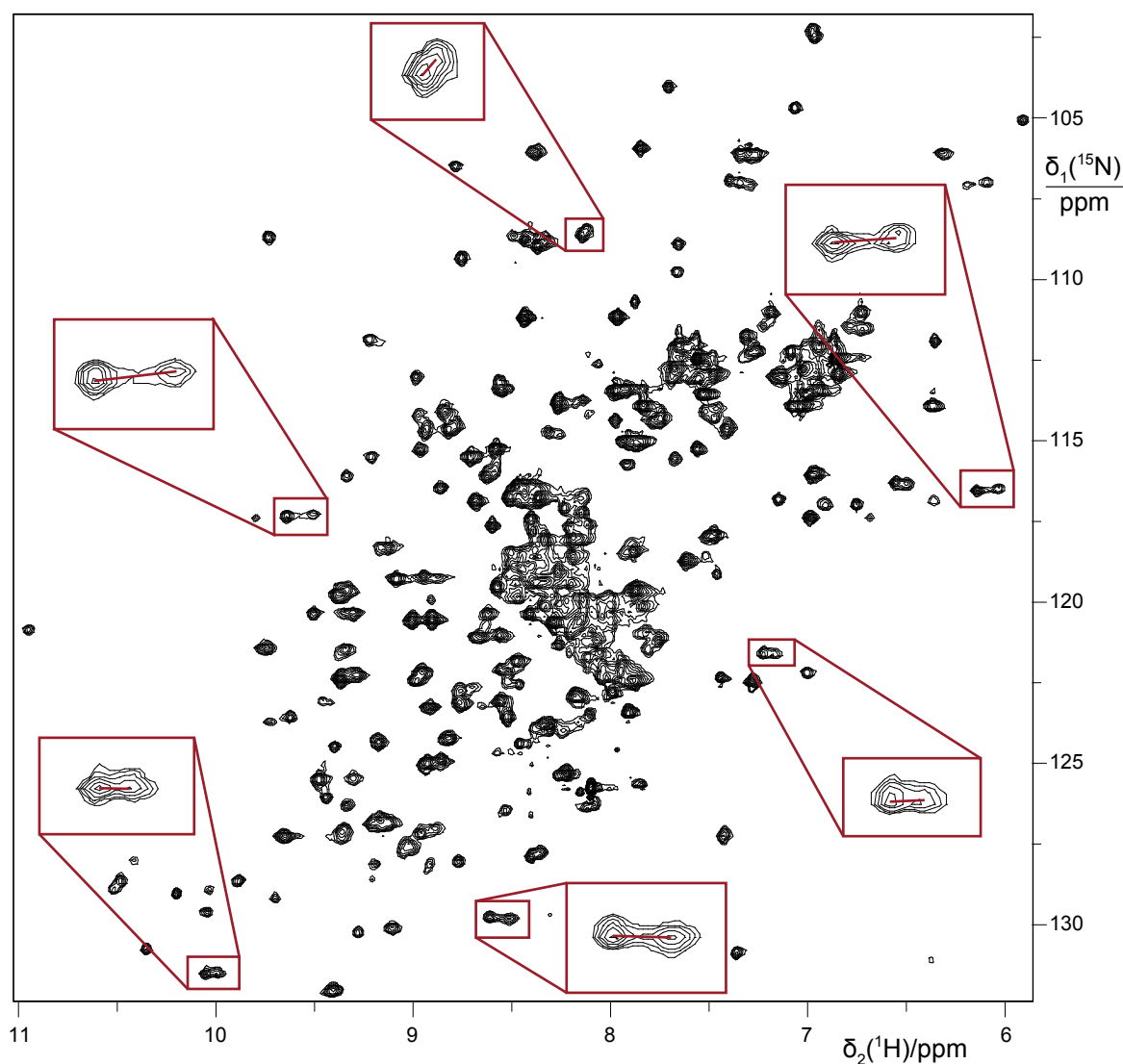


Figure 2-15 ^{15}N -HSQC spectrum of purple coloured IMP-1 metallo- β -lactamase. Several examples of peak doubling are highlighted in red boxes, with peaks belonging to the same residue linked by a red bar. This peak doubling is consistent with a mixed sample containing different metal cofactors.

To assess whether one of the metals present in Studier's $1,000 \times \text{Me Mix}$ ¹⁹⁸ was contaminating the protein preparation, a series of expressions lacking one of the trace elements was prepared and purified. All the preparations expressed reasonably, although there was an approximately 50% reduction of yield from the sample lacking zinc, and 25% reduction for the sample lacking iron. All the purified preparations were still slightly purple-tinged except for the sample lacking iron. A literature search revealed examples of other purple coloured iron proteins such as the purple acid phosphatases^{128,199}, and ferritin^{200,201}, which were reported to gain their colour due to an Fe(III)-tyrosinate complex.

The possibility of iron being associated with the IMP-1 sample was supported by mass spectrometry performed at the mass spectrometry facility at the University of

Wollongong^{*} under denaturing conditions (50% MeOH and 0.1% TFA). A fragmentation peak was observed with an isotope pattern matching an iron-containing complex (Figure 2-17).

A colourimetric test for iron was also run using 1,10-phenanthroline (section 2.9.8). The colour change suggested the presence of iron (Figure 2-18). Each of the metals included in Studier's 1000 × Me Mix¹⁹⁸ were then tested to ensure that the 1,10-phenanthroline test was specific for iron (Figure 2-19). No other metal in the trace metal mix reacted to give the red colour obtained for the IMP-1 sample, so it was concluded that iron was present in the enzyme preparation.

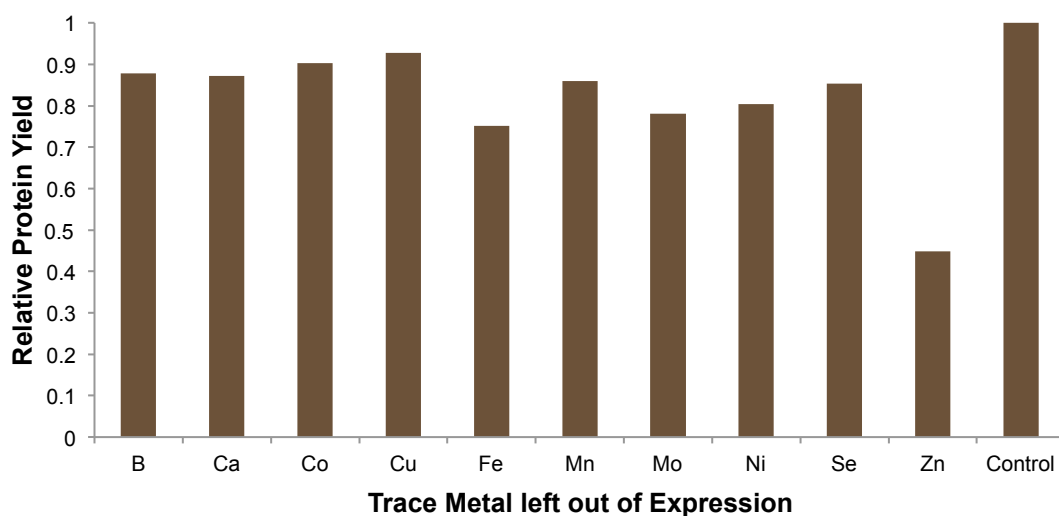


Figure 2-16 Expression yield estimate for samples expressed by omitting one of the metals at a time from the 1000 × Me Mix in Studier's defined media.¹⁹⁸ No attempt was made to remove all trace metal impurities from other buffers. 50% loss of yield was observed for the sample not supplemented with zinc, and yield of the sample without iron supplement was reduced by 25%. None of the samples performed as well as the control, indicating that a full complement of trace elements improves the protein yields.

^{*} Mass spectra were recorded by Prof. T. Huber and Dr K. Loscha

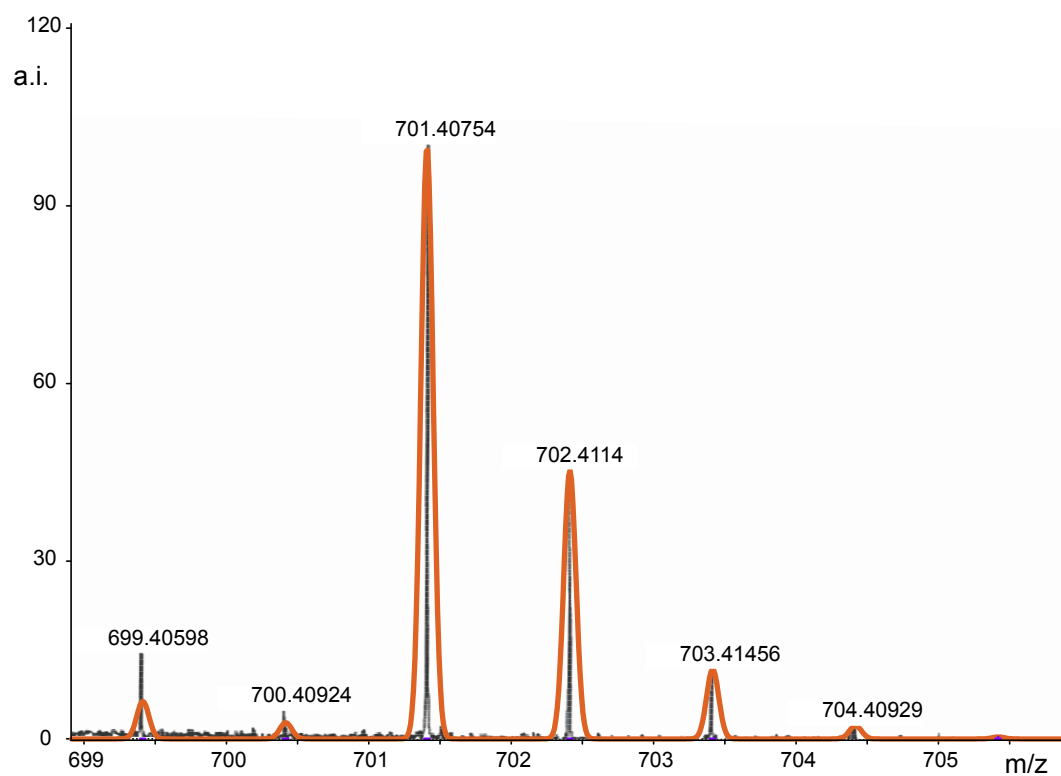


Figure 2-17 ESI+ mass spectrum of IMP-1 under denaturing conditions (50% MeOH, 0.1% TFA) in black. The peak at 701.4 displays the typical isotope distribution of iron, simulated in orange (for a $\text{FeC}_{39}\text{H}_{65}\text{O}_7$ molecule) using mMass.²⁰⁰

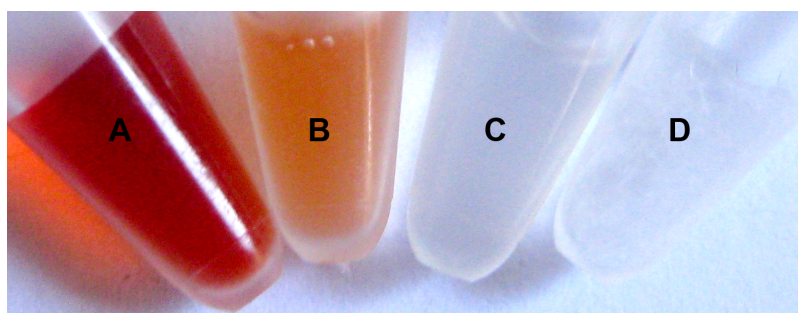


Figure 2-18 The Fe(II) complex with 1,10-phenanthroline (**A**) produces a strong blood red colour, whereas the Zn(II) complex (**D**) forms a white precipitate. After reduction with TCEP, treatment of the IMP-1 sample (**B**) produced the expected red colouration. A negative control (**C**) without 1,10-phenanthroline shows the background colour of the reduced sample.

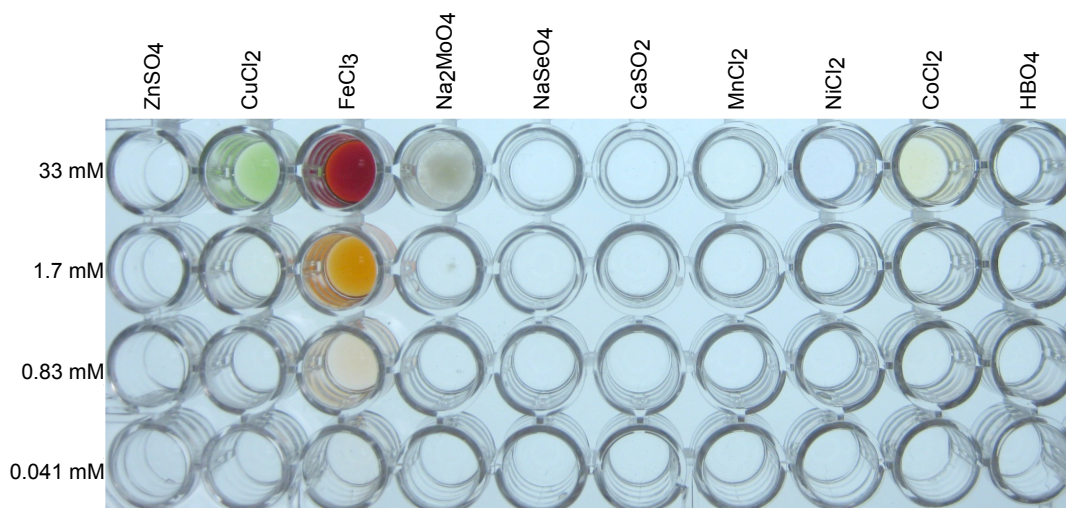


Figure 2-19 1,10-phenanthroline was found to be specific for the presence of iron among the metals of Studier's 1000 x Me Mix.¹⁹⁸ Metal solutions were reduced with approximately 100 mM TCEP prior to treatment with 1,10-phenanthroline.

Finally, quantitative metal analysis using inductively coupled plasma optical emission spectroscopy (ICP-OES) (section 2.9.9) at the microanalysis unit at the Research School of Chemistry, ANU confirmed that up to 0.7 equivalents of iron per protein molecule were present in the purple preparation of IMP-1 (Figure 2-20).

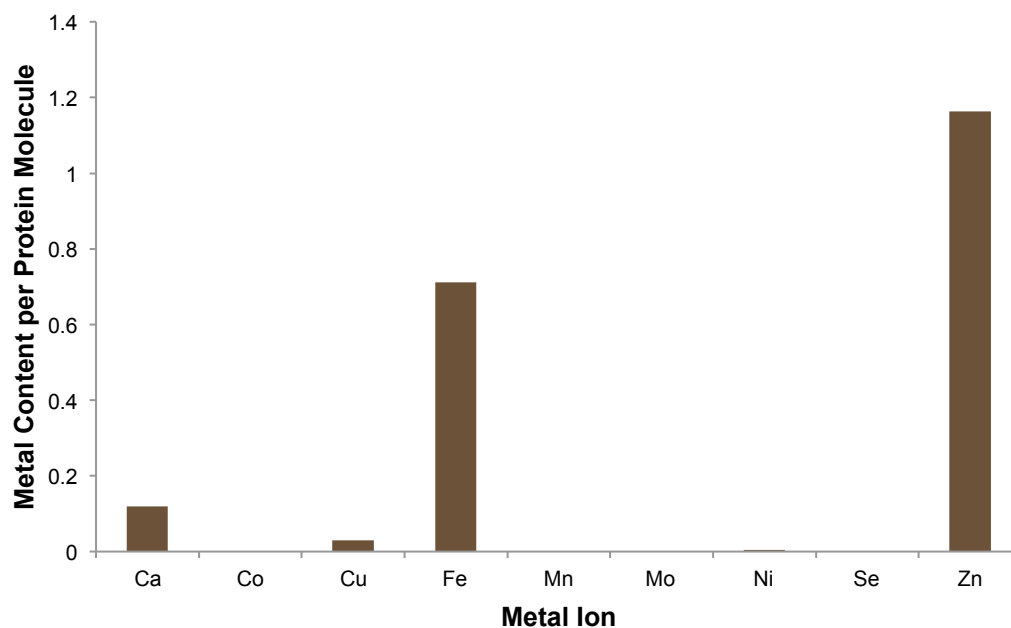


Figure 2-20 ICP-OES metal analysis of violet IMP-1. Results show cobalt, manganese, molybdenum, nickel, and selenium at trace levels. 0.03 equivalents of copper and 0.12 equivalents of calcium were also found, however, were not observed at as high a level after optimisation of the ICP-OES experiment conditions. 0.71 equivalents of iron and 1.16 equivalents of zinc were determined to be the main products present in the protein sample. These results are accurate relative to each other but are only approximate relative to protein concentration due to inaccurate concentration determination of the unknown mixture of [FeZn]IMP-1 and [ZnZn]IMP-1 (section 2.4.1).

The degree of iron substitution varied significantly between preparations of protein expressed in LB rich media,²⁰² so all future expressions were performed using the high-cell density method described in section 2.9.2 using defined media, where results were much more reproducible. The variation in metal content was attributed to subtle differences in metal ion composition between batches of the commercial tryptone and yeast extracts used in LB media.¹⁹⁸

2.3.2 Attempted De-Metallation of IMP-1

To simplify analysis, it was desirable to obtain the pure zinc-substituted IMP-1 enzyme reliably in high yield. Several attempts have been made to remove the active site metals of IMP-1 to form the apo-enzyme and then generate non-zinc substituted proteins, however, both metal ions remained tightly bound by IMP-1, as evidenced by their retention after exposure to chelators, prolonged dialysis, or purification in the absence of metal ions.^{79,203,204} Two recent publications had advertised independent methods for generating the apo-enzyme: Griffin *et al.*¹⁹⁴ utilised a dilute solution of the enzyme that was dialysed over several steps against either 1,10-phenanthroline or EDTA; and Yamaguchi *et al.*²⁰⁵ used a concentrated protein sample that was directly treated with EDTA at elevated temperature in the presence of 30% glycerol and 1 M NaCl (see section 2.9.10). Both of these methods were tested in this study, however, as shown in Figure 2-21, the Griffin method caused significant proteolysis of the enzyme, and the Yamaguchi method produced large amounts of precipitate that could not be refolded.

The soluble fractions from both of these methods were analysed for iron and zinc metal ion content by ICP-OES (Figure 2-22).

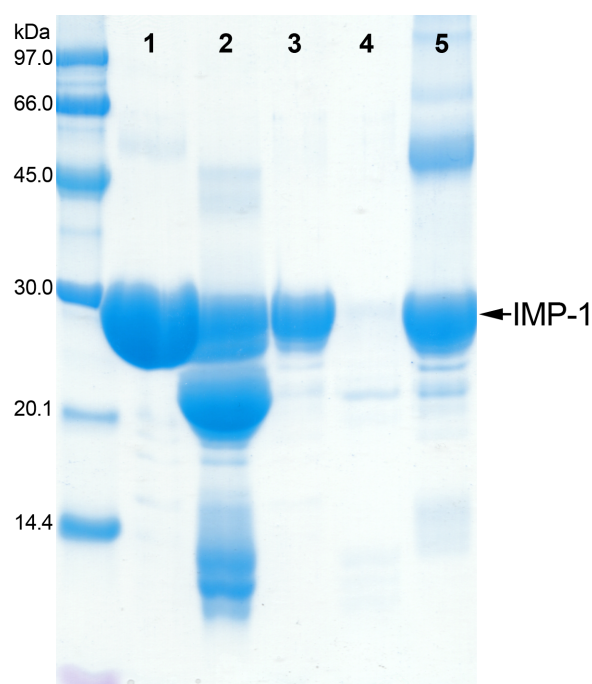


Figure 2-21 15% SDS-PAGE of de-metallation trials. Lane 1 contains the pre-treated sample control showing full-length IMP-1 protein. The Griffin method¹⁹⁴ produced large amounts of proteolytically degraded enzyme (lane 2), with some insoluble protein (lane 3), whereas the Yamaguchi method²⁰⁵ did not cause cleavage of the enzyme (lane 4), but generated lots of insoluble denatured protein (lane 5), which could not be refolded.

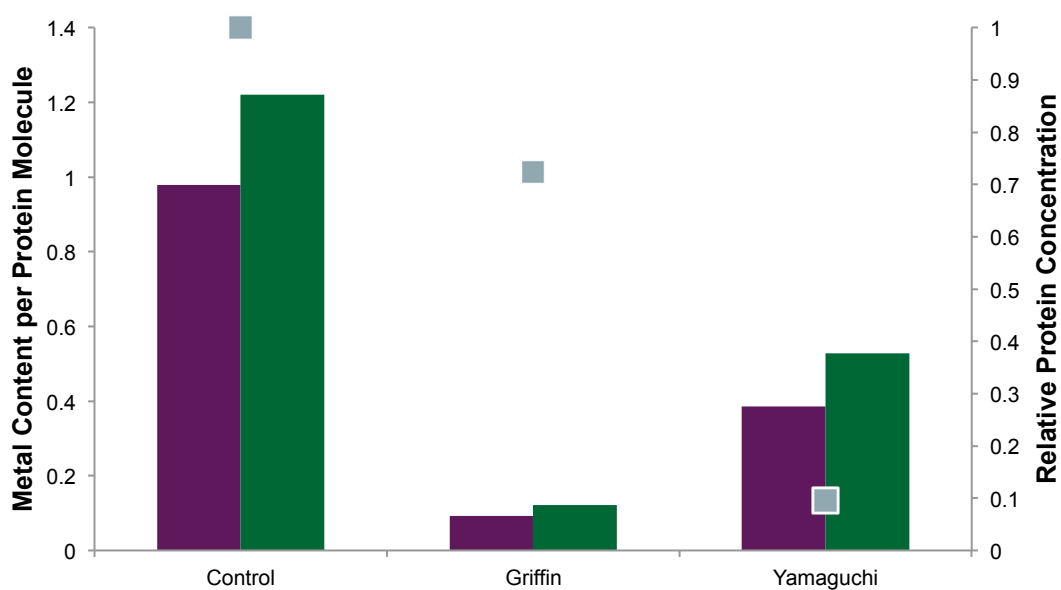


Figure 2-22 ICP-OES metal analysis of de-metallation attempts. Iron is indicated by purple bars, and zinc is indicated by green bars. The relative soluble protein yield is indicated by silver squares. While the Griffin method¹⁹⁴ appears to reduce the metal content significantly, the majority of the protein sample has been cleaved into smaller fragments (**Figure 2-21**). The Yamaguchi method¹⁸⁴ is also imperfect, producing a yield of about 6% soluble apo-enzyme. Protein concentration estimates assumed a mixed sample of 80% [FeZn]IMP-1 and 20% [ZnZn]IMP-1 for determination of the ϵ_{280} value.

While the Griffin method¹⁹⁴ appears to have largely succeeded in removing the bound metals from the protein, the majority of the product had been proteolysed as shown in Figure 2-21, requiring repurification. In contrast, the Yamaguchi method²⁰⁵ was successful in removing about 60% of the metals, however, only 9% of the total protein remained soluble, equating to a yield of approximately 6% apo-enzyme. It was concluded that neither of these methods was suitable for generating high-yielding protein samples for NMR or X-ray crystallography studies.

2.3.3 Control of Metal Ion Content of IMP-1 via Expression Conditions

As it proved difficult to reconstitute the IMP-1 protein with zinc, the expression conditions were adjusted to favour the [ZnZn] form. A series of small-scale expressions was prepared with increasing amounts of extra ZnSO₄ added to the minimal media. A titration of FeCl₃ was also trialled in parallel. ICP-OES data showed that control of the metal substitution in the active site could be achieved by supplementing the expression media with either 500 μ M ZnSO₄ or FeCl₃ (Figure 2-23).

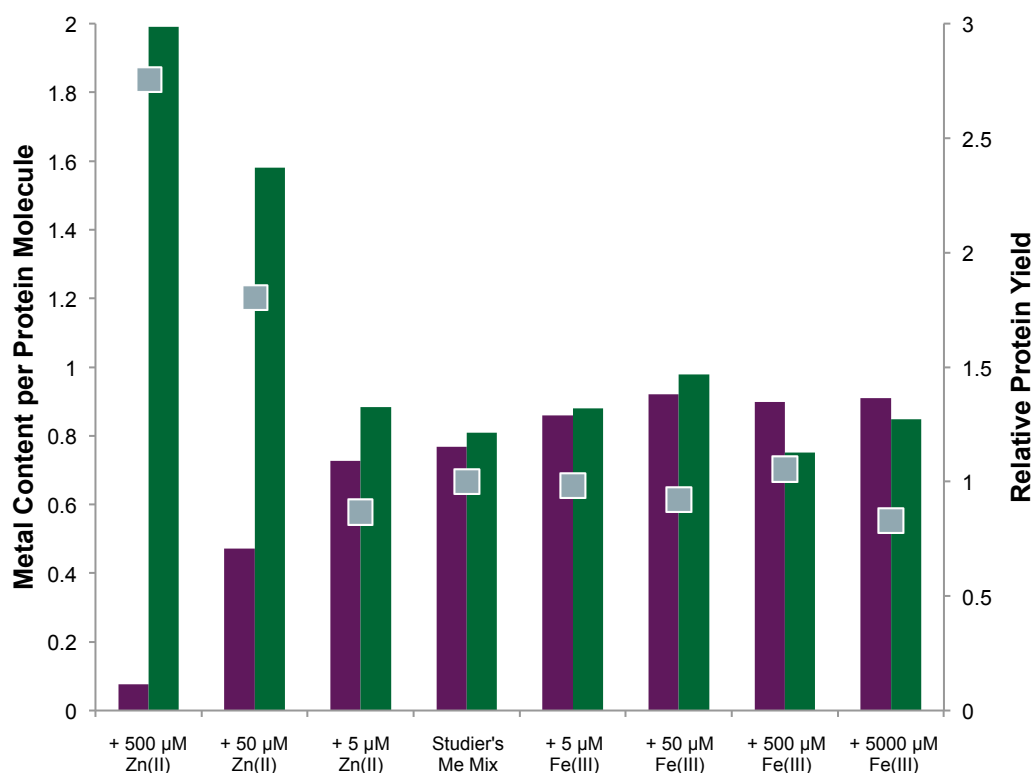


Figure 2-23 ICP-OES metal analysis of zinc (green) and iron (purple) titration. Up to 2.0 equivalents of zinc per protein molecule could be obtained by supplementing the expression media with 500 μ M ZnSO₄. Even in the presence of excess iron, never more than one equivalent of iron was detected. Protein concentration (silver square) was determined using a calculated ϵ_{280} value assuming a mixed population of [FeZn]IMP-1 and [ZnZn]IMP-1 species defined by the ratio of metals (section 2.4.1).

It was determined that IMP-1 would bind close to one equivalent of iron even in relatively low iron concentrations. This raised the possibility of iron being a biologically relevant active-site metal for IMP-1. It was also interesting to note that the protein would only ever incorporate a maximum of one equivalent of iron, even in a large excess of iron, which also suggested that the iron was binding to a specific metal site, or that the presence of one iron ion prevented the binding of a second.

Now that pure [ZnZn]IMP-1 sample could be made, most of the peak doubling was resolved in the NMR spectra (Figure 2-24).

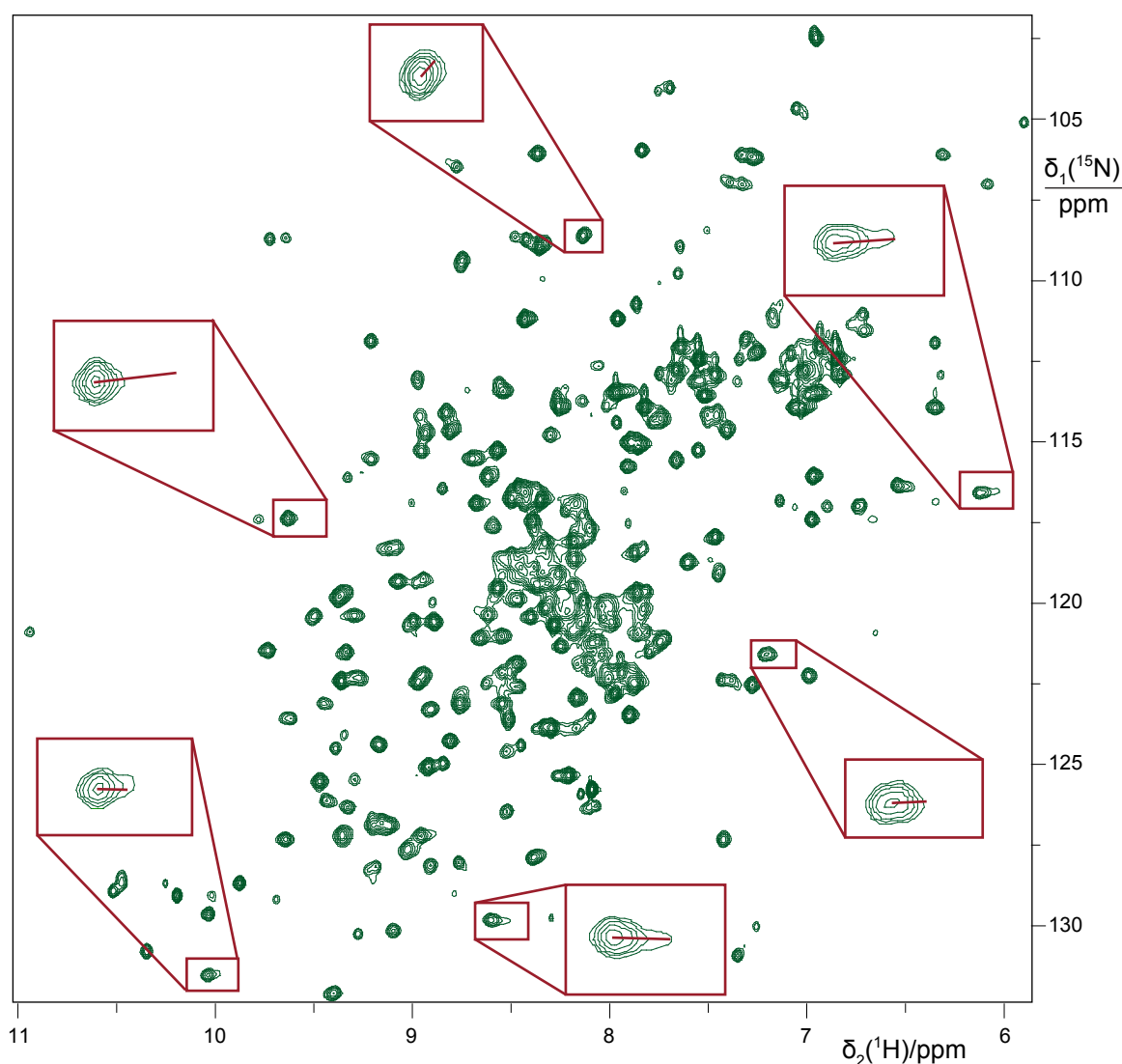


Figure 2-24 ^{15}N -HSQC spectrum of [ZnZn]IMP-1. Control over metal substitution simplified NMR spectra into mostly a single metal coordinated species. The same cross-peaks are highlighted as in **Figure 2-15**. Very small amounts of [FeZn]IMP-1 are still evident in the spectrum, but are significantly attenuated.

2.3.4 Validation of [FeZn]IMP-1 Existence in Periplasm

In the natural system, IMP-1 is transported to the periplasm via membrane-bound transport proteins that recognise and cleave an 18 amino-acid, N-terminal signal peptide. To ensure that the observed metal character was not an experimental artefact of the protein being expressed into the cytosol, the signal peptide was cloned onto the N-terminus of the protein in pET47b(+), and the construct transformed into BL21(DE3) cells. To verify that the native membrane transport proteins recognised the signal peptide, a simple agar antibiotic plate assay was then run.

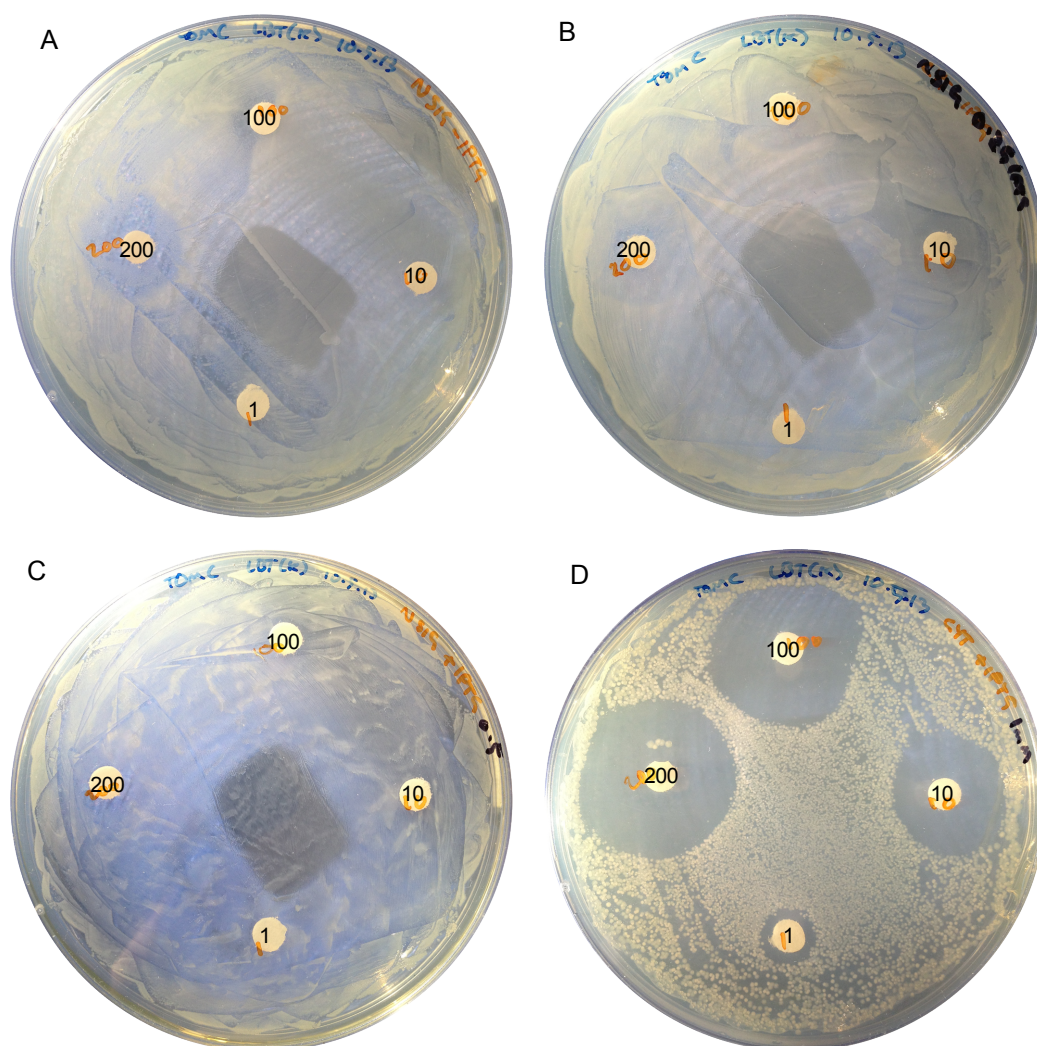


Figure 2-25 *In vivo* β -lactamase activity assay showing transport of IMP-1 to the periplasm is essential for antibacterial resistance. The radius of inhibition is an indication of the inhibitory concentration of ampicillin. Filter paper disks were supplemented with 20 μ L of 1, 10, 100 or 200 mg/mL ampicillin as marked. Even without induction (A), the 'leaky' expression of IMP-1 with the N-terminal signal peptide to transport the enzyme to the periplasmic space is enough to confer β -lactam resistance to the *E. coli* cells. With 0.25 mM IPTG induction (B), the cells can withstand over 100 mg/mL concentrations of ampicillin. With 0.5 mM IPTG induction (C), the cell growth is inhibited, presumably because the high level of overexpression of the IMP-1 enzyme overloads the native membrane transport proteins. If the N-signal peptide is absent (D), thus keeping the expressed enzyme in the cytosol (1 mM IPTG), little antibacterial resistance is observed with a MIC of < 1 mg/mL.

From the results in Figure 2-25 it was determined that the overexpression of IMP-1 with the N-terminal signal peptide limited the growth of the cells, and the enzyme was active *in vivo* in the *E. coli* strain BL21(DE3). While this assay is not quantitative, the results are compelling and consistent with the signal peptide being recognised and processed by the native BL21(DE3) membrane transport proteins.

The protein was then overexpressed (section 2.9.4), and the media, total cell, periplasm, and cytosolic fractions were analysed on SDS-PAGE (Figure 2-26).

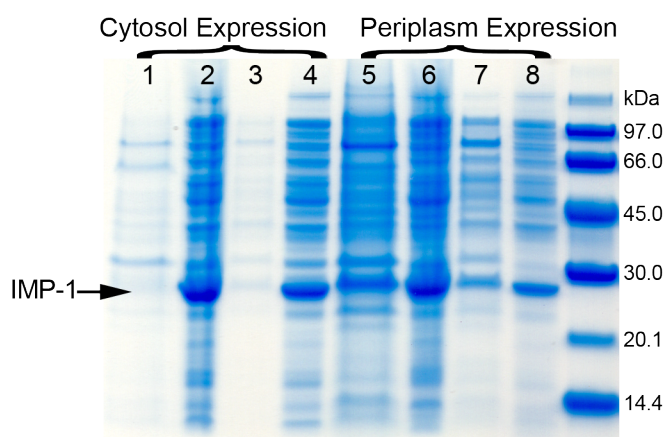


Figure 2-26 15% SDS-PAGE gel of periplasmic expression of IMP-1 with the N-signal peptide. The molecular mass of IMP-1 (25.5 kDa) is highlighted by the arrow. IMP-1 expressed without the N-terminal signal peptide (lanes 1 to 4) is only present in the cytosol (lanes 4 & 8, 2 μ L loaded) and total cell (lanes 2 & 6, 2 μ L loaded) fractions, whereas with the N-terminal signal peptide (lanes 5 to 8), the protein is present in the periplasm (lanes 3 & 7, 30 μ L loaded) and also in the medium (lanes 1 & 5, 30 μ L loaded) fraction. Note that much more protein (IMP-1 and other proteins) was released into the medium for the N-signal peptide sample. This may be attributed to cell-lysis due to stress on the membrane transport proteins or to up-regulation of membrane transport proteins.

It was found that the majority of the expressed protein was released into the medium during expression, which is consistent with results reported for other metallo- β -lactamases.¹²⁸ The medium fraction was concentrated then diluted with salt-free buffer until the salt concentration was low enough for ion exchange chromatography.

It was noted that the total protein level in the media was higher for the periplasmic expression than for the cytosolic expression. This could be due to the cells up-regulating their membrane transport proteins in response to the overexpression of the periplasmic form of IMP-1, or might be explained by cell lysis. To ensure the media fraction contained protein transported to the periplasm, rather than protein released from lysed cells, mass spectrometry was performed on the sample. This was diagnostic as protein transported to the periplasm would have had the N-terminal signal peptide cleaved by the membrane transport proteins (expected mass = 25,041.6, observed mass = 25,046.2), whereas any protein from lysed cells would still have the signal peptide

attached (expected mass = 27,120.1). It was concluded that the protein purified from the media had been transported to the periplasm and that the N-terminal signal peptide had been cleaved (Figure 2-27).

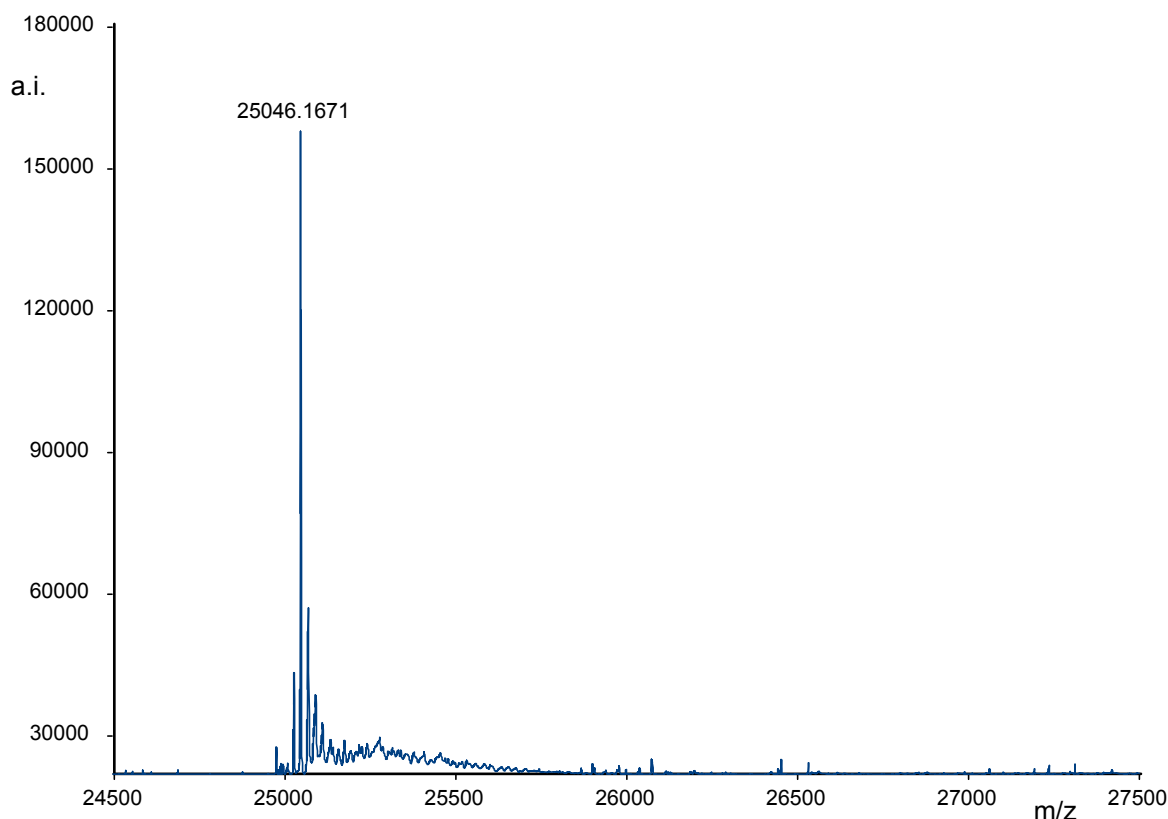


Figure 2-27 MaxEnt reconstructed ESI-MS spectrum under denaturing conditions (1% formic acid) showing [FeZn]IMP-1 protein collected from the media has been cleaved and transported to the periplasm. Expected mass: 25,041.6 observed: 25,046.2. None of the uncleaved product from the cytosol is observed (27,120). MaxEnt reconstruction run in Waters MassLynx 4.1, figure generated in mMass²⁰⁰.

The protein product was then expressed *in vivo* under different media conditions, specifically high zinc (supplemented with 500 μM ZnSO_4), 0.5 \times Studier's Me Mix ratio¹⁹⁸, and high iron (supplemented with 500 μM FeCl_3). The protein was harvested and purified from the media (section 2.9.3), then analysed for iron and zinc content by ICP-OES analysis. Clearly, the [FeZn] species was not limited to cytosolic expressions, and was even more prevalent in samples expressed in the periplasm. Up to 24% of the IMP-1 protein population was in the [FeZn] form even in the sample expressed under the same excess zinc conditions used to produce [ZnZn]IMP-1 in the cytosol (Figure 2-28).

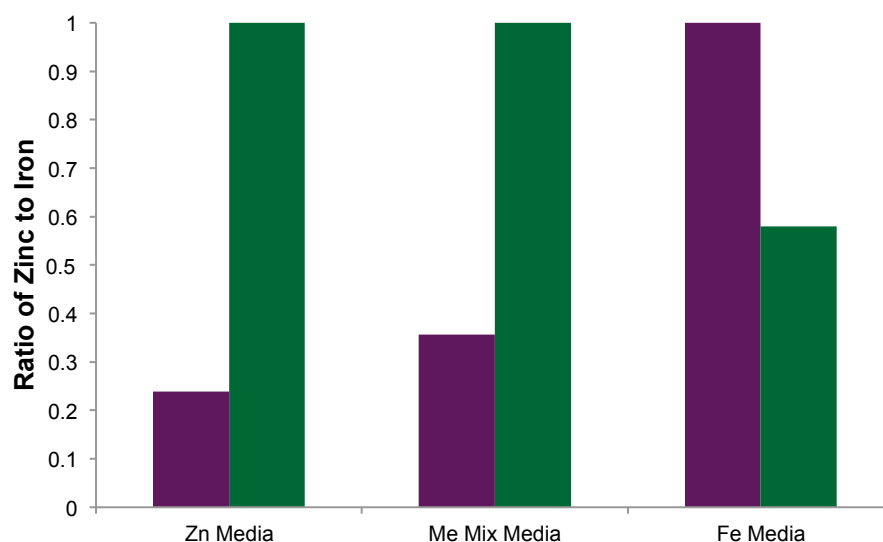


Figure 2-28 ICP-OES metal analysis of periplasmic expression study. Iron is indicated in purple and zinc is indicated in green. Periplasmic expressions with $0.5 \times$ Studier's Me Mix¹⁹⁸ ratio of metals indicated up to 36% of expressed protein was in the [FeZn] form, and even in the presence of excess zinc, up to 24% of the protein was the [FeZn] form. In excess iron conditions, up to 100% of the protein produced was in the [FeZn] form. Due to difficulties with protein concentration measurements of these particular samples, a [FeFe]IMP-1 species cannot be ruled out, however, no other experiment performed in this study supports the possibility of iron binding to both sites of IMP-1.

2.4 Results: Biochemical Comparison of [FeZn]IMP-1 and [ZnZn]IMP-1

2.4.1 Protein Concentration Measurements

Estimates of native-fold extinction coefficients for determining protein concentration are usually quite reliable, however, using this method for concentration determination of [FeZn]IMP-1 requires a specific correction between the native and denatured protein estimates as the iron forms a chromophore in the native state. Thus the ϵ_{280} value was established using a method described by Kelly *et al.*²⁰⁶

A Cary UV-VIS spectrometer was used for calibration of the ϵ_{280} values. A suitable amount of protein in buffer (20 mM MES, pH 6.5, 100 mM NaCl) was determined to give an absorbance at 280 nm of approximately 0.8 over a 10 mm path length. 250 μ L of this sample was then diluted with either 750 μ L of buffer, or 750 μ L of 8 M guanidine hydrochloride, and absorbance at 280 nm over a 10 mm path length was measured. This was performed in triplicate for both [FeZn]IMP-1 and [ZnZn]IMP-1, and an average correction factor of the absorbance of the denatured state was established (1.220 and 0.989 respectively). An estimate of the extinction coefficient for the denatured protein was then made using the following formula,²⁰⁷

$$\epsilon_{280} = 5690 W + 1280 Y + 120 CC \quad (2.3)$$

where W is the number of tryptophan residues (6), Y is the number of tyrosine residues (8), and CC is the number of disulfide bonds (0).²⁰⁷ For IMP-1, this gives a value of 44,380 $\text{M}^{-1}\text{cm}^{-1}$. This estimate does not suffer the problem of the iron chromophore, so it is more reliable than the estimate for the folded protein.

The value was then multiplied by the determined correction factor to arrive at the corrected ϵ_{280} values. [FeZn]IMP-1 was determined to have an $\epsilon_{280} = 54,130 \text{ M}^{-1}\text{cm}^{-1}$ and [ZnZn]IMP-1 to have an $\epsilon_{280} = 43,870 \text{ M}^{-1}\text{cm}^{-1}$. As a comparison, the predicted value for the protein by the folded estimate method described by Pace *et al.*²⁰⁸ was $\epsilon_{280} = 44,920 \text{ M}^{-1}\text{cm}^{-1}$, which is close to the determined [ZnZn]IMP-1 value as expected. The ϵ_{280} estimate reported in the literature^{116,193} is quite varied with $\epsilon_{280} = 44,380 \text{ M}^{-1}\text{cm}^{-1}$ to 49,000 $\text{M}^{-1}\text{cm}^{-1}$. These values fall between the [ZnZn]IMP-1 and [FeZn]IMP-1 estimates described here, as would be expected for a mixed sample of [ZnZn] and [FeZn] forms.

It is worth noting that with the corrected ϵ_{280} values calculated here, all ICP-OES measurement results became significantly more accurate. For example, where the previous concentration estimate determined 1.62 equivalents of metal (iron plus zinc) for one sample of [FeZn]IMP-1, the new estimate determined 2.02 equivalents of metal.

2.4.2 UV/Vis Absorption

The absorption spectrum in the UV and visible range was measured, and shows a weak, broad absorption band at 520 nm, which gives rise to the visible purple colouration of [FeZn]IMP-1 samples. A strong, broad absorbance band is also present at around 300 nm, responsible for the protein concentration determination issues highlighted in section 2.4.1.

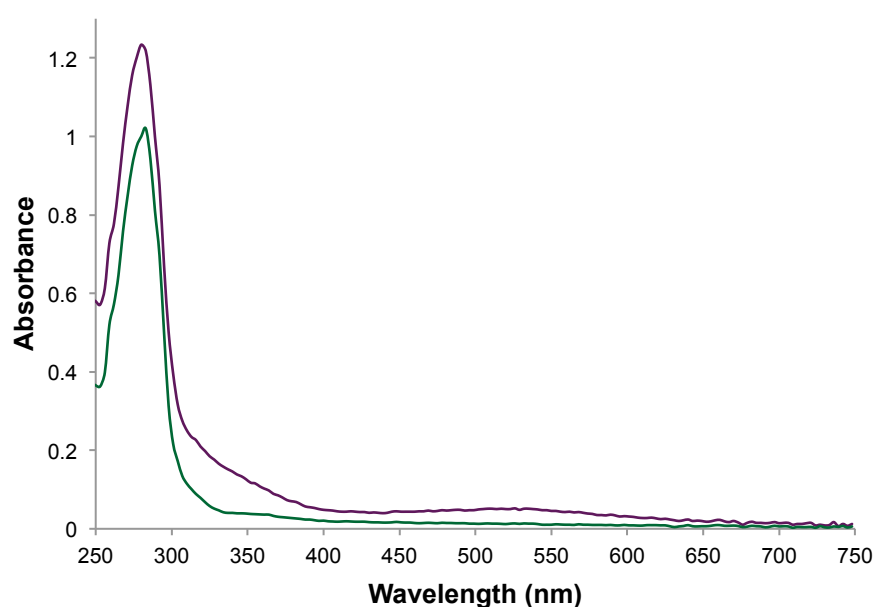


Figure 2-29 UV/Vis absorption spectrum of [FeZn]IMP-1 (purple) and [ZnZn]IMP-1 (green). The [FeZn] form has a weak, broad absorbance band at 520 nm and a strong, broad absorbance band at ~300 nm. Spectra were recorded on a NanoDrop NV1000 with a 1 mm and 0.1 mm pathlength. Absorbance is scaled to show the UV/Vis absorbance spectrum of 0.23 mM protein (A_{280} of 1 for the [ZnZn]IMP-1 with a 1 mm pathlength).

In an attempt to probe the oxidation state of the iron, the visible absorbance spectra were acquired of the [FeZn]IMP-1 enzyme after either reduction with TCEP or oxidation with H_2O_2 . This resulted in a red-shift in the absorbance band at 520 nm to 570 nm after treatment with TCEP, and little change after oxidation, which would suggest the iron was in the 3+ oxidation state (Figure 2-30). This result was later confirmed by NMR data collected on cell-free samples (Figure 2-58).

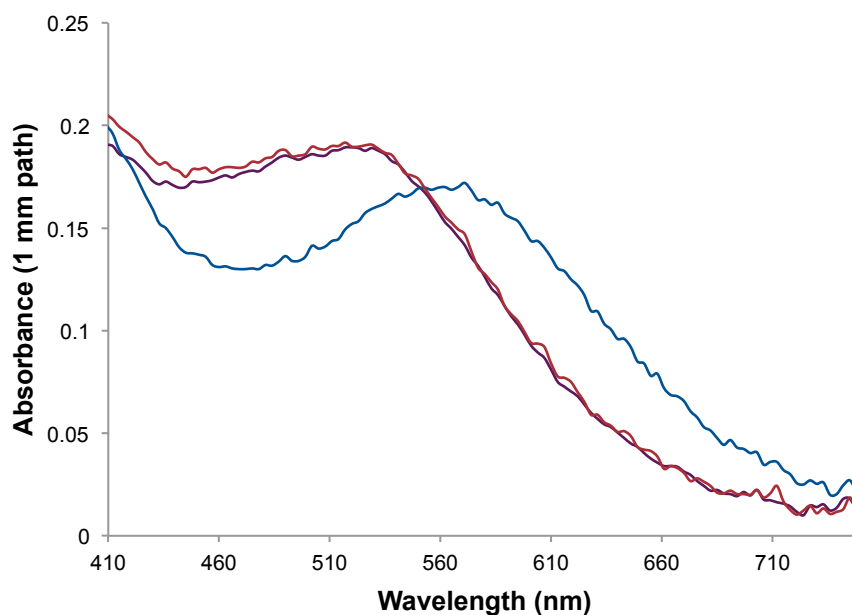


Figure 2-30 Visible absorbance spectrum of 1.8 mM [FeZn]IMP-1 before treatment (purple), after reduction with 40 mM TCEP (blue) and after oxidation with 1.2 mM H₂O₂ (red). 2 μ L samples of \sim 1.8 mM protein in 30 mM HEPES (pH 7.5), 180 mM NaCl were measured on a NanoDrop ND-1000 with a pathlength of 1 mm.

2.4.3 Circular Dichroism

Circular Dichroism Spectroscopy

Differences in the secondary structure content between the [FeZn]IMP-1 and [ZnZn]IMP-1 species were probed using circular dichroism (CD). The CD spectra observed in the far UV were essentially identical between the two samples, indicating similar secondary structure (Figure 2-31A). There is only a subtle intensity difference at 193 nm and even less at 230 nm, which is perhaps indicative of a subtle change in the α -helical component, but this difference may not be significant. The near UV region is more indicative of tertiary structure changes and differences between the two preparations become more apparent, specifically in the region from 300 to 380 nm, where the [FeZn]IMP-1 has a consistently higher intensity (Figure 2-31B). However, the curves are still very similar, suggesting that any differences in tertiary fold of the two species are minimal. Visible CD is possible with coloured proteins, and a signal is apparent for the [FeZn]IMP-1 species (Figure 2-31C) that is significantly different to the [ZnZn]IMP-1 signal. This is indicative of the binding environment of the iron, but no conclusions can be drawn in comparison to the [ZnZn]IMP-1 sample.

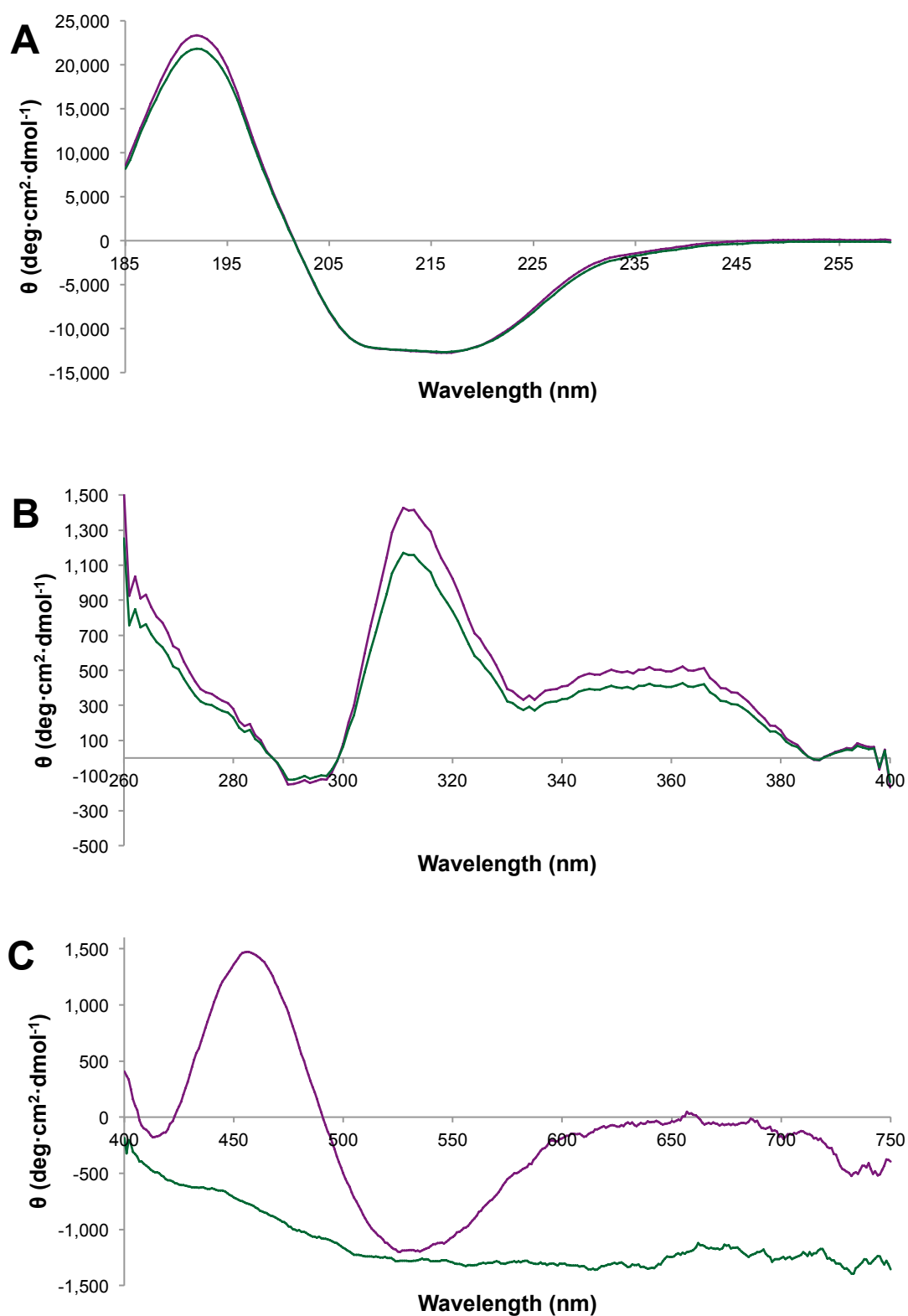


Figure 2-31 Comparison of CD spectra of [FeZn]IMP-1 (purple) and [ZnZn]IMP-1 (green). **A**) Mean residue ellipticity in the far UV of approximately 5 μ M protein, 1 mm pathlength **B**) Molar ellipticity in the near UV of approximately 50 μ M protein, 10 mm pathlength **C**) Molar ellipticity in the visible range of approximately 50 μ M protein, 10 mm pathlength. All samples were measured in 50% D₂O, chloride-free 23 mM phosphate buffer, pH 7.0, 19 mM Na₂SO₄ at 293 K.

Circular Dichroism Thermal Denaturation

The CD spectra in the far UV range during a thermal melt of [ZnZn]IMP-1 and [FeZn]IMP-1 are shown in Figure 2-32. ‘Smeared’ isosbestic points are present near 202 nm and 230 nm in the [ZnZn]IMP-1 spectra, indicating a multiple-step unfolding pathway. The isosbestic point at 202 nm is not smeared in the [FeZn]IMP-1 melt, suggesting that the [FeZn] has at least different denaturation kinetics, if not also an alternate denaturation pathway. Significant secondary structural elements are still present in both species even at 90 °C. Interestingly, the spectra acquired at 90 °C from each species differ significantly (Figure 2-32C). These differences are irreversible and are still evident after cooling to 25 °C. Unfortunately, a small degree of precipitant formed over the course of the thermal melts, complicating spectral analysis. Although attenuation of the CD signal appears minor, indicating little or no light scattering due to large protein aggregates, comparison of the structures at 90 °C between the two species is not possible.

Several wavelengths were selected and thermal melting curves were fitted with a simple sigmoidal function (Figure 2-33). All fits had an R^2 value greater than 0.987. Statistical analysis was performed on the two spectral regions (208-220 and 186-198 nm) as two independent groups to determine if the two regions reflected the same average melting temperature (T_m) or relative slope (d_x). Table 2-7 shows the mean and standard deviation of the T_m and d_x results, along with a Student’s t -test calculated in Microsoft Excel.

The two peaks give insignificantly different melting temperatures for the [ZnZn] species (likelihood of different mean = 68.5%), but there is a significant difference in d_x . While the two peaks could have the same mean T_m , the observation of different slopes (d_x) suggests non-uniform melting of the protein. The [FeZn] species has significantly different T_m between the two peaks (likelihood of different mean = 99.87%), and also a significant difference between the d_x . This could be explained if the presence of iron promotes one of the steps required for unfolding, or stabilises a structurally different denaturation product. The T_m values for [ZnZn]IMP-1 and [FeZn]IMP-1 were then compared using a pooled global average of all the points fitted in Figure 2-33. Table 2-8 shows the means and standard deviations of the T_m and d_x results.

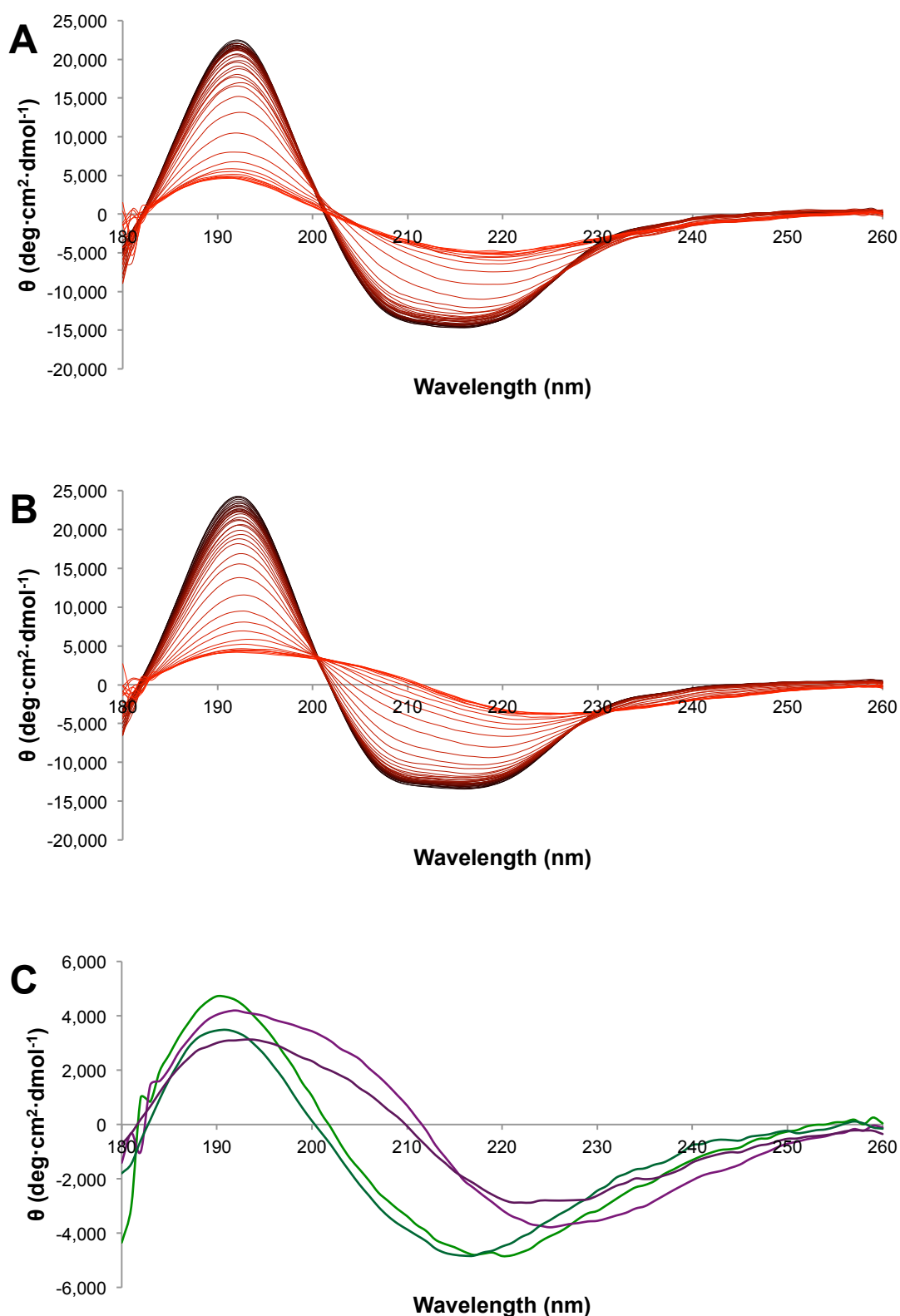


Figure 2-32 Far UV mean residue ellipticity during thermal melt of **A)** [ZnZn]IMP-1 and **B)** [FeZn]IMP-1. The thermal melt was applied stepwise in two degree increments from 10 °C (black) to 90 °C (red). The thermal melt in both cases was irreversible. Even at 90 °C there is evidence of residual secondary structure in both samples. **C)** Comparison of the CD spectrum of [ZnZn]IMP-1 (green) and [FeZn]IMP-1 (purple) at 90 °C (dark) and subsequent cooling to 25 °C (light). The change in the CD spectrum of IMP-1 under these conditions is irreversible. The protein does not exhibit a typical random coil CD spectrum, even at 90 °C in either case, potentially indicating residual β -sheet structures or protein aggregates.

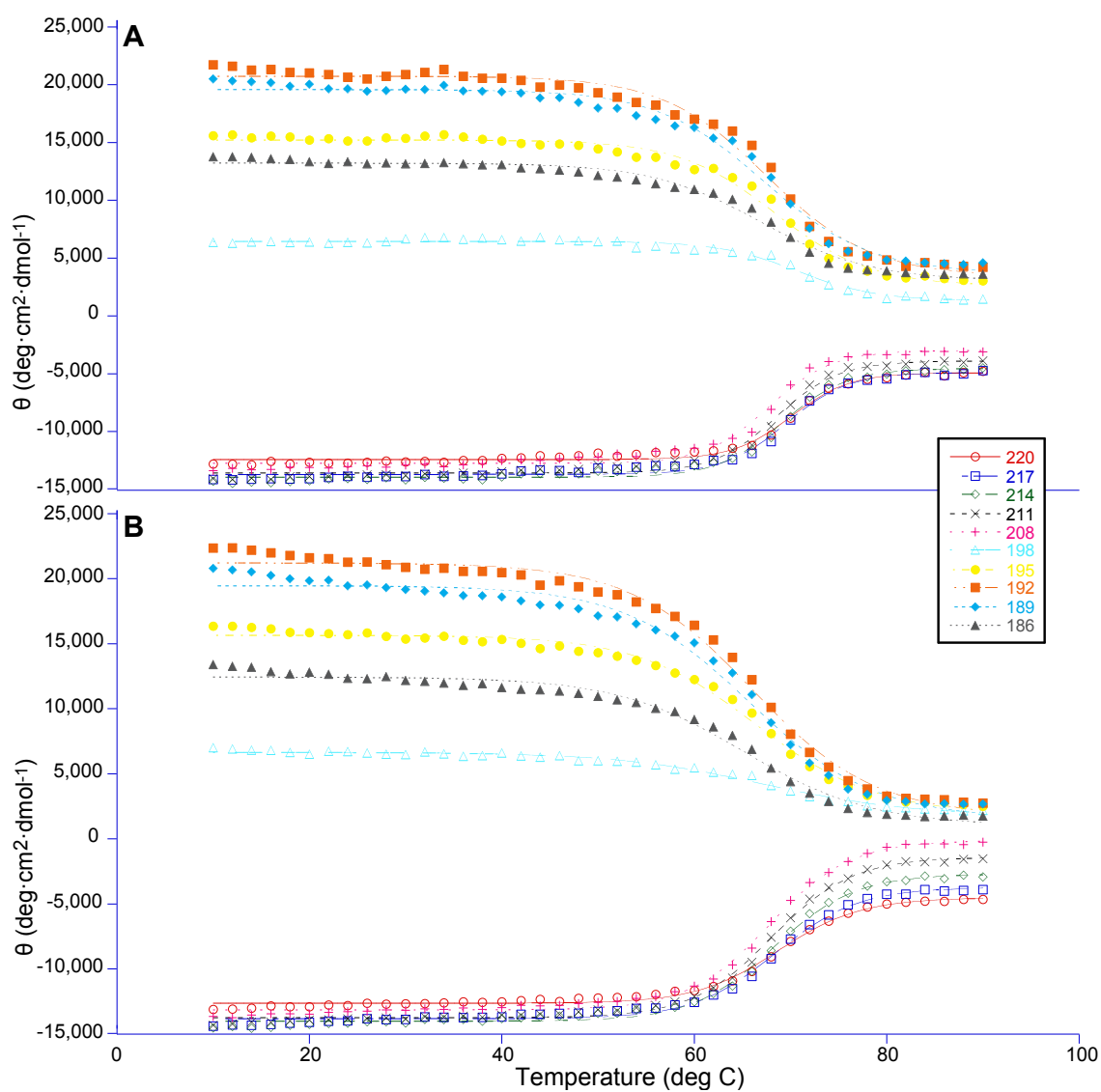


Figure 2-33 Sigmoid function fit of CD mean residue ellipticity thermal melt for **A)** [ZnZn]IMP-1 and **B)** [FeZn]IMP-1. The sigmoid function was fit independently to each wavelength using KaleidaGraph software. Each fit had an $R^2 > 0.987$.

Table 2-7 Statistical analysis of CD temperature melt – comparison of the signal at 198-186 nm to the signal at 220-208 nm for the [ZnZn]IMP-1 and [FeZn]IMP-1 species individually.ⁱ

[ZnZn]IMP-1	220-208 peak		198-186 peak	
	T_m (°C)	d_x	T_m (°C)	d_x
mean	69.03	3.22	68.2	5.12
standard deviation	0.91	0.11	1.5	0.65
significance (t -test) ⁱⁱ	31.5%	0.24%		

[FeZn]IMP-1	220-208 peak		198-186 peak	
	T_m (°C)	d_x	T_m (°C)	d_x
mean	68.26	4.229	66.10	6.65
standard deviation	0.38	0.039	0.76	0.57
significance (t -test) ⁱ	0.13%	0.065%		

ⁱ Mean and standard deviation are calculated from the different wavelength fits on a single thermal melt run for each [ZnZn]IMP-1 and [FeZn]IMP-1.

ⁱⁱ A two-tailed Student's t -test with 5% confidence. Results highlighted in blue indicate high likelihood that the two samples are independent and have different mean values. Results highlighted in red indicate statistical insignificance.

Table 2-8 Analysis of CD temperature melt - comparison of [ZnZn]IMP-1 and [FeZn]IMP-1 using all data points measured (global).ⁱ

Global Average	[ZnZn]IMP-1		[FeZn]IMP-1	
	T_m	d_x	T_m	d_x
mean	68.6	4.2	67.2	5.4
standard deviation	1.3	1.1	1.3	1.3

ⁱ Mean and standard deviation are calculated from the different wavelength fits on a single thermal melt run for each [ZnZn]IMP-1 and [FeZn]IMP-1.

2.4.4 Exogenous Metal Exchange

Cadmium Exchange

Siemann *et al.*²⁰³ described the facile exchange of cadmium into the binding site of IMP-1, and tentatively designated the cadmium-binding site to the Zn₂ site. This experiment was repeated with both the [ZnZn]IMP-1 and [FeZn]IMP-1 samples and assayed using mass spectrometry (Figure 2-34). While it was evident that cadmium did exchange into the protein in place of an active-site metal, the mass accuracy was not high enough to determine conclusively whether it was iron or zinc that was replaced. To ascertain which metal was exchanged by cadmium, samples were prepared and analysed by ICP-OES (Figure 2-35).

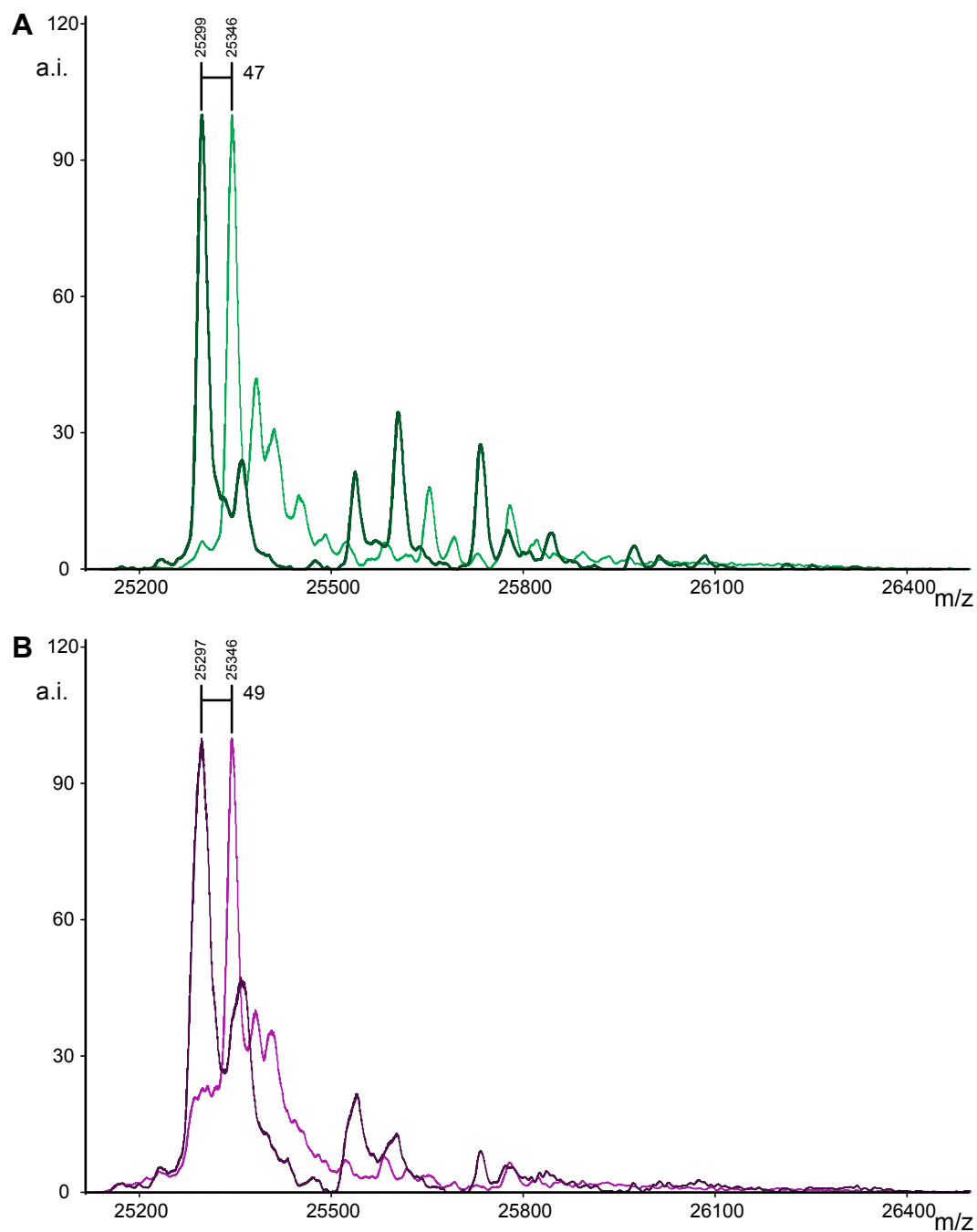


Figure 2-34 Deconvoluted +ESI-MS spectrum in 100 mM ammonium acetate for **A)** [ZnZn]IMP-1 and **B)** [FeZn]IMP-1 before (dark) and after (light) treatment with CdCl₂. Both species rapidly exchange one cadmium ion for an active-site metal. Expected difference for Zn replaced by Cd: 47, Expected difference for Fe replaced by Cd: 57. Observed for [ZnZn]IMP-1: 47. Observed for [FeZn]IMP-1: 49.

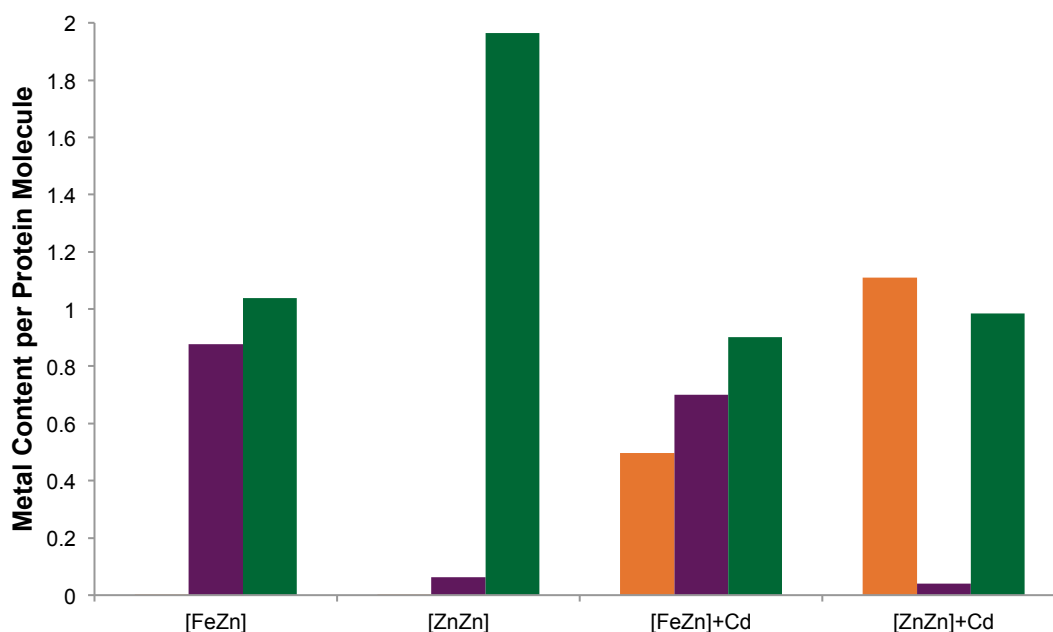


Figure 2-35 ICP-OES result for cadmium (orange), iron (purple) and zinc (green) in the cadmium ion exchange experiment. Only two equivalents of metal were observed for the treated samples. Protein ϵ_{280} values used for concentration estimates are scaled using the ratio of iron to zinc and assume ϵ_{280} of the [CdZn] protein is the same as the [ZnZn] protein, and that ϵ_{280} of the [FeCd] form is the same as the [FeZn] protein.

Only 2.0 ± 0.1 metal equivalents were observed for all samples before and after treatment, confirming cadmium exchanges with one of the active site metals. 0.18 equivalents of iron and 0.14 equivalents of zinc were lost from the [FeZn]IMP-1 sample after cadmium treatment and substituted with 0.50 equivalents of cadmium within the 5 minute treatment time. The total metal content of the [FeZn]IMP-1 sample increased from 1.9 to 2.1 equivalents after treatment. The [ZnZn]IMP-1 sample lost 50% of zinc after cadmium treatment, and has 1.1 equivalents of cadmium per protein molecule within the 5 minute treatment period.

Zinc and Iron Exchange

Using the same conditions as the cadmium exchange experiment, an attempt was made to exchange zinc or iron into the active site of either [FeZn]IMP-1 or [ZnZn]IMP-1. Exchange of metals was evident, and the treatment of [FeZn]IMP-1 with zinc did reduce the iron content as expected. Unexpectedly, a significant excess of metal was present in the case of the addition of iron(III), where 19.56 and 19.48 equivalents of iron were observed in the [FeZn] and [ZnZn] forms respectively. This was very close to the excess of iron that was used to treat the samples. The results were reproducible even after using two desalting steps in series on new NAP-5 and PD-10 columns and in the presence of 100 mM NaCl.

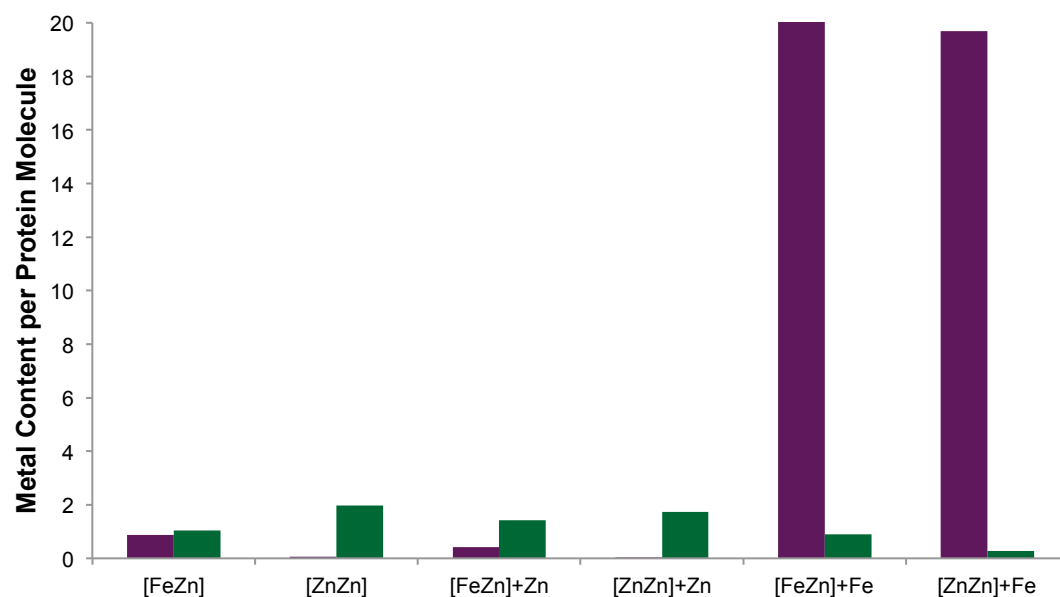


Figure 2-36 ICP-OES result for iron (purple) and zinc (green) in the zinc and iron ion exchange experiment. The treatment of [FeZn]IMP-1 with zinc does reduce the iron content. Protein concentrations for the iron treated samples were estimated from measurements of the [FeZn] and [ZnZn] forms treated with cadmium, as the strong yellow colour from the dissolved iron interfered with A_{280} measurements.

2.4.5 Comparison of Activity of [FeZn]IMP-1 and [ZnZn]IMP-1

The activity of both forms of IMP-1 was assayed against benzylpenicillin at pH 7.5 at 37 °C (Table 2-9).

Table 2-9 Relative kinetic parameters of the purified [FeZn]IMP-1 enzyme compared to the [ZnZn]IMP-1 enzymeⁱ

	[ZnZn]IMP-1	[FeZn]IMP-1
k_{cat} (s^{-1}) ⁱⁱ	461	135
K_{m} (μM)	275	1340
$k_{\text{cat}}/K_{\text{m}}$ ($\mu\text{M}^{-1} \cdot \text{s}^{-1}$)	1.676	0.101

ⁱ The values for [ZnZn]IMP-1 were independently measured. Data are means of three measurements. Standard deviations never exceeded 10%.

ⁱⁱ The $\Delta\epsilon$ value for benzylpenicillin in the plate assay was not directly determined. Results for k_{cat} were therefore approximated by scaling the result for k_{cat} to match the report by Iyobe *et al.*¹⁴² (see section 2.9.14 for further details).

2.5 Results: X-Ray Diffraction Structure Determination of [FeZn]IMP-1 and Anomalous Scattering

2.5.1 Crystallisation Screening

A number of automated protein crystallisation screens, using commercial high-throughput screening plates, were attempted at different protein concentrations and temperatures. Constructs with and without the N-terminal MASMTG expression tag were trialled, and the addition of an inhibitor (captopril¹²³⁻¹²⁵) also attempted.

The addition of excess iron was attempted for the [FeZn]IMP-1 sample. It was observed that 2 to 3 equivalents of FeCl₃ increased the solubility of the enzyme and reduced precipitant in almost every condition screened in the high-throughput format, even at high concentrations of protein.

It was noticed from NMR spectra that a number of peaks would be lost or would shift after about 2 weeks of measurement at 37 °C (Figure 2-37), and from mass spectra that N-terminal residues were cleaved over time (data not shown). Consequently, a heat incubation step, followed by removal of any precipitant via filtration, was trialled in crystallisation screening. Successful crystallisation of [FeZn]IMP-1 (without the MASMTG N-terminal tag and with no other additives) required that the protein be heat treated for a minimum of 5 days at 37 °C. Single crystals large enough for X-ray analysis were successfully grown at 24 °C over 2 weeks using the hanging drop vapour diffusion method and microseeding by mixing 1 µL of 25 to 30 mg/mL protein in 10 mM HEPES pH 7.0 with 1 µL of the microseeding solution over a 1 mL reservoir containing 0.2 M sodium acetate, 0.2 M sodium citrate and 26% PEGMME 2K (Figure 2-38).

Two crystals were selected and flash cooled with liquid nitrogen in a cryoprotecting buffer of 0.2 M sodium acetate, 0.2 M sodium citrate and 35% PEGMME 2K prior to shipping to the Australian Synchrotron.

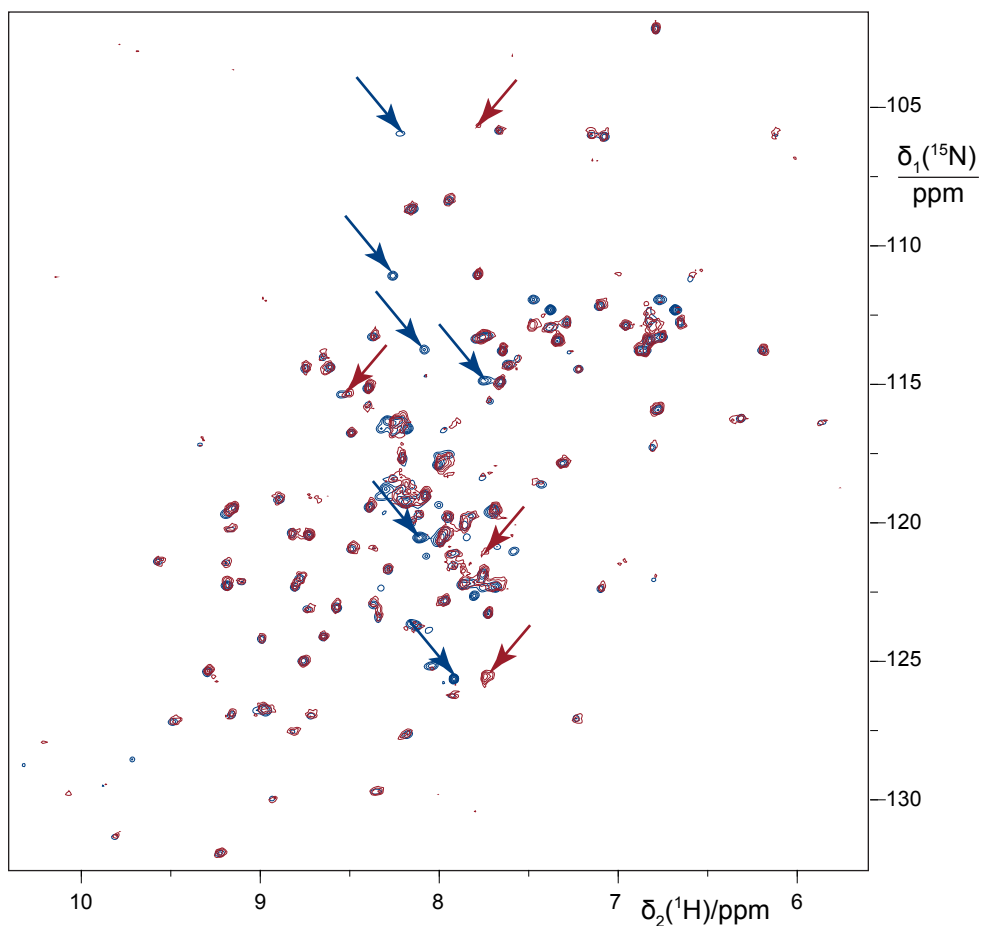


Figure 2-37 ^{15}N -HSQC spectrum of [FeZn]IMP-1 before (blue) and after (red) 2 weeks of measurement at 310 K. The older sample was exchanged into fresh NMR buffer prior to measurement to remove the possibility of pH shift. A few strong peaks get weaker or are lost (blue arrows) and some new peaks appear (red arrows) indicating the enzyme is aged over the course of time at 310 K.

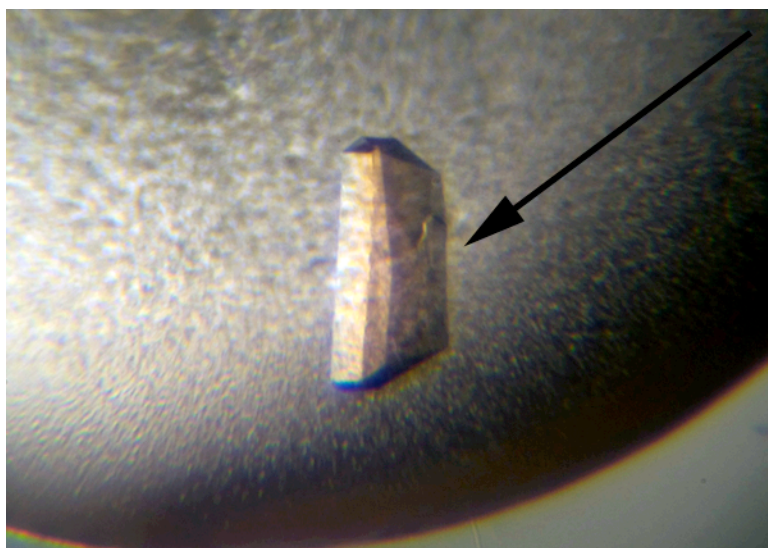


Figure 2-38 Micrograph of one of the crystals used for X-ray diffraction studies. Conditions were 0.2 M sodium acetate, 0.2 M sodium citrate and 26% PEGMME 2K at 28 °C.

2.5.2 X-Ray Diffraction Structure

Two crystals of [FeZn]IMP-1 were submitted for X-ray diffraction experiments* at the Australian Synchrotron. The protein crystals were found to have unit cell dimensions of $a = 49.99 \text{ \AA}$, $b = 75.91 \text{ \AA}$, $c = 82.36 \text{ \AA}$, $\alpha = 83.45^\circ$, $\beta = 75.30^\circ$, $\gamma = 74.01^\circ$ and consisted of four monomer chains per asymmetric unit in the $P1$ space group. The crystals were quite resilient to X-radiation damage and numerous complete data sets were measured successfully with little sample degradation. Both crystals diffracted to a resolution of 1.8 \AA . The structure was solved via molecular replacement, with the published crystal structure of IMP-1 having the most similar crystallography conditions (PDB code: 2DOO¹⁸³). Electron density was observed in the active site and found to be citrate from the crystallisation conditions. A structure for the citrate (FLC) substrate was obtained from the PDB (PDB code: 1C5R²⁰⁹) and was modelled into the active site.

After several rounds of refinement, a structure of the [FeZn]IMP-1 was determined. Monomers A and C included residues 4 to 221, and monomers B and D included residues 4 to 220. The unit cell contained 465 resolved water molecules. The crystallographic R factor was 0.18, the R_{free} was 0.21, and the RMSDs from ideal bond lengths and angles were 0.022 \AA and 1.386° , respectively. The four monomers had backbone RMSD to each other of between 0.20 \AA (A-D) and 0.32 \AA (A-C). The atoms with the largest difference were at the C-terminus (residues 216-221), and the flap (residues 23-32). When these residues were excluded, the backbone RMSD of each monomer to each other monomer ranged from 0.12 \AA (A-D) to 0.21 \AA (B-C). The metal ions were separated by 3.75 \AA (D) to 3.81 \AA (C), and the active residues had a backbone and sidechain RMSD between the four monomers of 0.08 \AA (A-B) to 0.11 \AA (B-C). The average B factor for each of the monomers was 28.53 \AA^2 (A), 28.74 \AA^2 (B), 27.74 \AA^2 (C) and 28.76 \AA^2 (D).

The A chain had a calculated backbone nitrogen RMSD of 0.344 \AA to the model used for molecular replacement (PDB code: 2DOO) and 0.616 \AA to another IMP-1 structure with a similar active-site ligand at 1.8 \AA resolution (PDB code: 1JJE¹²⁰) (Figure 2-39). The diffraction-component precision index (DPI)²¹⁰ for the [FeZn]IMP-1 structure was calculated to be 0.11 \AA with an estimated maximal error of 0.09 \AA .

* All X-Ray diffraction experiments were performed by Dr P. Carr (RSC, ANU) with assistance from staff at the Australian Synchrotron

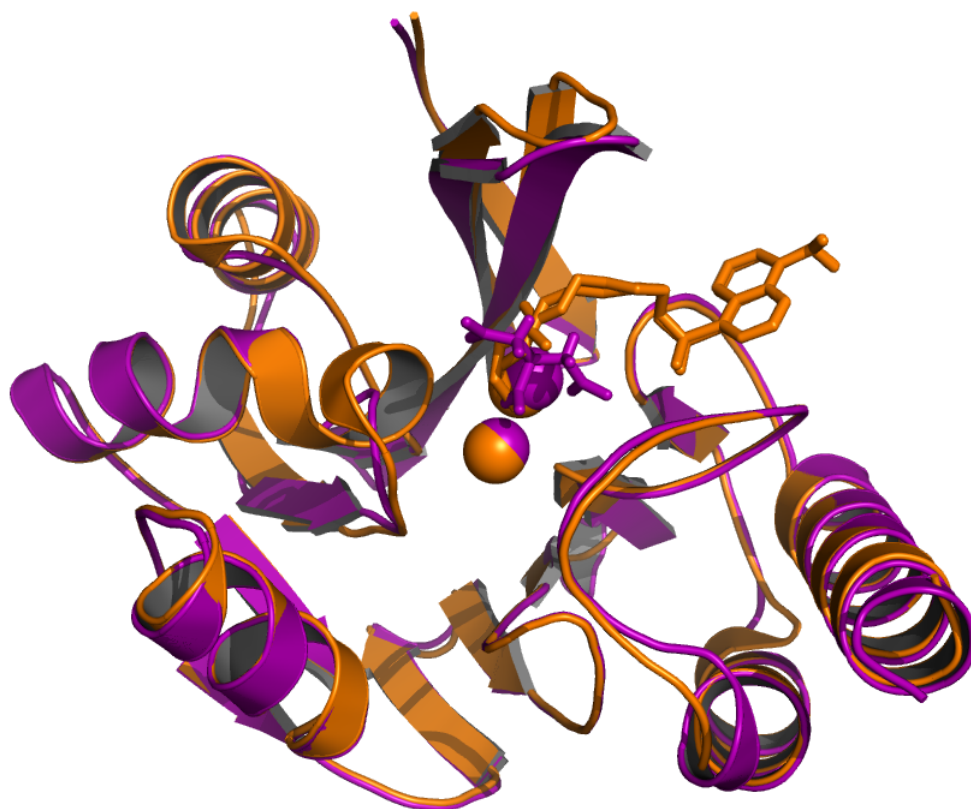
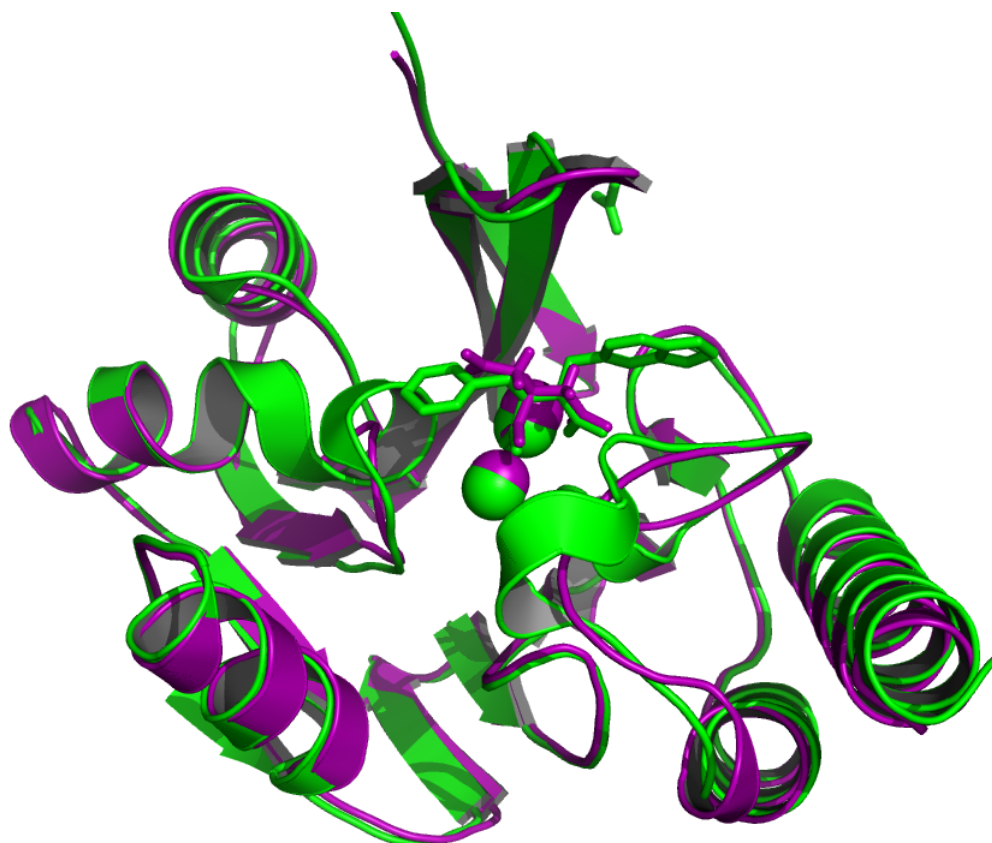
A**B**

Figure 2-39 Cartoon structural alignment between [FeZn]IMP-1 (purple) and **A**) 2DOO (orange) or **B**) 1JJE (green). The global structure is almost identical, and the calculated backbone nitrogen RMSD was 0.34 Å to 2DOO and 0.63 Å to 1JJE. Metal ions in the active site are shown as spheres. The ligand in the active site (citrate for [FeZn]IMP-1, succinic acid derivative for 1JJE and a fluorescent probe for 2DOO) is shown as sticks.

2.5.3 Determination of Iron-Binding Site

The X-ray fluorescence* scan observed after excitation at the Se-K edge is seen in Figure 2-40. Strong fluorescence bands assigned to Zn K α 1, K α 2 and K β 1 are present at 8,638, 8,615 and 9,572 eV. Weaker fluorescence bands are present for Fe K α 1 (6,404 eV), K α 2 (6,391 eV) and the K β 1 band at 7,058 eV is close to the noise level. Anomalous scattering experiments were run on the [FeZn]IMP-1 crystal above the iron and zinc absorption edges (7,162.0 and 9,660.0 eV). The anomalous scattering data maps obtained after refinement are shown in Figure 2-41.

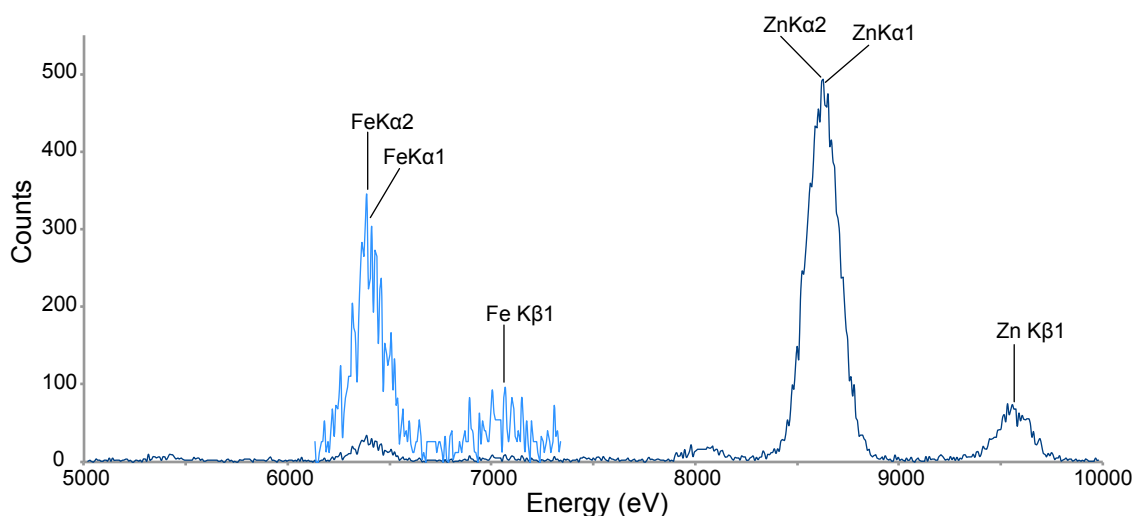


Figure 2-40 X-ray fluorescence scan at the Se-K edge. Assignments of iron and zinc K α 1, K α 2 and K β 1 fluorescence bands are indicated. An unassigned fluorescence is present around 8,000 eV, which could correlate with the Cu-K α band, but no appreciable amount of copper was determined in the protein via ICP-OES. The fluorescence for iron is weak and is highlighted with a cyan curve that has been multiplied by 10.

The scattering maps were inconsistent with what was expected from the experiment, as the metal ion in the Zn₁ site displayed the maximal anomalous scattering at both the zinc and iron ion edges rather than only one edge. This unexpected anomaly was corrected after close examination of the crystal temperature *B* factors of the metal ions and the citrate substrate. Initial rounds of refinement produced structures with metal ion *B* factors that differed greatly between the active-site metals and the active-site ligands. By refining the occupancy of the metal ions and of the citrate substrate using Coot²¹¹, the *B* factors of the metals aligned more reasonably with those of the atoms from the protein that were directly ligating the metal ions (Table 2-10).

* All X-ray diffraction experiments were performed by Dr P. Carr (RSC, ANU) with assistance from staff at the Australian Synchrotron

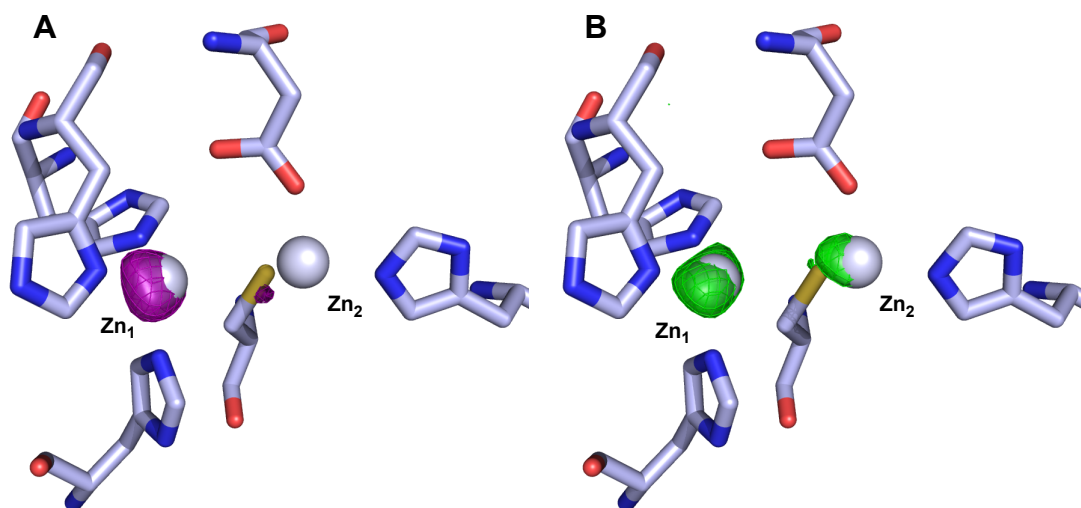


Figure 2-41 Anomalous scattering map showing anomalous diffraction around both active-site metals. **A)** Scattering at the iron ion edge (purple) is only around the metal in the Zn₁ site, whereas **B)** anomalous scattering at the zinc ion edge (green) is in both the Zn₁ site and the Zn₂ site. Spheres represent the metal ions, and the active site residues are represented as sticks. Scattering maps are scaled to just see the signal on the sulfur of the cysteine ligand at the Zn₂ site.

Table 2-10 Comparison of *B* factors prior and post active-site metal occupancy refinement

Atom	<i>B</i> factor	Metal ion	<i>B</i> factor before occupancy refinement	<i>B</i> factor after occupancy refinement (occupancy)
H77-N ^{ε2} ⁱ	15.45	Zn ₁	21.19	16.52 (0.81)
H79-N ^{δ1} ⁱ	12.92			
H139-N ^{ε2} ⁱ	14.61			
D81-O ^{δ2} ⁱⁱ	19.76	Zn ₂	40.94	16.96 (0.31)
C158-S ^γ ⁱⁱ	19.91			
H197-N ^{ε2} ⁱⁱ	24.96			

ⁱ atoms coordinating the Zn₁ metal site

ⁱⁱ atoms coordinating the Zn₂ metal site. The higher *B* factors indicate higher flexibility, consistent with a low occupancy of the Zn₂ metal ion-binding site

Table 2-11 Anomalous scattering values before and after metal occupancy refinement.

	Raw ⁱ		Corrected ⁱⁱ		Ratio ⁱⁱⁱ		Expected ^{iv}	
	Fe edge	Zn edge	Fe edge	Zn edge	Fe edge	Zn edge	Fe edge	Zn edge
Zn ₁ Site	0.1267	0.1447	0.1567	0.1786	1.00	0.57	1.00	0.60
Zn ₂ Site	ND ^v	0.0972	ND ^v	0.3135	ND ^v	1.00	0.20	1.00

ⁱ raw anomalous scattering data measured using COOT²¹¹ anomalous scattering map

ⁱⁱ scaled to account for an occupancy of 0.81 for the Zn₁ site and 0.31 for the Zn₂ site

ⁱⁱⁱ experimental ratio between anomalous scattering in the Zn₁ and Zn₂ site

^{iv} expected ratio between anomalous scattering assuming iron in the Zn₁ site and zinc in the Zn₂ site¹⁸⁸

^v anomalous scattering for the Zn₂ site at the iron ion edge was below the background noise of the experiment

With these refined metal occupancies, the anomalous scattering data were reanalysed and also became more consistent, suggesting that the Zn₁ site was occupied

by iron (81% occupancy) and the Zn₂ site was occupied by zinc (31% occupancy (Table 2-11).

2.5.4 Structural Comparison of [FeZn]IMP-1 to [ZnZn]IMP-1

The crystal structure of [FeZn]IMP-1 was compared to two [ZnZn]IMP-1 structures with similar resolutions and similar active-site ligands (PDB code: 1JJE¹²⁰ and 1DD6¹⁸²) (Figure 2-42). Analysis was performed using chain A of the [FeZn]IMP-1 structure, as this monomer was the most similar to the other three chains in the unit cell. Two chains are present in both 1JJE and 1DD6 but comparison was performed against only chain A in both cases. A global alignment between the structures yielded a backbone RMSD of 0.49 Å (1JJE) and 0.35 Å (1DD6). The active-site residues (backbone and side chain) aligned with an RMSD of 0.30 Å (1JJE) and 0.40 Å (1DD6).

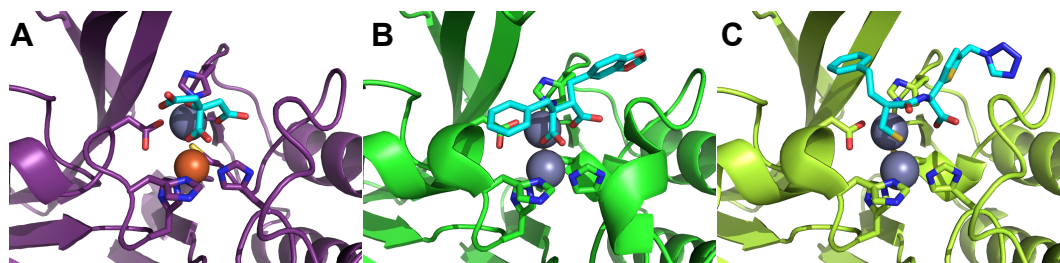


Figure 2-42 Structure of the active site of A) [FeZn]IMP-1, B) 1JJE and C) 1DD6. The bound ligand in all cases is shown in cyan sticks, and the side chains of the protein responsible for metal binding are also shown in sticks. The metal ions are shown in spheres, with zinc in grey and iron in orange. A very high degree of structural similarity is evident between 1JJE and [FeZn]IMP-1 in terms of the bound ligand, with an oxygen from a carboxylic acid group bridging between the two metal ions. In the absence of a ligand, the metal ions are likely bridged by a water/hydroxide ion. In 1DD6, a sulfur atom forms the bridge.

Table 2-12 Metal-ligand distances from [FeZn]IMP-1, 1JJE and 1DD6

	Zn ₁ site				Zn ₂ site		
	[FeZn] (Å) ⁱ	1JJE (Å)	1DD6 (Å)		[FeZn] (Å) ⁱ	1JJE (Å)	1DD6 (Å)
H77-N ^{ε2}	2.09	2.08	2.19	D81-O ^{δ2}	2.04	2.03	2.10
H79-N ^{δ1}	2.02	2.06	2.15	C158-S ^γ	2.38	2.15	2.33
H139-N ^{ε2}	2.12	1.99	2.16	H197-N ^{ε2}	2.18	2.28	2.26
L-1	2.00	2.00	2.24	L-1 ⁱⁱ	2.44	2.14	2.40
				L-2 ⁱⁱ	2.24	2.30	
				L-3 ⁱⁱ	2.26		

ⁱ [FeZn] is the structure solved in this work

ⁱⁱ L-1 is the atom in the bridging water/hydroxide ion position from the ligand. L-2 is the second carboxylic oxygen for both the succinic acid derivative in 1JJE and the citrate ion in [FeZn]IMP-1. L-3 is the alcohol oxygen in the citrate ion in [FeZn]IMP-1

The inter-metal distance was 3.56 Å in 1JJE, 3.60 Å in 1DD6 and 3.80 Å in the [FeZn]IMP-1 structure. Other key distances are listed in Table 2-12. It is worth noting

that the ligands in 1JJE and [FeZn]IMP-1 provide extra oxygen ligands to the Zn₂ site. The metal molecular geometries for the three structures are also included in Table 2-13.

Table 2-13 Active site metal-ligand geometryⁱ

[FeZn] ⁱⁱ	Zn ₁ – 4 ligands				Zn ₂ – 6 ligands				
	H79-N ^{δ1}	H139-N ^{ε2}	L-1 ⁱⁱⁱ		C158-S ^γ	H197-N ^{ε2}	L-1 ⁱⁱⁱ	L-2 ⁱⁱⁱ	L-3 ⁱⁱⁱ
H77-N ^{ε2}	101.2	109.7	123.5	D81-O ^{δ2}	99.2	104.8	86.7	161.9	87.4
H79-N ^{δ1}		106.3	108.5	C158-S ^γ		109.1	100.1	93.4	163.6
H139-N ^{ε2}			106.5	H197-N ^{ε2}			146.1	83.1	83.3
				L-1 ⁱⁱⁱ				78.2	65.1
				L-2 ⁱⁱⁱ					77.2

1JJE	Zn ₁ – 4 ligands				Zn ₂ – 5 ligands			
	H79-N _{δ1}	H139-N _{ε2}	L-1 ⁱⁱⁱ		C158-S ^γ	H197-N ^{ε2}	L-1 ⁱⁱⁱ	L-2 ⁱⁱⁱ
H77-N ^{ε2}	97.7	105.0	122.6	D81-O ^{δ2}	106.9	89.9	91.3	150.6
H79-N ^{δ1}		107.8	113.3	C158-S ^γ		107.9	110.2	102.5
H139-N ^{ε2}			109.1	H197-N ^{ε2}			139.7	79.6
				L-1 ⁱⁱⁱ				79.9

1DD6	Zn ₁ – 4 ligands				Zn ₂ – 4 ligands		
	H79-N ^{δ1}	H139-N ^{ε2}	L-1 ⁱⁱⁱ		C158-S ^γ	H197-N ^{ε2}	L-1 ⁱⁱⁱ
H77-N ^{ε2}	108.0	108.4	124.6	D81-O ^{δ2}	112.8	100.0	105.3
H79-N ^{δ1}		107.5	107.2	C158-S ^γ		106.9	118.8
H139-N ^{ε2}			99.9	H197-N ^{ε2}			111.6

ⁱ all angles in degrees

ⁱⁱ [FeZn] is the structure solved in this work

ⁱⁱⁱ L-11 is the atom in the bridging water/hydroxide ion position from the ligand. L-2 is the second carboxylic oxygen for both the succinic acid derivative in 1JJE and the citrate ion in [FeZn]IMP-1. L-3 is the alcohol oxygen in the citrate ion in [FeZn]IMP-1

It was noted, however, that the local RMSD significantly reduced for 1JJE if structural alignments were performed only for the N-terminal or C-terminal regions (Figure 2-43). When residues 1 to 120 were aligned, a backbone RMSD of 0.45 Å was measured. The global RMSD with this alignment was 0.69 Å and the RMSD of the C-terminal half was 0.88 Å. Similarly, if residues 120 to 221 were aligned, a backbone RMSD of 0.45 Å was measured, with a global RMSD of 0.65 Å and an N-terminal half RMSD of 0.80 Å. The improvement of alignment with 1DD6 was not as drastic, with the N-terminal alignment yielding RMSDs of 0.36 Å to the N-terminal region, 0.43 Å to the C-terminal region and 0.40 Å globally. The C-terminal alignment yielded RMSDs for the N-terminal region of 0.45 Å, the C-terminal region of 0.28 Å, and globally of 0.38 Å.*

* All RMSD calculations excluded the most mobile regions including residues 1 to 4 of the N-terminus, residues 23-32 of the flap, and 216-221 of the C-terminus.

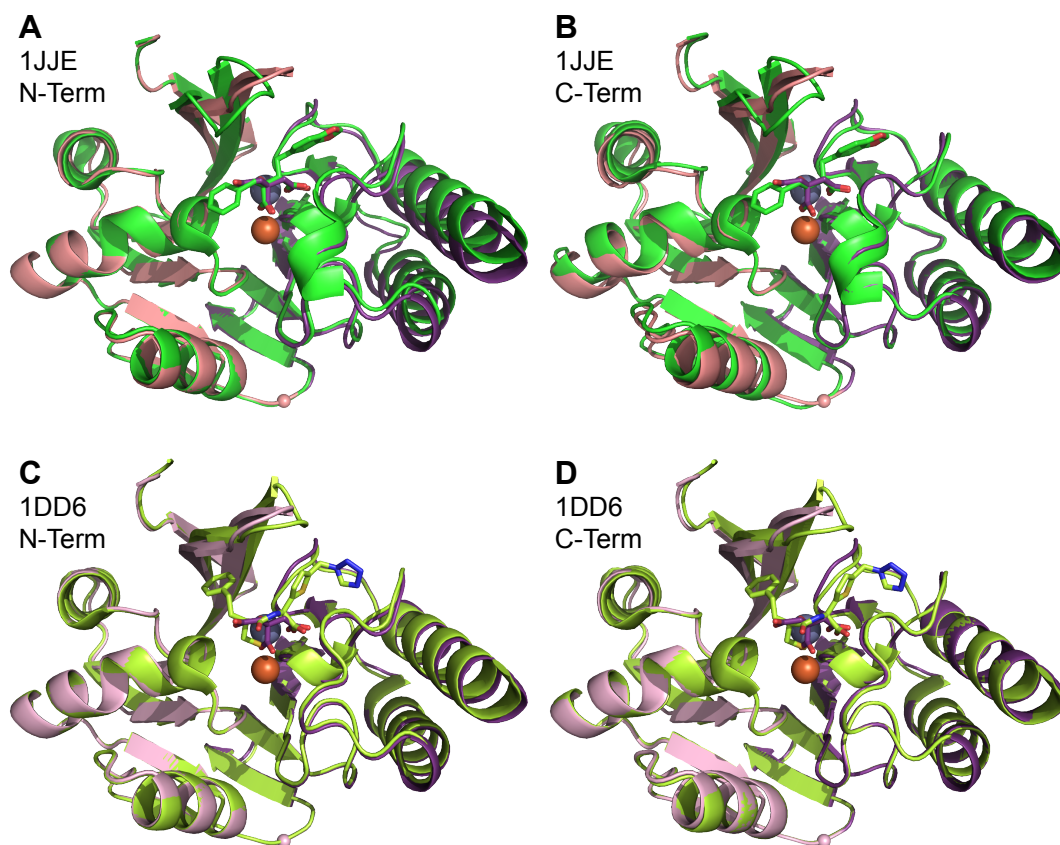


Figure 2-43 Structural alignment of the N- and C-terminal halves of the solved crystal structure of [FeZn]IMP-1 to 1JJE (green) and 1DD6 (light green). The N-terminal half of [FeZn]IMP-1 is coloured pink, where the C-terminal half is coloured purple. **A)** When residues 1 to 120 of the N-terminal half are aligned to 1JJE (RMSD: 0.45 Å) an offset of the C-terminal half is evident to 1JJE (RMSD: 0.88). **B)** Conversely, when only the C-terminal domain is aligned (RMSD: 0.45 Å) the N-terminal domain is also offset by a similar amount (RMSD: 0.80 Å). Alignment of the **C)** N-terminal domain or the **D)** C-terminal domain to 1DD6 does not have as drastic an effect. The Ca atom of Gly120 is indicated as a small sphere at the bottom of each structure. The flap region (excluded from RMSD calculations) is evident at the top of each structure. Only the metal ions from the [FeZn]IMP-1 structure are shown as spheres, with iron in orange and zinc in grey. The ligands co-crystallised in each structure are indicated as sticks.

The difference from 1JJE would seem to suggest that the sandwich $\alpha\beta/\beta\alpha$ -fold of the enzyme is somewhat flexible, enabling a slightly larger opening in the active site groove. This can be quantified by measuring the angle defined by the three Ca atoms of Ala53, Gly120 and Leu205. The [ZnZn] form in 1JJE has an angle of 66.5° and for the [FeZn] form an angle of 68.8° is present. This difference is probably not due to the metal substitution as the same angle measured in 1DD6 is 68.9° (Figure 2-44).

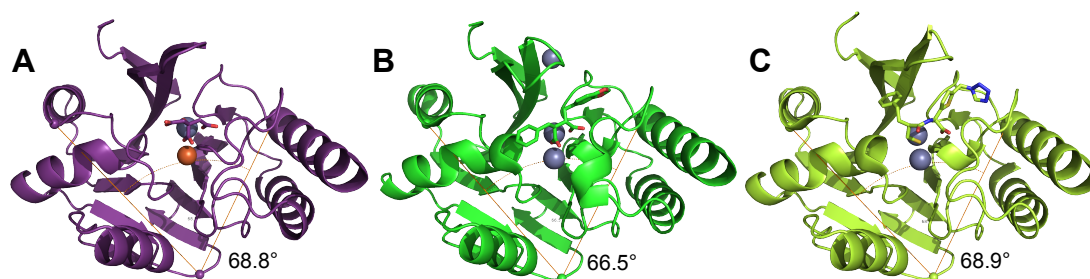


Figure 2-44 $\alpha\beta/\beta\alpha$ -fold opening angle. **A)** The [FeZn]IMP-1 structure solved in this work has a wider opening than **B)** the 1JJE structure, but **C)** a very similar opening to 1DD6. Small spheres highlight the Ca atoms of A53, G120 and L205 that were used to measure the reported angles. The two active-site metals are shown in spheres, with zinc in grey and iron in dark orange. Active-site ligands are shown as sticks.

Finally, packing-density analysis of chain A from the [FeZn]IMP-1 structure and chain A from the 1JJE and 1DD6 structures was performed using Voronoia software.²¹² The results are listed in Table 2-14 below. Of the [ZnZn]IMP-1 structures, 1DD6 had the least efficient packing density (0.716) with 15 internal cavities. 1JJE had a buried packing density of 0.709 with 19 internal cavities. The [FeZn]IMP-1 structure had a packing density of 0.710, and 15 internal cavities. The cavities are visualised in Figure 2-45. Of the cavities found, 8 are shared between all structures. The [FeZn]IMP-1 structure has 4 unique cavities, and of particular interest is the location of one directly under the active site. This is highlighted in Figure 2-45D.

Table 2-14 Results from packing-density calculations

Protein ⁱ	Av. VdW volume (Å ³) ⁱⁱ	Av. solvent excluded (Å ³) ⁱⁱⁱ	Av. total volume (Å ³) ^{iv}	Av. packing density ^v	Number of cavities ^{vi}
[FeZn]IMP-1	10.90	5.35	16.25	0.710	15
1JJE	10.83	5.38	16.21	0.709	19
1DD6	10.92	5.22	16.15	0.716	15

ⁱ Surface atoms are defined by rolling a virtual water molecule (a 1.4 Å radius sphere) over the protein. Any atom that is touched by the probe is assigned to the surface and excluded from the density analysis. All other atoms are defined as buried.

ⁱⁱ Average Van-der-Waals radii calculated volume per atom analysed

ⁱⁱⁱ Average volume of solvent excluded per atom analysed excess to the Van-der-Waals volume

^{iv} The average sum of Van-der-Waals volume and solvent excluded volume per atom analysed

^v Average packing density, defined as column 3 divided by the sum of column 4 and 5

^{vi} Number of cavities identified as a void that a virtual 1.4 Å radius probe could fit where there is no escape path out of the protein without collision with a protein atom.

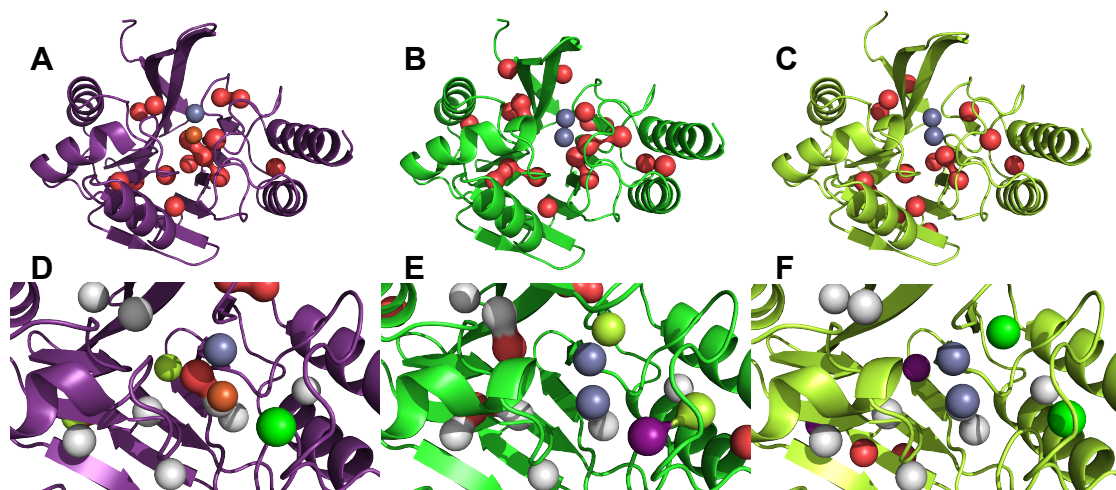


Figure 2-45 Visualisation of calculated cavities large enough to fit a 1.4 Å radius sphere (water molecule) for **A)** [FeZn]IMP-1, **B)** 1JJE and **C)** 1DD6. The cavities are indicated by red surfaces. 19 cavities were found in the 1JJE structure whereas only 15 cavities were found in the [FeZn] form and 1DD6. Cavities around the active site are highlighted in **D-F)** where cavities common to all three structures are coloured white, cavities common to 1JJE are coloured green, cavities common to 1DD6 are coloured light green, cavities common to [FeZn]IMP-1 are coloured purple, and unique cavities are coloured red. Of particular note is the unique cavity found under the metal ions in the [FeZn]IMP-1 structure.

2.6 Results: NMR Analysis of IMP-1

2.6.1 Protein Samples Prepared by Cell-Free Synthesis with Combinatorial and Individual ^{15}N -Labelling

NMR assignments and analyses were aided by the cell-free production of IMP-1 with combinatorial-labelling,^{213-215*} however, total control over the metal substitution of the enzyme was not attained even after the addition of excess zinc. This resulted in spectral overlap of some of the peaks in the [FeZn] form with peaks from the [ZnZn] form (Figure 2-46), and was especially problematic since the method relies on accurate superposition of the spectra from different samples for amino-acid type identification. The resulting occasional misassignment of amino-acid type was resolved by the individual labelling of 19 samples in cell-free protein synthesis,[†] which was supplemented with exogenous zinc. While complete control over the metal incorporated into the enzyme was still not attained, the amino-acid typing of the [ZnZn]IMP-1 was rendered reliable (Figure 2-47).

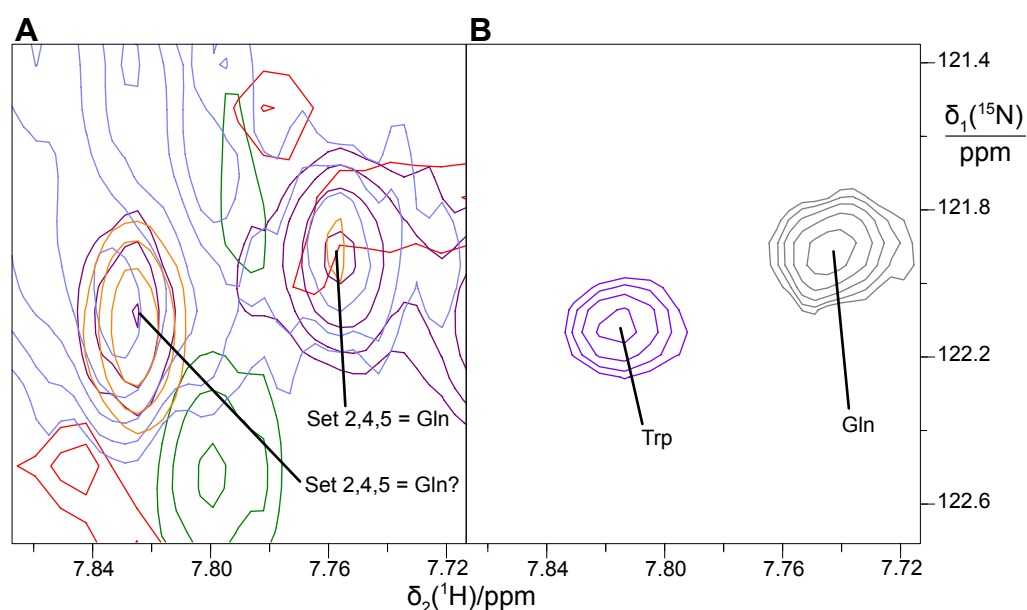


Figure 2-46 **A)** Combinatorial labelling failed to correctly identify a Trp residue due to overlap of [FeZn]IMP-1 peaks with [ZnZn]IMP-1 peaks. Overlapping peaks from set 1 (red), set 2 (orange), set 3 (green), set 4 (blue) and set 5 (purple) imply the highlighted peak on the left is a Gln residue, but **B)** single labelling with ^{15}N -Gln (grey) and Trp (purple) resolves the overlap issue and significantly simplifies analysis.

* Samples with combinatorial ^{15}N -labelling were synthesised with assistance from Mr J. Chew

† Samples with individual ^{15}N -labelling were synthesised by Ms E. Cliff under supervision by Dr C.T. Loh and the author

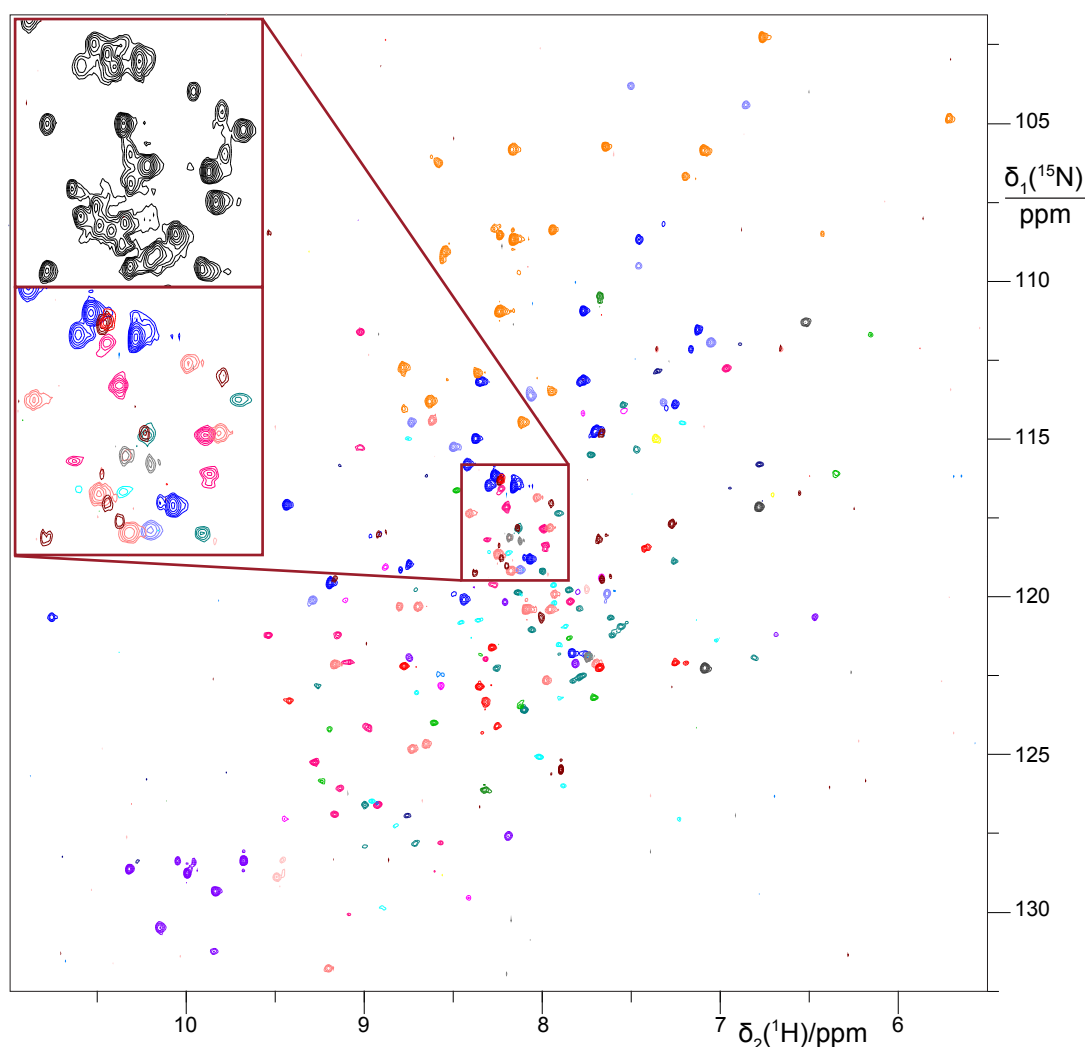


Figure 2-47 Overlay of 19 ^{15}N -HSQC spectra used for amino-acid typing. Comparison to a $[\text{H-}^{15}\text{N}]$ -TROSY spectrum of an *in vitro* uniformly $^2\text{H}/^{13}\text{C}/^{15}\text{N}$ -labelled $[\text{ZnZn}]$ IMP-1 sample (black) is highlighted for an overlapped region. Amino acids are coloured as follows: alanine (red), arginine (dark grey), asparagine and aspartate (maroon), cysteine (light pink), glutamine (grey), glutamate (mid pink), glycine (orange), histidine (green), isoleucine (mid green), leucine (cyan), lysine (teal), methionine (sky blue), phenylalanine (navy), serine (blue), threonine (mid blue), trptophan (mauve), tyrosine (magenta), valine (pink).

The amino-acid pairs serine-threonine and serine-serine only occur once in the IMP-1 sequence, enabling individual assignments of two residues close to the active site, Ser92 and Thr99, by ^{15}N -Thr and $^{13}\text{C}^{15}\text{N}$ -Ser labelling using cell-free protein synthesis.* When a ^{15}N -HSQC spectrum was measured with ^{13}C decoupling only for the $\text{C}\alpha$ region, two doublets were observed corresponding to a $^1J_{\text{NC}}$ coupling of approximately 14 Hz (Figure 2-48) corresponding to either an ST or SS dipeptide sequence. Comparison with the spectra of combinatorial or single amino-acid labelled samples allowed distinction between the two cases.

* Samples with $^{13}\text{C}^{15}\text{N}$ -labelled serine and ^{15}N -labelled threonine were synthesised with assistance from Mr J. Neeman

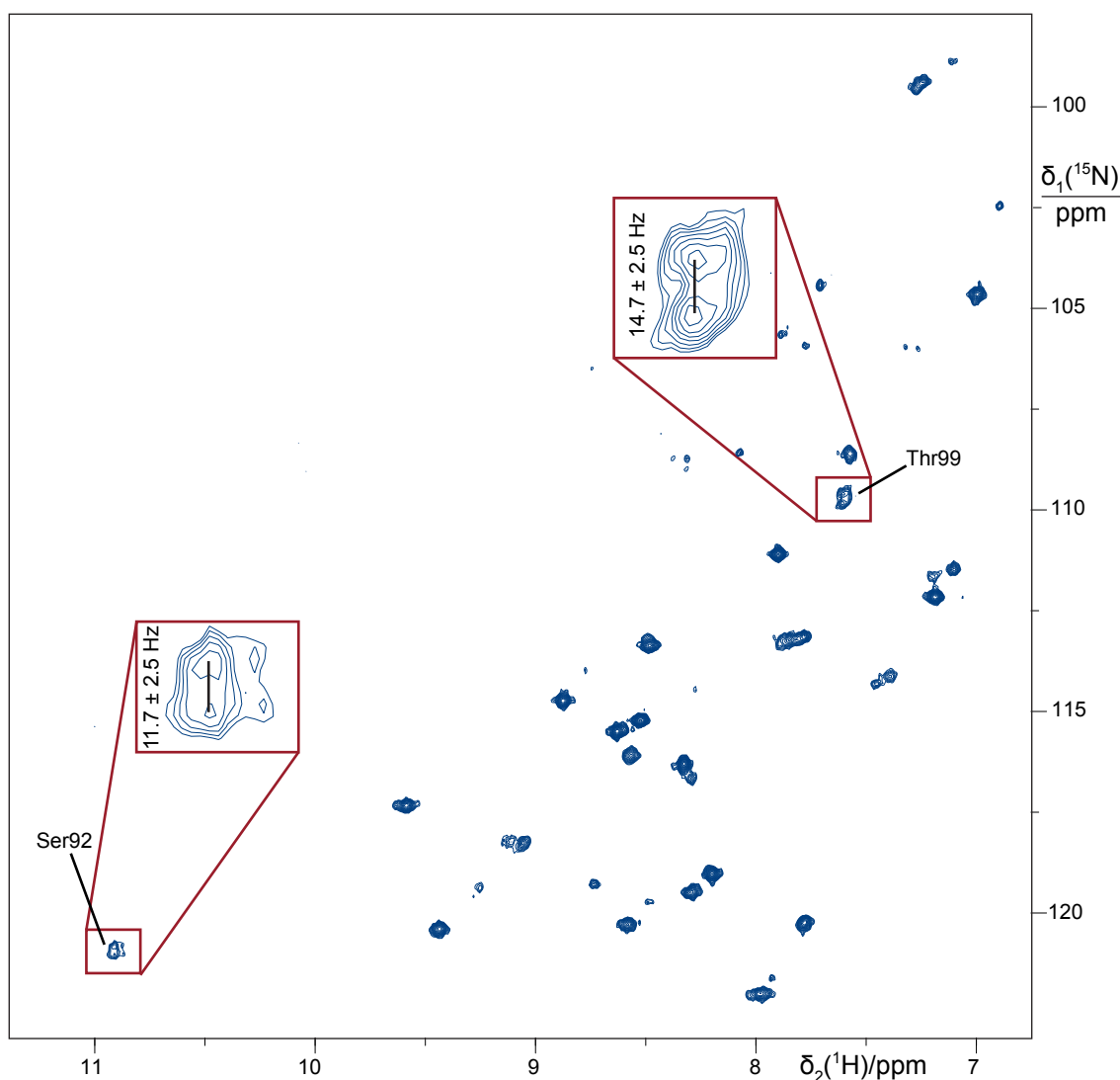


Figure 2-48 ^{15}N -HSQC NMR spectrum of ^{15}N -Thr and $^{13}\text{C}^{15}\text{N}$ -Ser labelled IMP-1 recorded with ^{13}C decoupling of C' but not $\text{C}\alpha$. Assignments were made by identifying two peaks with doublet splitting in the nitrogen dimension due to $^1J_{\text{NC}'}$ couplings of approximately 14 Hz (highlighted by red boxes). The two peaks can be assigned to serine or threonine by comparison with other spectra where serine or threonine residues were selectively labelled with ^{15}N .

2.6.2 Assignment of Backbone Resonances via 3D NMR Experiments

HNCA, HN(CO)CA, HNCACB and CBCA(CO)NH experiments were recorded of the [ZnZn]IMP-1 *in vivo* sample for assignment purposes. Approximately 50% of the non-proline backbone amide resonances were assigned this way, however significant overlap made further assignment impossible.

To address the problem of overlapping cross-peaks, a $^2\text{H}/^{13}\text{C}/^{15}\text{N}$ -labelled sample was expressed *in vivo* and $[^1\text{H}-^{15}\text{N}]$ -TROSY, TROSY-HNCA, TROSY-HNCACB, TROSY-HNCO and TROSY-HN(CA)CO experiments were recorded. As the enzyme could not be refolded, back-exchange of the amide protons could only be achieved by exposure to H_2O as it occurs, for example, during protein purification. The

spectral resolution obtained from the triple-labelled sample was vastly improved and enabled the deconvolution of many overlapping peaks, but amides of buried residues were not easily observed due to limited back-protonation.

The issue of proton back-exchange prompted the project described in chapter 3. In brief, a protein sample uniformly labelled with $^2\text{D}/^{13}\text{C}/^{15}\text{N}$ amino acids was made by cell-free synthesis in H_2O .^{*} This made the need for back-exchange of amide protons dispensable. With this sample, $[^1\text{H}-^{15}\text{N}]$ -TROSY, TROSY-HNCA, TROSY-HNCACB, TROSY-HNCO and TROSY-HN(CA)CO experiments were recorded.

Using the information from the combinatorially ^{15}N -labelled samples, the individually ^{15}N -labelled cell-free samples, the *in vivo* ^{15}N -labelled $[\text{ZnZn}]$ samples and the triple-labelled sample prepared by cell-free synthesis, 89.5% of the non-proline backbone amide resonances of the $[\text{ZnZn}]$ IMP-1 protein were assigned.[†] These assignments were mapped onto the NMR spectra of the $[\text{FeZn}]$ IMP-1 sample assuming similarity of backbone amide shifts, and confirmed where possible by checking for similarity of $\text{C}\alpha$ chemical shifts.[‡] All completed assignments of $[\text{ZnZn}]$ IMP-1 and $[\text{FeZn}]$ IMP-1 are listed in Table 2-15 and Table 2-16, respectively.

Regions of the $[\text{ZnZn}]$ protein with unassigned backbone resonances were limited to β -turns and to flexible loops near the active site (Figure 2-49).

^{*} The sample with uniform $^2\text{H}/^{13}\text{C}/^{15}\text{N}$ -labelled amino acids in H_2O cell-free protein synthesis reaction was performed by Dr C.T. Loh in consultation with the author

[†] Degree of assignment (including proline residues) of $[\text{ZnZn}]$ IMP-1 including the N-terminal MASMTG tag: H 196/219, N 196/233, $\text{C}\alpha$ 212/233, $\text{C}\beta$ 175/212, C' 168/233.

[‡] Degree of assignment (including proline residues) of $[\text{FeZn}]$ IMP-1 including the N-terminal MASMTG tag: H 156/219, N 156/233, $\text{C}\alpha$ 162/233.

Table 2-15 Table of backbone assignments of [ZnZn]IMP-1ⁱ

Residue		H	N	Ca	Cβ	C'	Residue		H	N	Ca	Cβ	C'
-4	Met						61	Thr	8.50	115.2	67.1	68.9	175.1
-3	Ala						62	Trp	7.82	122.1	62.3	29.5	179.6
-2	Ser						63	Phe	7.36	112.8	63.6	39.0	179.0
-1	Met	8.57	122.5			176.9	64	Val	8.98	124.1	66.2	31.4	182.1
0	Thr	8.07	113.7			175.6	65	Glu	8.69	120.3	58.7	28.6	178.1
1	Gly	8.24	111.0	45.4	-	174.5	66	Arg	6.79	117.1	56.0	29.4	175.5
2	Glu	8.08	120.3	56.4	30.1	176.8	67	Gly	7.64	105.7	45.3	-	174.5
3	Ser	8.16	116.4	58.2	63.7	174.3	68	Tyr	7.69	119.5	57.5	39.0	175.1
4	Leu	8.03	125.1	52.9	41.5	175.1	69	Lys	8.15	119.9	54.6	33.5	176.3
5	Pro	-		62.3	30.5	175.5	70	Ile	8.60	124.0	59.2	33.8	176.1
6	Asp	7.66	119.4	53.7	42.2	175.7	71	Lys	8.71	127.8	54.2	32.9	176.9
7	Leu	7.95	120.2	55.9	42.6	176.8	72	Gly	6.75	102.1	45.6	-	171.5
8	Lys	9.01	127.9	54.7	35.3	175.7	73	Ser	8.38	113.3	56.2	66.6	173.6
9	Ile	8.13	123.5	61.1	40.1	175.6	74	Ile	9.21	124.3	57.9	40.3	173.8
10	Glu	8.73	124.7	54.4	34.1	175.0	75	Ser	7.86	121.8	58.8	65.2	174.3
11	Lys	9.00	126.6	58.1	32.5	175.5	76	Ser	10.78	120.6	60.3	63.7	173.8
12	Leu	8.89	129.8	55.3	44.5	175.2	77	His	7.68	110.3	55.4	27.2	175.9
13	Asp	8.24	116.3	51.4	43.6	175.4	78	Phe	9.15	115.7	59.9	39.2	175.0
14	Glu	9.16	122.1	58.1	28.3	177.7	79	His					
15	Gly	8.63	113.7	46.5	-	173.6	80	Ser					
16	Val	7.99	117.9	61.9	34.7	174.0	81	Asp			55.0	38.1	173.8
17	Tyr	9.46	126.9	56.5	41.1	175.4	82	Ser	7.46	108.4	60.7	66.9	178.0
18	Val	9.54	121.1	60.0	33.8	176.8	83	Thr	7.48	109.6	61.3	71.7	176.7
19	His	8.32	126.0	52.6	34.9	174.5	84	Gly	8.37	113.0	47.7	-	176.1
20	Thr	9.32	120.1	61.6	70.5	172.4	85	Gly	8.61	106.3	45.5	-	174.6
21	Ser	8.44	120.0	56.0	67.5	173.0	86	Ile	7.87	121.4	67.2	36.8	177.1
22	Phe	8.67	116.2	57.6	43.6	174.6	87	Glu	8.80	120.3	60.6	28.6	178.9
23	Glu	7.91	120.0	54.5	31.3		88	Trp	8.74	122.0	62.9	28.4	180.6
24	Glu	8.69	124.7	55.9	29.8	175.9	89	Leu	8.46	120.8	58.8	40.2	179.9
25	Val	8.57	127.9	61.3	33.2	176.7	90	Asn	9.17	119.3	55.4	36.4	180.8
26	Asn						91	Ser	8.07	118.8	61.1	62.6	174.9
27	Gly			45.5	-	174.4	92	Arg	7.09	122.3	54.2	28.8	175.5
28	Trp	8.21	120.3	57.7	31.4	176.3	93	Ser	7.76	111.0	59.1	61.0	174.3
29	Gly	8.24	108.4	44.7	-	173.2	94	Ile	7.72	123.3	58.4	38.1	174.9
30	Val	8.33	122.1	63.0	31.4	176.6	95	Pro	-		64.3	33.0	174.9
31	Val	9.07	130.0	58.8	34.3		96	Thr	7.05	111.9	58.4	72.0	174.9
32	Pro	-		61.2	32.6	176.9	97	Tyr	9.11	120.0	56.8	41.7	176.5
33	Lys	8.74	119.8	53.3	35.1	175.7	98	Ala	8.29	121.5	51.3	21.0	174.3
34	His	9.83	128.8	53.7	29.4	176.2	99	Ser	9.44	117.1	57.2	64.1	174.8
35	Gly	8.79	112.7	43.1	-	172.9	100	Glu	7.93	120.3	59.9	29.1	179.4
36	Leu	8.78	115.1	53.0	46.2	178.3	101	Leu	7.96	119.7	57.5	40.5	178.8
37	Val	9.15	121.2	63.0	34.0	174.9	102	Thr	8.15	119.1	66.6	67.2	176.6
38	Val	8.94	126.5	60.4	34.2	174.7	103	Asn	8.21	119.0	54.9	37.0	179.0
39	Leu	8.96	126.4	53.3	41.2	177.6	104	Glu	7.98	122.6	59.4	28.8	179.4
40	Val	9.28	125.3	61.5	32.6	176.3	105	Leu	7.93	121.5	57.8	38.9	180.4
41	Asn			55.9	37.1	174.5	106	Leu	8.36	120.7	58.3	40.9	179.1
42	Ala	8.33	123.4	52.8	17.8	176.2	107	Lys	7.84	119.8	59.4	31.7	181.5
43	Glu	8.18	119.2	55.2	31.5	174.5	108	Lys	8.07	121.0	59.2	31.6	177.8
44	Ala	8.78	122.1	50.1	21.4	176.2	109	Asp	7.29	117.7	54.2	42.1	176.8
45	Tyr	8.90	119.0	56.6	40.5	175.5	110	Gly	7.94	108.4	46.2	-	175.2
46	Leu	8.72	122.9	55.3	41.3	175.2	111	Lys	8.02	119.3	53.3	33.8	176.0
47	Ile	9.25	125.8	60.5	33.9	175.2	112	Val	7.84	120.1	63.5	31.6	175.9
48	Asp	8.91	117.9	57.2	38.8	175.1	113	Gln	7.75	121.8	55.7	31.0	177.9
49	Thr	6.87	104.5	58.3	67.9	173.5	114	Ala	8.36	122.7	51.7	18.5	179.1
50	Pro			62.5	33.2	173.6	115	Thr	8.74	114.5	63.8	69.5	174.8
51	Phe	6.86	111.9	61.2	41.0	177.6	116	Asn	8.38	119.3	52.7	41.6	173.4
52	Thr	7.13	99.5	58.6	73.8		117	Ser	8.38	115.0	55.9	65.9	174.2
53	Ala			55.6	17.9	179.9	118	Phe	6.81	116.0	55.2	40.4	174.0
54	Lys	8.15	117.9	59.2	31.2	179.6	119	Ser	8.43	115.8	57.1	65.2	174.3
55	Asp	7.69	118.1	56.8	40.6	178.8	120	Gly	8.17	108.8	44.4	-	174.3
56	Thr	7.65	119.9	68.6	66.9	174.6	121	Val	8.20	117.2	64.4	32.1	175.1
57	Glu	7.70	122.1	58.8	27.8	179.5	122	Asn	7.68	114.9	52.1	42.0	174.0
58	Lys	7.60	121.2	60.1	32.3	178.8	123	Tyr	8.58	122.9	57.1	41.7	174.1
59	Leu	7.87	120.9	58.1	42.2	177.6	124	Trp	8.21	127.5	55.4	28.0	174.4
60	Val	8.23	116.5	67.4	31.4	178.5	125	Leu	7.23	127.1	56.8	42.0	177.1

Residue		H	N	Ca	Cβ	C'	Residue		H	N	Ca	Cβ	C'
126	Val	6.96	112.8	61.3	34.5	176.9	178	Lys	7.26	118.9	59.9	31.5	180.3
127	Lys			59.2	30.9	175.9	179	Ser	8.74	118.9	60.4		
128	Asn	5.89	116.2	56.1	37.6	173.9	180	Ala	9.43	123.2	55.0	18.2	
129	Lys	7.73	115.5	56.9	35.8	176.4	181	Lys	8.26	122.3	60.1		
130	Ile	8.49	116.7	62.1	40.9	173.5	182	Leu	7.74	121.9	58.1		
131	Glu	9.22	131.7	54.6	32.1	174.0	183	Leu	8.18	118.6	58.3	41.4	178.2
132	Val	9.16	126.9	60.9	32.0	175.1	184	Lys	7.94	117.4	59.2	31.9	177.9
133	Phe	8.76	126.9	55.5	43.1	173.2	185	Ser	7.74	113.1	60.8	62.9	176.2
134	Tyr	8.45	129.5	52.5	38.9	171.8	186	Lys	7.54	120.7	57.9	32.6	178.2
135	Pro						187	Tyr	7.55	114.1	56.7	37.4	175.5
136	Gly				-		188	Gly	7.14	105.9	47.1	-	174.6
137	Pro	-					189	Lys	7.48	115.4	55.2	30.7	176.2
138	Gly				-		190	Ala	7.66	122.1	53.8	18.8	176.6
139	His			59.1			191	Lys	9.27	122.7	57.9	33.3	176.9
140	Thr	7.50	103.8	59.6			192	Leu	7.21	114.5	53.1	46.8	175.4
141	Pro	-		65.2			193	Val	9.07	122.0	60.6	32.7	174.2
142	Asp	9.54	108.4	53.2			194	Val	9.13	126.0	59.1	33.1	174.7
143	Asn	6.57	116.7	54.8	39.4	175.6	195	Pro	-				
144	Val	9.03	115.3	59.2	34.3	176.1	196	Ser					
145	Val	9.01	111.6	58.7	32.3	175.0	197	His			54.8		
146	Val	8.27	118.1	60.7	34.7	173.0	198	Ser	7.08	111.5	57.6	63.2	
147	Trp	9.81	131.1	54.3	33.6	173.9	199	Glu	8.30	117.3	57.0	29.9	176.6
148	Leu	7.90	125.9	50.2	39.6	175.3	200	Val	7.96	118.3	64.0	31.4	176.5
149	Pro	-		64.2	32.1	179.1	201	Gly	8.12	114.2	45.1	-	172.1
150	Glu	8.61	114.4	59.1	29.2	178.4	202	Asp	7.99	120.6	52.3	41.5	
151	Arg	6.55	111.3	52.9	30.4	175.1	203	Ala	8.20	116.2	55.1	17.5	
152	Lys	7.53	114.1	57.1	28.9	175.6	204	Ser	9.18	119.5	62.3		
153	Ile	6.37	116.2	60.0	41.1	173.0	205	Leu	8.11	119.7	58.3	40.9	
154	Leu	8.82	127.2	52.4	45.7	175.9	206	Leu					
155	Phe	10.29	128.4	57.1	38.2	174.4	207	Lys					
156	Gly	7.93	113.4	43.9	-		208	Leu			58.1		
157	Gly	5.72	104.9	47.4	-	176.5	209	Thr	7.32	113.9	67.6	69.4	
158	Cys	9.32	128.7	60.1	27.0	174.0	210	Leu	7.02	121.3	58.7		
159	Phe	6.97	116.5	60.4	40.5	174.7	211	Glu	8.03	116.8	59.5	29.4	
160	Ile	6.18	111.6	57.9	35.3	179.3	212	Gln	8.18	118.0	58.0	31.4	
161	Lys	6.80	121.9	59.4			213	Ala	8.25	124.1	55.0		
162	Pro	-		63.3			214	Val	8.27	119.7	67.0		
163	Tyr	7.77	114.1	55.9			215	Lys	7.79	120.4	59.7	32.3	
164	Gly				-		216	Gly	8.17	105.9	46.4	-	
165	Leu						217	Leu	7.90	123.3	57.7		
166	Gly				-		218	Asn	8.23	118.7	55.9	38.3	
167	Asn						219	Glu	8.26	118.7	58.0	29.7	
168	Leu			55.0			220	Ser	7.71	114.7	60.1	63.8	
169	Gly	8.54	109.1	48.1	-		221	Lys	7.56	121.0	55.9	32.3	
170	Asp	7.96	117.1	54.0			222	Lys	7.79	122.6			
171	Ala	7.24	122.1	52.2	21.0		223	Pro	-		63.2	32.1	
172	Asn	8.25	118.4	51.6	38.1		224	Ser	8.30	116.5	58.3	64.1	
173	Ile	8.35	121.8	62.8			225	Lys	8.11	123.7	54.1	32.9	
174	Glu	7.95	117.7	59.1	29.7	178.6	226	Pro	-		63.4	32.1	
175	Ala	7.47	118.6	53.0	20.3	179.1	227	Ser	8.27	116.2	58.3	63.9	173.9
176	Trp	7.81	119.8	61.3	26.9		228	Asn	7.90	125.4	55.0	40.2	179.7
177	Pro	-		66.8	30.5	180.0							

ⁱ Chemical shifts reported in ppm. Shifts highlighted in red were not observable in the TROSY-type experiments that contained constant time elements, and were measured of non-deuterated protein using conventional HNCA or HNCACB NMR experiments. Blank fields indicate unassigned resonances. The six metal-coordinating residues are highlighted in bold type.

Table 2-16 Table of backbone assignments of [FeZn]IMP-1ⁱ

Residue		H	N	Ca	Residue	H	N	Ca	
-4	Met				61	Thr	8.55	115.3	67.3
-3	Ala				62	Trp	7.88	122.2	62.6
-2	Ser				63	Phe	7.39	112.9	63.9
-1	Met			56.0	64	Val	9.00	124.2	66.6
0	Thr	8.09	113.7	62.1	65	Glu	8.74	120.4	59.0
1	Gly	8.26	111.0	45.5	66	Arg	6.82	117.2	56.1
2	Glu	8.11	120.5	56.6	67	Gly	7.68	105.8	45.4
3	Ser	8.19	116.6	58.2	68	Tyr	7.71	119.5	57.7
4	Leu	8.05	125.1	53.1	69	Lys	8.16	120.0	54.7
5	Pro	-		62.6	70	Ile	8.65	124.1	59.4
6	Asp	7.72	119.6	53.7	71	Lys	8.74	128.1	54.2
7	Leu	8.00	120.2	56.2	72	Gly	6.80	102.2	45.7
8	Lys	9.09	128.1	54.9	73	Ser	8.38	113.2	56.3
9	Ile	8.18	123.7	61.2	74	Ile	9.27	124.8	
10	Glu	8.76	124.9	54.5	75	Ser	7.93	121.9	58.9
11	Lys	9.04	126.8	58.4	76	Ser			
12	Leu	8.94	130.0	55.2	77	His			
13	Asp	8.27	116.4	51.4	78	Phe			
14	Glu	9.20	122.2	58.2	79	His			
15	Gly	8.66	114.0	46.6	80	Ser			
16	Val	8.01	117.9	62.1	81	Asp			
17	Tyr	9.50	127.1	56.7	82	Ser			
18	Val	9.59	121.3	60.2	83	Thr			
19	His	8.38	126.1	52.6	84	Gly			
20	Thr	9.43	120.4	62.0	85	Gly			
21	Ser				86	Ile	7.88	121.3	67.6
22	Phe				87	Glu	8.83	120.3	60.9
23	Glu				88	Trp	8.79	122.0	63.2
24	Glu				89	Leu	8.50	120.9	59.1
25	Val				90	Asn	9.16	119.4	55.4
26	Asn				91	Ser	8.09	119.0	61.3
27	Gly				92	Arg	7.11	122.4	54.2
28	Trp	8.22	120.3	57.1	93	Ser	7.79	111.0	59.2
29	Gly	8.24	108.6	44.6	94	Ile	7.73	123.3	58.6
30	Val				95	Pro	-		64.5
31	Val				96	Thr	7.11	112.2	58.5
32	Pro	-			97	Tyr	9.18	120.2	56.9
33	Lys				98	Ala	8.29	121.7	51.2
34	His				99	Ser	9.34	117.1	57.2
35	Gly				100	Glu	7.99	120.4	60.2
36	Leu			53.1	101	Leu	7.96	119.8	57.8
37	Val	9.20	121.4	63.2	102	Thr	8.14	119.2	66.8
38	Val	8.97	126.8	60.6	103	Asn	8.22	119.2	54.9
39	Leu	8.99	126.6	53.3	104	Glu	7.97	122.8	59.5
40	Val	9.30	125.3	61.7	105	Leu	7.92	121.6	58.2
41	Asn			56.1	106	Leu	8.37	120.9	58.5
42	Ala	8.35	123.4	52.9	107	Lys	7.84	119.8	59.7
43	Glu	8.20	119.2	55.3	108	Lys	8.08	121.2	59.6
44	Ala	8.81	122.3	50.2	109	Asp	7.32	117.9	54.1
45	Tyr	8.90	119.1	56.7	110	Gly	7.95	108.3	46.2
46	Leu	8.75	123.1	55.4	111	Lys	8.01	119.4	53.5
47	Ile				112	Val	7.86	120.1	63.7
48	Asp				113	Gln	7.76	121.8	55.8
49	Thr				114	Ala	8.38	122.9	51.8
50	Pro	-			115	Thr	8.76	114.4	64.0
51	Phe				116	Asn	8.40	119.4	52.7
52	Thr				117	Ser	8.40	115.1	56.0
53	Ala				118	Phe	6.79	115.9	55.3
54	Lys	8.20	117.9	59.6	119	Ser	8.40	115.7	57.1
55	Asp	7.76	118.3	57.0	120	Gly	8.15	108.6	44.4
56	Thr	7.74	120.1	69.0	121	Val	8.21	117.6	64.8
57	Glu	7.76	122.3	59.1	122	Asn	7.66	114.9	52.1
58	Lys	7.68	121.5	60.1	123	Tyr	8.58	123.0	57.1
59	Leu	7.92	121.1	58.2	124	Trp	8.18	127.6	55.3
60	Val	8.27	116.7	67.7	125	Leu	7.24	127.0	56.9

Residue	H	N	Ca	Residue	H	N	Ca
126 Val	6.96	112.9	61.6	178 Lys	7.33	118.5	60.2
127 Lys			59.4	179 Ser	8.74	119.2	60.6
128 Asn	5.86	116.3	56.3	180 Ala	9.54	123.6	55.2
129 Lys	7.72	115.6	57.1	181 Lys	8.33	122.3	60.4
130 Ile	8.50	116.8	62.2	182 Leu			
131 Glu	9.23	131.9	54.7	183 Leu	8.16	118.6	58.2
132 Val	9.17	126.9	61.2	184 Lys	7.95	117.5	59.2
133 Phe	8.73	127.0	55.4	185 Ser	7.79	113.3	61.1
134 Tyr	8.36	129.7	52.5	186 Lys	7.68	120.9	58.1
135 Pro	-			187 Tyr	7.62	114.3	56.9
136 Gly				188 Gly	7.08	106.1	47.2
137 Pro	-			189 Lys	7.49	115.4	55.1
138 Gly				190 Ala	7.69	122.3	54.0
139 His				191 Lys	9.24	123.0	58.2
140 Thr				192 Leu	7.22	114.4	53.1
141 Pro	-			193 Val	9.11	122.1	60.7
142 Asp				194 Val	9.03	126.1	59.3
143 Asn				195 Pro	-		
144 Val				196 Ser			
145 Val	8.98	111.8	58.7	197 His			
146 Val			60.7	198 Ser			
147 Trp	9.82	131.3	54.2	199 Glu	8.42	117.7	57.2
148 Leu	7.94	126.2	50.3	200 Val	7.99	118.4	64.3
149 Pro	-		64.4	201 Gly	8.07	114.7	45.1
150 Glu	8.62	114.4	59.3	202 Asp	8.01	120.6	52.3
151 Arg	6.52	111.4	52.9	203 Ala	8.23	116.3	55.3
152 Lys	7.57	114.1	57.2	204 Ser	9.18	119.7	62.6
153 Ile	6.32	116.2	60.2	205 Leu	8.11	119.7	58.3
154 Leu	8.82	127.5	52.3	206 Leu			
155 Phe	10.23	128.0	57.6	207 Lys			
156 Gly			57.9	208 Leu			
157 Gly	6.81	122.0	59.7	209 Thr	7.28	113.8	67.7
158 Cys				210 Leu	7.01	121.5	59.0
159 Phe				211 Glu	7.98	116.6	
160 Ile				212 Gln	8.16	118.0	
161 Lys				213 Ala	8.39	124.5	55.2
162 Pro	-			214 Val	8.32	119.6	67.2
163 Tyr				215 Lys	7.85	120.5	60.1
164 Gly				216 Gly	8.23	105.9	46.7
165 Leu				217 Leu	8.07	123.9	58.2
166 Gly				218 Asn	8.24	118.8	56.1
167 Asn				219 Glu	8.31	118.8	58.2
168 Leu				220 Ser	7.76	114.8	60.2
169 Gly				221 Lys	7.59	121.0	56.2
170 Asp				222 Lys	7.81	122.6	54.7
171 Ala				223 Pro	-		63.4
172 Asn	8.26	118.4		224 Ser	8.33	116.6	58.5
173 Ile	8.37	122.0		225 Lys	8.13	123.7	54.2
174 Glu	8.01	117.6	59.3	226 Pro	-		63.4
175 Ala	7.44	118.6	53.0	227 Ser	8.30	116.3	58.4
176 Trp	7.81	119.7		228 Asn	7.93	125.6	55.1
177 Pro	-		67.3				

ⁱ Chemical shifts reported in ppm. All measurements were made on non-deuterated protein using a conventional HNCA NMR experiment. The backbone amide resonance assignments were readily transferred to the [FeZn] form as the chemical shifts varied only subtly from those of the [ZnZn] form. This was possible in crowded spectral regions by using HNCA spectra. Blank fields indicate unassigned resonances. HNCACB and HNCO NMR spectra were not recorded for [FeZn]IMP-1, so C β and C' resonances were not assigned for the [FeZn] form. The six metal-coordinating residues are highlighted in bold type.

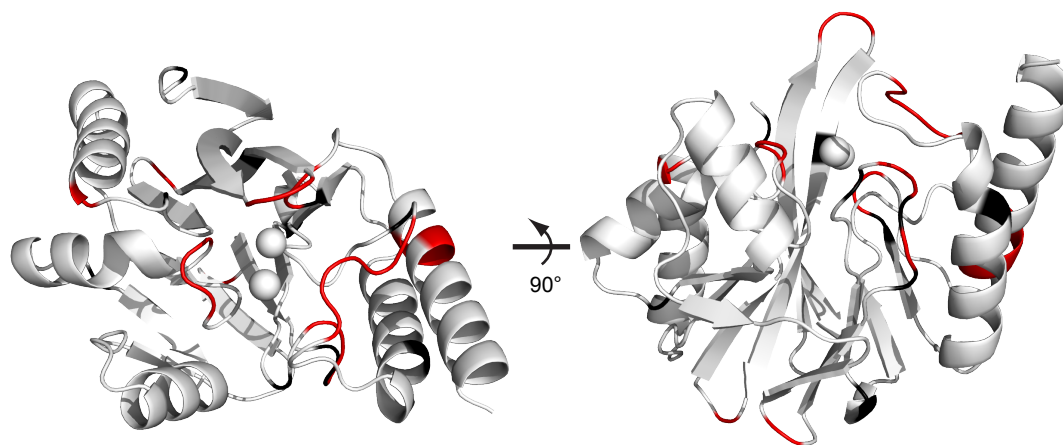


Figure 2-49 Cartoon representation of unassigned backbone amides (red) mapped onto the crystal structure of IMP-1. Practically all unassigned residues are in flexible turns, particularly in regions near the active site, which may be attributed to line broadening owing to conformational exchange. Segments with proline residues are coloured black, and the two zinc ions are depicted as spheres.

2.6.3 Missing Cross-Peaks

Notably, certain regions of the protein yielded very weak or unobservable cross-peaks in the TROSY-HNCA spectrum of the triple labelled cell-free protein sample, while they were observable in the HNCA spectrum of the $^{13}\text{C}/^{15}\text{N}$ -labelled sample expressed *in vivo*. The loss of the $\text{C}\alpha$ cross-peaks was attributed to the long constant time period (approximately 40 ms) used in the TROSY-HNCA experiment, leading to loss of magnetization for any signals broadened by conformational exchange. Mapping onto the protein structure shows that these resonances are mostly from the C-terminal region of the protein structure, specifically the final two helices and the loop linking these helices (Figure 2-50).

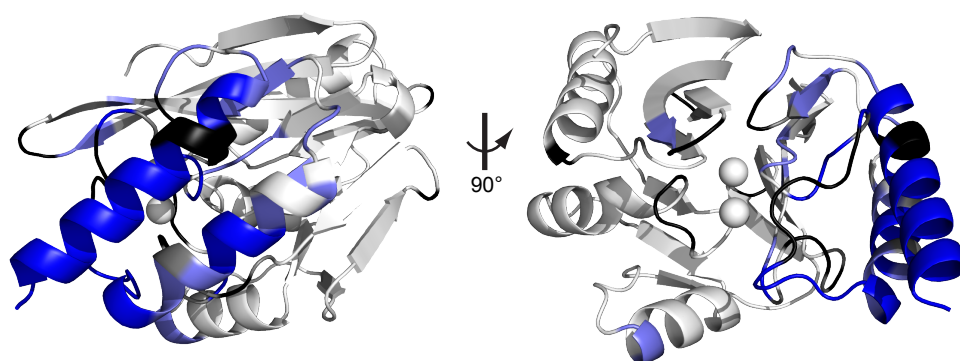


Figure 2-50 Cartoon representation highlighting regions for which $\text{C}\alpha$ cross-peaks were missing in the TROSY-HNCA spectrum of the triple-labelled protein prepared by cell-free synthesis. Signals from the dark blue regions were completely absent, and light blue colour identifies very weak peaks (with the *i*-1 $\text{C}\alpha$ cross-peak not observable). Proline and unassigned residues are coloured in black, and the two zinc ions are depicted as spheres.

2.6.4 Chemical Shift Changes After Ageing

As mentioned previously (section 2.5.1), significant changes in the NMR spectra were evident after incubation of the enzyme at 37 °C for 5 to 10 days. Mapping the chemical shift changes observed in ^{15}N -HSQC spectra of [ZnZn]IMP-1 before and after incubation onto the structure shows that the largest chemical shift changes were associated with the three N-terminal β -strands and an active-site loop near the N-terminus (Figure 2-51). A plausible explanation attributes these chemical shift changes to the cleavage of N-terminal residues as indicated by mass spectrometry results in section 2.5.1.

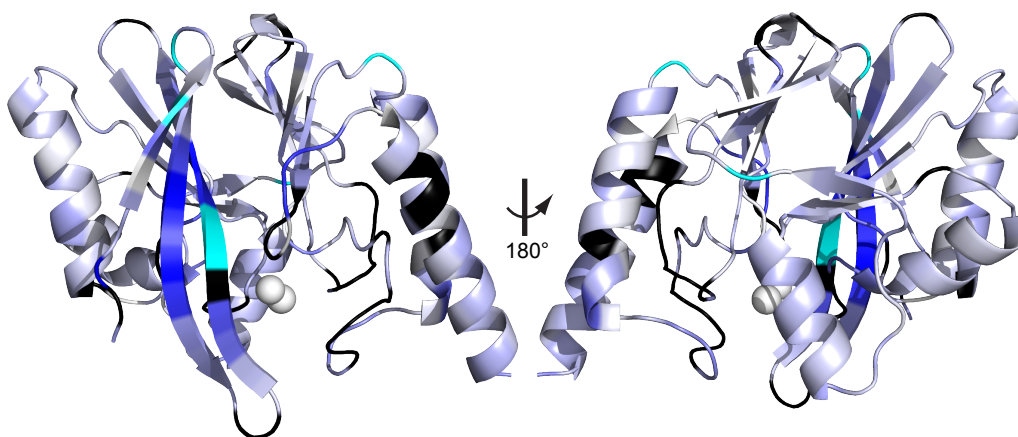


Figure 2-51 Cartoon highlighting the degree of chemical shift changes after ageing of the protein. Chemical shift perturbations are depicted on a colour scale ranging from 0.00 ppm (white) to ≥ 0.08 ppm (blue). The largest chemical shift change was 0.11 ppm. Residues that could not be found in the aged sample either due to peak broadening or chemical shift changes too large to identify are highlighted cyan. Unassigned and proline residues are coloured in black, and the two zinc ions are depicted as spheres.

2.6.5 Cross-Peak Characteristics

Peak doubling owing to sample heterogeneity was more pronounced for the [ZnZn] form while it was largely absent from the [FeZn] form. The effect was distinct from the small population of [FeZn]IMP-1 still present in the [ZnZn] sample (Figure 2-52). Mapping those residues that displayed peak doubling onto the structure shows them spread across the entire protein, although they can be grouped into three main clusters (Figure 2-53). Residues near the N-terminus have multiple peaks or appear heterogeneous. This could be attributed to the N-terminal expression tag having significant flexibility and multiple conformations. The effect was observed in both [FeZn] and [ZnZn] forms of the enzyme, although it was less obvious in the [FeZn] form, which may be explained by the generally broader line width in the paramagnetic sample. The second group includes residues on either side of an unassigned residue

located in a β -turn. This doubling can again be attributed to flexibility and occurs in both [FeZn] and [ZnZn] forms of the enzyme. The last group includes the majority of residues showing peak doubling. These are all concentrated near the active site. Unlike the apparent cross-peak heterogeneity of the residues near the N-terminus or β -turns, these residues typically displayed two clearly resolved peaks indicative of two distinct populations (Figure 2-52A). Most of these residues are not observable in the [FeZn] form as PREs broaden the signals below the level of the noise due to their proximity to the iron(III) ion. This also excludes the possibility of assigning one of the peaks to contamination of the sample with the [FeZn] form.

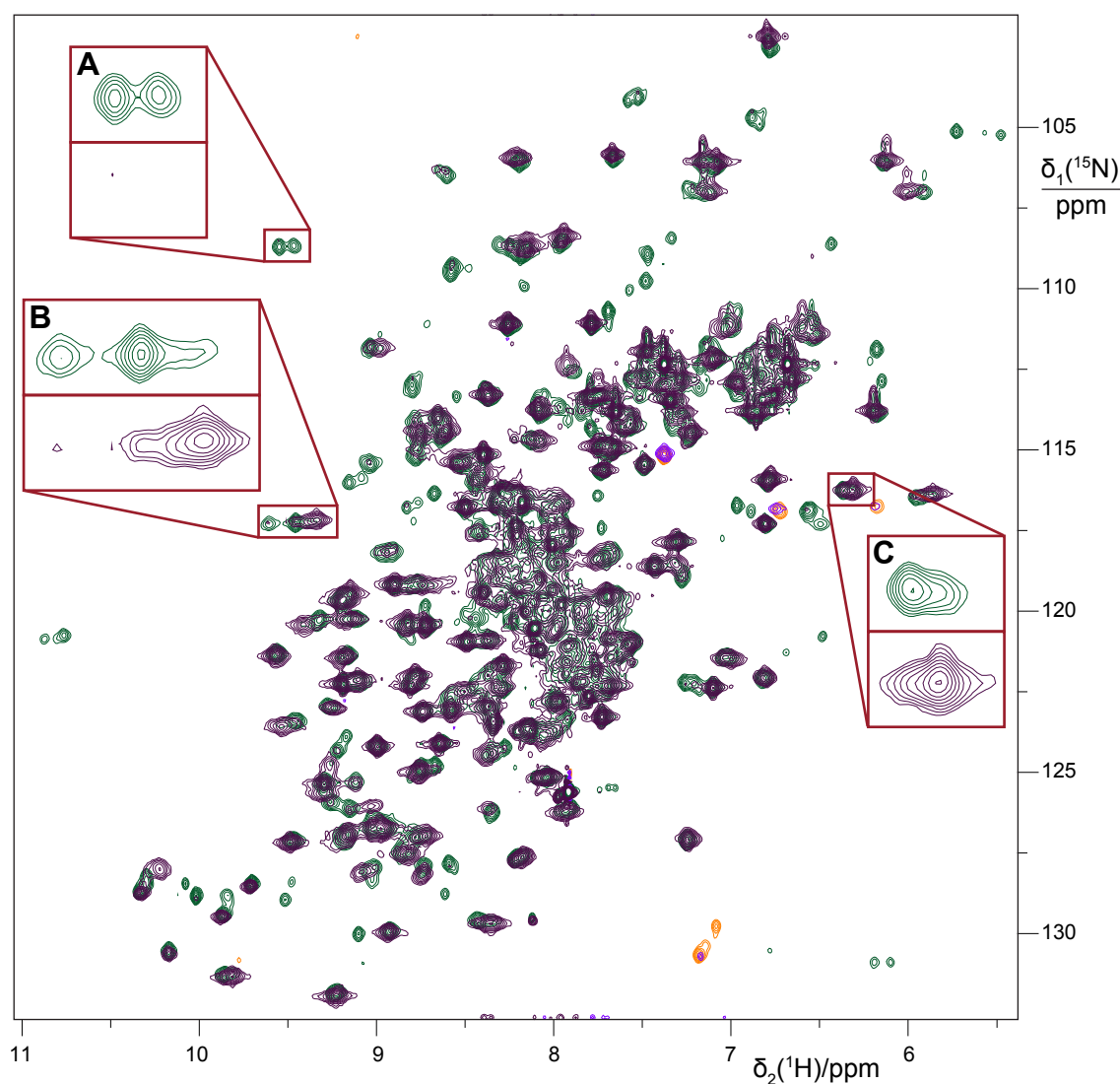


Figure 2-52 Cross-peak heterogeneity in the [ZnZn]IMP-1 sample (green) compared to the [FeZn]IMP-1 sample (purple). Three examples are highlighted in red boxes. In box A, two peaks assigned to Asp142 are clearly evident in the [ZnZn]IMP-1 spectrum. There is no corresponding [FeZn]IMP-1 peak due to significant peak broadening by PRE. In box B, three peaks assigned Ser99 are observed in the [ZnZn]IMP-1 spectrum, but the resonance most upfield in the proton dimension can be attributed to a minor population of the [FeZn]IMP-1 form. The other two resonances are assigned to the [ZnZn] form and reflect conformational or chemical heterogeneity of the corresponding region of the protein. In box C, the peak doubling observed for residue Ile153 in the [ZnZn] protein is due to a strong peak from the contaminating [FeZn]IMP-1 form.

If the [ZnZn]IMP-1 sample is incubated at 37 °C for two weeks, a large number of the peak doubling instances resolve to a single species (Figure 2-54). As expected, residues with peak doubling near the N-terminus are largely resolved into either fewer or single peaks as the N-terminal residues are cleaved over time. Conversely, those peaks that were doubled due to flexibility of β -turns remain doubled (Figure 2-54B). Interestingly, the residues with peak doubling near the active site consolidate into a single peak that overlaps with one of the two previous peaks (Figure 2-54A). This suggests that the active site of the fresh enzyme exists in two conformations, one of which is increasingly populated with time. Cross-peak heterogeneities observed for [FeZn]IMP-1 similarly decrease with time.

Ageing affects the NMR spectra of [FeZn]IMP-1 in a more subtle way, due in part to there being fewer residues with peak doubling in the fresh sample. Clear changes do occur for the residues near the N-terminal polypeptide segment. Most noticeably, ageing reduces the signals from the [ZnZn] form contaminating the sample. However, the signal-to-noise ratio was insufficient to determine whether the [ZnZn] form selectively dropped in concentration after incubation.

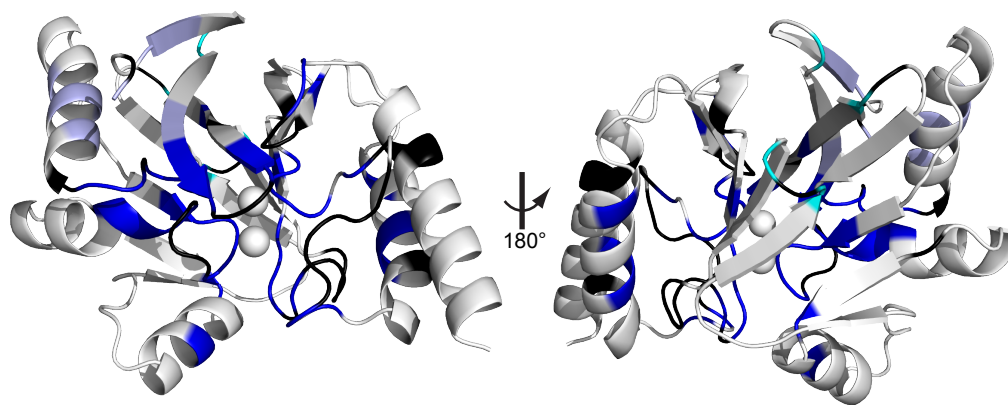


Figure 2-53 Cartoon highlighting residues for which peak doubling was observed in the ^{15}N -HSQC spectrum of [ZnZn]IMP-1. Residues for which peak doubling was assigned to flexibility in the N-terminal polypeptide segment are indicated in light blue. Residues with peak doubling attributed to conformational exchange at β -turns are highlighted in cyan. Solid blue highlights residues with significant peak doubling concentrated near the active site. Unassigned and proline residues are coloured in black, and the two zinc ions are depicted as spheres.

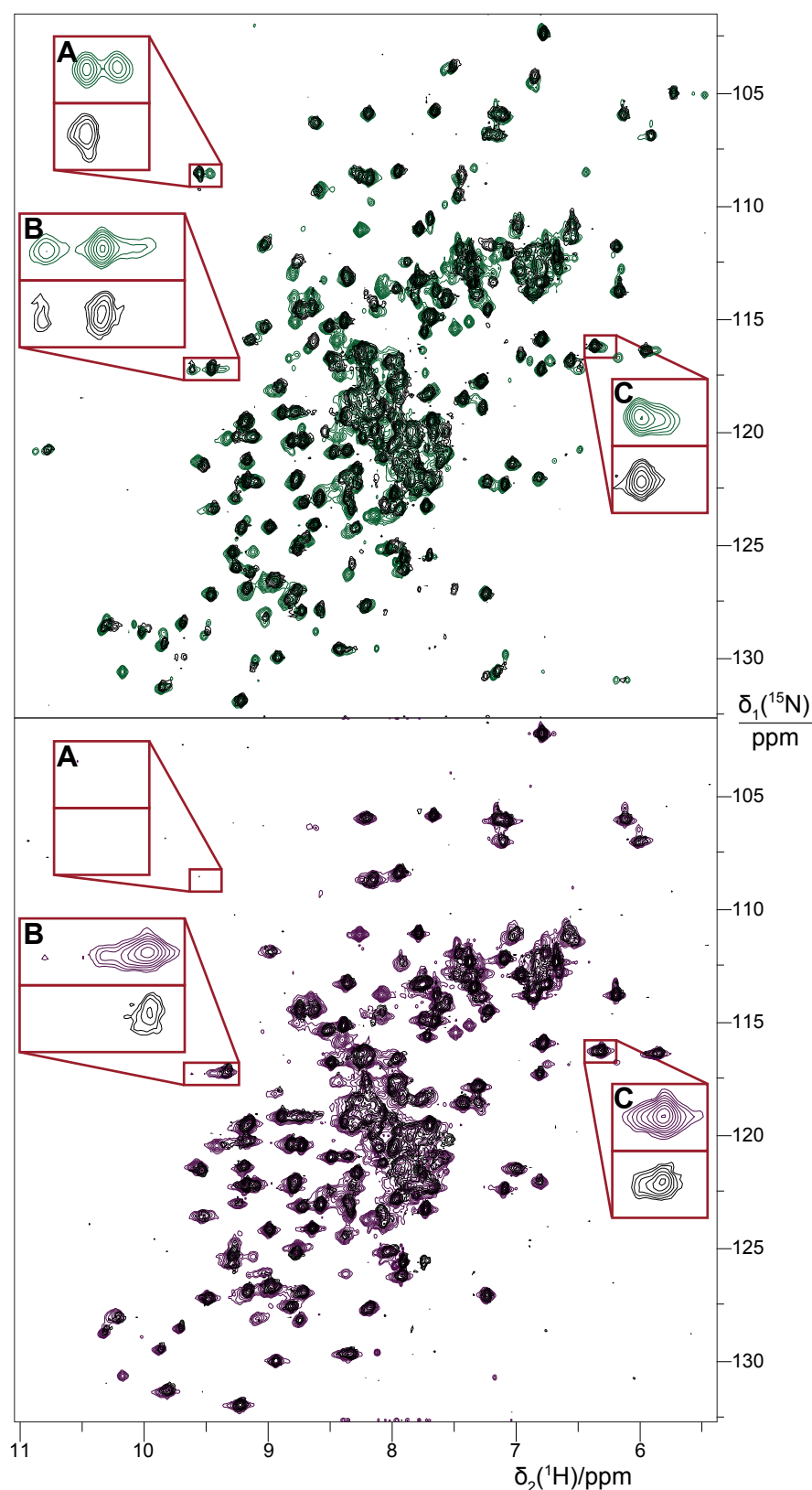


Figure 2-54 Peak doubling in fresh [ZnZn]IMP-1 (green, **top**) is largely resolved in the aged sample (black). The same residues are highlighted as in **Figure 2-52**. Peaks close to the active site (box **A**) resolve into a single species. Peaks near inherently flexible regions like β -turns (box **B**) remain doubled. Interestingly, the degree of [FeZn]IMP-1 contamination in the [ZnZn] sample also decreases (box **C**). Ageing also seems to simplify the spectrum of [FeZn]IMP-1 (purple, **bottom**), while the limited signal-to-noise ratio prohibits analysis of any minor [ZnZn] form present.

2.6.6 PRE Analysis of [FeZn]IMP-1

Fewer cross-peaks were observable for samples of [FeZn]IMP-1 than for [ZnZn]IMP-1. This is attributed to the PRE induced by the iron(III) paramagnetic centre. Figure 2-55 shows the ratio of peak-heights for each backbone amide signal between the [FeZn] and [ZnZn] forms. Mapping the intensity ratios onto the crystal structure of [FeZn]IMP-1 shows a clear distance dependence relative to the metals in the active site (Figure 2-56). While the paramagnetic centre is clearly in the active site, the resolution of the PRE experiment is insufficient to distinguish between the two metal ion sites identified by the anomalous X-ray scattering experiment.

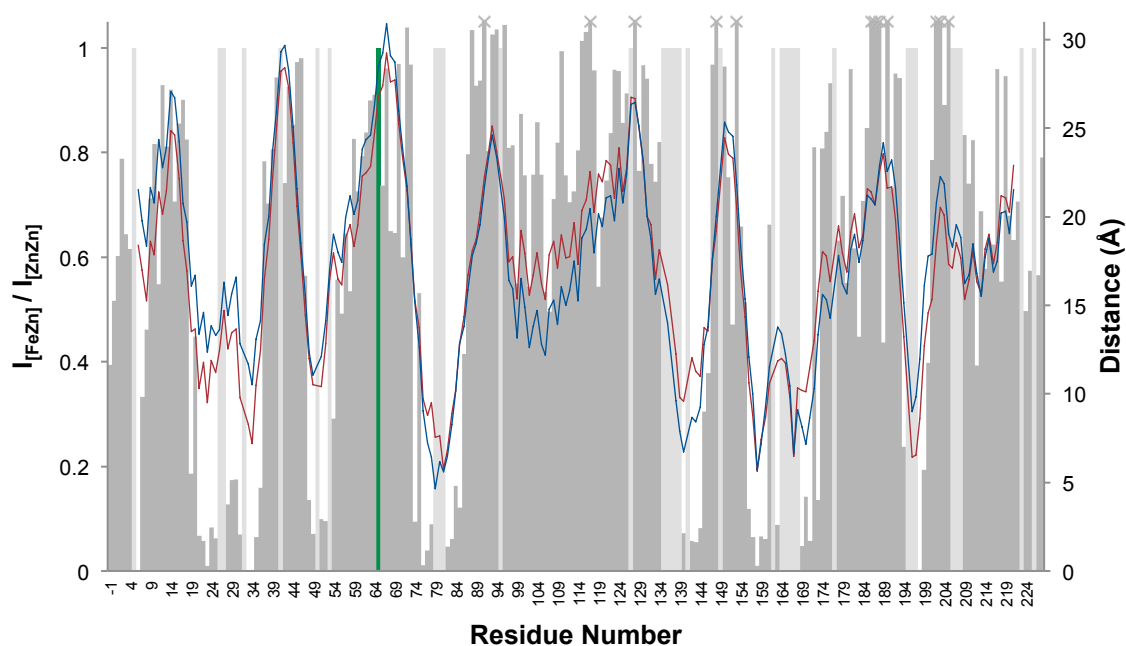


Figure 2-55 The ratio of amide ^{15}N -HSQC cross-peak intensities (grey bars) between [FeZn]IMP-1 and [ZnZn]IMP-1 correlates with the distance of the amide protons to the Zn_1 site (blue line) and Zn_2 site (red line). Peaks unaffected by PRE are expected to have an intensity ratio of 1 whereas the ratio is 0 for peaks broadened beyond detection. Proline and unassigned residues are identified by light grey bars plotted with a ratio value of 1. Any residues with a ratio greater than 1.05 (i.e. the peak was stronger in the [FeZn]IMP-1 sample) are marked with a cross. The cross-peaks of Glu65 (green bar) were used as a reference (ratio set to 1) to scale the two datasets, as its peaks were well resolved and the amide proton is more than 26.7 Å from either of the metal sites.

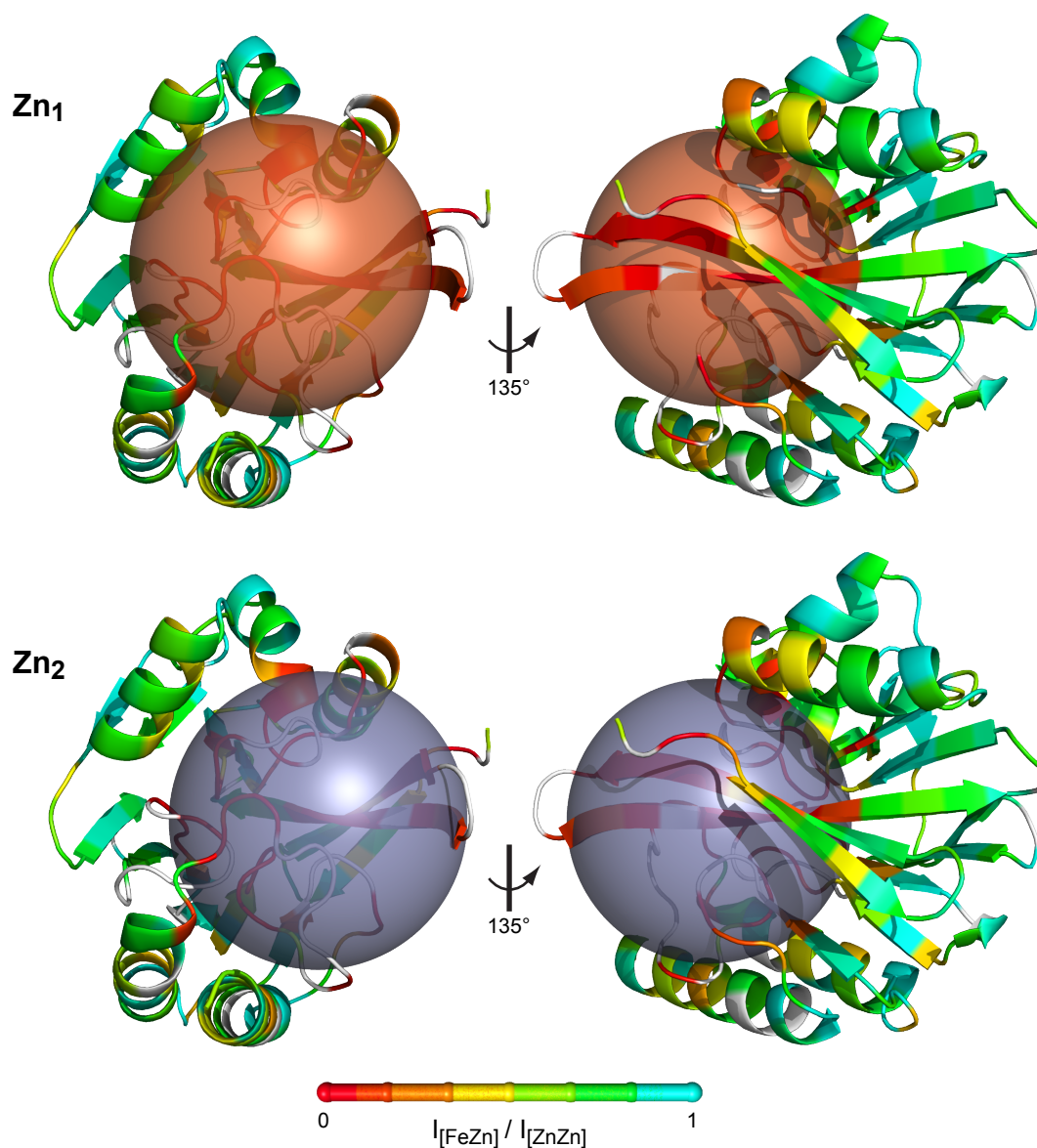


Figure 2-56 Cartoon representation of the intensity ratio $I_{[\text{FeZn}]} / I_{[\text{ZnZn}]}$ from **Figure 2-55** mapped onto the crystal structure of [FeZn]IMP-1 determined in this work. Residues with amide cross-peaks broadened by PREs beyond detection are indicated in red, while unaffected residues are indicated in light blue (as per the scale). A 12 Å sphere centred at either the Zn_1 or Zn_2 site is depicted in orange and grey, respectively.

2.6.7 Oxidation States of Iron

A series of samples was synthesised cell-free in the presence of iron.* It was noted that initial samples did not appear to be coloured purple as were samples expressed *in vivo* at similar concentrations, and that the NMR peaks from the [FeZn]IMP-1 samples did not always overlay with the [FeZn]IMP-1 samples expressed *in vivo*. It was discovered that, in the cell-free system, IMP-1 could incorporate either Fe(II) or Fe(III) into the active site depending on the oxidation state of iron added to the cell-free feed buffer (Figure 2-57). This was unexpected since the cell-free system has a reducing agent present and it was assumed that any iron introduced into the system would be iron(II). A set of [Fe(II)Zn]IMP-1 and [Fe(III)Zn]IMP-1 samples was then synthesised and analysed by NMR.

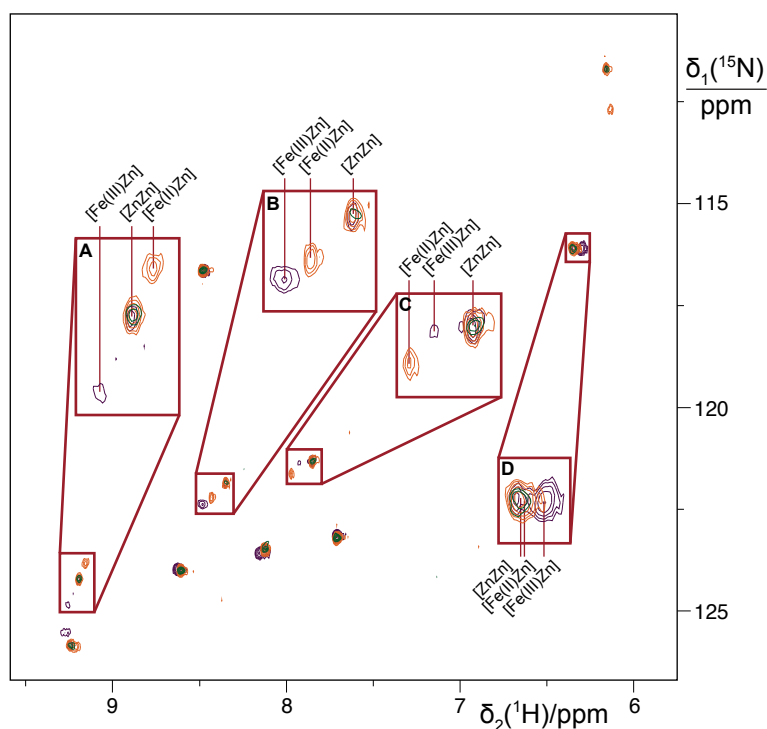


Figure 2-57 ^{15}N -HSQC spectrum of ^{15}N -Ile-labelled IMP-1 synthesised in the presence of zinc (green), iron(II) (orange) or iron(III) purple. Three species are evident and assigned as [ZnZn]IMP-1, [Fe(II)Zn]IMP-1 and [Fe(III)Zn]IMP-1 as marked. Different PCSs are evident for the Fe(II) and Fe(III) species, indicative of different $\Delta\chi$ tensors.

In agreement with the UV/Vis experiment in Figure 2-30, comparison between [Fe(II)Zn] and [Fe(III)Zn] forms synthesised cell-free to [FeZn]IMP-1 synthesised *in vivo* confirmed that the *in vivo* protein was [Fe(III)Zn]IMP-1 (Figure 2-58).

* Samples with iron(II) and iron(III) were synthesised by Ms E. Cliff under supervision of Dr C.T. Loh and the author.

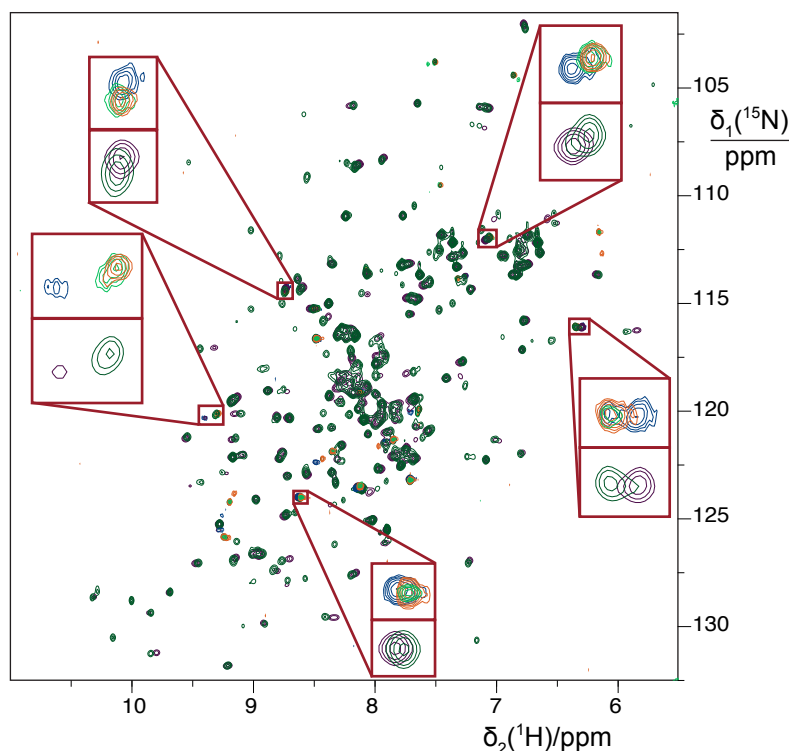


Figure 2-58 Comparison of the ^{15}N -HSQC spectra of [Fe(III)Zn]IMP-1 (dark blue), [Fe(II)Zn]IMP-1 (orange) and [ZnZn]IMP-1 (light green) from cell-free expression with ^{15}N -isoleucine and ^{15}N -threonine to [FeZn]IMP1 (purple) and [ZnZn]IMP1 (green) from *in vivo* expression with uniform ^{15}N -labelling. Red boxes highlight the comparison, showing the cell-free samples above the *in vivo* samples.

2.6.8 PCS Analysis

It was expected that the [FeZn]IMP-1 sample would induce PCSs in the NMR spectrum, explaining the variability in the chemical shifts measured in the assignment for the enzyme. Closer examination, however, identified a number of peaks that were shifted much further in the nitrogen dimension than in the proton dimension, which could not be explained by PCSs alone (for example see Figure 2-57A). As analysis of the crystal structures of [FeZn]IMP-1 and [ZnZn]IMP-1 suggested very little structural difference between the two forms, the differences in the NMR peaks could potentially arise either from mobility differences between the two structures or subtle structural differences not resolved by X-ray crystallography.

Gallium(III) had been used previously as a diamagnetic reference for iron(III) due to it having both the same charge and similar ionic radius.²¹⁶⁻²²³ Another series of samples* was made by cell-free synthesis in the presence of exogenous $\text{Ga}_2(\text{SO}_4)_3$, which indeed appeared to serve as a better diamagnetic reference, yielding more

* Samples with gallium(III) were synthesised by Ms K. Dugdale under supervision of Dr C.T. Loh and the author.

plausible PCSs (Figure 2-59). ICP-OES was performed for the Ga^{3+} sample and a gallium signal was detected, however, due to the poor sensitivity of the gallium ICP-OES signal, incomplete saturation of the enzyme and the small amount of cell-free sample available for analysis, quantitative data was not attainable.

It was noted that many residues in the gallium samples gave rise to multiple peaks. Some of these could be explained as coming from residual $[\text{ZnZn}]$ IMP-1 or $[\text{Fe(III)Zn}]$ IMP-1, but in many cases there were at least two unique resonances present. After closer examination, the $[\text{Fe(III)Zn}]$ IMP-1 sample expressed in the cell-free system also appeared to have multiple peaks that were not present in the *in vivo* samples. This made accurate measurement of PCSs more difficult. An example from Gly72, a residue close to the active site, is shown in Figure 2-60.

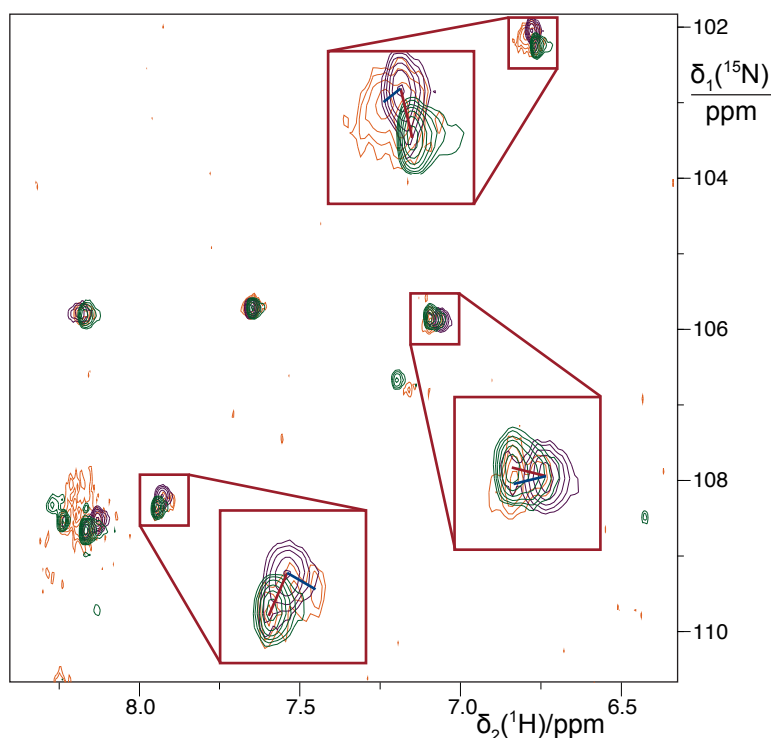


Figure 2-59 Comparison of the ^{15}N -HSQC spectra of ^{15}N -Gly-labelled $[\text{Fe(III)Zn}]$ IMP-1 (purple), $[\text{ZnZn}]$ IMP-1 (green) and $[\text{Ga(III)Zn}]$ IMP-1 (orange). Red bars indicate PCSs measured using the $[\text{ZnZn}]$ form as the diamagnetic reference, where blue bars indicate PCSs measured using the $[\text{GaZn}]$ form as the diamagnetic reference. While not perfect, the $[\text{GaZn}]$ form performs as a better diamagnetic reference for $[\text{FeZn}]$ IMP-1 than the $[\text{ZnZn}]$ form.

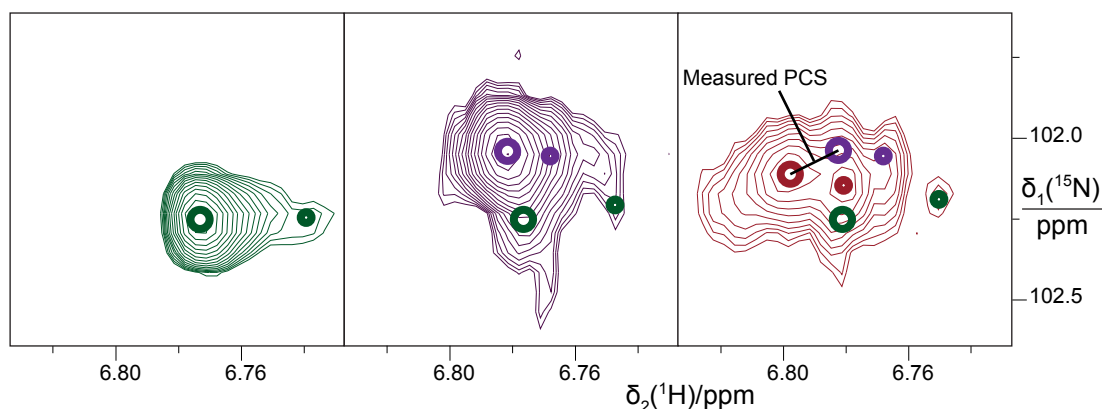


Figure 2-60 Example of multiple cross-peaks observed for Gly72 in the cell-free samples of [ZnZn]IMP-1 (green), [Fe(III)Zn]IMP-1 (purple) and [Ga(III)Zn]IMP-1 (red). A large circle highlights the major cross-peak for each species, while apparent minor cross-peaks are highlighted by a small circle. The measured PCS for this residue is also highlighted by a black bar on the [Ga(III)Zn]IMP-1 spectrum.

Analysis was carried out by selecting the most intense peak for each residue in the [Fe(III)Zn] and [Ga(III)Zn] samples that did not overlap with the [ZnZn] form.* Initially, 39 resolved PCSs were identified, measured and used for fitting of a $\Delta\chi$ tensor to the crystal structure of [FeZn]IMP-1 (Table 2-17). Using the tensor to back-calculate the PCSs produced large deviations from the experimental PCSs for a few residues, regardless of whether the tensor was centred on the Zn₁ or Zn₂ metal site. Closer inspection of the NMR data for these residues revealed problems that had been overlooked in the initial PCS measurements. The cross-peaks of Thr56, which showed the largest deviation between experimental and back-calculated PCSs, appeared heterogeneous in both [FeZn] and [GaZn] samples. The PCS of Lys178 also fitted poorly, especially for the fit to the Zn₁ site, and its cross-peaks also displayed heterogeneous line shapes. The PCS of Thr102 showed a large deviation in the Zn₂ fit and proved uncertain due to a very weak cross-peak in the spectrum of [GaZn]IMP-1. Thr115 and Phe118 deviated significantly in the Zn₂ site fit, but the cross-peaks were strong in both the diamagnetic and paramagnetic samples, and were hence retained in the fits. Irrespective of whether any of the PCSs discussed above were removed from the fits or not, the best $\Delta\chi$ -tensor fits with the smallest root-mean-square deviation between experimental and back-calculated PCSs were obtained for tensors centred on the Zn₁ site (Table 2-18).

* In cases where a ‘major’ peak was difficult to identify, assignments of the *in vitro* [FeZn] form were chosen by reference to the *in vivo* [FeZn] form, and assignments of the [GaZn] form were chosen to be the peak where the change in proton chemical shift ($\Delta\delta$) was most similar to the $\Delta\delta$ of ¹⁵N with respect to the *in vivo* [FeZn] form.¹⁵

Using the $\Delta\chi$ tensor solved for run 3 in Table 2-18 (omitting the PCSs of Thr56 and Lys178), it was possible to assign a further 11 PCSs by looking for previously ignored peaks matching the back-calculated shifts. Those within 0.05 ppm from the prediction for the Zn₁ metal site were added to the PCS data set. The 48 PCSs used in the final fitting protocol are listed in Table 2-19. These PCSs came from residues dispersed over the entire protein, as shown in Figure 2-61.

Table 2-17 PCS data used for the initial fixed-metal-position fitting of a $\Delta\chi$ tensor to [Fe(III)Zn]IMP-1ⁱ

Residue	PCS (ppm)	Residue	PCS (ppm)
I9	+0.040	K108	±0.000
K11	+0.058	G110	+0.030
Y17	-0.028	K111	+0.036
T20	+0.098	T115	-0.069
Y45	-0.051	F118	-0.071
I47	-0.056	Y123	-0.072
K54	+0.040	K129	-0.045
T56	-0.021	I130	-0.041
T61	-0.020	F133	-0.135
F63	-0.040	K152	-0.010
G67	±0.000	I153	-0.089
Y68	-0.047	K161	-0.029
K69	+0.002	K178	-0.027
I70	-0.032	K181	+0.047
G72	-0.021	G188	-0.035
I86	+0.069	K189	-0.017
I94	-0.053	K191	-0.066
T96	-0.010	G201	-0.047
Y97	-0.024	K215	+0.040
T102	-0.082		

ⁱ Data measured using [GaZn]IMP-1 as the diamagnetic reference. Only PCSs identified with high confidence were included in the fit. PCS values were measured using ¹H chemical shifts.

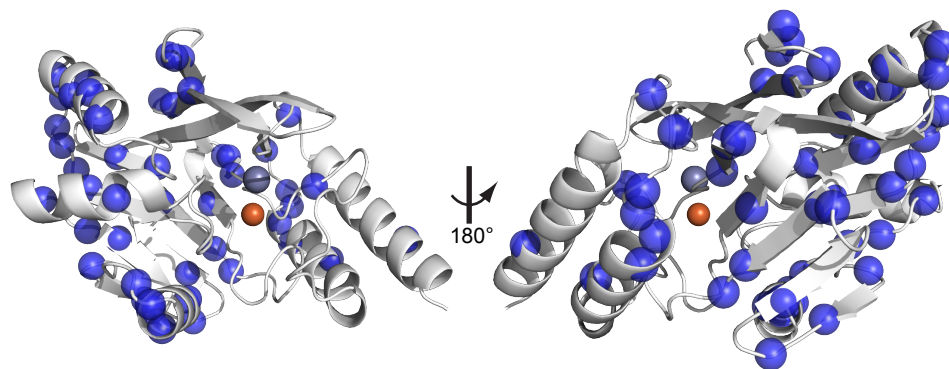
Table 2-18 RMSD scores of the iterative $\Delta\chi$ -tensor fitting protocol for the Zn₁ and Zn₂ metal sites.

Run	Subset of PCSs	RMSD (ppm)	
		Zn ₁	Zn ₂
1	39 PCSs	0.03308	0.03454
2	38 PCSs (without 56)	0.03009	0.03270
3	37 PCSs (without 56, 178)	0.02682	0.03211
4	37 PCSs (without 56, 102)	0.02986	0.03015
5	36 PCSs (without 56, 178, 102)	0.02670	0.02930
6	34 PCSs (without 56, 178, 102, 115, 118)	0.02556	0.02609
7	32 PCSs (without 56, 178, 102, 94, 63)	0.02514	0.02801

Table 2-19 PCS data used for the final fixed-metal-position fitting the $\Delta\chi$ tensor to [FeZn]IMP-1ⁱ

Residue	PCS (ppm)	Residue	PCS (ppm)
K8	+0.081	K108	± 0.000
I9	+0.040	G110	+0.030
K11	+0.058	K111	+0.036
G15	-0.008	T115	-0.069
Y17	-0.028	F118	-0.071
T20	+0.098	G120	-0.034
Y45	-0.051	Y123	-0.072
I47	-0.056	K129	-0.045
K54	+0.040	I130	-0.041
K58	+0.042	F133	-0.135
T61	-0.020	Y134	-0.077
F63	-0.040	W147	-0.081
G67	± 0.000	K152	-0.022
Y68	-0.047	I153	-0.089
K69	+0.002	F155	-0.119
I70	-0.032	K161	-0.029
K71	-0.007	K181	+0.047
G72	-0.021	K186	-0.007
I86	+0.069	Y187	-0.038
I94	-0.053	G188	-0.035
T96	-0.010	K189	-0.017
Y97	-0.024	K191	-0.066
T102	-0.082	G201	-0.047
K107	+0.015	K215	+0.040

ⁱ Data measured using [GaZn]IMP-1 as the diamagnetic reference. 11 shift assignments were aided by back prediction from the $\Delta\chi$ -tensor determined from run 3 in Table 2-18. PCS values were measured using ¹H chemical shifts.

**Figure 2-61** PCS measurements were made for residues dispersed all over the protein. The backbone N-atom of each amide for which a PCS could be measured is depicted as a blue semi-transparent sphere. The Zn₁ and Zn₂ sites are depicted as orange and grey spheres, respectively.

A pyParaTools³⁴ fit to the data fixing the metal position at either the Zn₁ or the Zn₂ site yielded $\Delta\chi$ tensors with parameters shown in Table 2-20. The RMSD value for the Zn₁ site was 1.2 times smaller than for the Zn₂ site. The quality of each fit is shown graphically in Figure 2-62 by correlations between experimental and back-calculated PCSs.

Table 2-20 Final $\Delta\chi$ tensor parameters after fitting to either the Zn₁ or Zn₂ metal site

	Zn ₁	Zn ₂
x^i	33.087	33.940
y^i	13.399	16.627
z^i	59.360	58.603
$\Delta\chi_{ax}^{ii}$	-1.106	-0.935
$\Delta\chi_{rh}^{ii}$	-0.680	-0.327
α^{iii}	132.20	151.78
β^{iii}	37.44	41.46
γ^{iii}	158.72	153.64
RMSD ^{iv}	0.02412	0.02932
degrees of freedom	43	43

ⁱ metal ion coordinate (Å) in the protein frame set to either the Zn₁ or Zn₂ site (not fitted)

ⁱⁱ in units of 10⁻³² m³

ⁱⁱⁱ Euler rotations in ZYZ convention (degrees)

^{iv} in units of ppm

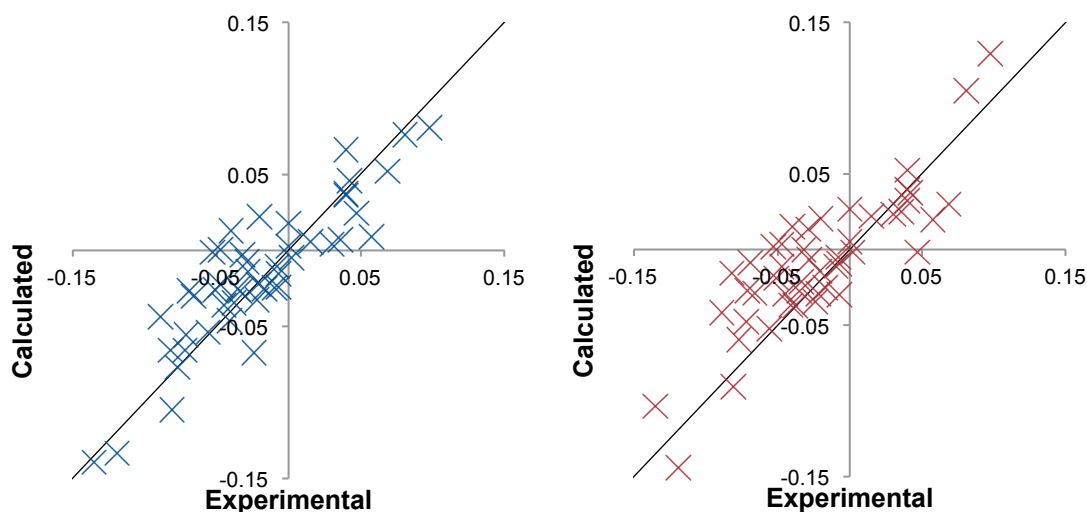


Figure 2-62 Experimental versus back-calculated PCS values (in ppm) for the Zn₁ (blue) and Zn₂ (red) metal site. A perfect fit would have data points lying along the black line (slope = 1). The points align more closely with the diagonal for the Zn₁-site fit.

Finally, a grid search of different metal positions was performed to find any local minima for the metal site that could indicate a different binding site. The RMSD values, when plotted against distance to either the Zn₁ or Zn₂ positions, converged to a minimum close to the active-site metals (Figure 2-63A/B). A second grid was calculated at a higher resolution around the active-site metals. This fit more clearly depicted the better fit for the Zn₁ site (Figure 2-63C/D).^{*} The results from the whole grid and the

^{*} It is worth noting that the same trend of convergence at the active site and closer to the Zn₁ metal position was evident for the same grid search using the initial set of PCSs listed in Table 2-17, however, the average RMSD value was higher.

active-site grid were also plotted onto a cartoon of the IMP-1 structure with the RMSD values indicated by a colour gradient (Figure 2-64 and Figure 2-65).

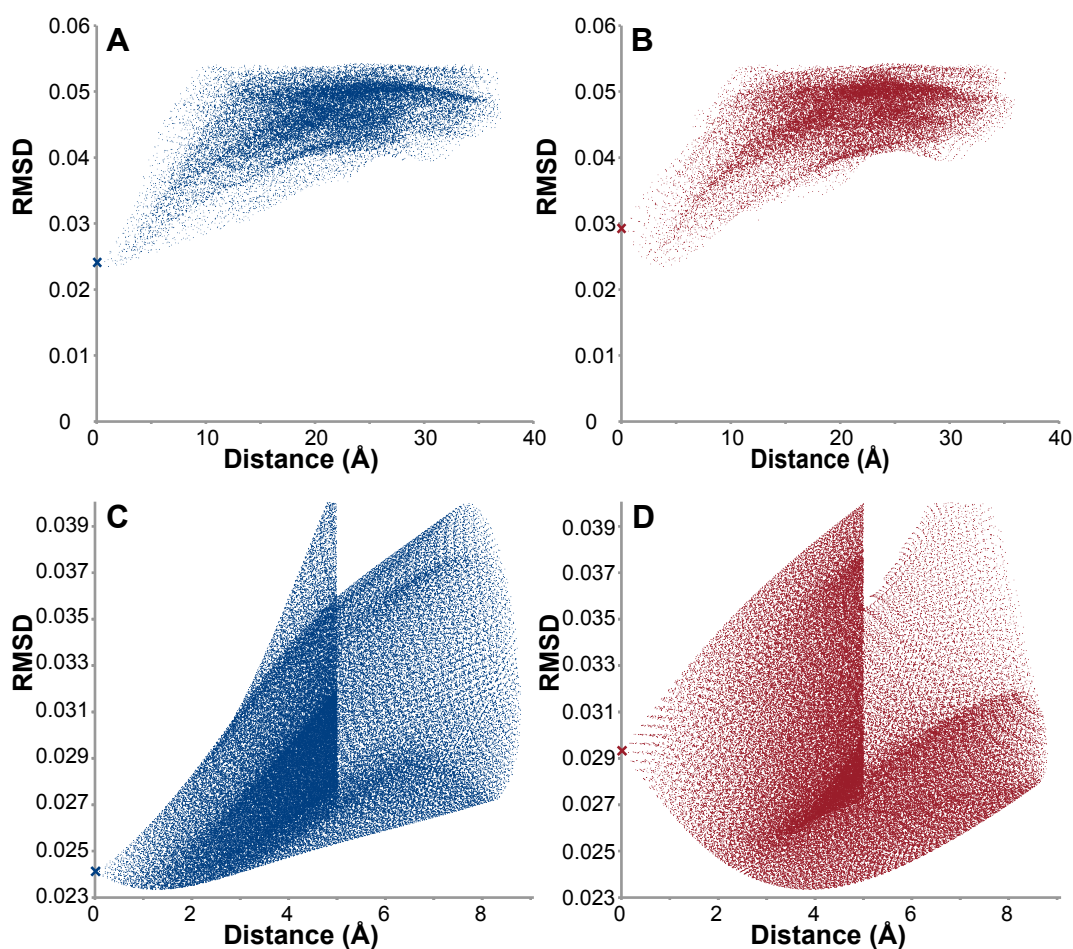


Figure 2-63 Quality of PCS fit plotted versus distance from the Zn_1 (A, C) and the Zn_2 (B, D) site. A cross on the y-axis depicts the RMSD value for the Zn_1 or Zn_2 site fits, respectively. A and B: plots of the coarse grid over the whole protein show convergence of the RMSD value near the active site. C and D: the fine grid near the metal ions produces the smallest RMSD value (0.0234) at a distance of about 1.30 Å from the Zn_1 site, and 3.90 Å from the Zn_2 site.

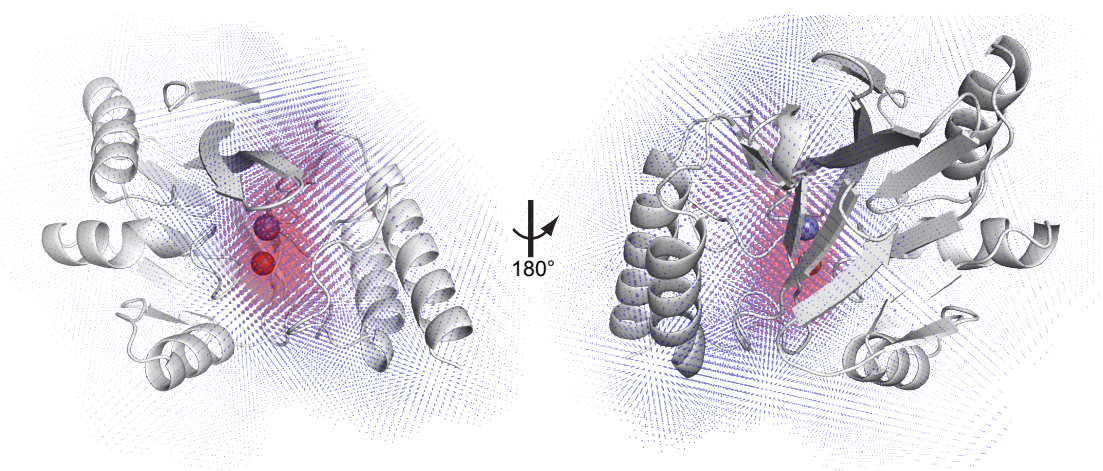


Figure 2-64 Graphical representation of the grid search for metal positions with minimal RMSD in the $\Delta\chi$ -tensor fits. The grid points are depicted as transparent spheres that are coloured by RMSD value from red (0.023 ppm) to blue (0.038 ppm or greater). A cluster of red points comprising the active-site metals (shown as full spheres) locates the paramagnetic centre to those metal sites. The sphere radii were scaled with the RMSD value for improved visualisation in a 2D display.

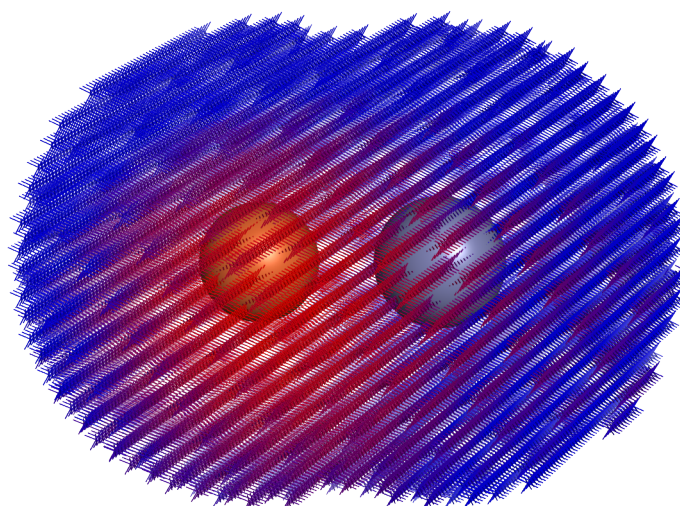


Figure 2-65 Graphical representation of the active-site grid search for metal positions with minimal RMSD value. The grid points are depicted as crosses that are coloured by RMSD values from red (0.023 ppm) to blue (0.029 ppm or greater). The best results cluster around the Zn_1 metal site identified by an orange sphere on the left. A grey sphere indicates the Zn_2 site.

Figure 2-66 shows PCS isosurfaces plotted onto the protein structure, indicating the magnitude of PCSs induced at different sites across the protein. Three levels are plotted – 0.02, 0.04 and 0.16 ppm. It can be seen from Table 2-19 that the magnitude of PCSs were in this range for the majority of resonances.

Finally, the orientation of the principal axes of the $\Delta\chi$ tensor in its coordination environment is shown in Figure 2-67. Interestingly, the principal axes are oriented so as to minimise overlap of any one axis with the coordinating ligands. The oxygen ligand, being the most electronegative ligand, is positioned almost perfectly between the three

axes. The three nitrogen ligands are then placed to minimise overlap with a priority order of His79-N^{δ1}, His139-N^{ε2} and finally His77-N^{ε2}.

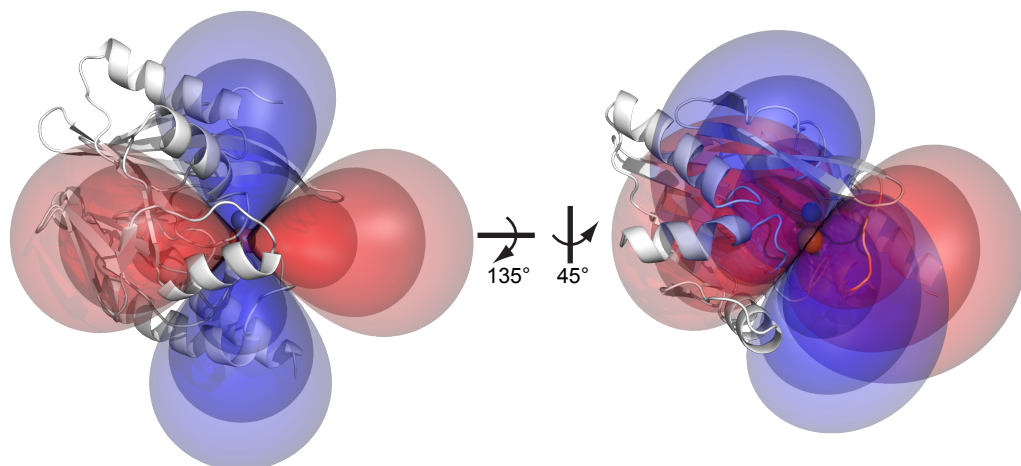


Figure 2-66 Depiction of PCS isosurfaces. Nuclear spins positioned on the same isosurface experience the same PCS. Positive and negative PCS values are plotted as blue and red isosurfaces, respectively. Three levels are shown – the largest lobes indicate a 0.02 ppm shift, the medium lobes indicate a 0.04 ppm shift and the smallest lobes indicate 0.16 ppm shift. The two active-site metals are shown as spheres, Zn₁ in orange and Zn₂ in grey.

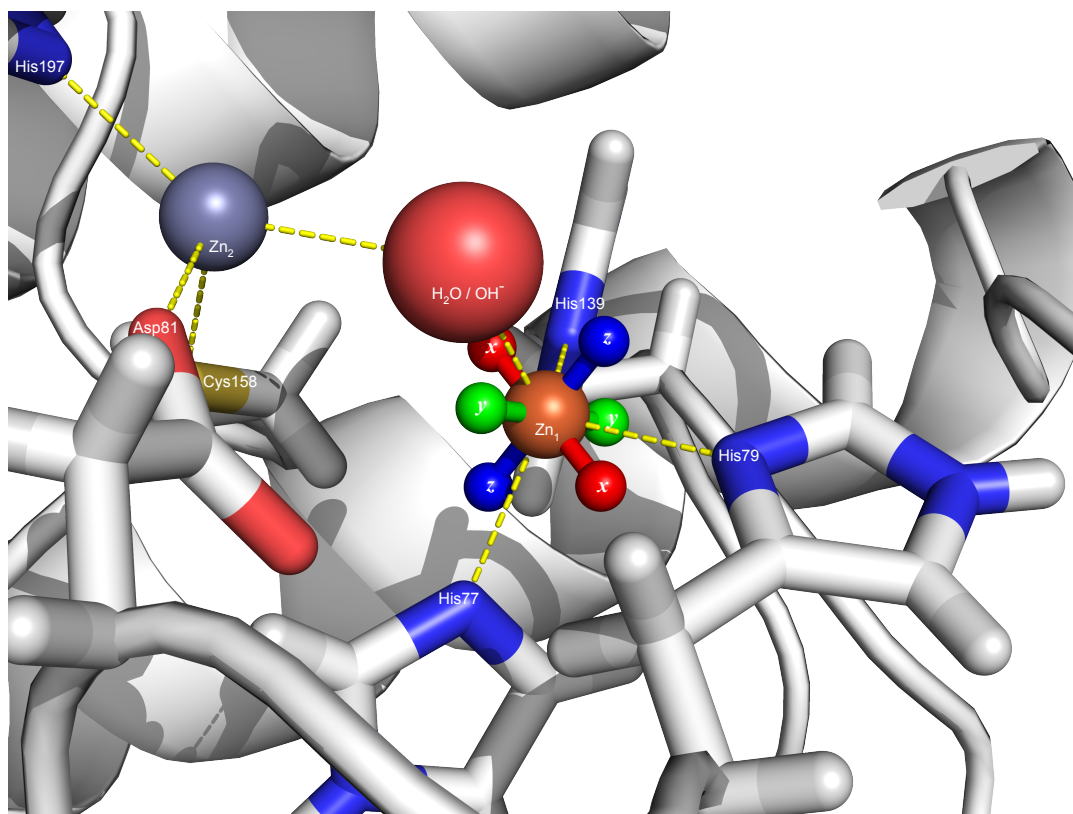


Figure 2-67 Orientation of the principal axes of the fitted $\Delta\chi$ -tensor, highlighting the different axes as red (x), green (y) and blue (z) ball-and-sticks attached to the Zn₁ site. The principal axes are oriented to place the oxygen (the most electronegative ligand) so as to avoid lining up with any of the axes. The three nitrogen ligands (less electronegative than the oxygen) are then placed to minimise lining up with any other axis. The Zn₁ and Zn₂ sites are depicted as orange and grey spheres, respectively. The bridging water/hydroxide ion (taken as the coordinating oxygen atom from the citrate ligand in the [FeZn]IMP-1 structure) is depicted as a red sphere.

2.7 Discussion

2.7.1 General Observations and Comments on Methodology

DNA – a Potential Binding Partner for IMP-1

Desalting or dialysis with buffer is typically all that is required prior to NMR measurement after cell-free protein synthesis of isotopically labelled proteins.²²⁴ It was therefore surprising to find it necessary to purify labelled cell-free protein synthesis samples of IMP-1 for observation by NMR. Washing the sample with 20 mM buffer via ultrafiltration alone failed to produce NMR cross-peaks. This observation suggests that IMP-1 interacts with very large molecules present in the cell-free reaction mixture, such as plasmid DNA.

The hypothesis that IMP-1 binds to DNA is supported by two factors. First, IMP-1 has a pI value greater than 8, so is positively charged at the pH chosen for NMR (6.5). Second, treating *in vivo* preparations with DNase I was found to reduce the viscosity of the cell-lysate as well as increase the protein yield obtained after filtration. Weak binding to negatively charged plasmid DNA in the cell-free reaction mixture thus presents a plausible explanation for why only the most flexible residues proved to be observable in the NMR spectrum unless the protein was purified further, for example by using a cation-exchange column with relatively high concentrations of salt to dissociate any bound plasmid DNA.

In principle, interaction with DNA would be straightforward to assay by adding an aliquot of DNA to a purified protein sample to observe the loss of NMR cross-peaks, however, as IMP-1 is excreted to the periplasm in the native system, this interaction probably has little biological relevance. Considering that the majority of β -lactam antibiotics are either zwitterionic or negatively charged at biological pH, the positive pI value of IMP-1 may be beneficial for attracting the substrate and improving its activity.

Protein Crystallisation Conditions Screening of [FeZn]IMP-1

Previous reports indicated that crystallisation of IMP-1 is difficult to reproduce¹²⁰ and, specifically, that IMP-1 crystals are unstable if they are not incubated at 37 °C until crystal growth is complete. In the present work, successful crystallisation conditions required ageing of the protein by incubation at 37 °C for approximately a

week as a pre-treatment prior to crystallisation at 24 °C. All previously published crystallisation conditions* were performed at temperatures of 20 to 37 °C†.

The ageing process was not entirely benign. Mass spectrometry indicated that the N-terminal residues are sensitive to proteolysis over time at room temperature. Electron density was missing for the first 3 residues in the crystal structure obtained in this work, suggesting that cleavage of these residues may be essential for crystal formation. Previous investigators also reported that removing the six most C-terminal residues improved crystallisation reliability.¹²⁰ These six residues were not resolved in the current work, nor in most other IMP-1 structures.^{118,120,182-184} Future crystallisation attempts may be more successful with a Δ 4-222 construct of IMP-1, or by attaching a C-terminal StrepII tag as in the PDB structures 4G6H and 4F6Z¹⁰⁹ where the C-terminus is resolved.

X-Ray Diffraction Structure

In the present work, citrate was observed in the active site of each of the monomers of the solved X-ray crystal structure. Citrate is observed in the active site of at least one member of each class of metallo- β -lactamase (in each case, citrate has been a component of the crystallisation buffer).²²⁵ The crystal diffracted to 1.8 Å resolution, which is on par with the highest resolution¹²⁰ structure of the native enzyme to date.

Citrate has earlier been established as an inhibitor of IMP-1 and is known to cause the loss of up to 1.7 equivalents of zinc from a [ZnZn] enzyme at pH 5.⁷⁹ Loss of metal from the enzyme is consistent with the reduced occupancy of the Zn₂ metal site observed in the crystal structure.

Treatment of IMP-1 with FeCl₃

The metal exchange experiment with FeCl₃ reported close to 20 equivalents of iron by ICP-OES. Considering it is unlikely that there are 20 high-affinity iron-binding sites on the surface of the native protein (especially as the enzyme has a pI value greater

* Crystals of IMP-1 in the presence of a mercaptocarboxylate inhibitor (1DD6) can reportedly be grown at 4 °C,¹⁸² but the coordinate file in the PDB indicates a crystallization temperature of 293 K.

† The PDB database reports a crystallisation temperature of 334 K for the structure 1JJE.¹²⁰ This is inconsistent with the original paper (37 °C) and with the conditions listed for another crystal structure from the same article (1JJT¹²⁰ – also 37 °C). In the ‘crystal growth procedure’ field for 1JJE both “310 K” and “temperature 334K” are present. It was assumed that this is an error in the database.

than 8.0) and that the amount of iron found was stoichiometrically similar to the amount used for treatment, the desalting columns appeared to have been inefficient at removing non-bound metals ions. Unexpectedly, however, the iron content remained unchanged even after two steps of desalting purification with fresh NAP-5 and PD-10 columns. This result is not yet understood but may be due in part to pH instability, as the stock solution of FeCl_3 was solubilised in about 5 to 8 mM HCl. Combined with the 20 mM MES buffer (pK_a 6.15, actual pH 6.5) in the protein sample prior to treatment, the addition of the FeCl_3 stock required to achieve 20-fold molar excess of iron would have come close to overwhelming the buffering capacity. Normally denaturation of IMP-1 is accompanied by precipitation (as evidenced by all de-metallation attempts). The absence of precipitation despite a very likely sudden drop in pH¹⁹³ in the metal exchange experiment is interesting. The presence of FeCl_3 (stock solution in 0.1 M HCl) also noticeably reduced precipitation in the high-throughput crystal screens. Further experiments would be needed to investigate this phenomenon. Initially, treating the protein with iron in the presence of a higher concentration of buffer to maintain the pH could shed more light on these observations.

Cell-Free Protein Synthesis

Cell-free protein synthesis proved to be a powerful tool in the analysis of [FeZn]IMP-1. The ability to generate protein in which single amino-acid types were individually ^{15}N -labelled significantly simplified the backbone assignment and enabled the measurement of PCSs in crowded regions of the ^{15}N -HSQC spectrum. As sample heterogeneities caused significant peak overlap in conventionally prepared samples, the samples prepared by cell-free synthesis proved invaluable and enabled the reliable fitting of a $\Delta\chi$ -tensor. The cell-free protein synthesis method also enabled the generation of a perdeuterated IMP-1 sample, as described in chapter 3 of this work. This sample, along with the single amino-acid labelled samples, was instrumental in obtaining the backbone assignments that proved much more difficult than for a conventional protein of this size.

Finally, the cell-free method enabled the generation of metal-substituted species that were not easily made *in vivo*. The ability to overwhelm the system with a large excess of metal ions, not possible *in vivo*, enabled the substitution of IMP-1 with non-biological metals such as gallium. In fact, gallium is toxic to bacteria and is a potentially useful antimicrobial,²²⁶⁻²³⁰ impeding any *in vivo* preparation of [GaZn]IMP-1.

NMR Cross-Peak Characteristics

The NMR spectra of [ZnZn]IMP-1 displayed three types of peak heterogeneity that were attributed to the flexible N-terminal expression tag, mobile loops and multiple distinct active site environments. Resonances for residues in the C-terminal helices were also missing in experiments with longer evolution times. Possible reasons are discussed below.

The N-Terminal MASMTG Tag

Several resonances assigned to residues in close proximity to the N-terminus displayed significant cross-peak heterogeneity. This was attributed to conformational or chemical heterogeneity of the MASMTG T7 gene 5 expression tag appended to the N-terminus of the enzyme concurrently with the transfer of *bla*_{IMP-1} into pETMCSI.* Ageing of the sample resulted in the loss of cross-peaks from the N-terminal tag, consistent with the mass spectral analysis that identified N-terminal degradation over time.

The expression tag is not required for *in vivo* expressions and may not be needed for cell-free expressions either.† It is the author's recommendation that future NMR experiments should be performed on IMP-1 protein lacking the N-terminal expression tag if possible.

Flexible Loops

Due to inherent mobility of the β -turns and flexible loops of IMP-1, little can be done to reduce the peak heterogeneity for these residues. Measurements at a different temperature or in the presence of an inhibitor may alter the degree of mobility in the enzyme and simplify the NMR spectrum.

* The pET47b(+) plasmid in which the gene was originally supplied was not suitable for cell-free protein expression, due to the presence of the *lacO* and *lacI* genes.

† The effect of the MASMTG tag on expression yields independent of the expression plasmid has yet to be analysed for IMP-1.

The Active Site

In general, each resonance of the active site displayed two distinct peaks that simplified to a single resonance after incubation at 37 °C for a few weeks. One explanation for the peak multiplicity could be that the enzyme was measured in metal-limiting conditions with no exogenous zinc present. This raises the possibility of there being a slow equilibrium between a mono- and di-zinc form of IMP-1 under NMR conditions. It is consistent with observations that after ageing some enzyme may denature and precipitate, releasing zinc ions into the solution. A small increase in exogenous zinc concentration may shift the equilibrium to the purely di-zinc form, leading to the loss of cross-peaks of the mono-zinc form. This explanation of peak heterogeneity is contradicted by the observation that enzyme purified under metal-limiting conditions still maintained ICP-OES metal analysis results of approximately 2 metal ions per protein molecule.*

A more plausible explanation for the peak doubling attributes the effect to multiple active-site conformations. Flexibility of the active site of MβLs is well-documented and presumed to assist in substrate promiscuity.^{109,110} A genuine possibility is the existence of two distinct active-site conformations in solution without inhibitor, and exchange between these two states that is slow with respect to the ms – μs timescale could explain the peak doubling observed for these residues. In this case, the loss of one conformation by ageing has interesting implications for the biological activity of the enzyme.

If the peak doubling arises from alternative conformations of the active site, it would be interesting to assess the peak doubling in the presence of an inhibitor or substrate. It would also be interesting to monitor these resonances in the presence of excess zinc, as the exchange of metals described in section 2.4.4 may be reflected in the NMR spectra. An activity assay comparing fresh and aged protein would also be informative.

Notably, the spectrum of [FeZn]IMP-1 generally displayed a much smaller degree of peak multiplicity than the [ZnZn] form. This indicates that the presence of

* The NMR experiments in this work were performed at 37 °C. It is not known whether this temperature encourages the release of any of the active site metals. Purifications were typically performed at 4 °C, potentially increasing the enzyme's ability to retain the metals even in a metal-limiting environment.

iron in the active site discourages either metal loss or active site mobility, however, direct comparison of the active-site resonances was not possible due to excessive line broadening by PRE. In future, the active-site resonances of the gallium-substituted enzyme could be analysed for peak doubling.

Missing NMR Cross-Peaks

The fact that cross-peaks from the C-terminal helices were missing in 3D NMR experiments recorded with long constant-time evolution times is most readily attributed to line broadening due to conformational mobility. Interestingly, X-ray crystallography analysis of the C-terminal helices did not indicate significantly higher *B*-factors than elsewhere in the protein structure, suggesting that the low-temperature measurements froze out the lowest-energy conformation. NMR relaxation studies could be performed to confirm and quantify the mobility of these residues. It is unclear, however, whether and how this mobility would impact the activity of the enzyme.

Gallium as a Diamagnetic Reference for Iron

The use of [GaZn]IMP-1 as a diamagnetic reference for [FeZn]IMP-1 relied on some fundamental assumptions.²¹⁶⁻²²³ Firstly, it is essential that the gallium ion occupy the same metal-binding site as iron in the *in vivo* [FeZn] form. In view of the ionic radius and charge state of gallium, this assumption appears reasonable and was shown to be true. Additional evidence, however, pointed to the possibility that gallium (and iron) can also occupy the other metal-binding site when the protein is expressed in the cell-free system. This would explain the additional cross-peak heterogeneities observed in cell-free samples that made it more difficult to assign PCSs even in singly-labelled samples. Therefore, the PCS measurements used only the strongest cross-peak for each residue.

Secondly, it was assumed that the [GaZn] form would have nearly identical structural and mobility characteristics as the [FeZn] form. Indeed, the ¹⁵N-HSQC cross-peaks produced by the [GaZn] form were a much better diamagnetic reference than the [ZnZn] form, even if not perfect for all amino-acid residues. The remaining small differences in structure or mobility between [GaZn] and [FeZn] forms would add some error in the fit of the PCS $\Delta\chi$ -tensor.

To the best of my knowledge, this is the first example of a gallium-substituted metallo-enzyme being produced in cell-free protein synthesis, the first gallium-

substituted metallo- β -lactamase and the first example of a gallium-substituted enzyme that does not require prior de-metallation to form an apo-enzyme.

2.7.2 Characterisation of the Iron in [FeZn]IMP-1

Oxidation State of Iron

The oxidation state of the iron bound to IMP-1 was investigated by several methods, all of which supported the presence of Fe(III) in the active site. Treatment of the enzyme with a reducing agent altered the visible spectrum, causing a red shift in absorbance. Treatment with an oxidising agent had no significant effect. This was corroborated by NMR analysis and expression of protein using the cell-free protein synthesis method. If a ferrous salt was provided to the cell-free reaction, a very lightly coloured protein was obtained and the NMR spectra were distinctly different from samples of either [ZnZn]IMP-1 or [FeZn]IMP-1 made *in vivo*. If a ferric salt was provided to the cell-free reaction, the deep purple colour was evident in the preparation and the NMR spectra were closely similar to those of typical samples prepared *in vivo*. This suggests that the IMP-1 protein can incorporate both iron(II) and iron(III), and that the protein maintains the oxidation state of the iron for at least the time it takes to purify and measure an NMR spectrum of a sample from a cell-free protein synthesis reaction in buffers without reducing agents. This indicates that the oxidation state of the iron in IMP-1 depends on the environmental conditions when the iron is incorporated into the protein. In oxidative extracellular conditions, ferric iron would be expected to be the predominant iron species in the bacterial periplasm, where IMP-1 is folded.²³¹

Determination of the Iron-Binding Site

As Fe(III) has a relatively small ionic radius and a high electronegativity, it was expected that the unpaired electrons of the nitrogen ligands of the Zn₁ site should be favourable for the formation of stable complexes.²³² The identification of the Zn₁ site as the Fe(III) binding site was supported by anomalous X-ray diffraction data and multiple NMR experiments.

Anomalous X-Ray Diffraction Scattering

Unexpectedly, the maximal anomalous scattering signal was observed in the Zn₁ site at both the iron and zinc ion edges, raising the possibility that iron binds at either

metal site. Correcting the metal-site occupancies from the electron density scattering data (independent of the anomalous scattering signal), however, produced an excellent match with theoretical predictions, supporting the conclusion that, at least in the single crystal, iron exclusively populates the Zn₁ site.

NMR Analysis of [FeZn]IMP-1 using PREs

PRE effects resulted in significantly different peak intensities in ¹⁵N-HSQC spectra of [ZnZn] and [FeZn] enzymes, which correlated clearly with the distance from the active-site metal ions, identifying the active site as the paramagnetic centre. The PREs were, however, not sufficiently accurate to discriminate between the two metal-binding sites, which are only about 3 Å apart. To achieve the necessary accuracy of measurement, PREs would need to have been measured for nuclear spins less than 10 Å from the metal.^{7,11} In view of the small number of amide protons in this distance range and the fact that flexible loops (as present in the active site of IMP-1) easily lead to bigger PREs than expected, PREs were of limited value for identifying the iron-binding site. Nonetheless, the PREs conclusively located the metal in the active site and demonstrated that there was no other iron-binding site elsewhere in the protein.

NMR Analysis of [FeZn]IMP-1 using PCS

A grid search to find the metal positions that produce the best $\Delta\chi$ -tensor fits also located the paramagnetic metal in the active site. Furthermore, the grid search pinpointed the paramagnetic metal to a position located about 1.3 Å and 3.9 Å from the Zn₁ and Zn₂ sites respectively. $\Delta\chi$ -tensor fits restricted to either metal-binding site also confirmed the Zn₁ site as the better fitting site.

To my knowledge, this is the first time PCSs have been used successfully to pick the paramagnetic centre in a choice between two metal-binding sites that are located within 4 Å of each other. This result highlights the accuracy with which PCSs can determine structural features in biological macromolecules.

A Single Iron-Binding Site?

All data collected on [FeZn]IMP-1 in this work confirm the Zn₁ site as the primary binding site for iron.

Firstly, the ICP-OES results indicated that, even protein expressions in the presence of an excess of iron resulted in only a single iron ion per protein molecule.* Strictly speaking, this result does not imply that only one site can bind iron, as the possibility remains that only one site *at a time* incorporates iron. Arguably, the ICP-OES data do not even exclude the possibility that an [FeFe]IMP-1 species exists, as long as there was also an equal amount of [ZnZn]IMP-1 present in the sample. However, this scenario disagrees with the NMR spectra of a sample containing one equivalent each of iron and zinc, which was largely devoid of cross-peaks assigned to [ZnZn]IMP-1.

Secondly, the anomalous X-ray scattering experiment matched theoretical predictions at the zinc ion edge after the adjustment of the occupancies of the two metal sites. For a significant population of zinc in the Zn₁ site, the zinc ion edge anomalous signal would have been expected to be stronger in the Zn₁ site and weaker in the Zn₂ site. This confirms that iron can exist in the Zn₁ site. Observation of iron in the Zn₂ site may require different crystallisation conditions.

Finally, the paramagnetic NMR spectra of [FeZn]IMP-1 provided key diagnostic evidence of only a single iron-binding site. Even though signals from residues close to the active site were largely unobservable due to PREs, distant residues displayed single cross-peaks due to a single PCS. If iron had also been present at the Zn₂ site, this would have produced a distinctly different $\Delta\chi$ -tensor and, hence, different PCSs. By the same argument, slow exchange of iron between the Zn₁ and Zn₂ sites would have produced two distinct cross-peaks for most of the NMR spectrum of [FeZn]IMP-1, even at distances far from the active site. This was observed for [FeZn]IMP-1 samples produced *in vivo*, and is the strongest evidence for a single preferred iron-binding site.†

* Among many measurements, a single ICP-OES result indicated the presence of more iron than zinc (Figure 2-28), which may be attributed to the loss of zinc rather than the excess of iron. Unfortunately, quantification of the metal-to-protein ratio was not possible for this sample.

† This result is based on the NMR spectra of [FeZn]IMP-1 using the typical *in vivo* synthesis, harvest and purification method described in sections 2.9.2 and 2.9.6. Periplasmic expressions of ¹⁵N-labelled [FeZn]IMP-1 were of too low a yield for detailed analysis by NMR.

Notably, peak doubling was observed for [FeZn]IMP-1 samples produced by cell-free synthesis. It is not clear whether this reflects multiple metal-binding sites or (more likely) an artefact of the significantly higher concentration of iron available in the cell-free reaction mixtures than *in vivo*. Ultimately, the main point of interest would be the situation in the periplasm. As the protein yields are relatively low in periplasmic expressions, sensitive methods such as EPR and XAFS experiments would be beneficial to characterise the environment of iron in the active site and identify any small populations of iron in the Zn₂ site or di-iron active sites. These techniques have previously been performed successfully on iron forms of glyoxalase II.²³³

Spin State of Iron

The iron in the Zn₁ site has a slightly distorted tetrahedral coordination geometry, for which crystal field theory predicts very low splitting energies.²³⁴ Its coordination involves three imidazole-nitrogen ligands (histidine) and a water oxygen ligand, all of which create moderate ligand field strengths. Finally, the iron(III) ion is a d^5 ion, so has very high mean electron pairing energies. This strongly suggests that the iron(III) in the enzyme is high-spin.

High-spin iron(III) is fully consistent with the paramagnetic NMR data, where high-spin iron(III) is expected to have slower electron relaxation rates than low-spin iron(III) or iron(II), and therefore significantly stronger PREs^{24,28} – evidenced in IMP-1 by the large radius (12 Å) around the metal site for which no cross-peaks could be observed in the ¹⁵N-HSQC spectrum of [FeZn]IMP-1.

High-spin iron(III) typically has a negative $\Delta\chi_{ax}$ component,^{22,25,235} whereas low-spin iron(III) usually has a positive $\Delta\chi_{ax}$ component.^{22,235-237} Consistent with this notion, the sign of the $\Delta\chi$ -tensor was determined to be negative for [FeZn]IMP-1 in the present work.

2.7.3 Structural Comparison of [FeZn]IMP-1 to [ZnZn]IMP-1

CD Spectroscopy

The CD spectra in the far-UV region of both the [FeZn] and [ZnZn] proteins are almost identical, indicating that the backbone structure is preserved between the two forms. Even in the near-UV region, differences between the two forms were minimal, pointing to only minor conformation or environmental changes in the aromatic side

chains. The structural similarity of [FeZn]IMP-1 and [ZnZn]IMP-1 was confirmed by the X-ray crystal structure.

X-Ray Crystal Structure

Of particular importance to this study was the ability to directly compare the [FeZn]IMP-1 structure with two structures of [ZnZn]IMP-1 at high resolution and with ligands bound to the active site. Only a single IMP-1 structure had been co-crystallised with citrate (4F6Z¹⁰⁹), but this structure was not suitable for comparison due to an active site mutation (C158G). Of the remaining wild-type enzyme structures, the succinic acid derivate in 1JJE¹²⁰ (1.8 Å resolution) has very similar coordinating atoms and was initially chosen for comparison. Although the ligand is slightly bigger than citrate, structural alignments showed that the ligand binds to the metal ions in a very similar way. In contrast, the ligand bound in 1DD6¹⁸² is much larger than citrate and has a sulfur atom in place of the bridging-water or hydroxide ion ligand. This structure is also of slightly lower resolution (2.0 Å). Given these differences in ligand properties, it was surprising to find that the backbone RMSDs indicate greater similarity of the [FeZn]IMP-1 structure to 1DD6 than 1JJE.

The inter-metal distance was practically the same in 1DD6 (3.60 Å) and 1JJE (3.56 Å), despite the different bridging ligands. In contrast, the metal-metal distance was larger for the [FeZn]IMP-1 structure (3.80 Å). This inter-metal distance is the largest of any of the published crystal structures of IMP-1 with two metal ions.

All of the distances from the protein ligands to the metal of the Zn₁ site were subtly smaller in [FeZn]IMP-1 than in 1DD6, by up to 0.13 Å. This is consistent with Fe(III) having a smaller ionic radius than Zn(II). In contrast, the differences in metal-ligand distances for His77 and His79 were insignificant for the Zn₁ site between [FeZn]IMP-1 and 1JJE, while the distance for His139-N^{e2} was larger ($\Delta=+0.13$ Å). This small distance change is readily explained by a slight opening in 1JJE of the $\alpha\beta/\beta\alpha$ -sandwich constituting the two main subdomains. As expected, the distance between the coordinates of the metal and the sulfur ligand was greater in 1DD6 ($\Delta=+0.24$ Å) than the distance from the metal to the oxygen of the ligand in either [FeZn]IMP-1 or 1JJE.

The Zn₁ site in 1DD6 has a slightly distorted tetrahedral geometry, specifically in the displacement of the sulfur ligand. The Zn₁ coordination geometry is similar in [FeZn]IMP-1 and 1JJE, with a subtle displacement of the side-chain of His77. In

contrast, the Zn₂ site has different coordination geometries due to the different number of coordinating atoms provided by the bound active-site ligands, making structural comparisons for this site uninformative.

Using the coordinates of Ala53, Gly120 and Leu205 to define the opening angle of the $\alpha\beta/\beta\alpha$ -sandwich, the 1JJE structure is more closed in comparison to the [FeZn]IMP-1 and 1DD6 structures. Gly120 is located at the hinge of the opening angle. If such a hinge motion occurs in solution, it would explain many of the subtle structural differences observed between 1JJE and 1DD6. It could also be biologically important, enabling promiscuity of the active site by expanding the range of substrates that can be accommodated in the catalytic region. The hinge is more open in the [FeZn]IMP-1 structure, similarly to 1DD6, which explains the significantly smaller RMSD values after alignment of [FeZn]IMP-1 to only the N- or C-terminal regions of 1JJE.

Analysis of the packing density showed very little difference in the efficiency of internal packing between the three crystal structures. The presence of a unique cavity large enough to fit a water molecule underneath the metal-binding site in the [FeZn]IMP-1 structure was interesting and could result from subtle changes in amino-acid side-chain conformations in response to the smaller ferric metal ion.

It is important to note that the structural differences highlighted are very subtle and the significance of these comparisons is limited by the resolution and quality of the solved crystal structures and by the presence of different active-site ligands. For example, the 2.3° difference in the $\alpha\beta/\beta\alpha$ -sandwich opening-angle could be attributed to crystal packing effects, as the structures compared had different space groups, different unit cell measurements and different numbers of monomers per unit cell. The diffraction-component precision index (DPI)²¹⁰ for the [FeZn]IMP-1 structure was 0.11 Å, suggesting that differences greater than 0.11 Å (such as the inter-metal distance) are significant. Clearly, any structural difference between [FeZn]IMP-1 and [ZnZn]IMP-1 is minor and near the limit of detection at the resolution of the crystals structures available.

Structure Comparison by NMR Spectroscopy

The similarity in chemical shifts between [FeZn]IMP-1 and [ZnZn]IMP-1 provides evidence for a very similar three-dimensional structure of the two forms of the enzyme. Nonetheless, not all chemical shift differences could be explained by PCSs

induced by the paramagnetic iron. This may point to a small difference in the structure and/or mobility between the two forms.

The problem of non-PCS-like shift differences prompted the use of a [GaZn] species, which indeed presented a better diamagnetic reference for [FeZn]IMP-1. To elucidate any structural differences induced by a triply versus doubly charged metal ion, future NMR experiments could employ the diamagnetic [GaZn] form for detailed comparison with the [ZnZn] form.

Are There Any Significant Structural Differences?

The chemical shift changes observed by NMR suggest that the [FeZn] form may be structurally more different from the [ZnZn] form than indicated by the X-ray crystal structural comparison.

Firstly, NMR experiments identified at least two distinct conformations of the protein residues close to the active site of [ZnZn]IMP-1, although only one of the conformations remained after incubation for a week at 37 °C. Clearly, the chemical environment in the catalytically relevant area changes with time. All available crystal structures of IMP-1, including the one solved in this work, involved crystallisation at or above room temperature over the course of several weeks. By the time crystals form, the single crystal may contain an enzyme population that was not even present in the fresh solution. It is thus always possible that the structural similarity between the [FeZn] and [ZnZn] forms in the single crystal is a crystallisation artefact.

Secondly, the resolution of 1.8-2.0 Å of the presently solved and previously available X-ray structures is not sufficient to interpret very small differences in inter-atomic distances, and one must be careful not to over-interpret the coordinates.²³⁸ The influence of different ligands, space groups and unit cell dimensions is also difficult to assess. While the NMR chemical shifts and cross-peak multiplicities observed in solution with fresh protein preparations suggested that [ZnZn] and [FeZn] forms differ, albeit subtly, the NMR data are more difficult to interpret in structural terms.

2.7.4 Enzyme Stability Comparison of [FeZn]IMP-1 and [ZnZn]IMP-1

Thermal Stability

The [FeZn] form of IMP-1 melts approximately 1.4 to 1.9 °C lower than the [ZnZn] form, but this does not necessarily indicate that the [FeZn] form is less stable at ambient temperature. Firstly, the CD spectra recorded of both species at 90 °C differed significantly, were potentially complicated by precipitation or aggregation and were not consistent with expectations for a completely unfolded random coil protein. Secondly, the thermal treatment was irreversible, making it difficult to obtain accurate melting temperatures. Regardless, the thermal stability of the two forms is similar.

Along with the imperfect isosbestic points in both the [ZnZn]IMP-1 and [FeZn]IMP-1 melt, fitting sigmoid functions to different regions of the CD spectrum suggested at least a two-step denaturation pathway. This denaturation pathway of [FeZn]IMP-1 is different as evidenced by the change in isosbestic point at 202 nm. It is not clear whether the earliest unfolding event is reversible. Previous studies on the thermal stability of [ZnZn]IMP-1 utilised differential scanning calorimetry (DSC) measurements.^{205,239} The best way of comparing the stability of the [ZnZn] and [FeZn] forms at ambient temperature would be a denaturation experiment using increasing amounts of urea.

Exogenous Metal Exchange

The metal ions of IMP-1 are bound very tightly, and both are functionally important.^{194,240} The enzyme retains two metal ion equivalents even during long size-exclusion and ion exchange chromatography separations in metal-limiting conditions. Therefore, it was surprising to find just how rapidly cadmium was able to exchange into the active site of both [FeZn] and [ZnZn] forms of IMP-1.

Remarkably, cadmium replaced both iron and zinc after treatment of [FeZn]IMP-1. As the present study identified the iron to occupy the Zn₁ site, this result suggests that cadmium exchanges with either metal-binding site. Lack of selectivity for the metal-binding site has been reported for other doubly-charged ions such as Co²⁺,^{203,239} but Cd²⁺ has previously been reported to occupy the Zn₂ site exclusively.²⁰³ The evidence presented by Siemann *et al.*²⁰³ was based on their observation that only a single equivalent of cadmium was ever observed exchanging into their protein sample – a result replicated in the current work. An alternative explanation, however, would be

that the presence of a cadmium ion in IMP-1 prevents binding of a second cadmium ion as Cd^{2+} has a larger ionic radius (0.97 Å) than Zn^{2+} (0.74 Å) or Fe^{3+} (0.64 Å).

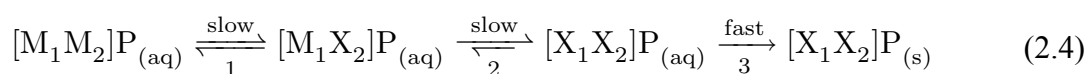
Interestingly, addition of an excess of cadmium resulted in an exchange of one cadmium for a zinc in the [ZnZn]IMP-1 sample in less than 5 minutes. This facile metal exchange is unexpected in view of the high metal affinity of IMP-1. Siemann *et al.*²⁰³ also noted this ‘unusual kinetic lability’ and compared the rapid exchange to metallothioneins, a class of enzymes capable of rapid transfer of tightly bound zinc ions to acceptor proteins. Remarkably, compared to this family of metal-transfer enzymes, IMP-1 shows about 10 times faster exchange rates.²⁰³

Although cadmium also exchanged into the [FeZn] form, only half a stoichiometric equivalent was found per protein molecule after the 5-minute treatment. As expected, the addition of zinc to the [ZnZn] sample hardly changed the metal content of the enzyme, but zinc treatment did dilute the iron bound to the [FeZn] form. Like the cadmium exchange, this addition of zinc was incomplete after 5 minutes. The fact that the presence of Fe^{3+} in the active site of the enzyme slows the metal-ion exchange process has potentially broad implications for the stability or activity of the enzyme.^{194,203-205,239,240}

It is proposed that, for future studies of IMP-1, more successful substitution of other ions into the active site may be possible via the metal-ion induced exchange process, making this method preferable to attempting the formation of the apo-enzyme, as per the currently typical procedure for metallo-enzymes.^{194,204,205,239,240}

The Effect of Metal Substitution on IMP-1 Stability

At least two unfolding events were detected using the thermal CD denaturation experiment for both [ZnZn] and [FeZn] forms of the enzyme. The attempts to remove the metal ions demonstrated that the presence of metal ions in the active site stabilises the enzyme and keeps it soluble. It is thus tempting to associate the two unfolding events with the sequential loss of the two metal ions prior to a fast denaturation of the apo-enzyme as per scheme (2.4):



where M denotes a site occupied with a metal ion, and X denotes a site without a metal ion. Both IMP-1 (current work) and BcII²⁴¹ (class B1) have been shown via X-ray

crystallography to lose metal from the Zn_2 site under crystallisation conditions, so it is reasonable to assume that this site loses its metal first during thermal denaturation.

Attempts to refold precipitated protein have been unsuccessful,^{203,240} implying that step 3 is irreversible, at least in the typical refolding conditions used so far. Previous works have described near full recovery of activity after partial de-metallation^{205,239} suggesting that step 1 is readily reversible, although others describe this step as being irreversible,²⁴⁰ so it would seem the conditions used are important. At least two groups^{194,205} describe the recovery of activity after complete de-metallation, suggesting that step 2 is also reversible. In the present work, irreversible denaturation (step 3) always seemed to predominate the reverse pathway (step 2).

In the scenario of sequential metal loss, stabilisation of the $[\text{M}_1\text{X}_2]\text{P}$ intermediate by metal substitution with a tighter binding ion could drastically increase the likelihood of the protein remaining folded *in vivo*. This would increase the chances for a partially de-metallated enzyme to regain a second catalytic metal ion and recover full activity. Equilibria between forms at different stages of de-metallation would also impact on the enzyme stability at different pH values. It is quite possible that the $[\text{FeZn}]$ form is more stable over a different pH range than the $[\text{ZnZn}]$ form.

2.7.5 Functional Comparison of $[\text{FeZn}]\text{IMP-1}$ and $[\text{ZnZn}]\text{IMP-1}$

The enzymatic activity at pH 7.5 against benzylpenicillin (a penam) is higher for $[\text{ZnZn}]\text{IMP-1}$, with a k_{cat} value 3.5 times faster and a K_{m} value almost 5-fold lower than for $[\text{FeZn}]\text{IMP-1}$. This yields a 17-fold higher $k_{\text{cat}}/K_{\text{m}}$ for $[\text{ZnZn}]\text{IMP-1}$ under the tested conditions. This is a significant difference, but it also shows that the enzyme is still active in the $[\text{FeZn}]$ form.

A more rigorous study of the relationship between pH and the activity of the different forms of IMP-1 could yield important results, but the activity differences probably also depend on the substrate. It would also be interesting to quantify any effect the 37 °C treatment that was required for crystal formation would have had on the activity of the enzyme.

2.7.6 General Discussion

An Iron-Binding IMP-1 Species

Iron has been found in metallo- β -lactamases previously. In particular, inactive iron species have been reported for members of class B3 (L1^{242,243} and GOB-18^{242,244}) following expression in the cytosol of *E. coli*. It is well documented that bacteria concentrate zinc and iron ions in the cytosol even under metal-limiting conditions,^{244,245} whereas the metal content of the periplasm is largely dependent on the extracellular environment and ion pumps that deplete the region of metal ions.^{243,245} ICP-OES metal analyses of *E. coli* cytosol and periplasmic soluble fractions indicate that the concentration of zinc and iron is approximately 45 μ M in metal-limiting conditions, and while iron concentrations increase three-fold in the cytoplasm in response to the addition of 100 μ M iron, zinc concentrations are relatively stable even in the presence of excess zinc.^{127,243} It is thus not surprising to find iron in the active site of IMP-1 metallo- β -lactamase even when the protein is expressed under conditions of relatively low concentrations of iron and high concentrations of zinc.

It is important to remember, however, that in the wild metallo- β -lactamases are translocated to the periplasmic space in a metal-free unfolded state,^{127,242,243,246} and therefore fold in a metal ion environment that is very different to the cytosol. For the L1 and GOB-18 enzymes, isolation from periplasmic extracts yielded exclusively active zinc(II)-bound enzymes.^{231,242,243,246} In fact, the secretion mechanism of unfolded metallo- β -lactamases led to the proposal that the secretory machinery may play an important role in determining the metals that are ultimately taken up by a given apo-enzyme.^{231,243} In metal-limiting conditions, periplasmic extracts typically contain less than 1 μ M zinc or iron, however, both metals are concentrated to close to 1.23 mM zinc and 2.83 mM iron after the addition of 100 μ M metal to the media.^{243,247} Expression of IMP-1 in the periplasm did not yield pure [ZnZn]IMP-1, and actually increased the likelihood for iron to be substituted into the active site. Even under conditions known to favour the [ZnZn] form during intra-cellular expression, up to 25% of the product was the [FeZn] species.

The fact that iron successfully competes for the active site of IMP-1, even when zinc is supplied in 20-fold excess, can be put in context partially by metal stability predictions. The Irving-Williams bivalent metal stability series^{248,249} does not describe the relationship between Zn^{2+} and other metals except for copper(II), but suggests that

the larger ionic radius and smaller ionic charge of Zn^{2+} makes zinc(II) complexes less stable than iron(III) complexes, whereas the stability of zinc(II) and iron(II) complexes should be comparable. For example, pyridine complexes of Fe^{3+} are more stable than those of Zn^{2+} .²⁴⁷ In the oxidising environment of the periplasm, a strong preference for iron(III) over zinc(II) is not unexpected.

Iron-Binding in the Metallo- β -Lactamase Superfamily

The metal binding specificity of IMP-1 is not unusual in the context of the entire metallo- β -lactamase superfamily where at least three families of the superfamily exclusively bind iron. Members of a fourth family (glyoxalase II) have been reported to bind zinc, iron and manganese. Like group 3a metallo- β -lactamases, this family has a dinuclear metal-binding site, with the Zn_1 site coordinated by three histidines. The Zn_2 site differs, however, as its coordinating residues are a histidine and two aspartates. The two active-site metals of glyoxalase II are bridged by a catalytic water/hydroxide ion, but differ from IMP-1 in that an oxygen atom from an aspartate residue constitutes an additional bridging ligand. An additional ligand, from either a bound inhibitor or the solvent, coordinates each of the zinc ions, providing both metals with six ligands in distorted octahedral coordination geometries (Figure 2-68).

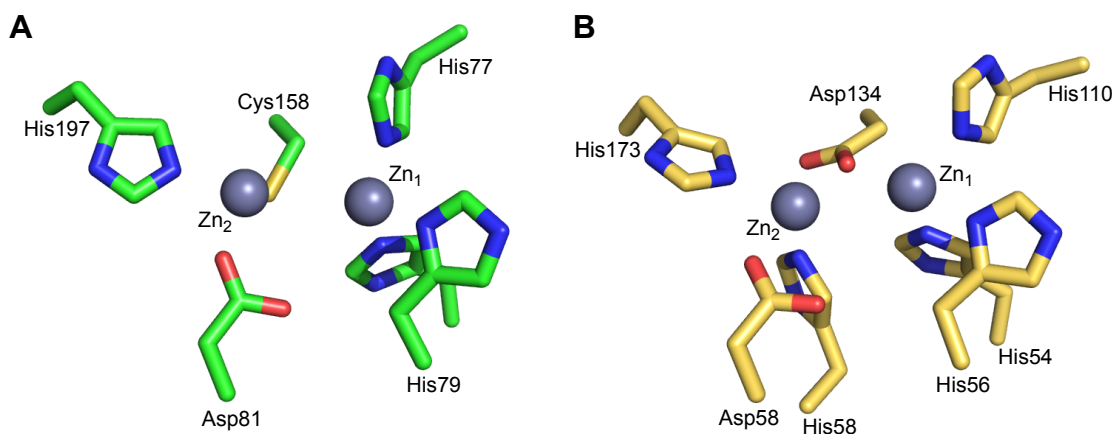


Figure 2-68 Comparison between the active-site metals and side-chains of coordinating residues in **A**) IMP-1 (1JJE)¹²⁰ and **B**) human glyoxalase II (1QH3)²⁵⁰. Zinc ions are depicted as grey spheres with a 50% reduced radius compared to the ionic radius for better visibility of the amino-acid side-chains. The bridging water/hydroxide ion and bound inhibitors are not shown. Nitrogen, oxygen and sulfur atoms are shown in blue, red and yellow, respectively.

The human wild-type glyoxalase II has been observed with 0.7 equivalents of iron and 1.5 equivalents of zinc per protein molecule, but was originally assigned as a pure zinc enzyme.^{233,250} Data published on the glyoxalase II from *Arabidopsis thaliana* in 2003, however, showed significant levels of iron, zinc and manganese in protein recombinantly expressed in the cytoplasm of *E. coli*.²³³ As in the present work on

IMP-1, the degree of substitution was dependent on the environmental availability of the different metal ions, with conventional expression media yielding approximately 0.8 ± 0.2 equivalents of iron per protein molecule.^{233,241} Higher iron availability did not yield greater than 1 equivalent of iron per protein molecule, and reduction of the iron content was achieved by supplementing the expression media with 250 μ M of the competing metal. For the iron-containing species, EPR measurements identified an Fe(III) spin in an environment consistent with a [Fe(III)Zn(II)] metal centre. An [Fe(III)Fe(II)] form was also identified.

Why Has Iron Not Been Found in IMP-1 Before?

Identification of which metal is present in a metallo-protein has traditionally been achieved by isolating the protein, forming the apo-enzyme and subsequently identifying which metals can recover maximal activity *in vitro*. The original work on IMP-1¹³³ applied such a protocol and indicated a 100% loss of activity after treatment with EDTA, and a 54% recovery of activity after treatment with zinc. This result has been put in question by more recent work where EDTA has been proven to be highly inefficient in removing metals from the active site of IMP-1.⁷⁹ Divalent cations other than zinc were tested for recovery of activity, but iron(III) was not tested.^{133,138}

The first thorough biochemical analysis of IMP-1 in 1999 assayed several metal ions, including zinc, cadmium, cobalt, calcium, copper, manganese and nickel, but not iron.⁷⁹ This may be attributed to the limited iron sensitivity of the ICP-MS technique²⁵¹⁻²⁵³ used for metal analysis.*

Since the initial reports of IMP-1 as a zinc-binding enzyme, most studies of IMP-1 have utilised purification buffers with at least 10 μ M zinc salts.[†] As zinc readily occupies both binding sites, the iron form of the enzyme was easily missed. Previous purification protocols employed long size-exclusion and dialysis steps in the presence of zinc salts, during which any population of [FeZn]IMP-1 could have been converted to the [ZnZn] form. Anecdotal reports from others working with this enzyme described

* Argon from the plasma and oxygen from the sample matrix combine to form $^{40}\text{Ar}^{16}\text{O}^+$ with an atomic mass equivalent to the main isotope of iron, ^{56}Fe . ArOH^+ is also formed, equivalent to the next-most abundant iron isotope. Commercial research and development of ICP-MS instrumentation has only recently started to address this problem.^{251,253,254} The method of metal ion quantification in the present study (ICP-OES) does not suffer from this limitation.

[†] In fact, even early work by Watanabe *et al.* and Laraki *et al.* employed exogenous zinc in the purification buffers.^{79,133}

a purple colour present in their enzyme preparations, which dissipated over the course of size exclusion chromatography in 500 μM ZnCl_2 .²⁵⁵ Again, this points to metal exchange during protein purification. The problem associated with large amounts of metal being present during purification, with respect to establishing the wild-type composition and activity, has been discussed previously.^{241,256,257} It is finally beginning to be recognised that the traditional practice of oversupplying a single metal ion in metallo-enzyme preparation can cause experimental artefacts.^{256,257}

The Metals in the Active Site of IMP-1 *in vivo*

One or Two Metals?

Previously, several class B1 metallo- β -lactamases have been purified with only a single metal present, and there is still some disagreement over the degree of metal saturation *in vivo*.^{241,258,259} A common argument is that the saturation of the metal-binding sites may be an artefact of the expression and purification of metallo- β -lactamases in the presence of excess zinc. In the present study, IMP-1 was expressed with excess metal present, but was purified under metal limiting conditions. In practically all preparations, almost two equivalents of metal were observed per protein molecule. This supports the notion of IMP-1 having very tight metal binding affinity, and that once the metals are incorporated into the enzyme they are not easily released.^{79,203} This is also consistent with data collected on BCII (another B1 M β L) that showing the metal binding is cooperative²⁶⁰

In the native environment, the enzyme is located in the periplasm in the presence of siderophores and the metal ion concentration fluctuates with environmental conditions. As IMP-1 has been shown to be less active in the mono-metal form,¹⁹⁴ it is advantageous for the enzyme to bind its metal cofactors tightly.

[ZnZn]IMP-1, [FeZn]IMP-1 or Both?

It is clear that IMP-1 can exist and is active in either [ZnZn] or [FeZn] form. In the native environment of bacteria, however, the pool of metals available for enzyme binding is limited. Under these conditions, the metal affinity of the enzyme relative to the gamut of other metal-binding proteins can determine the uptake of specific metals in the enzyme.^{231,241} In the case of clinically relevant metallo-enzymes, the metals

available in the pathological environment also govern the metal species present in the enzyme. Unfortunately, this is particularly difficult to assess.

Compelling evidence has been collected over the last two decades showing [ZnZn]IMP-1 exists in clinically relevant infections, but there is little evidence for or against the existence of [FeZn]IMP-1 in the clinical environment. It thus remains unclear whether the [FeZn] form is a laboratory artefact or whether it is an essential feature of IMP-1 to retain at least partial activity under unusual environmental conditions. The latter idea is supported by the discovery of several examples of zinc-dependent enzymes over the last decade, which had to be reclassified as cambialistic or even iron-dependent enzymes *in vivo*.^{257,261,262}

One example of a cambialistic enzyme is LpxC from *E. coli* that has been shown to use either iron or zinc cofactors *in vivo*.^{261,262} The enzyme was originally classified as a Zn²⁺-dependent deacetylase, as metal chelators reversibly inhibit it, and it contained Zn²⁺ when purified under aerobic conditions. Unfortunately, the original research did not evaluate the ability of Fe²⁺ to activate LpxC. The mis-assignment of the native metal cofactor as only Zn²⁺ has been attributed to the aerobic purification of these enzymes, leading to the oxidation of Fe²⁺ to Fe³⁺ and subsequent substitution with Zn²⁺ at the active site.^{261,262} Consistent with the current study, the ratio of iron to zinc in the enzyme was found to depend on the iron to zinc ratio in the cell lysate, implying that the metal co-factors in the enzyme depend on the relative metal abundance in the environment.^{257,262}

Another example is MshB from mycobacteria. This enzyme prefers an Fe²⁺ cofactor in anaerobic or low zinc environments, whereas it prefers Zn²⁺ in aerobic or high-zinc environments.^{257,263} The ability to switch between co-factors under changing environmental conditions is likely an important feature of metallo-enzymes that carry out critical cellular functions, such as the antibiotic resistance provided by metallo- β -lactamases.

2.7.7 Future Prospects using High-Throughput Paramagnetic NMR

The present work determined the backbone NMR resonance assignments for most of IMP-1, identified conditions for the controlled formation of [ZnZn] and [FeZn] forms *in vivo*, and established [GaZn]IMP-1 as a suitable diamagnetic model of the [FeZn] enzyme. This presents a firm basis for future paramagnetic NMR studies on

IMP-1. In addition, the development of high-yielding *in vivo* and cell-free protein expression systems and a rapid purification procedure open the door to high-throughput experiments.

While high-spin iron(III) is mostly regarded as a problematic cofactor for high-resolution protein NMR,²⁸ in the case of IMP-1 it provides interesting possibilities for high-throughput ligand screening using NMR. As it has been shown that the [FeZn] form is catalytically active with an almost identical structure, it is a good model for the [ZnZn] protein.

In the case of a weakly binding fragment suitable for fragment based drug design (low mM to high μ M binding affinity), the small molecule would enter and leave the active site in the fast-exchange regime of the NMR time-scale. In a sample with excess ligand, this would result in NMR signals averaged between the narrow signals of the unbound ligand and the significantly broadened signals from the bound ligand. Comparison with samples without protein would highlight any attenuated signals as arising from ligands that closely approach the active site. Such measurements could be performed without perdeuteration using only small amounts of protein (nM concentrations), which is ideal for a high-throughput procedure.

In the case of a tightly binding, drug-like fragment (low μ M to nM binding affinity), the exchange of the ligand in and out of the active site is likely to be slow on the NMR time-scale, implying lifetimes of seconds or longer. In this case, the signals from any bound compound would be broadened beyond detection by PRE from the paramagnetic iron centre. At the same time, the presence of the ligand in the active site would change the electronic environment at the paramagnetic centre, resulting in a change of the $\Delta\chi$ -tensor and, hence, different PCSs. Monitoring a few NMR ‘reporter’ signals from elsewhere in the protein could identify this change. Unnatural fluorinated amino acids²⁶⁴ incorporated in the protein outside the active site are an attractive option as a reporter signal. This would provide unique and sensitive NMR nuclei in the protein that could be measured using simple 1D NMR experiments, without the need for expensive protein isotope labelling. More protein sample would be required in this regime (μ M concentrations), however, due to the stability of IMP-1, it would be possible to recycle the protein by passing it through a short desalting column.

Even though NMR is inherently a linear process, limiting the applicability to high-throughput protocols, small libraries of fragments could be tested simultaneously

to increase parallel throughput in either of the above cases. Along with automated NMR sampling and processing systems, this method provides a potentially powerful method for drug-lead identification.

2.8 Conclusion

An [Fe(III)Zn(II)]IMP-1 variant was identified and structurally characterised. X-ray diffraction analysis revealed only subtle differences when compared to the [ZnZn] form of the enzyme, but NMR analysis suggests subtle differences in structure and/or mobility between the two species. Paramagnetic NMR and anomalous X-ray scattering techniques were successfully used to identify the preferential iron-binding site as the Zn₁ site. While initial activity assays indicate that the [ZnZn] form is more active at pH 7.5, the [FeZn] variant still shows significant catalytic activity.

The discovery of the iron-substituted variant has clinical implications for the design of inhibitors intended for IMP-1, as a drug developed solely against [ZnZn]IMP-1 might not be as effective against [FeZn]IMP-1.

2.9 Experimental Methods

2.9.1 Constructs and Bacterial Strains

The *bla*_{IMP1} gene in pET-47b(+) was generously donated by A/Prof. G. Schenk (University of Queensland) and was used unchanged for *in vivo* over-expression (Figure 2-69). This construct was not suitable for cell-free expression due to the presence of the *lac* operon repression system, therefore the gene was also subcloned into pETMCSI²⁶³ with an N-terminal expression MASMTG tag for cell-free protein synthesis (Figure 2-70).^{*} In order to remove any competition for the active site metals, neither construct included a His₆ purification tag. The DNA sequence encoding the native N-terminal signal peptide (MSKLSVFFIFLFC SIATAA) responsible for transport of the protein to the periplasm was appended via overlapping PCR and restriction digest ligation onto the 5' end of the gene in pET-47b(+) for periplasm expression studies.

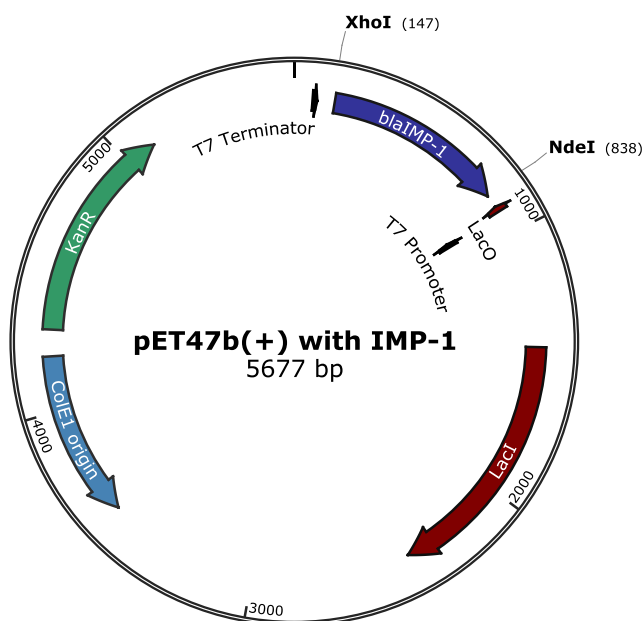


Figure 2-69 pET47(b) with *bla*_{IMP-1}. The gene without the N-terminal signal peptide (purple) is inserted between *Nde*I and *Xho*I restriction sites, removing the N-terminal His₆ tag from the vector. A stop codon is inserted prior to the thrombin cleavage site and the STag coding sequence. The *lac* operon repression system is present (*lacO* and *lacI* - red) making this vector unsuitable for *in vitro* expression. Antibiotic selection is by kanamycin (green) making it suitable for *in vivo* activity assays of IMP-1. Figure generated using SerialCloner²⁶⁵ and SnapGene Viewer²⁶⁶.

^{*} Cloning of the MASMTG construct into pETMCSI was performed by Dr R. Qi (RSC, ANU) prior to the commencement of this PhD project

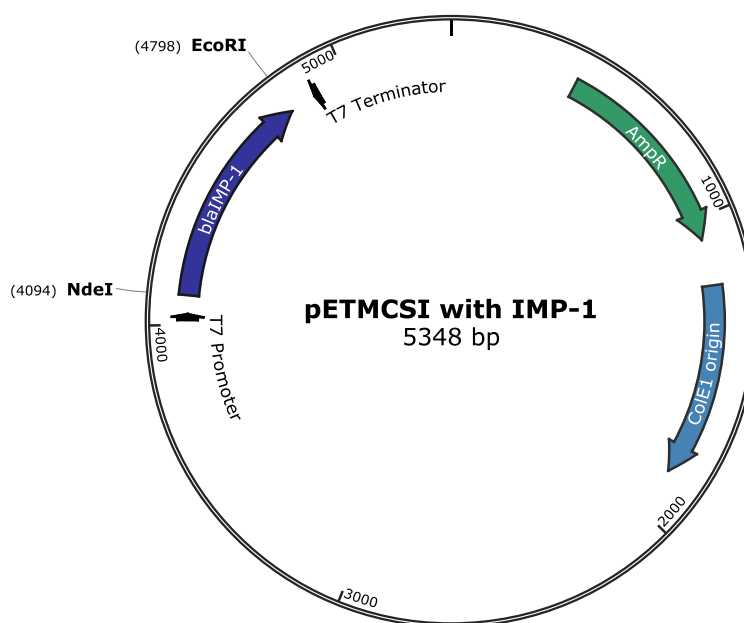


Figure 2-70 pETMCSI with *bla*_{IMP-1}. The gene (purple) is inserted between *NdeI* and *EcoRI* restriction sites. The N-terminal signal peptide is removed, and a MASMTG T7 expression tag is appended to the N-terminus. The *lacI* and *lacO* repression system is not present. Antibiotic selection is by ampicillin (green), making it not ideal for *in vivo* assays of the IMP-1 protein. Figure generated using SerialCloner²⁶⁵ and SnapGene Viewer²⁶⁶.

2.9.2 Cytosolic Protein Synthesis

Highest yields of soluble protein were obtained by using a high cell density expression system based on the method by Sivashanmugam *et al.*,¹⁹² with a number of key modifications. In brief, 50 mL of LB media²⁰² with either 100 mg/L ampicillin or 50 mg/L kanamycin was inoculated with a scraping from a -80 °C DMSO stock of BL21(DE3)recA strain containing either pETMCSIII or pET47b(+) with the *bla*_{IMP1} gene (section 2.9.1) and incubated in a 125 mL flask with shaking at 37 °C for eight to twelve hours to an OD₆₀₀ of 0.2 to 0.5. This culture was used to inoculate 1 L of antibiotic LB media in a 2 L baffle flask, which was subsequently incubated at 37 °C with fast shaking (> 200 rpm) for 12 to 16 hours to an OD₆₀₀ of 5 to 8. The cells were then harvested by gently centrifuging at 1,700 g for 10 minutes and resuspended gently in 200 mL of room temperature defined minimal media consisting of 50 mM Na₂HPO₄, 25 mM KH₂PO₄, 10 mM NaCl, 5 mM MgCl₂, 0.1 mM CaCl₂, 0.5 × Me Mix¹⁹⁸ (25 μM FeCl₃, 10 μM CaCl₂, 5 μM MnCl₂, 5 μM ZnCl₂, 1 μM CoCl₂, 1 μM CuCl₂, 1 μM NiCl₂, 1 μM Na₂SeO₃, 1 μM H₃BO₃), 0.25 × RPMI 1640 vitamin mix (Sigma), 1% glucose, 0.1% NH₄Cl, pH 8.2 with either 50 mg/L kanamycin or 100 mg/L ampicillin in a 2 L baffle flask. Either 500 μM ZnSO₄ or FeCl₃ was added to the defined minimal media for generation of either [ZnZn]IMP-1 or [FeZn]IMP-1, respectively (section 2.3.3).

The pH of the resuspended culture was measured and adjusted directly with dilute NaOH or KOH to between 8 and 8.4. The culture was then incubated at 25 °C for one to two hours with fast shaking (> 200 rpm). Protein production was induced by the addition of 1 mM IPTG and incubated with fast shaking (> 200 rpm) for 20 to 22 hours at 25 °C. Cells were harvested by centrifuging at 4,730 g for 15 minutes, then resuspended in 15 mL of 50 mM HEPES (pH 7.5) buffer. 1 unit of DNase I (NEB) per 200 mL culture was added, and cells were lysed by a minimum of two slow passes through a French pressure cell (12,000 psi). The lysate was centrifuged at 32,000 g for one hour and then clarified by filtration through a 0.45 µm syringe filter unit (Millipore) prior to purification.

For ¹³C- or ¹⁵N-labelled protein for NMR, the glucose and/or ammonium chloride was supplied in labelled form and was otherwise treated identically. For ²H/¹³C/¹⁵N-labelled samples, single colonies were selected from 70% deuterated minimal media plates for optimal expression in deuterated minimal media culture. The above protocol was then implemented, with all media consisting of solids being first dissolved into 100% D₂O and sterilised by filtration through a 0.22 µm pore size filter. Deuterated glucose was not used. As the protein cannot be successfully refolded, proton back-exchange onto the amides was achieved by incubating the protein in H₂O-based buffers during purification.

2.9.3 Periplasmic Antibiotic Plate Assay

Rich LB²⁰² media agar plates supplemented with 50 mg/mL kanamycin were spread with a solution of IPTG to a final concentration of 1, 0.5, 0.25 or 0 mM IPTG. Once dry, the plates were spread with 200 µL from a 5 mL rich media overnight culture of BL21DE3(recA) containing the pET47b(+) plasmid with *bla*_{IMP1} with or without the N-terminal signal peptide (section 2.9.1). Four filter paper disks were placed onto each plate, and 20 µL of 1, 10, 100 or 200 mg/mL ampicillin was pipetted onto each disk. The plates were incubated for 16 hours at 37 °C.

2.9.4 Periplasmic Protein Synthesis

For overexpression of periplasmic protein, a similar protocol was used as for the cytosolic expression (section 2.9.2) with the exception that, in an attempt to reduce the overload on the native *E. coli* membrane transport proteins, only 0.5 mM IPTG was used for induction.

After expression, cells were harvested by centrifugation at 4,730 g for 15 minutes. The medium was retained as the medium fraction and the cells were resuspended in 5 mL of chilled 500 mM sucrose, 100 mM Tris·Cl, pH 8.0 and incubated on ice for 1 to 1.5 hours. Sphereoblasts were removed by centrifugation at 30,000 g for 30 minutes and the supernatant was collected as the periplasmic fraction. The spheroblasts were then resuspended in 5 mL of chilled 500 mM sucrose, 100 mM Tris·Cl, pH 8.0. 1 unit of DNase I (NEB) was added and the spheroblasts were processed through a French pressure cell (12,000 psi). The lysate was centrifuged at 32,000 g for one hour and the supernatant collected as the cytosolic fraction.

2.9.5 Cell-Free Protein Synthesis

Protein was synthesised with single or selectively isotope-labelled amino acids using a dialysis-fed cell-free protein synthesis system.²⁶⁷ Cell-free extracts were reduced with NaBH₄ for labelling with single amino acids prone to PLP-cofactor-dependant aminotransferase activity.²⁶⁸ *N*-acetyl-glutamate was used in place of the glutamate of the buffer system when labelling glutamate.²¹⁵ In an attempt to control the metal ion content of the enzyme, additional 10 µM zinc, 110 µM iron(II) chloride, 110 µM iron(III) chloride or 110 µM gallium(III) sulfate (220 µM gallium) was added to the outer buffer. Typical yield of purified protein was approximately 0.8 mg/mL of reaction mixture.

2.9.6 Protein Purification

Clarified lysate or 50-fold diluted crude cell-free mixture was loaded onto either a 35 mL or 5 mL SP Sepharose cation exchange column pre-equilibrated with 50 mM HEPES, pH 7.5. The protein was washed with one column volume of buffer, followed by a one-column volume wash using buffer with 100 mM NaCl. Bound protein was eluted in a single peak using a linear gradient from 100 to 500 mM NaCl over five column volumes. Pure protein was concentrated using a 30 kDa cut-off ultrafiltration device (Millipore), and desalted by one or two passes through a PD-10 or NAP-5 column pre-equilibrated with the desired buffer system via gravity flow. Protein intended for crystallography trials was also run through a 300 mL S300 or S200 Sepharose gel filtration column in 10 mM HEPES pH 7.0, 100 mM NaCl to ensure greater than 99% purity.

For higher-throughput cell-free protein synthesis samples, a purification method that could be run in parallel was implemented.* Amicon Pro Affinity Concentrators (Millipore) with Sepharose SP cation exchange resin was used. The concentrator was washed with a high-salt buffer (50 mM HEPES, pH 7.5, 500 mM NaCl), followed by five washes with a low salt buffer for equilibration (50 mM HEPES, pH 7.5). The cell-free protein samples were diluted 1 in 10 in low salt buffer and then incubated for 30 minutes (30 °C) with shaking, prior to spinning off residual liquid. Protein was eluted using the high-salt buffer.

2.9.7 Protein Storage

Purified protein in MES or HEPES buffer at pH 6.5 to 7.5 containing a minimum of 100 mM NaCl was successfully stored frozen for long periods at -20 °C only after snap freezing in liquid nitrogen. Otherwise, protein stored at 4 °C would often precipitate slightly once, but would remain stable at 4 °C for months after removal of precipitant by centrifugation. NMR samples kept in 20 mM MES pH 6.5, 100 mM NaCl were stable and gave almost identical NMR spectra even after over 12 months of storage at 4 °C.

2.9.8 Presumptive Test for Iron

To ascertain the presence of iron, two qualitative tests were performed.

Colourless potassium thiocyanate reacts with Fe^{3+} in solution to form $[\text{Fe}(\text{NCS})(\text{H}_2\text{O})_5]^{2+}$, which has a strong blood-red colour. 20 μL of a 0.1 mM protein sample was treated with 40 μL of 0.2 M potassium thiocyanate.

1,10-phenanthroline in complex with Fe^{2+} turns deep red, and in complex with Fe^{3+} turns light blue. 20 μL of 0.1 mM protein sample was treated with 40 μL of 0.1 M 1,10-phenanthroline in 50% acetone and 10 μL of 0.5 M TCEP.

2.9.9 Inductively Coupled Plasma Optical Emission Spectroscopy

Quantitative metal analysis was performed on a Perkin Elmer Optima 2100 DV inductively coupled plasma optical emission spectrometer (ICP-OES). Protein samples

* Dr C. T. Loh adapted the general protocol used for *in vivo* sample purifications for parallel purification of cell-free samples in consultation with the author. The final protocol was modified to increase yield by the author.

for analysis were exchanged into the analysis buffer (typically 50 mM HEPES, pH 7.5, 100 mM NaCl) via passing through a PD-10 or NAP-5 size exclusion column. Due to foaming caused by nitric acid denaturation of protein, most accurate results were obtained by using masses for dilution factors rather than volumes. Depending on concentration, 500 to 3,000 mg of the eluent were mixed with 590 mg of 69% nitric acid in pre-acid washed glass or plastic ware and incubated for 20 minutes before dilution up to 10 g with Milli-Q grade water. The sample was then passed through a 0.45 μm filter to remove insoluble denatured protein. A blank was also prepared by treating a buffer sample identically.

The instrument was calibrated prior to each run with 0.5, 1.0, 2.0, 5.0 and 10.0 mg/mL solutions of either CCS4 or CCS6 ICP-MS Standard (Inorganic Ventures). A linear standard curve was generated having an $R^2 \geq 0.9999$. Wavelengths for analysis were chosen for best sensitivity and minimal overlap with other peaks (Table 2-21). 1.0 or 2.0 ppm quality controls were measured every 5 to 10 samples to ensure minimal calibration shift.

Table 2-21 Wavelengths used for ICP-OES analysisⁱ

Element	Wavelength (nm)	Element	Wavelength (nm)
Calcium	317.933	Iron	238.204
Cadmium	228.802	Manganese	257.610
Cobalt	228.616	Nickel	231.604
Chromium	261.716	Selenium	196.026
Copper	327.393	Zinc	206.200
Gallium	417.206		

ⁱ optimised by microanalysis staff at RSC, ANU

Results in mg/L would be converted into a molar concentration, then scaled to the dilution factor and protein concentration measured by absorbance at 280 nm on the pre-acid treated sample. Typical analysis for the [FeZn]IMP-1 yielded 0.99 iron ions and 1.01 zinc ions per protein molecule. Typical analysis for the [ZnZn]IMP-1 yielded 0.04 iron ions and 1.98 zinc ions per protein molecule. Only insignificant trace levels of other metals were present in typical preparations.

2.9.10 De-Metallation Trials

Griffin Method

50 mL of 27 μM IMP-1 were treated by four 12 hour dialysis steps against 1 L of 50 mM HEPES, pH 6.8 with 10 mM EDTA at 4 °C, followed by six 12 hour dialysis

steps against 1 L of Chelex* treated 50 mM HEPES, pH 6.8, 50 mM NaCl. The protein sample was then concentrated to 1 mL, had two 20-minute centrifugation steps at 15,000 g applied to remove any precipitated protein, and was subjected to ICP-OES analysis for metal ions.

Yamaguchi Method

The reaction was performed in a 2 mL polypropylene tube that had been soaked in 1 M nitric acid overnight to remove any metal ions then washed with Milli-Q water 20 times. 142.7 μ L of 200 mM EDTA in 50 mM MOPS (pH 6.5), 1.0 M NaCl was added drop-wise to 428 μ L of a 1.2 mM IMP-1 protein sample in 50 mM MOPS (pH 6.5), 1.0 M NaCl, 30% glycerol and incubated with stirring under nitrogen gas at 30 °C for 48 hours.

The sample was then cooled to 4 °C and two 20-minute centrifugation steps at 15,000 g applied to remove any precipitated protein. The supernatant was passed through a PD-10 column pre-equilibrated with 50 mM MOPS (pH 6.5), 1.0 M NaCl, 30% glycerol to remove all EDTA. The protein sample was subsequently concentrated to 1 mL, had two 20-minute centrifugation steps at 15,000 g applied to remove any precipitated protein, and was subjected to ICP-OES analysis for metal ions.

2.9.11 Metal Ion Exchange

20-fold molar excess of 0.1 M CdCl₂, 0.1 M FeCl₃ in 0.1 M HCl or 0.1 M ZnSO₄ was incubated for 5.0 min at room temperature with either [FeZn]IMP-1 or [ZnZn]IMP-1 in 20 mM MES (pH 6.5), 100 mM NaCl. Excess metals were rapidly removed via two steps of desalting by eluting from a NAP-5 column directly onto a PD-10 column to ensure complete removal of all non-bound metal ions. Samples were analysed as per typical ICP-OES samples or mass spectrometry samples.

2.9.12 UV/Vis Absorbance and Fluorescence Spectroscopy

UV/Vis spectra were typically obtained on a NanoDrop ND-1000. Absorbances were measured on 2 μ L samples. The inbuilt 'Normalise' function for A₂₈₀ measurements assumes the absorbance to be zero at 340 nm, which is not an appropriate

* Chelex treatment was applied through a short column as per manufacturer (Bio-Rad) recommendations.

reference for the [FeZn]IMP-1 sample due to an additional absorbance in this range. Results, however, became less reliable when not using the normalisation function. To achieve reproducible results, A_{280} measurements were performed using the UV/Vis option, which normalises to the lowest absorption between 400 and 700 nm. Measurements were made at 1.0 and 0.1 mm pathlengths for concurrent normal and high absorbance measurements.

Alternatively, a SPECTRAmax M2e spectrophotometer was used with a quartz cuvette for 10 mm pathlength absorbance and fluorescence measurements.

2.9.13 Circular Dichroism

Samples for CD analysis were measured on an Advanced Photophysics Chirascan Circular Dichroism instrument with Quantum Northwest TC 125 temperature control unit. Best results were obtained in chloride free 23 mM phosphate buffer, pH 7.0, 19 mM Na_2SO_4 (ionic strength = 0.1 M)²⁶⁹ made from the corresponding acids and bases in 50% D_2O , and purged with nitrogen gas. Measurements were made in a Starna CD quartz cuvette with a 1 mm or 10 mm pathlength, and were averaged from three measurements. Thermal melts were run in a step-wise manner in 2-degree increments. Thermal equilibration of the sample was assumed after holding at each step prior to data acquisition for 30 seconds after the thermocouple on the cuvette holder had reached the desired temperature.

Fitting of thermal denaturation curves was applied using KaleidaGraph 4.1²⁷⁰. Five wavelengths were assessed for each of the regions 186 to 198 nm, and 208 to 220 nm. Each wavelength was fitted individually with the following equation,²⁷⁰

$$\Delta\epsilon = m_1 + \frac{m_2 - m_1}{1 + e^{-\left(\frac{T - T_m}{d_x}\right)}} \quad (2.5)$$

where $\Delta\epsilon$ is the mean residue ellipticity, m_1 is the left asymptote, m_2 is the right asymptote, T is the temperature, T_m is the denaturation temperature, and d_x is the slope at $T = T_m$.

2.9.14 Activity Assay

Activity assays were performed in a multicomponent buffer of 25 mM MES, 25 mM HEPES, 25 mM CHES and with a constant ionic strength of 100 mM (NaCl).²⁶⁹ Acetate and citrate buffers were avoided due to the potential for competition in the

active site. Constancy of the pH was assured by measurement of the buffer sample prior to and after the assay using a microsample pH meter.

Benzylpenicillin substrate (Fluka, $\geq 98\%$ penicillin G sodium salt) was prepared from dry powder as a 4 mM stock in multicomponent buffer at the pH of the assay. Hydrolysis of benzylpenicillin was assayed at 235 nm. Up to 16 concentrations of substrate (31.25 μM to 2 mM) were used for fitting Michaelis-Menten kinetics curves. Protein concentrations of approximately 0.5 to 15 nM were used for [FeZn]IMP-1.

The assays were performed on a SPECTRAmax M2e spectrophotometer with 200 μL per well of a Thermo Scientific Nunc 96 Well UV transparent plate. Substrate and protein solutions were incubated at 37 °C for 10 min prior to rapid mixing and measurement. Initial velocities were measured from initial linear rates (typically from 20 to 100 seconds), using SoftMax Pro software with R-values greater than 0.98.

Michaelis-Menten constants were obtained via fitting the function (2.6) using KaleidaGraph software²⁷⁰ (yielding R-values greater than 0.95).²⁷⁰

$$\frac{V_{\max}[S]}{K_m + [S]} \quad (2.6)$$

An accurate $\Delta\epsilon$ value was not determined for benzylpenicillin in the plate assay format, meaning that it was not possible to determine an accurate k_{cat} value for either enzyme. To obtain an approximate value for k_{cat} , it was assumed that the [ZnZn]IMP-1 enzyme was as active as that reported by Iyobe *et al.*¹⁴² for IMP-1 in subtly different conditions (461 s^{-1}). The k_{cat} value for [FeZn]IMP-1 was then scaled by the same factor to yield an approximate (but accurate relative to [ZnZn]IMP-1) k_{cat} value. It is worth noting that the determined K_m for [ZnZn]IMP-1 in this work was within the margin of error reported by Iyobe *et al.*¹⁴²

2.9.15 X-ray Protein Crystallography

Automated Crystal Condition Screening Runs

Six commercial crystallisation screens from Hampton Research were trialled: Peg/Ion (HR2-139), Grid Screen Salt (HR2-248), Crystal Screen (HR2-130), Peg RX (HR2-086), Salt RX (HR2-136), Index (HRR-134). Each screen of 96 conditions was set up in an Intelli-Plate 96-3 plate using a Genomic Solutions Cartesian Honeybee

Nano Dispensor. Typically, 50 μL reservoir solution was used with 0.5 μL of reservoir and 0.5 μL of 25 to 10 mg/mL protein per sitting drop.

Plates were incubated at 4, 18 or 28 °C for several weeks. Crystal conditions were attempted for both [FeZn]IMP-1 with and without the N-terminal MASMTG cell-free expression tag. Crystal conditions were also attempted in the presence of FeCl_3 .

Manual Crystal Condition Screen

Manual screens were performed around previously published conditions and around conditions identified from the automated run. Typically, 1 μL of 15 to 32 mg/mL protein with 1 μL of reservoir liquid per hanging drop was used over 500 to 1,000 μL mother liquor.

Plates were incubated at 4, 18 or 28 °C for several weeks. Crystal conditions were attempted for both [FeZn]IMP-1 with and without the N-terminal MASMTG T7 expression tag. Crystal conditions were also attempted in the presence of FeCl_3 or an inhibitor (captopril).¹²³⁻¹²⁵

Microseeding was applied by breaking up unusable crystals, pipetting up and down the total hanging drop solution from a partially successful crystallisation condition. The microcrystal suspension was then recovered and serial-diluted into the appropriate reservoir solution. The diluted solution was then used in place of the reservoir liquid in the hanging drop as per the above procedure.

2.9.16 X-ray Diffraction and Structure Refinement

X-ray scattering experiments were performed on the MX1 beamline at the Australian Synchrotron, Victoria, Australia.* Crystals were found to be in the P1 space group, so 360° acquisition of scattering data was required for anomalous difference measurements.

The CCP4²⁷¹ workspace was used to determine the X-ray diffraction structure.[†] iMosflm was used to process the raw image files, followed by analysis of the cell content by Mathews_coeff which gave probabilities of 28 and 57% for 4 and 5

* Diffraction experiments were carried out by Dr P. Carr (RSC, ANU) in consultation with Dr C. Jackson (RSC, ANU) and staff from the Australian Synchrotron.

† The structure was solved and refined by Dr P. Carr (RSC, ANU) in consultation with the author.

molecules per asymmetric unit respectively. Phaser²⁷² was then used for molecular replacement to search for 4 molecules of chain A from PDB 2DOO¹⁸³ per asymmetric unit. Several rounds of refinement were applied using REFMAC5²⁷³ and Coot.²¹¹ The structure of citrate was taken from the PDB (1C5R²⁰⁹). Average *B* factors were calculated using BAVEAGE.

Anomalous scattering experiments were performed at 7,162.0 eV (iron ion edge) and 9,660.0 eV (zinc ion edge). 360° data were acquired for 9,660.0 eV, and 1,080° data were acquired for 7,162.0 eV. BDFMs (Bijvoet difference Fourier maps)²⁷⁴ were calculated using FFT.²⁷⁵ The intensities of the anomalous peaks ($e/\text{\AA}^3$) at the Zn₁ and Zn₂ site were determined using Coot.²¹¹

2.9.17 Protein Structure Analysis and Image Rendering

All protein 3D structures were analysed using PyMOL software.^{276,277} Structural alignments between homologous sequences were carried out on backbone atoms (name CA+C+N+O) by minimising the RMSD iteratively with the ‘align’ command. Reported RMSD values were calculated using the ‘rms_cur’ command between backbone atoms after the iterative ‘align’ command. All RMSD values were only calculated for backbone atoms unless otherwise stated. Angles and distances were either measured between 3 points using the ‘get_angle’ and ‘get_distance’ commands or manually calculated from the PDB file mathematically.

Electron or anomalous scattering density maps were exported from CCP4 with ‘.map.ccp4’ file extensions, and imported into PyMOL. Figures of isosurface lobes depicting the magnitude of PCS due to the $\Delta\chi$ tensor were generated in PyMOL using density maps generated by Numbat.³⁰ Figures with coloured scales utilised the ‘data2bfactor.py’ script²⁷⁸ and the inbuilt ‘spectrum’ command. All 3D protein structures shown in figures were rendered using PyMOL’s inbuilt ray-tracing rendering engine.

Volume and cavity calculations were performed using Voronoia software.²¹² Chain A of the PDB aligned structure was exported from PyMOL as a PDB without water molecules or active site ligands, and imported into Voronoia. Packing density was then calculated including heteroatoms (metals) and surface atoms with the ProtOr radii.²⁷⁹ Due to the small differences being measured, a grid distance of 0.01 Å was

used. The resultant .vol files were then processed, again in Voronoia, to calculate the number of cavities (that can fit a 1.4 Å sphere), and other packing statistics.

2.9.18 NMR Acquisition, Processing and Analysis

All spectra were acquired on either a 600 or 800 MHz Bruker NMR spectrometer with AVANCE II console and TCI cryoprobe. Cell-free samples were measured in a 3 mm tube or a 5 mm Shigemi tube. *In vivo* samples were measured in a 5 mm tube or a 5 mm Shigemi tube. All NMR experiments were performed in 20 mM MES, pH 6.5, 100 mM NaCl at 310 K.

Aged NMR samples were incubated at 37 °C for one to three weeks either in the NMR magnet or in an air incubator in NMR buffer inside a 5 mm NMR tube. The samples were recovered and centrifuged to remove any precipitant and the pH was measured prior to NMR measurement. The NMR buffer was not exchanged or refreshed unless the pH shifted.

Calibration of chemical shift was calculated using the water signal and the Fortran script ‘calibrate’ that implements the chemical shift referencing described by Wishart *et al.*²⁸⁰ The correction was applied during conversion of raw Bruker-type ser files using bruk2pipe²⁸¹ scripts. Raw data were then processed with nmrPipe,²⁸¹ and analysed using ccpNMR Analysis v2.3.1 software.^{282,283} Typical processing scripts applied linear prediction in all indirect dimensions doubling the number of points in the indirect dimensions.

Chemical shift perturbations using a weighted distance score were calculated in ccpNMR Analysis v2.3.1 using the equation:²⁸³

$$\sqrt{\Delta\delta_{1H}^2 + (0.15 \times \Delta\delta_{15N})^2} \quad (2.7)$$

Evidence of PREs was defined by measuring the peak height of the paramagnetic and diamagnetic samples separately. A distant resonance (Glu65 at > 26 Å) was used as a normalisation resonance with an assumed null PRE. Evidence of PREs was shown as the ratio of the normalised paramagnetic intensity divided by the diamagnetic intensity.

The solved X-ray crystal structure of [FeZn]IMP-1 determined in this work was used for $\Delta\chi$ -tensor fitting. Only backbone amide proton shifts were used for $\Delta\chi$ -tensor fitting. Python scripts were written to complete the grid search based $\Delta\chi$ -tensor fits.

First, the script calculated a grid of metal positions at a defined resolution over the protein and then a pyParaTools³⁴ fit for each metal position was applied using the T1M1FM protocol. Any points that did not converge were excluded from further processing. The scripts then wrote out a pdb file of the grid points with the χ^2 value in the *B* factor column and the $\Delta\chi_{ax}$ component in the occupancy column. This ‘grid’ pdb file was then overlaid with the protein structure in PyMOL and visually analysed using a colour gradient scaled to the RMSD score. Alternatively, the grid pdb file was imported into Microsoft Excel and the RMSD value plotted against the distance from the Zn₁ or Zn₂ sites. Two grid searches were performed. A coarse grid with a spacing of 1 Å between points covered the entire protein and a fine grid with a spacing of 0.1 Å was calculated within the region of 5 Å from the two metal sites.

3 Cell-free protein synthesis with $^2\text{H}/^{15}\text{N}/^{13}\text{C}$ -labelled amino acids in H_2O for the production of perdeuterated proteins with ^1H in the exchangeable positions

3.1 Introduction

3.1.1 Perdeuteration

NMR studies of proteins larger than 20 kDa are hindered by low signal-to-noise due to fast relaxation rates caused by slow molecular tumbling. In addition, the larger number of signals results in spectral overlap. Short T_2 relaxation times also cause significant line broadening, which increases the overlap problem. Some of the spectral overlap can be resolved by using multi-dimensional NMR experiments at high magnetic field strengths, however, long pulse sequences are required to exploit the available extra resolution. For magnetisation to persist during longer pulse sequences, perdeuteration is often requisite. Replacing all non-exchangeable protons with deuterium nuclei increases the relaxation times by reducing dipole-dipole relaxation. Consequently, the signal-to-noise ratio is increased and high-resolution constant-time experiments are possible.

A common method of isotope-labelling for NMR is to overexpress the protein of interest in bacteria that are cultured in defined media with ^{13}C -labelled glucose and ^{15}N -labelled ammonium chloride. A high percentage of deuteration is possible by simply replacing the H_2O in the media with D_2O , however, to achieve near complete deuteration, deuterated glucose must also be used. For optimal yields, the bacteria need to be adapted to grow under deuterated conditions by increasing the D_2O content for a series of growth generations and/or selecting optimally expressing colonies from D_2O agar plates.¹⁹² If the purpose is to record NMR experiments such as ^{15}N -HSQC, HNCA, or HNCB spectra, protons must be back-exchanged onto the backbone amides. This can be achieved by denaturing and refolding the protein in an H_2O based buffer, which enables solvent access and spontaneous proton exchange throughout the entire protein.

The proton back-exchange step poses a problem for proteins such as IMP-1 (chapter two) that cannot be refolded in good yield. Hence, exchange of the backbone amide hydrogens is only possible for amino acids that are solvent accessible. An alternative method for perdeuteration is described in this chapter. By using a cell-free protein-synthesis expression system in H₂O with ²H/¹³C/¹⁵N-labelled amino acids, perdeuterated samples of IMP-1 can be prepared, where all amide hydrogens are protons rather than deuterons right from the start and back-exchange is unnecessary.

3.1.2 Cell-Free Protein Synthesis

Cell-free protein synthesis has become an economical and useful technique of protein production for NMR purposes. The technique uses cellular extracts rather than live cells to express the protein of interest. *Escherichia coli* based S30 extracts are commercially available or can be made by lysing cultured cells through a French pressure cell, followed by centrifuging at 30,000 g to remove cellular debris and genomic DNA. Final preparation of the extract is performed via dialysis against a PEG solution to concentrate the extract and remove any small molecules.²⁶⁷

Typical yields of about 1 mg of protein per mL of reaction mixture are obtained in the constant-feed cell-free protein synthesis system described by Apponyi *et al.*²⁶⁷ This system has an inner reaction mixture inside a small dialysis bag immersed in an outer feed buffer. The inner reaction buffer contains the target DNA with a T7 promoter, the cellular S30 extract, tRNA and a eukaryotic ATP regeneration system (creatine kinase). Supplying T7 RNA polymerase is no longer required if BL21(DE3) cells induced with IPTG have been used to prepare the S30 extract. The outer feed buffer is typically 10 times the volume of the inner reaction mixture and constantly replenishes the inner reaction mixture with small molecules and cofactors such as salts, amino acids, ATP, ribonucleotides and folinic acid. It also provides the benefit of diluting any inhibitory molecules formed during the reaction.

Of particular relevance to perdeuteration are enzymatic conversions between amino acids.²⁸⁴ Enzymatic metabolism of the labelled amino acids in an H₂O environment has the potential to dilute the deuterium labelling with protons.²⁸⁵ In the cell-free protein synthesis system, a large number of enzymes responsible for catalysing amino-acid transformations *in vivo* are inactivated, typically by the loss of cofactors. Further inactivation of these enzymes can be achieved by the addition of inhibitors of

specific metabolic reactions,²⁸⁶ but unfortunately these inhibitors are often expensive. Alternatively, bacterial strains have been genetically modified to suppress certain conversion pathways,²⁸⁷ however, these auxotrophic cell lines are often less viable and therefore give lower protein expression yields.

Fortunately, chemical treatment of the entire cellular S30 extract with NaBH₄ has been identified as a low-cost method to almost completely suppress amino-acid conversions.²⁶⁸ The key reaction is reduction of the Schiff base (aldimine) formed in pyridoxal 5'-phosphate (PLP) dependant enzymes.²⁸⁸ These enzymes include all transaminases and many other enzymes responsible for decarboxylations, racemization, eliminations and replacement of α -amino groups.²⁸⁸ While these enzymes are not required for protein synthesis, they catalyse the conversion between amino acids *in vivo*, so inhibition of these pathways is beneficial for maintaining specific isotope labelling in cell-free protein synthesis reactions.²⁶⁸

3.2 Results

3.2.1 Synthesis of Perdeuterated IMP-1

To improve the NMR spectral resolution of IMP-1 (the topic of Chapter Two), production of a ²H/¹³C/¹⁵N-labelled protein was attempted as per section 2.9.5. As the protein could not be refolded, back-exchange of ¹H onto the exchangeable sites was attempted simply by performing all purification steps in H₂O-based buffers. From the peaks measured in a ¹⁵N-HSQC spectrum of the sample, it was evident that complete back-exchange had not occurred (Figure 3-1). Complete back-exchange was still not achieved in a ²H/¹³C/¹⁵N sample stored at 4 °C in a H₂O buffer for over 1 year (data not shown).

In an attempt to obtain more complete back-exchange of ¹H onto the exchangeable positions, a 2 mL cell-free protein synthesis expression of IMP-1 with 20 uniformly ²H/¹³C/¹⁵N-labelled amino acids (20AA) was performed.* The protein expressed with high yield and was purified. The expression yielded 1.8 mg of concentrated, purified protein (Figure 3-2).

* All cell-free protein synthesis reactions for this chapter were performed by Dr C.-T. Loh in consultation with the author

An expression was also trialled using the cheaper algal amino-acid mixture (AlgalAA), supplemented with the four amino acids missing from the mixture (Asn, Gln, Cys and Trp). This sample, however, produced only poor yields (Figure 3-2).

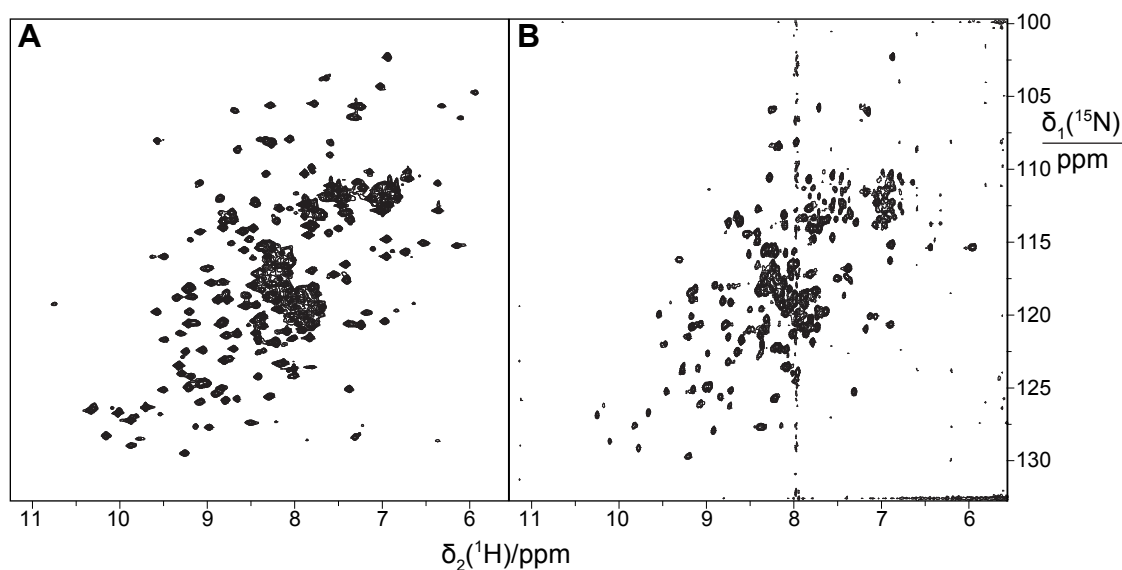


Figure 3-1 A) $^{15}\text{N}, ^1\text{H}$ -HSQC spectrum of $^{13}\text{C}/^{15}\text{N}$ -labelled IMP-1 and B) $^{15}\text{N}, ^1\text{H}$ -TROSY spectrum of $^2\text{H}/^{13}\text{C}/^{15}\text{N}$ -labelled IMP-1. Both samples were prepared using *in vivo* methods. Although the peak shape is narrower in the perdeuterated sample, many peaks are weak or missing, indicating incomplete back-exchange of ^1H . Even storage of the perdeuterated sample at 4 °C in an H_2O buffer for over 1 year did not significantly increase the amount of back exchange (data not shown).

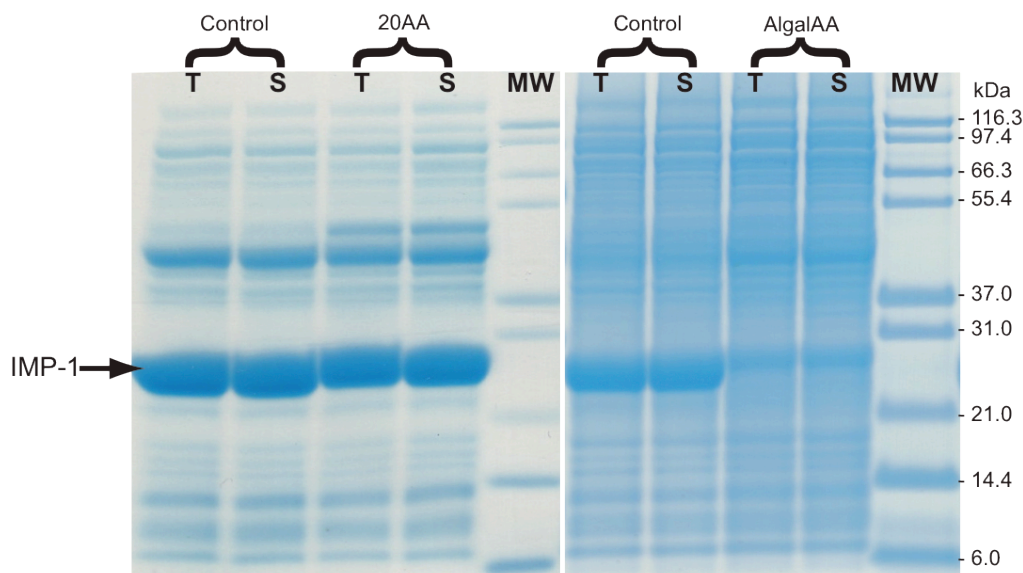


Figure 3-2 15% SDS-PAGE of total (T) and soluble (S) fractions from cell-free expressions of IMP-1 using either 20 individual $^2\text{H}/^{13}\text{C}/^{15}\text{N}$ -labelled amino acids (20AA) or the algal amino-acid mixture supplemented with cysteine, asparagine, glutamine and tryptophan (AlgalAA). Control samples were performed using 20 individual unlabelled amino acids.

3.2.2 NMR Analysis

$[\text{}^{15}\text{N}, \text{}^1\text{H}]$ -TROSY spectra were recorded for both of the 20AA and AlgalAA perdeuterated samples (Figure 3-3). It was evident that the cell-free protein synthesis method produced high quality spectra and that all the backbone resonances observed for a $\text{}^1\text{H}/\text{}^{15}\text{N}$ -labelled *in vivo* sample were present without the need for refolding. While the AlgalAA sample produced enough protein for 2D NMR, it required 10 hours to record the spectrum in Figure 3-3B due to the low yield of protein from the cell-free extract. In contrast, the 20AA sample gave well-resolved and high-signal-to-noise NMR spectra after only 30 minutes.

A TROSY-HNCA experiment was performed on the 20AA sample. To assess the extent of $\text{C}\alpha$ protonation, the standard Bruker pulse sequence (trhncaetgp2h3d) was modified to remove the proton decoupling pulse during the $\text{C}\alpha$ evolution time. The strongest and most resolved peak for each amino-acid type was identified and the degree of proton substitution at the $\text{C}\alpha$ position was determined by integration of the two 3D satellite peaks arising from the $^1J_{\text{HC}}$ coupling. Percentage protonation estimated for each amino-acid type is listed in Table 3-1.

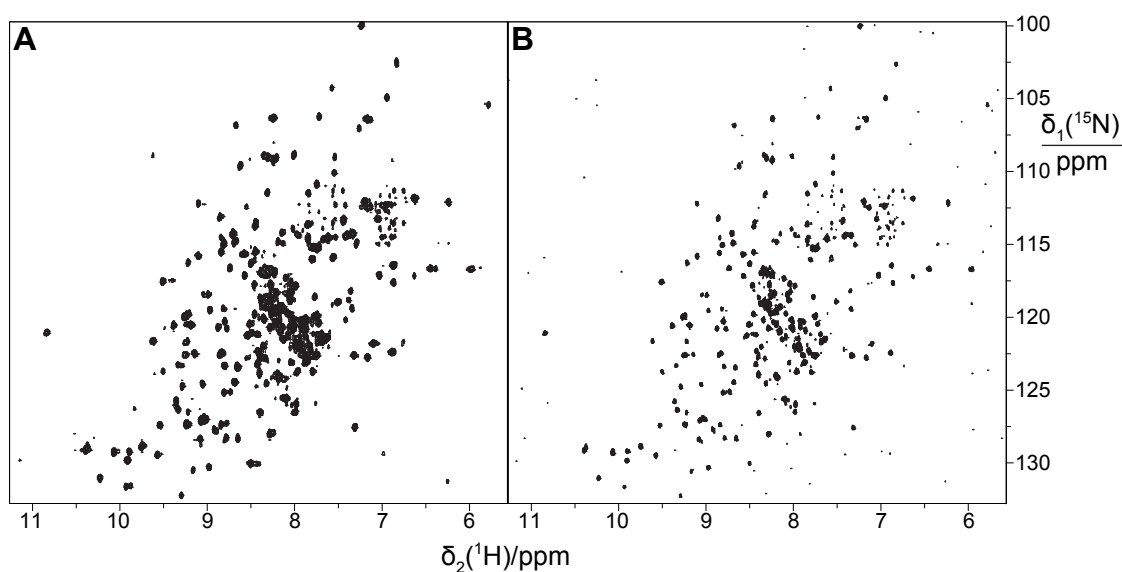
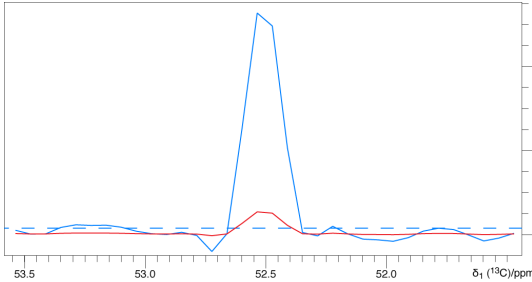
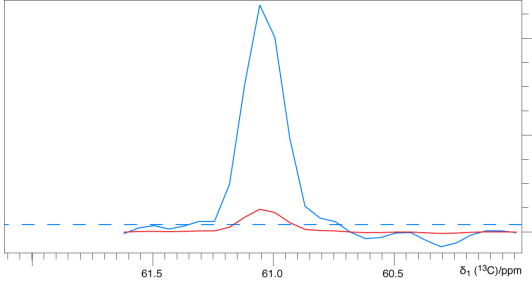
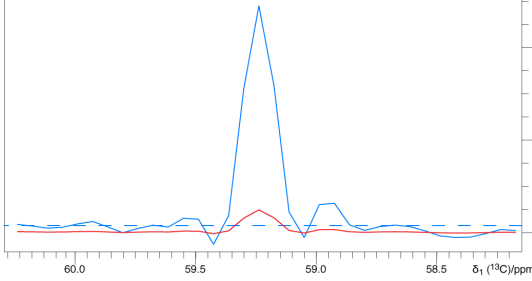
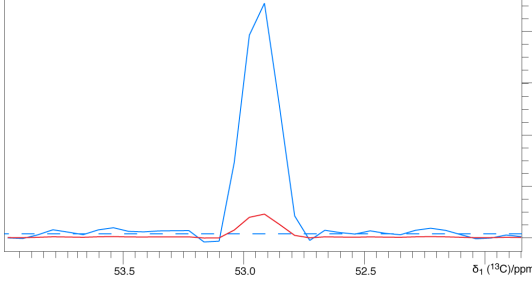
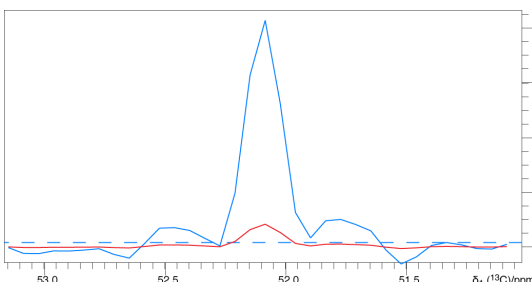
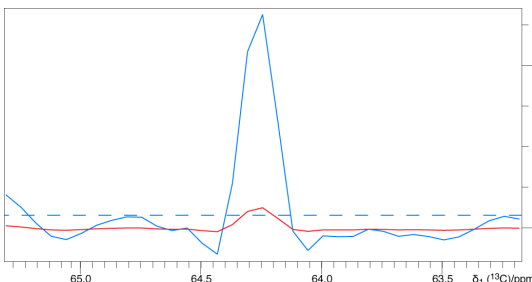


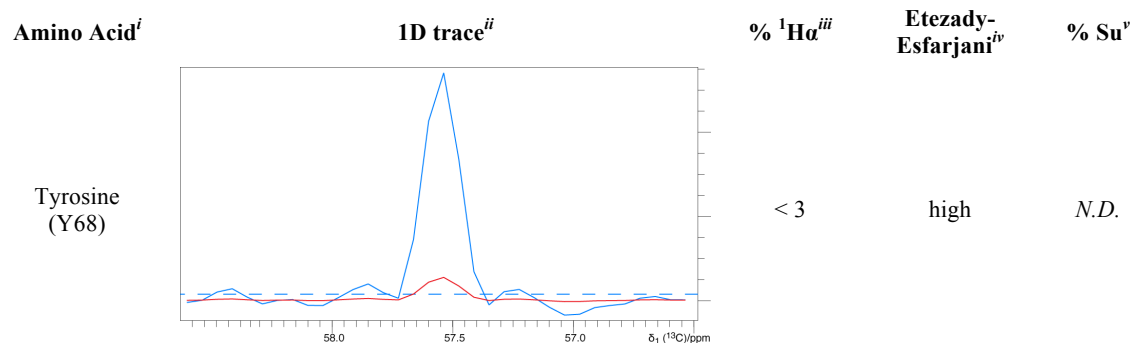
Figure 3-3 $[\text{}^{15}\text{N}, \text{}^1\text{H}]$ -TROSY spectra of perdeuterated IMP-1 prepared by different cell-free reactions. A) Spectrum of the 20AA sample recorded in 30 min. This spectrum shows all the peaks observed in the $\text{}^1\text{H}/\text{}^{15}\text{N}$ -labelled sample prepared *in vivo* in H_2O . B) Spectrum of the AlgalAA sample recorded in 10 hours. This spectrum also displays a complete set of cross-peaks, but the low protein yield obtained in the cell-free reaction affected the NMR sensitivity.

Table 3-1 Percentage proton substitution onto Ca

Amino Acid ⁱ	1D trace ⁱⁱ	% ¹ H α ⁱⁱⁱ	Etezady-Esfarjani ^{iv}	% Su ^v
Alanine (A98)		< 3	high	0.4
Cysteine (C158)		8	high	N.D.
Aspartic acid (D6)		< 3	very high	2.1
Glutamic acid (E150)		< 3	very high	3.0
Phenylalanine (F63)		< 3	high	4.2
Glycine (G120) ^{vi}		< 3	high	1.0

Amino Acid ⁱ	1D trace ⁱⁱ	% ¹ H α ⁱⁱⁱ	Etezady-Esfarjani ^{iv}	% Su ^v
Histidine (H19)		< 3	low	N.D.
Isoleucine (I9)		< 3	medium	N.D.
Lysine (K54)		7	medium	N.D.
Leucine (L4)		< 3	medium	N.D.
Methionine ^{vii}	N.D.	-	low	N.D.
Asparagine (N122)		13	very high	0.5
Proline (P95) ^{ix}		< 3	N.D.	N.D.

Amino Acid ⁱ	1D trace ⁱⁱ	% ¹ H α ⁱⁱⁱ	Etezady-Esfarjani ^{iv}	% Su ^v
Glutamine (Q113)		< 3	very high	3.0
Arginine (R92)		< 3	medium	N.D.
Serine (S117)		14	high	1.0
Threonine (T96)		6	low	N.D.
Valine (V16)		6	medium	N.D.
Tryptophan (W124)		< 3	high	4.0



ⁱ Amino acid measured indicated in parenthesis

ⁱⁱ 1D traces (blue solid line) were selected to emphasise satellite peaks and were often not directly through the centre of the main peak. This means that substitution may appear exaggerated in the 1D traces. For reference, the red solid 1D trace is equivalent to 10% of the blue trace, and the dashed blue line is twice the estimated noise level. Vertical scale is relative between peaks.

ⁱⁱⁱ Percentage of protonation on the C α of each amino acid as estimated by volume measurement of C α satellites in the TROSY-HNCA spectrum. All amino acids were supplied with 97 to 99% deuteration, so any result below 3% is insignificant. ¹J_{C α -H α} coupling constants for all significant protonation samples were about 125 \pm 15 Hz (spectral resolution of 20 Hz).

^{iv} Degree of protonation of the C α as reported by Etezady-Esfarjani *et al.*²⁸⁵

^v Percentage of protonation on the C α of each amino acid as reported by Su *et al.*²⁶⁸ for amino acids treated with reduced S30 extract. These values do not include the contribution to protonation present in the commercially available amino acids (up to 3%). N.D.: Not detected or reported.

^{vi} Glycine C α peaks are negative in sign in the Bruker trhncaetgp2h3d NMR experiment. The 1D trace has been inverted to facilitate comparison.

^{vii} No methionine signals were observed for IMP-1 in the TROSY-HNCA NMR experiment

^{ix} The proline signal for Pro95 was observed via the *i*-1 peak of Thr96

3.2.3 Cost analysis

The costs of the different labelled materials as advertised by CIL²⁸⁹ are listed in Table 3-2. From this table it can be calculated that the labelled components for a 100 mL *in vivo* ²H/¹³C/¹⁵N-labelled IMP-1 sample for NMR using the method described in section 2.9.2 would cost approximately US\$540 with ¹³C-labelled glucose or US\$800 using ²H/¹³C-labelled glucose. Conversely, the labelled components used for the sample prepared via cell-free synthesis with individual ²H/¹³C/¹⁵N-labelled amino acids would have cost a little under US\$505 (\$252 per mL).

Table 3-2 Cost of isotope labelled components required for perdeuteration of proteins (Jan 2014)

Component	Product code	Amount (g)	Cost ⁱ
<i>in vivo</i>			
¹⁵ N ammonium chloride	NLM-467-1	1.0	\$48
¹³ C glucose	CLM-1396-1	1.0	\$194
² H/ ¹³ C glucose	CDLM-3813-1	1.0	\$454
² H ₂ O	DLM-4-99-1000	1000.0	\$680
cell-free protein synthesis components			
² H/ ¹³ C/ ¹⁵ N L-alanine	CDNLM-6800	0.25	\$1,099
² H/ ¹³ C/ ¹⁵ N L-cysteine	CDNLM-6809	0.25	\$1,643
² H/ ¹³ C/ ¹⁵ N L-aspartic acid	CDNLM-6803	0.25	\$722
² H/ ¹³ C/ ¹⁵ N L-glutamic acid	CDNLM-6804	0.25	\$785
² H/ ¹³ C/ ¹⁵ N L-phenylalanine	CDNLM-6811	0.25	\$1,529
² H/ ¹³ C/ ¹⁵ N glycine	CDNLM-6799	0.25	\$474
² H/ ¹³ C/ ¹⁵ N L-histidine:HCl:H ₂ O	CDNLM-6806	0.25	<i>Not advertised</i> ⁱⁱ
² H/ ¹³ C/ ¹⁵ N L-isoleucine	CDNLM-6807	0.25	\$1,213
² H/ ¹³ C/ ¹⁵ N L-lysine:2HCl	CDNLM-6810	0.25	\$1,529
² H/ ¹³ C/ ¹⁵ N L-leucine	CDNLM-6808	0.25	\$1,097
² H/ ¹³ C/ ¹⁵ N L-methionine	CDNLM-6798	0.25	<i>Not advertised</i> ⁱⁱ
² H/ ¹³ C/ ¹⁵ N L-asparagine:H ₂ O	CDNLM-6802	0.25	\$1,485
² H/ ¹³ C/ ¹⁵ N L-proline	CDNLM-6812	0.25	\$1,560
² H/ ¹³ C/ ¹⁵ N L-glutamine	CDNLM-6805	0.25	\$1,559
² H/ ¹³ C/ ¹⁵ N L-arginine:HCl	CDNLM-6801	0.25	\$1905
² H/ ¹³ C/ ¹⁵ N L-serine	CDNLM-6813	0.25	\$1,097
² H/ ¹³ C/ ¹⁵ N L-threonine	CDNLM-6814	0.25	\$1,675
² H/ ¹³ C/ ¹⁵ N L-valine	CDNLM-6817	0.25	\$1,097
² H/ ¹³ C/ ¹⁵ N L-tryptophan	CDNLM-6816	0.25	\$2,888
² H/ ¹³ C/ ¹⁵ N L-tyrosine	CDNLM-6815	0.25	\$1,560

ⁱ cost in US\$ on 13 January 2014

ⁱⁱ prices for histidine and methionine are not listed on the CIL website. For cost analysis estimates, these were overestimated to be \$4,000 for 0.25 g.

3.3 Discussion

3.3.1 Cell-Free Protein Synthesis

Labelling with 20 Individual $^2\text{H}/^{13}\text{C}/^{15}\text{N}$ Amino Acids

Isotope labelling with the 20 individual $^2\text{H}/^{13}\text{C}/^{15}\text{N}$ -labelled amino acids (20AA) produced almost the same yields as an unlabelled control. This confirms that amino acids labelled with ^2H , ^{13}C or ^{15}N do not compromise the protein synthesis system if it is based on a conventional S30 extract treated with NaBH_4 . In contrast to *in vivo* systems, where optimal yields depend on using bacteria that have been conditioned to grow in D_2O , the S30 extract does not need to be conditioned to perform optimally with deuterated amino acids.

Supplemented Algal Amino-Acid Mixture

Even after supplementing the algal amino-acid mixture with asparagine, glutamine, cysteine and tryptophan (AlgalAA), this approach resulted in poor protein yields. This is most likely due to the cell-free protein synthesis reaction running out of one or more amino acids. The amino-acid composition of the algal amino-acid mixture is listed in Table 3-3.

It is worth noting that the algal amino-acid mixture had an amino-acid content of only 77.4%,* so that the final concentration of amino acids present in the cell-free protein synthesis reaction was in fact lower than initially anticipated. From Table 3-3, it can be seen that 7 of the 16 amino acids in the algal amino-acid mixture were supplied at less than 80% of the minimal amino-acid concentration recommended by Apponyi *et al.*,²⁶⁷ and at least 5 were present at less than 55% of the recommendations.

As the S30 extract is treated with NaBH_4 to limit proton exchange particularly onto the $\text{C}\alpha$ or $\text{C}\beta$ atoms, the cell-free S30 extract cannot rely on residual PLP-cofactor-dependent transaminase activity to correct for any imbalance of amino-acid concentration. Supplementing the mixture by adding individual amino acids so that no single amino acid is limiting could potentially rectify this, however, since the key

* Algal amino-acid mixture (CDNLM-2496-0) certificate of analysis for lot PR-19646, CIL

motivation for using the algal amino-acid mixture is to avoid the high cost of purchasing individual amino acids, this is clearly not ideal.

Future experiments should take the issue of limited amino-acid availability into account by increasing the amount of algal amino-acid mixture supplied to the cell-free protein synthesis reaction by at least 1.6 fold to 2.5 mg/mL of reaction and feed buffers.* This increase would provide all the amino acids except for methionine and phenylalanine at greater than 80% of the Apponyi *et al.*²⁶⁷ recommendations (Table 3-3). These two amino acids could be supplemented along with the four missing amino acids.

It is worth noting that the use of algal amino-acid mixture without supplementation may well be useful for uniform labelling of $^{13}\text{C}/^{15}\text{N}$ samples not requiring deuteration, as the PLP enzymes would not need to be inhibited and interconversion between amino acids by the transaminases could be allowed to occur freely. This has been previously discussed by Yokoyama *et al.* who found that by performing a cell-free protein synthesis reaction with additional ^{15}N -labelled ammonium acetate, ($^{13}\text{C}/^{15}\text{N}$ -labelled indole, sodium sulfide, PLP and acetyl coenzyme A, they could express proteins from the algal amino-acid mixture without needing to add the four missing amino acids.²⁹⁰ Using this system they were able to recover yields of uniformly $^{13}\text{C}/^{15}\text{N}$ -labelled protein close to that obtained using individual amino acids, at approximately 15% and 38% cost saving for uniformly ^{15}N - and $^{13}\text{C}/^{15}\text{N}$ -labelled samples, respectively.

* It is noted that solubility issues arise when making amino-acid stocks. Dissolving 27.5 mg of algal amino-acid mixture directly in 10 mL of the premade feed buffer prior to pH adjustment rather than making the amino acids in a separate stock can resolve this.

Table 3-3 Amino-acid content in the algal amino-acid mixture

Amino Acid	Molar% ⁱ	Mass% ⁱⁱ	mmol/g ⁱⁱⁱ	Conc. (x 1.6) ^{iv}	Apponyi ^v
Alanine	11.6	9.7	0.78	1.18 (1.89)	1.00
Cysteine ^{vi}	-	-	-	1.00	0.35
Aspartic acid	9.7	12	0.65	0.99 (1.58)	1.00
Glutamic acid	8.8	12	0.59	0.89 (1.43)	1.00
Phenylalanine	1.5	2.4	0.10	0.16 (0.25)	0.35
Glycine	7.8	5.5	0.53	0.80 (1.28)	1.00
Histidine	0.8	1.1	0.05	0.08 (0.13)	0.15
Isoleucine	3.4	4.3	0.23	0.35 (0.56)	0.15
Lysine	8.1	11.1	0.54	0.82 (1.32)	1.00
Leucine	7.2	8.9	0.49	0.74 (1.18)	1.00
Methionine	1.5	2	0.10	0.15 (0.24)	1.00
Asparagine ^{vi}	-	-	-	1.00	0.35
Proline	3.0	3.3	0.20	0.31 (0.49)	0.15
Glutamine ^{vi}	-	-	-	1.00	1.00
Arginine	4.3	7	0.29	0.44 (0.70)	0.35
Serine	5.0	4.9	0.34	0.51 (0.81)	1.00
Threonine	5.6	6.2	0.38	0.57 (0.91)	0.15
Valine	5.0	4.9	0.34	0.51 (0.81)	1.00
Tryptophan ^{vi}	-	-	-	1.00	0.05
Tyrosine	2.6	4.3	0.17	0.26 (0.42)	0.05

ⁱ Molar ratio of amino acids present in lot PR-19646 for the algal amino-acid mixture (CDNLM-2496-0).

ⁱⁱ Mass ratio of amino acids present in lot PR-19646 for the algal amino-acid mixture (CDNLM-2496-0).

ⁱⁱⁱ mmol of amino acid per gram of algal amino-acid mixture. Calculated with a correction applied for amino-acid content (77.4%) of the mixture, and increased amino-acid masses due to isotope labelling.

^{iv} Concentration in mM of amino acid present in the algal amino-acid cell-free reaction performed in this work. This was equivalent to 1.5 mg/mL of reaction and feed buffer. Concentration in parenthesis refers to the concentration using 2.5 mg of algal amino-acid mixture per mL of reaction and feed buffer, as recommended in this work.

^v Recommended amino-acid concentration in mM in Apponyi *et al.*²⁶⁷

^{vi} The amino acids cysteine, asparagine, glutamine and tryptophan were not present in the algal amino-acid mixture and were supplied independently at 1 mM concentration

3.3.2 NMR Analysis

NMR analysis of the C α protonation via the $^1J_{\text{HC}}$ satellites in the TROSY-HNCA experiment indicated that the cell-free reaction still allowed proton exchange at the C α position of some amino-acid types. The degree of deuterium labelling in the $^2\text{H}/^{13}\text{C}/^{15}\text{N}$ -labelled amino acids supplied by CIL are reported to be 97% to 99%. Therefore, satellite peaks with volumes of 3% of the main peak could not be regarded as significant and do not indicate metabolism by the cell-free extract. This applies for the amino acids alanine, aspartic acid, glutamic acid, phenylalanine, glycine, histidine, isoleucine, leucine, proline, glutamine, arginine, tryptophan and tyrosine (methionine was not observed). However, the integration of the satellite peaks suggests some additional degree of C α protonation for the remaining amino acids.

Integration of the satellite peaks of threonine (T112), valine (V16) and lysine (K54) suggested a C α protonation level of 6%, 6% and 7%, respectively, corresponding to about 3-4% proton substitution beyond the ^1H contamination reported by the manufacturer. Cysteine (C158) was measured to have 8% C α protonation, but this measurement is not reliable due to the poor signal-to-noise ratio of the single cysteine peak in the IMP-1 spectrum. Serine (S117) and asparagine (N122) displayed higher levels of protonation of the C α position at 14% and 13%, respectively.

Significant discrepancies between a previous study of C α protonation level²⁶⁸ and this work were unexpected and may be attributed to small differences in methodical approach. Even though careful quantitative NMR measurements are possible, the poor signal-to-noise ratio of the cross-peaks of some residues and the limited spectral resolution of the indirect ^{13}C dimension compromised the accuracy of the integral method used in this chapter. In the report by Su *et al.*,²⁶⁸ proton substitution was determined by performing a mock cell-free protein synthesis reaction using an amino-acid mixture without DNA present, but the mock reaction was performed for only half the time of a regular experiment and therefore potentially underestimated the degree of protonation. In addition, the earlier work used ^{13}C - ^1H cross-peaks of the residual 50 mM HEPES buffer from the cell-free protein synthesis reaction as internal reference to determine the concentration of the protonated amino acids, which could be less accurate than the direct comparison with the ^{15}N - ^{13}C -cross-peak of the C α - ^2H groups used in the present work. Finally, peak overlaps prevented the individual measurement of glutamate, lysine and arginine concentrations. It was assumed that lysine and arginine showed no significant protonation,²⁸⁵ but in this present work proton substitution of lysine exceeded that of glutamic acid. Serine and tyrosine peaks also overlapped in the previous study by Su *et al.*, preventing explicit assessment of these amino acids. Finally, no ^{13}C -HSQC peaks were observed for cysteine, histidine, isoleucine, leucine, proline, threonine or valine.

A better method in future studies could run a similar mock cell-free protein synthesis reaction for the full experimental time, followed by freeze-drying of the outer medium and redissolving in a minimal amount of D_2O . This concentrated sample could then be assessed by quantitative 1D ^{13}C -NMR without proton decoupling. Integration of the satellite peaks and comparison with the centre peak would give an independent percentage of proton substitution. If the resolution of the directly detected ^{13}C

experiment is insufficient, the amino acids could be separated by HPLC prior to NMR measurement.

Perdeuterating IMP-1 using the cell-free protein synthesis protocol described in this chapter produced higher quality spectra with narrower peak shapes than the *in vivo* sample even though the *in vivo* sample produced a more concentrated protein sample (Figure 1 of the attached application note). This can be attributed to the additional line-broadening arising from incomplete deuteration of the side-chain carbons in the *in vivo* sample, due to the use of uniformly ^{13}C -labelled glucose rather than $^2\text{H}/^{13}\text{C}$ -labelled glucose.

Regardless of the discrepancies between the Su *et al.* study²⁹¹ and the present work, it is clear that the NaBH_4 treatment of the cell-free S30 extract significantly reduces the extent of amino-acid metabolism, effectively minimises proton substitution at the C_α position, and produces higher levels of perdeuteration than *in vivo* expressions in D_2O that use ^{13}C -labelled glucose.

3.3.3 Cost Analysis

Although the initial cost of purchasing the individual $^2\text{H}/^{13}\text{C}/^{15}\text{N}$ -labelled amino acids for the cell-free protein synthesis system may appear high, it is in fact comparable to the cost of labelled components in an efficient, high-yielding *in vivo* expression system. Considering the benefits of the cell-free protein synthesis system, such as simplified purification and improved time-efficiency, perdeuterating proteins for NMR *via* cell-free protein synthesis is an economically viable and indeed attractive alternative.

It should be highlighted that the cost analysis performed in this chapter only compared the isotope-labelled materials, ignoring the costs associated with all other aspects of *in vivo* expression or the cell-free protein synthesis (such as generating the S30 extract). This simplification is reasonable though, as the most significant cost in either system is the isotope-labelled materials.

If the previously discussed problems with the algal amino-acid mixture could be resolved by simply increasing the amount of mixture provided to the cell-free synthesis reaction, this would further reduce costs and simplify the preparation of cell-free stock solutions. Using 2.5 mg of algal amino-acid mixture per mL of the reaction and feed-buffer solutions, along with supplementing 0.05 mM tryptophan, 0.1 mM methionine,

0.1 mM phenylalanine, 0.35 mM cysteine, 0.35 mM asparagine and 1 mM glutamine, would cost \$92/mL,^{*} a potential saving of 63% compared to using individual amino acids alone.

Finally, it is noted that CIL also offer a '20 amino-acid mix for cell-free' (catalogue number CDNLM-6784-0.5) at an advertised price of US\$2887 per 0.5 g. This mixture is similar to the algal amino-acid mixture in as much as the majority of the amino acids are derived from an algal source. Communication with CIL confirms that this mixture has all 20 amino acids in the molar ratio listed in Table 3-4. If 33 mg of this amino-acid mixture could be used per mL cell-free reaction (including 10 mL feed buffer), only three of the amino acids would be present at less than 80% of the recommended amount. Supplementing this mixture with less than 0.1 mM phenylalanine, 0.25 mM glutamine and 0.7 mM methionine would bring it to within 20% of the recommendations by Apponyi *et al.*²⁶⁷. Costs associated with this would equate to \$238/mL,[†] which is slightly cheaper than the system based on individual amino acids.

^{*} \$50 for 27.5 mg of algal amino-acid mixture (\$907 per 0.5 g), \$3 for 0.2 mg of tryptophan (\$2888 per 0.25 g), \$6 for 0.4 mg of methionine (~\$4000 per 0.25 g), \$2 for 0.4 mg of phenylalanine (\$1529 per 0.25 g), \$7 for 1 mg of cysteine (\$1643 per 0.25 g), \$7 for 1.2 mg of asparagine (\$1485 per 0.25 g), \$17 for 3.5 mg of glutamine (\$1559 per 0.25 g)

[†] \$190 for 33 mg of the 'cell-free' amino-acid mix (\$2887 per 0.5 g), \$2 for 0.4 mg of phenylalanine (\$1529 per 0.25 g), \$6 for 0.9 mg of glutamine (\$1559 per 0.25 g) and \$40 for 2.5 mg of methionine (overestimate of \$4000 per 0.25 g)

Table 3-4 Amino-acid composition of the ‘20 amino-acid mix for cell-free’

Amino Acid	Molar% ⁱ	Mass% ⁱⁱ	mmol/g ⁱⁱⁱ	Conc. ^{iv}	Apponyi ^v
Alanine	11.6	8	0.677	2.05	1.00
Cysteine	1.9	3.3	0.111	0.34	0.35
Aspartic acid	10	9.9	0.584	1.77	1.00
Glutamic acid	10	11.2	0.584	1.77	1.00
Phenylalanine	1.4	1.7	0.082	0.25	0.35
Glycine	7.4	4.2	0.432	1.31	1.00
Histidine	0.8	0.9	0.047	0.14	0.15
Isoleucine	3.4	3.5	0.198	0.60	0.15
Lysine	7.4	8.6	0.432	1.31	1.00
Leucine	7.2	7.5	0.420	1.27	1.00
Methionine	1.6	1.8	0.093	0.28	1.00
Asparagine	5.6	5.6	0.327	0.99	0.35
Proline	3.4	3	0.198	0.60	0.15
Glutamine	4.1	4.6	0.239	0.73	1.00
Arginine	4.2	5.7	0.245	0.74	0.35
Serine	4.8	3.8	0.280	0.85	1.00
Threonine	5.7	5.2	0.333	1.01	0.15
Valine	4.8	4.5	0.280	0.85	1.00
Tryptophan	2.3	3.6	0.134	0.41	0.05
Tyrosine	2.4	3.3	0.140	0.42	0.05

ⁱ Molar ratio of amino acids present in lot PR-19629 of the ‘20 amino-acid mix for cell-free’ (CDNLM-6784-0).

ⁱⁱ Mass ratio of amino acids present in lot PR-19629 of the ‘20 amino-acid mix for cell-free’ (CDNLM-6784-0).

ⁱⁱⁱ mmol of amino acid per gram of ‘20 amino-acid mix for cell-free’. Calculated with a correction applied for amino-acid content (83.4%) of the mixture, and increased amino-acid masses due to isotope labelling.

^{iv} Concentration in mM of amino acid present for a cell-free protein synthesis reaction supplied with 3 mg/mL ‘20 amino-acid mix for cell-free’ (i.e. 33 mg for a 1 mL reaction with a 10 mL feed buffer).

^v Recommended amino-acid concentration in mM in Apponyi *et al.*²⁶⁷

3.4 Conclusions

This work shows that using the cell-free protein expression method for the production of perdeuterated proteins for NMR is of particular value for proteins that are difficult to refold. While the direct cost of ²H/¹³C/¹⁵N-labelled amino acids for the cell-free protein synthesis experiment initially appears prohibitive, a considered cost analysis finds this method economically on par with other methods. A brief analysis of costs associated with the use of supplemented amino-acid mixes suggests the potential for further significant savings, but a more thorough experimental investigation is required to confirm this.

The cell-free protein synthesis system described here takes less time, simplifies product purification and produces more completely deuterated amino-acid side-chains while the backbone amides retain protons. Although particularly useful for proteins that are difficult to refold, this method could also be recommended for perdeuterating any protein for NMR.

3.5 Methodology

3.5.1 Protein Synthesis

The construct used for expression of the IMP-1 metallo- β -lactamase protein included an N-terminal MASMTG expression tag in the pET47b(+) vector as described in section 2.9.1.

Protein synthesis by *in vivo* methods was performed as per section 2.9.2. Cell-free protein synthesis followed the protocol of Apponyi *et al.*²⁶⁷ with the addition of NaBH₄ treatment to inhibit PLP-cofactor dependant enzymes,²⁶⁸ and supplying the reaction with 10 μ M ZnSO₄ to promote the formation of the [ZnZn] form of IMP-1.

The amino acids used were either individual ²H/¹³C/¹⁵N-labelled amino acids, part of a ²H/¹³C/¹⁵N-labelled amino-acid mixture (algal amino-acid mix) or amino acids at natural isotopic abundance. Control and individual ²H/¹³C/¹⁵N-labelled amino acids were supplied to the cell-free protein synthesis reaction at 1 mM concentration each. The algal amino-acid mixture was supplied at 1.5 mg/mL (inner and outer buffers) and supplemented with 1 mM cysteine, asparagine, glutamine and tryptophan. All labelled amino acids and amino-acid mixtures were purchased from Cambridge Isotope Laboratories (CIL).

Protein samples were purified via a short (10 mL) cation exchange column as per section 2.9.6.

3.5.2 NMR Acquisition and Analysis

NMR experiments were performed on a Bruker 800 MHz NMR Spectrometer with TCI cryoprobe. Samples were measured in 20 mM MES buffer (pH 6.5), 100 mM NaCl in a 5 mm Shigemi tube.

NMR spectra were processed using nmrPipe software²⁸¹ with a cosine apodisation function and no linear prediction. Integration of satellite peaks was performed on 3D spectra, using ccpNMR Analysis v2.2.2.^{282,283} Peaks were centred using Lorentzian peak fitting and the volume measured using the truncated box sum^{*}

^{*} The truncated box sum adds points consecutively within a given range (box) from the peak centre unless the intensity begins to rise again (i.e. due to an overlapping peak).

(box width ^1H : 50 Hz, ^{13}C : 120 Hz, ^{15}N : 120 Hz). The volume of each satellite was added and then a percentage of total protein calculated as per:

$$\frac{\sum(V_{\text{satellites}})}{\sum(V_{\text{all}})} \quad (3.1)$$

To maximise the accuracy of the measurement, only the most intense and resolved peak for each amino-acid type was measured.

3.5.3 Cost analysis

The estimated cost of uniform labelling *in vivo* was based on the use of 500 mL D_2O , 1.0 g of glucose and 0.1 g of ammonium chloride. This is enough for a 100 mL expression media with 400 mL starter culture, but does not include the labelled materials for adapting the bacteria to D_2O growth, or any other materials required.

The estimated cost of uniform labelling in the cell-free system was based on the use of 1 mM of each amino acid in a total volume of 22 mL. The mass was calculated to account for counterions and isotope labelling; for example, the mass of L-lysine:2HCl is approximately 220 g/mol (128 g/mol + 20 g/mol for the labels + 2 x 36.5 g/mol for 2HCl), so to attain 22 mL of a 1 mM solution, less than 4.8 mg is needed, which equates to a total cost of \$29.60. In the case of two amino acids where an exact price was not available, an overestimate of \$4,000 per 0.25 g was used. Calculations did not include the costs associated with making the S30 extract or any other materials required.

3.6 Reproduction of the Submitted Application Note

Carruthers, T.; Loh, C.-T.; Otting, G. (2013) Cell-free protein synthesis with $^2\text{H}/^{15}\text{N}/^{13}\text{C}$ -labeled amino acids in H_2O for the production of perdeuterated proteins with ^1H in the exchangeable positions. *Application Note for CIL*

Dr C. T. Loh was responsible for preparing and performing the cell-free synthesis reaction. I was responsible for the generation of genetic material for cell-free synthesis, providing recommendations for modifications to the cell-free protein synthesis for IMP-1, protein purification, NMR acquisition and analysis, and figure generation for the final manuscript. Prof. G. Otting wrote the manuscript, with editing advice provided by all authors.

Cell-free protein synthesis with $^2\text{H}/^{15}\text{N}/^{13}\text{C}$ -labeled amino acids in H_2O for the production of perdeuterated proteins with ^1H in the exchangeable positions

Thomas Carruthers, Choy-Theng Loh and Gottfried Otting

Research School of Chemistry, Australian National University, Canberra, ACT
0200, Australia

Perdeuteration is essential for NMR studies of big and immobile proteins (> 40 kDa) to slow down the relaxation rates of the remaining ^1H NMR signals. Uniformly $^2\text{H}/^{15}\text{N}/^{13}\text{C}$ -labeled proteins are typically produced by growing *E. coli* in minimal medium with ^{13}C -glucose as the only carbon source, ^{15}N -ammonium salts as the only nitrogen source, and perdeuteration achieved simply by making up the medium with D_2O instead of water. As the resulting protein product is uniformly labeled with ^2H , observation of the backbone amides by ^1H NMR requires prior ^2H - ^1H back-exchange of the amide hydrogens. This poses a dilemma for proteins that do not tolerate ^2H - ^1H back-exchange. For example, the hydrogen-exchange of amide deuterons buried in the interior of the protein depends on local (for some amides even global) unfolding of the protein to expose the amides to the solvent. Proteins for which back-exchange is difficult include the large class of proteins that cannot be reversibly denatured (usually leading to precipitation) and proteins of limited stability that don't tolerate long incubation times. Here we illustrate the finding that back-exchange is redundant if the protein of interest is produced by cell-free synthesis from perdeuterated amino acids in H_2O . Importantly, the costs associated with cell-free synthesis compare favorably with those of *in vivo* expression.

A brief description of cell-free protein synthesis

Cell-free protein synthesis uses a cell extract rather than live cells to produce the protein of interest in a coupled transcription-translation reaction. Using cell extracts has numerous advantages: (i) cell extracts are depleted of the DNA from the original organism so the synthesis machinery only produces the target protein encoded by the DNA that is supplied to the reaction mixture; (ii) the process of preparing the cell extract inactivates a number of enzymes that perform chemical transformations between amino acids *in vivo*, therefore metabolic conversions between different amino acids are suppressed; (iii) the chemical

1

environment in which the protein synthesis proceeds can readily be controlled and modified; and (iv) proteins can be produced from linear DNA amplified by PCR making it very easy to introduce mutations by site-directed mutagenesis.¹ Cell-free protein synthesis became an important tool in NMR spectroscopy in 1999 when Kigawa and co-workers established conditions for high-yield protein expression.² Cell extracts can readily be prepared from *E. coli* by breaking the cells, centrifugation, and collection of the supernatant. In our hands, homemade S30 extracts routinely sustain the production of about 1 mg of protein per ml of reaction mixture. The protocol involves the use of a dialysis system in which the reaction mixture containing the S30 extract is placed in a dialysis bag and immersed in an outer buffer that supplies low-molecular weight compounds to sustain the protein synthesis reaction, such as amino acids, nucleotides, and ATP. The target DNA is added to the reaction mixture together with any other macromolecules that aid in protein production, such as tRNA and RNA polymerase. The DNA can be the same plasmid DNA that directs the protein expression in conventional *in vivo* systems or it can be PCR-amplified DNA. Detailed protocols for the preparation of S30 extracts and cell-free reactions that we have established in our laboratory have been published.³

Cell-free synthesis of perdeuterated proteins in H₂O

Producing perdeuterated proteins by cell-free synthesis from perdeuterated amino acids in H₂O can be compromised by undesired residual activity of metabolic enzymes in the cell extract. For some amino acid types, these metabolic activities can substitute some of the carbon-bound deuterons by protons. The effect is most pronounced for hydrogens in the α -position and can be attributed to enzymes requiring the pyridoxal 5'-phosphate (PLP) cofactor. The cell-free synthesis method offers the crucial advantage that this ²H-¹H exchange can be suppressed in a straightforward manner by treating the S30 extract with NaBH₄ to reduce PLP and its adducts with the protein.⁴ This leads to irreversible inactivation of the PLP enzymes, none of which are required for protein production.

Analysis by NMR spectroscopy

Figure 1 shows a comparison between two [¹⁵N,¹H]-TROSY spectra of ²H/¹⁵N/¹³C-labeled metallo- β -lactamase from *Klebsiella pneumonia* (IMP-1), where one sample was prepared *in vivo* in *E. coli* using a minimal medium with D₂O (Figure 1A), while the other sample was prepared by cell-free synthesis in H₂O, supplying all amino acids in ²H/¹⁵N/¹³C-labeled form

(Figure 1B). Clearly, more cross-peaks can be observed for the sample prepared by cell-free synthesis. IMP-1 is a metallo-enzyme that we have been unable to refold following denaturation. The protein is also prone to precipitation during NMR measurement, making prolonged incubations for ^2H - ^1H back-exchange of amide hydrogens unpractical. As an added benefit of using highly perdeuterated amino acids, the cross-peaks in Figure 1B tend to be narrower than those in Figure 1A. We attribute this effect to incomplete perdeuteration in the sample prepared *in vivo*, as we used uniformly ^{13}C -labeled glucose rather than $^2\text{H}/^{13}\text{C}$ -labeled glucose.

Cost and yield

The protein sample of Figure 1B was prepared in a 2 ml reaction mixture in an outer buffer of 20 ml. Each of the labeled amino acids was supplied at a final concentration of 1 mM, i.e. the amino acids were supplied in total quantities ranging from 1.6 mg (glycine) to 4.7 mg (lysine:2HCl). For such small quantities of amino acids, the total cost of the amino acids from CIL ended up being significantly less than the pro-rata cost for accessing the 800 MHz NMR spectrometer to measure a 3D HNCA spectrum for backbone resonance assignment. Regarding the protein yield, purification by chromatography via an SP column, buffer exchange, and concentrating of the sample produced a total of 1.8 mg of purified IMP-1, corresponding to a 0.4 mM solution in a volume of 0.15 ml that was measured in a 5 mm Shigemi tube. The initial yield after synthesis was significantly higher but the protein is prone to degradation, precipitating heavily during the purification and concentration steps.

Final remarks

Cell-free protein synthesis offers additional advantages beyond those discussed here (for a review see, e.g., ref. 5). It has long been established that cell-free synthesis is the technique of choice for sample preparations in which only one or several amino acids are isotope labeled, because the amino acids are used sparingly and isotope scrambling is suppressed (see, e.g., ref. 6). As only a small fraction of the amino acids is incorporated into the final protein product, further dramatic improvements in protein yield are conceivable. Unfortunately, algal hydrolysates do not produce good protein yields in our hands, so that, counter to intuition, the purchase of the 20 individual amino acids is more economical. Even so, comparing only the cost of labeled compounds needed for the production of uniformly isotope labeled proteins, cell-free synthesis readily competes with *in vivo* preparations.

References

1. Wu, P.S.C.; Ozawa, K.; Lim, S.P.; Vasudevan, S.; Dixon, N.E.; Otting, G. **2007**. Cell-free transcription/translation from PCR amplified DNA for high-throughput NMR studies. *Angew Chem Int Ed*, *46*, 3356-3358.
2. Kigawa, T.; Yabuki, T.; Yoshida, Y.; Tsutsui, M.; Ito, Y.; Shibata, T.; Yokoyama, S. **1999**. Cell-free production and stable-isotope labeling of milligram quantities of proteins. *FEBS Lett*, *442*, 15–19.
3. Apponyi, M.; Ozawa, K.; Dixon, N.E.; Otting, G. **2008**. Cell-free protein synthesis for analysis by NMR spectroscopy. In *Methods in Molecular Biology*, *426*, Structural proteomics: high-throughput methods. B. Kobe, M. Guss, T. Huber, Eds. Humana Press, Totowa, USA, pp. 257-268.
4. Su, X.-C.; Loh, C.-T.; Qi, R.; Otting, G. **2011**. Suppression of isotope scrambling in cell-free protein synthesis by broadband inhibition of PLP enzymes for selective ^{15}N -labelling and production of perdeuterated proteins in H_2O . *J Biomol NMR*, *50*, 35-42. Erratum **2011**. *J Biomol NMR*, *51*, 409.
5. Ozawa, K.; Wu, P.S.C.; Dixon, N.E.; Otting, G. **2006**. ^{15}N -Labelled proteins by cell-free protein synthesis: strategies for high-throughput NMR studies of proteins and protein-ligand complexes. *FEBS J.*, *273*, 4154-4159.
6. Yokoyama, J.; Matsuda, T.; Koshiba, S.; Tochio, N.; Kigawa, T. **2011**. A practical method for cell-free protein synthesis to avoid stable isotope scrambling and dilution. *Anal Biochem*, *411*, 223-229.

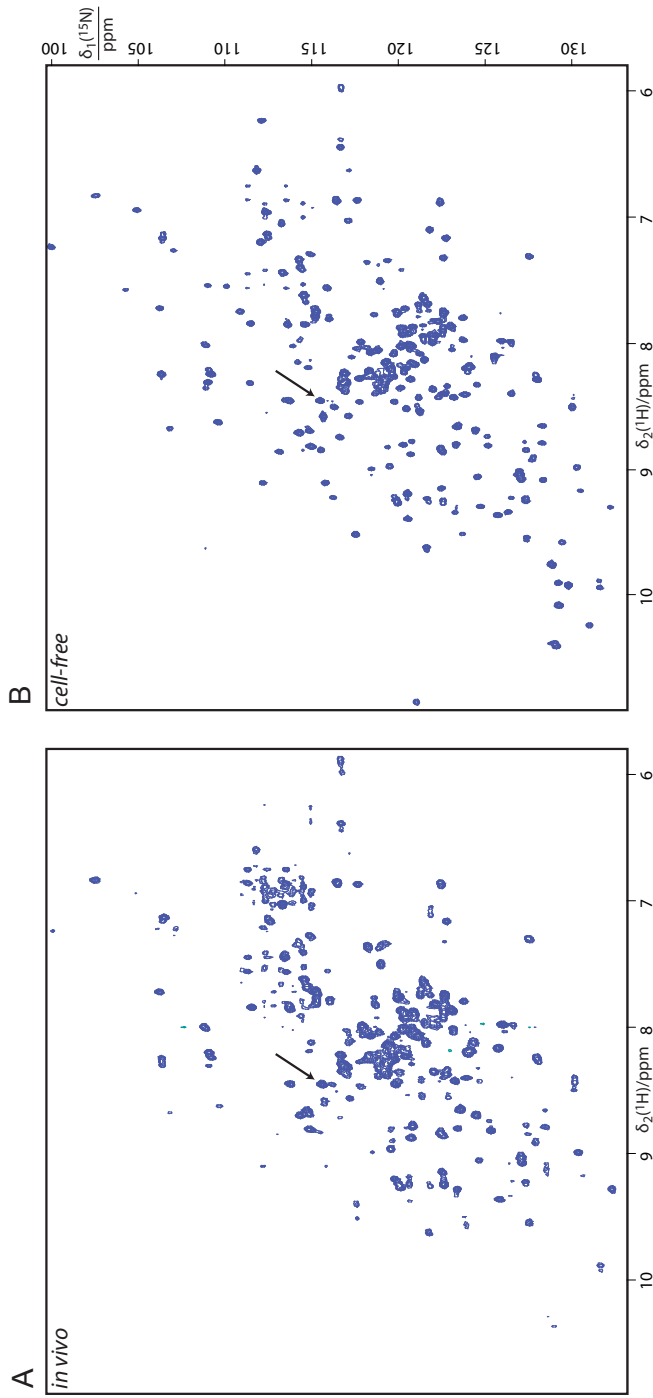


Figure 1. [^{15}N , ^1H]-TROSY spectra of *Klebsiella pneumoniae* metallo- β -lactamase (IMP-1). The spectra were recorded at 37 °C in a buffer of 20 mM MES, pH 6.5, 100 mM NaCl, 90% H_2O /10% D_2O on a Bruker 800 MHz NMR spectrometer. The spectra were scaled to display the cross-peak of a solvent exposed residue with complete ^2H - ^1H back exchange (identified by an arrow) with the same number of contour lines in both spectra. (A) Protein sample prepared using conventional *in vivo* expression in *E. coli* in D_2O . (B) Protein sample prepared by cell-free synthesis using CIL amino acids. The spectrum was recorded in about 0.5 h. There are fewer cross-peaks in (A), mostly due to insufficient ^2H - ^1H back-exchange of the amide hydrogens during purification of the sample. Complete back-exchange proved impossible even after months of storage in H_2O at 4 °C. In addition, the peaks in (A) tend to display broader line widths, which may be attributed to incomplete perdeuteration as the sample was prepared using ^{13}C -glucose instead of ^2H / ^{13}C -glucose.

4 The Set-Up, Optimisation and Operation of an In-House Built Para-Hydrogen Producing Rig

4.1 Introduction

The dihydrogen molecule can form two spin isomers with different nuclear spin configurations. The $\alpha\alpha$, $\beta\beta$ and $\alpha\beta+\beta\alpha$ nuclear configurations are referred to as the triplet state, or *ortho*-hydrogen (oH_2), and rapidly interconvert with each other.²⁹² The $\alpha\beta$ - $\beta\alpha$ state is termed the singlet state, or *para*-hydrogen (pH_2), and is more stable than oH_2 as it has access to a lower energy rotational state.²⁹² pH_2 is invisible in typical NMR experiments as the two nuclear spins are antiparallel.

Two mechanisms of conversion between oH_2 and pH_2 are known, chemical exchange of hydrogen nuclei and paramagnetic relaxation.^{293,294} The chemical exchange mechanism scrambles the nuclear spin alignment, requiring the molecular bond between the two hydrogen atoms to be broken.²⁹⁴ In contrast, the magnetic mechanism relaxes the spin states when the atoms of the hydrogen molecule experience significantly different magnetic fields. This is often achieved by the use of a paramagnetic catalyst, such as activated charcoal, or ferric chloride,^{292,295} however, there are numerous examples of other paramagnetic metals being used to catalyse this process.^{293,294} At room temperature, 25% of hydrogen gas consists of pH_2 , whereas the lower energy pH_2 state is favoured at low temperatures (Figure 4-1).²⁹⁶

The hyperpolarisation effect of pH_2 was predicted by Bowers and Weitekamp in 1986,²⁹⁷ and proved by the same authors a year later.²⁹⁸ This effect can theoretically provide up to 3.5×10^3 -fold NMR signal enhancement for 50% pH_2 enrichment,²⁹⁸ and has provided mechanistic insight into short-lived intermediates that would otherwise be impossible to observe.^{292,299}

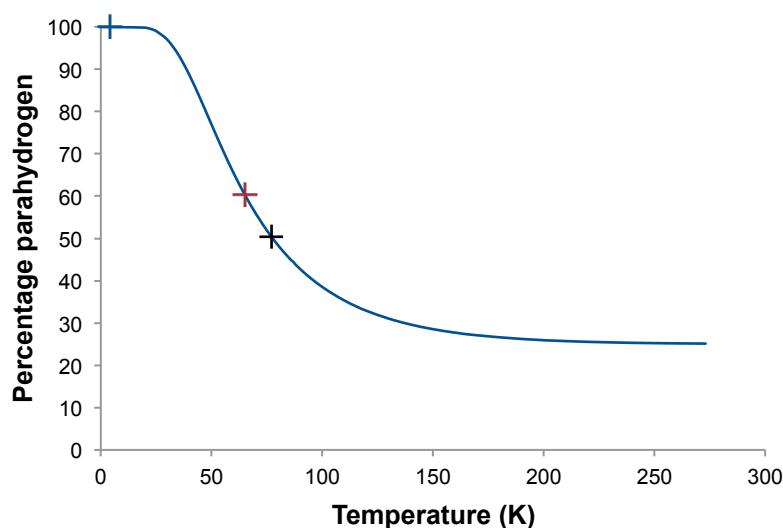


Figure 4-1 Temperature dependence of the percentage of $p\text{H}_2$ in equilibrium. A black, red and blue cross marks the phase transition temperatures of liquid nitrogen, solid nitrogen and liquid helium, respectively. Values are taken from Harkness and Deming.³⁰⁰

In the simplest example of $p\text{H}_2$ -induced hyperpolarisation (or PHIP), both atoms of a single hydrogen molecule are added to a double bond via a hydrogenation reaction. The two hydrogen atoms must remain coupled and become magnetically inequivalent for the hyperpolarised signal to be observed.^{292,301-303} Alternatively, the hydrogen atoms can be made non-degenerate by forming a metal dihydride.³⁰⁴ Hyperpolarisation can then be transferred to another molecule of interest via a temporary association with the metal complex in a system termed NMR-SABRE (NMR signal amplification by reverse exchange).³⁰⁴⁻³⁰⁸

Protons originating from $p\text{H}_2$ only populate the $\alpha\beta$ and $\beta\alpha$ spin states (Figure 4-2). As a consequence, very large population differences exist in the energy level diagram, which is the basis behind the hyperpolarization. In the presence of a high magnetic field this difference generates four hyperpolarized transitions. In contrast, in the absence of a high magnetic field the coupling between the spins is strong, so only the lower energy level of either $\alpha\beta$ or $\beta\alpha$ is populated and two transitions are possible.²⁹⁹

This presents two experimental outcomes for hydrogenation reactions with $p\text{H}_2$. In the first case, where hydrogenation is carried out at high magnetic field such as in the probe of an NMR magnet, antiphase multiplets are observed. This has been termed the PASADENA experiment (Parahydrogen And Synthesis Allow Dramatic Enhancement of Nuclear Alignment).^{298,301} In the second case, where hydrogenation occurs in low magnetic field, the two multiplets are in-phase but have opposite sign. This has been

called the ALTADENA experiment (Adiabatic Longitudinal Transport After Dissociation Engenders Net Alignment).³⁰⁹ Experimental results from both effects are shown in Figure 4-3.

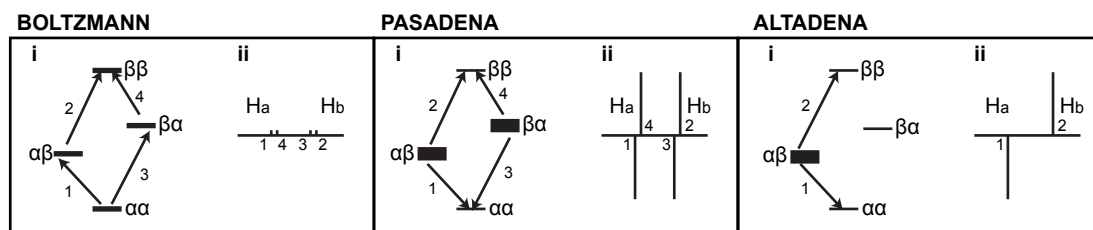


Figure 4-2 Energy diagram (i) and simulated NMR spectrum (ii) description of standard BOLTZMANN population distribution, PASADENA and ALTADENA experiments. Line thickness indicates spin state population. If the hydrogenation occurs at high magnetic field the PASADENA effect is observed, where the two spin states $\alpha\beta$ and $\beta\alpha$ are equally populated and give rise to four transients. In the absence of a strong magnetic field the ALTADENA effect occurs, where only the lower of either $\alpha\beta$ or $\beta\alpha$ is populated. This gives rise to only two transitions.

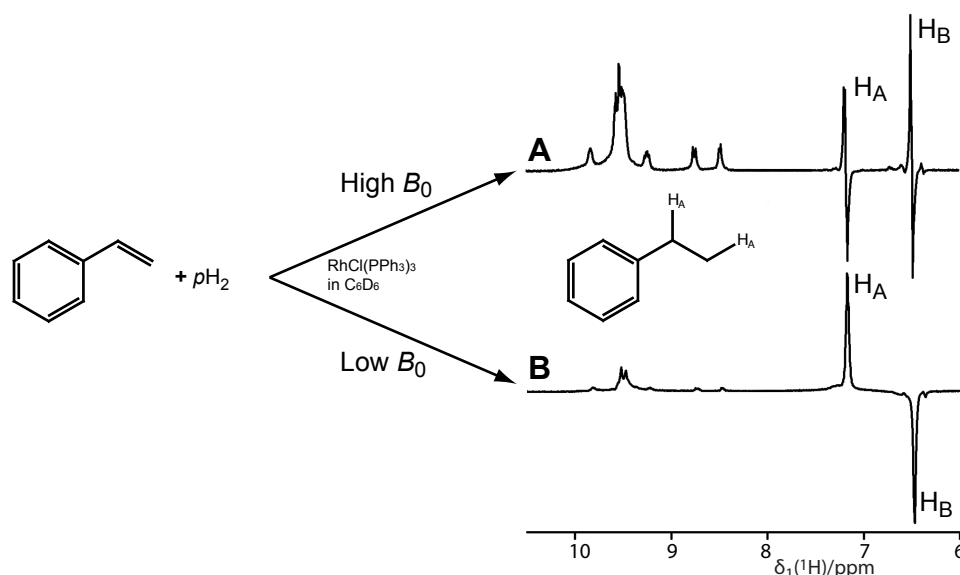


Figure 4-3 Experimental A) PASADENA and B) ALTADENA spectra. When hydrogenation occurs at high magnetic field, two antiphase multiplets are observed for H_A and H_B with high sensitivity. However, if the hydrogenation occurs in the absence of a magnetic field, the multiplets experience high signal intensity gains but have opposite sign. Figure adapted from the supplementary information of Kotunov *et al.*³⁰²

Contrast agents for MRI labelled with ^{13}C can also be hyperpolarised and enable high-resolution images to be acquired in short times. Bhattacharya *et al.* described a system in which a ^{13}C -labelled precursor was hydrogenated with pH_2 in the stray magnetic field of an MRI machine, followed by the transfer of the polarisation to ^{13}C via a radiofrequency pulse sequence.^{310,311} This hyperpolarisation was sufficiently long-lived to enable fast purification from the catalyst, injection into a rat model and subsequent 3D measurements. Later work in the same group demonstrated *in vivo* imaging of hyperpolarised 1- ^{13}C -succinate and 1- ^{13}C -maleate, and identified ^{13}C -

glutamate and ^{13}C -glutamine metabolic products of succinate as potential biomarkers for a rapid MRI based brain tumour assay.³¹²

To increase the hyperpolarisation spin lifetime, the hyperpolarised nuclei can be treated with a series of spin echoes or stored at zero magnetic field to remove the difference in resonance frequencies of the two spins. Alternatively, the singlet state can be stored if the two spins are made magnetically equivalent, such as in the case of $p\text{H}_2$. Warren *et al.*³¹³ described an interesting example for the system shown in Figure 4-4. Acetone was used to shift the equilibrium to the right and the degenerate ^{13}C nuclei were able to store the hyperpolarisation until it was recovered via an injection of water, restoring the magnetic inequivalence of the ^{13}C nuclei.

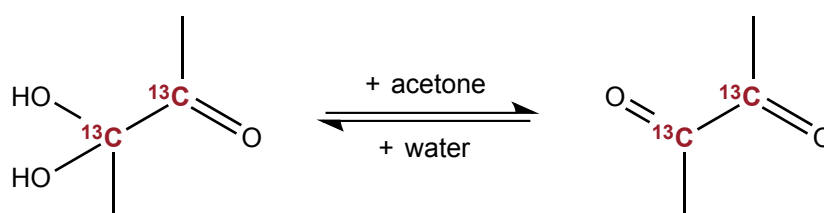


Figure 4-4 Equilibrium between 3,3-dihydroxybutan-2-one and biacetyl. In acetone, biacetyl is more stable and the ^{13}C spins are degenerate, storing hyperpolarisation for long periods. The addition of water favours the monohydrate, breaking the degeneracy and allowing the hyperpolarisation to relax.

Recently, methods for continuous feeding of hyperpolarised gas to an NMR sample have been described.^{314,315} By using gas-permeable membrane tubing typically used for degassing solvents or for gas exchange in clinical dialysis instruments, hyperpolarised xenon or hydrogen gas was added continuously to an NMR sample, enabling the acquisition of 2D NMR spectra.³¹⁴ Along with the SABRE method,^{305,306,316} this presents the possibility of continual hyperpolarisation transfer to large biomolecules via transient $p\text{H}_2$ -metal-protein complexes over the duration of a long multidimensional experiment. This would have obvious benefits for protein NMR, including higher signal-to-noise ratios as is required for non-uniform sparse sampling pulse sequences.

The work in this chapter is primarily concerned with refining an in-house built $p\text{H}_2$ rig to generate optimal yields for future hyperpolarisation experiments.

4.2 Results

4.2.1 Initial Design

Dr D. Shishmarev, Prof. G. Otting, Mr M. Hill, and Mr D. Bansner at the Research School of Chemistry, ANU performed the initial design of the $p\text{H}_2$ rig prior to my involvement. Figure 4-5 shows a schematic of the initial system design.

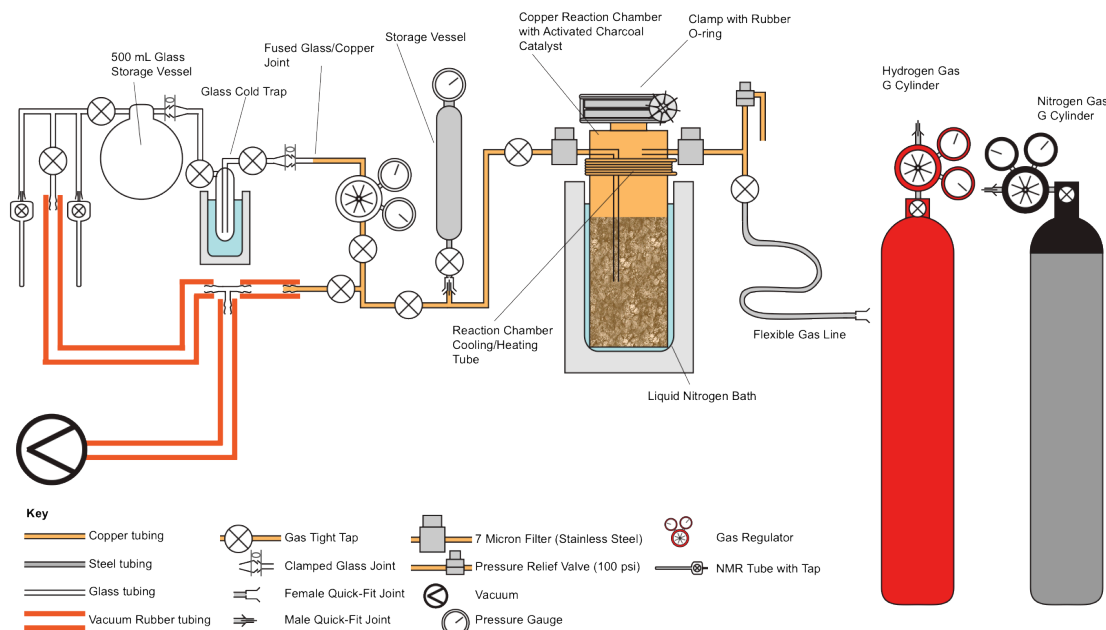


Figure 4-5 Initial design of the $p\text{H}_2$ producing rig.

The system was designed to utilise a copper reaction chamber containing an activated charcoal catalyst, which is cooled to liquid nitrogen temperature to effect the conversion of $o\text{H}_2$ to $p\text{H}_2$.

4.2.2 Improvements to Rig

The first iteration of the rig raised a number of safety concerns and had practical issues with regard to $p\text{H}_2$ generation.

Safety

Three safety concerns associated with the initial version had to be addressed. Firstly, any cylinder containing flammable gas such as hydrogen should be protected from the possibility of flashbacks, where an ignited gas-front burns along the gas line and into the gas cylinder. This risk can be addressed by incorporating a ‘flashback arrestor’ into the line close to the cylinder. The flashback arrestor forces any flame

rushing along the gas line through a fine mesh of flame resistant material, which dissipates heat and thus extinguishes the flame. Most quality flame arrestors also have a backflow prevention valve to stop a pressure wave from reaching the cylinder, and a heat sensitive cut-off valve that physically cuts off the flow to the cylinder if a flashback occurs. Whilst the risk associated with flashbacks in the pH_2 system would be low in general operation, the original protocol of conditioning the pH_2 rig for initial use and for post-use warming recommended the use of heat guns, introducing an ignition source. This problem was addressed by incorporating a BOC flashback arrestor (model B0304) into the system just after the pressure regulator on the gas cylinder.

The second safety modification was to adjust the orientation of the pressure relief valve outlet. This vent was orientated upwards to direct any hydrogen gas towards the intake of the fume hood and away from the hood opening. While hydrogen gas is lighter than air, the gas given off by the pH_2 rig out of this relief valve is still close to liquid nitrogen temperatures and exiting the rig at 690 kPa (100 psi) pressure. With the initial orientation of the valve outlet, hydrogen gas was escaping the fume hood, as was evident from the way the outlet gas disturbed the nitrogen vapour given off by the nitrogen Dewar. A change of orientation of the pressure relief valve outlet made a significant difference to the flow within the hood, and no more hydrogen gas was observed leaving the opening of the fume hood.

A third safety concern arose with the two NMR tube attachment points. It turned out to be practically impossible for a single user to hold both tubes against the rig while, at the same time, manipulating gas taps. This resulted in an incident where a tube flew off and exploded on impact with the base of the fume hood, propelled by the positive pressure in the tube. To prevent this from happening again, a wire arrest support was designed to allow the tube to come off the rig in the case of overpressure without becoming a dangerous projectile. The final iteration of this rig was designed to have a single NMR tube attachment, enabling the user to hold the NMR tube for the duration of its fill while adjusting the gas taps.

Pressure Leaks

The most significant problems hampering the usability of the rig resulted from gas leaks during either high- or low-pressure operation. The rig is required to be gas tight from 690 kPa (100 psi) to 20 Pa (0.003 psi) at temperatures ranging from -196 °C to +150 °C. This is difficult to achieve and gas leaks occurred from several of the joints

and the taps, especially after a number of heat/cool cycles. Tightening the joints *in situ* rectified most of these issues, however, a number of joints had to be remade by the workshop technical staff (M. Hill) due to sheering of the soft copper thread before a suitable seal was established.

One of the biggest leaks occurred at the cap that sealed the reaction chamber. No leaks were detected at room temperature at either high- or low-pressure, but little to no $p\text{H}_2$ could be obtained. It was subsequently discovered that the hydrogen gas cylinder was still releasing gas into the rig (the sound of gas passing through the flame arrestor could be detected) even after the system had come to a ‘cold’ equilibrium, indicating the presence of a significant leak. The leak turned out to have arisen from freezing of the rubber O-ring sealing the top of the reaction chamber when the reaction chamber was cooled to liquid N_2 temperatures. Attempts were made to keep the top of the chamber warm using heated reticulating water, but this posed the potential problem of water freezing in the warming tube and also caused much faster rates of liquid nitrogen boil-off, to the extent that the rig could not be left unattended for even 10 minutes. Redesigning the opening to the reaction chamber to incorporate an indium wire seal analogous to those used in cryogenic systems rectified the problem.

Other Modifications

Further modifications were made to render the system more usable. The majority of the glass section was removed from the rig and the remainder simplified and redesigned. This removed the glass cold trap, the 500 mL glass storage vessel, and a large length of glass tubing, which reduced the amount of gas wasted during purging of the system and made the $p\text{H}_2$ yields more reproducible.

It was also noted that initial designs used nitrogen gas to purge the rig prior to hydrogen treatment. However, as any residual nitrogen from purging would dampen the generation of $p\text{H}_2$,²⁹⁴ this was modified to an argon purge.

The rig was raised on supports and clamped to the fume hood to enable a laboratory jack to be included under the liquid nitrogen Dewar. This allowed the Dewar to be lowered away from the copper reaction chamber so that a warm-up of the system did not necessitate the boil-off of all the liquid nitrogen.

A cold trap was incorporated to protect the vacuum pump from any moisture that was pulled off the activated charcoal during conditioning. The cold trap used either liquid nitrogen or a dry ice/ethanol bath after purging with argon gas.*

A tap was introduced into the line prior to the NMR tube attachment glassware to enable purging of the low-pressure side without requiring the attachment of an NMR tube. Also, the NMR tubes initially constructed were too heavy for a normal airlift to eject the sample from the magnet, due to the large valve. This was temporarily addressed by attaching a fly line to the sample so it could be pulled out manually, and eventually a smaller tap was used (similar to a Young tap NMR tube), which proved light enough for the normal airlift.

Finally, a vacustat was included after the cold trap to assess the gas-tightness of the system and to identify leaks. This line was removed and placed in a gas bubbler when purging with a stream of gas (steps 7 and 9 in the following protocol).

4.2.3 Final Design and Method of $p\text{H}_2$ Generation

The final optimised design of the system is schematically described in Figure 4-6. A protocol for reproducible $p\text{H}_2$ generation based on recommendations from Prof. B. Messerle (School of Chemistry, UNSW) was developed with this rig and is as follows:

* Argon gas freezes at liquid nitrogen temperatures, so a dry ice/ethanol bath is recommended.

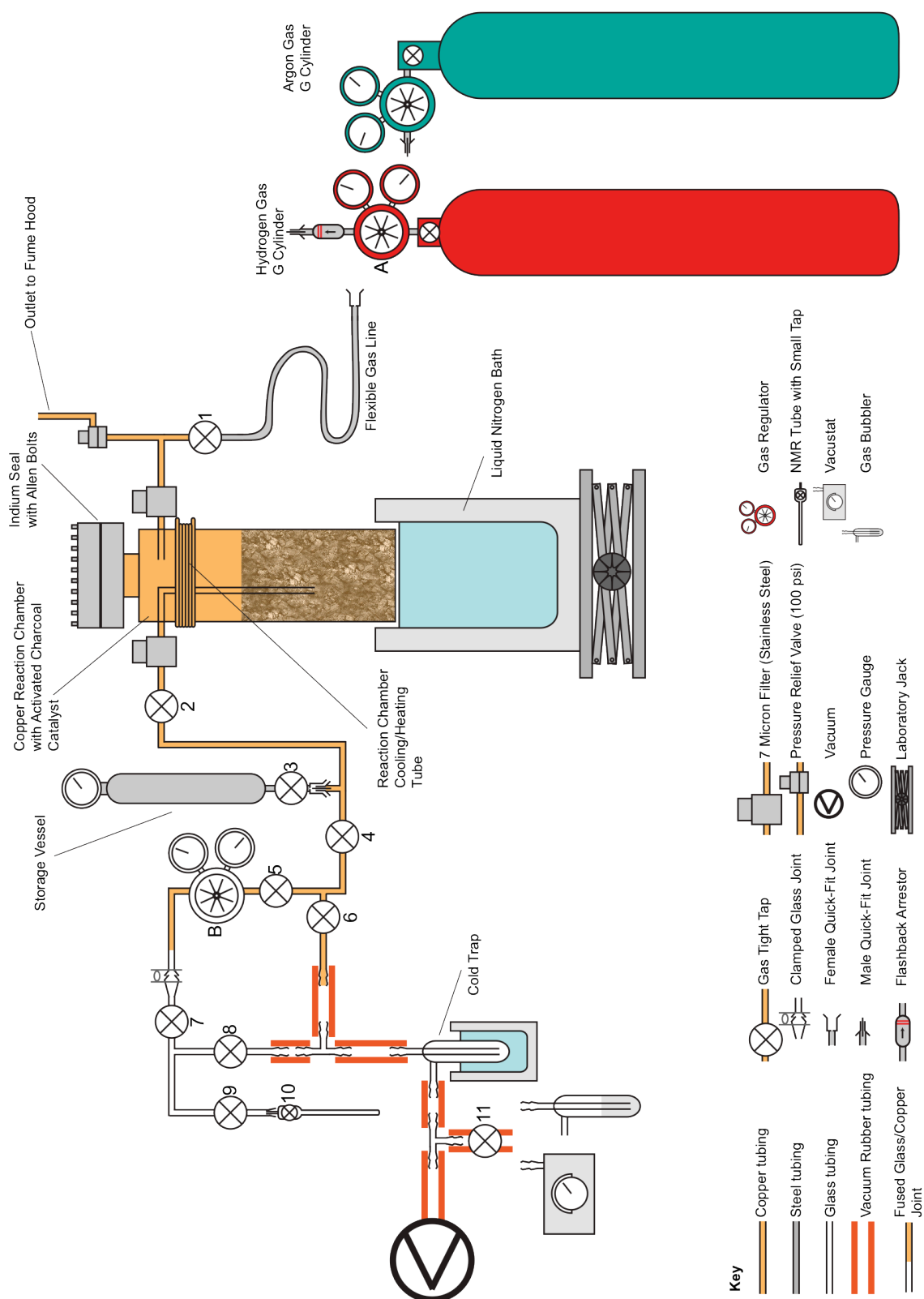


Figure 4-6 Final design of pH_2 generating rig. Taps are numbered 1 to 11 and referred to in text. Pressure regulators are designated A (on the gas cylinder) and B (in the rig). While the storage vessel is constructed from stainless steel, the inside is coated with Teflon to prevent the gas being exposed to the metal surface. The vacustat or gas bubbler is attached to the vacuum line with tap 11 as required. The cold trap is used with either liquid nitrogen or dry ice/ethanol as required (see text).

Conditioning Catalyst

The copper reaction chamber contains 500 g of activated carbon (granular Darco 4-12 mesh – Sigma). It is recommended the yield of $p\text{H}_2$ be assessed by the simple NMR experiment described in section 4.2.4 every time the rig is set up and to recondition the catalyst if the yields are sub-optimal. Reconditioning is also necessary if the pressure of the reaction chamber drops to atmospheric pressure. In this case, steps 5 to 10 should be sufficient and, because of the fragility of the indium seal, should be attempted prior to discarding and replacing the charcoal. Throughout this section, gas taps are indicated as being open (in bold) or closed (in superscript), such that (**1**²**3**^{4 5 6 7 8 9 10 11}) would state taps 1 and 3 are open, and taps 2 and 4-11 are closed.

1. The catalyst is initially conditioned by dismantling the reactor from the tubing with spanners and opening the top of the reactor with an Allen key. Care should be taken to recover the indium seal wire from the top of the reactor for either recycling or appropriate disposal. The activated charcoal can then be recovered from the reaction chamber and disposed of. The reaction chamber is subsequently cleaned thoroughly with water and rinsed several times with acetone prior to drying in an oven overnight.
2. After removing all rubber O-rings, removable glassware sections should also be washed with water, rinsed with acetone and dried. O-rings should be inspected and replaced if stretched or brittle.
3. 500 g of activated charcoal (granular Darco 4-12 mesh – Sigma) is then replaced in the reaction chamber, and the chamber with charcoal is dried again in a glassware oven overnight.
4. The apparatus is then reassembled, with care taken to ensure all O-rings are in good condition and properly positioned. A fresh section of indium wire (or the recycled indium after being redrawn into a wire and rinsed with dilute hydrochloric acid^{*}) is placed around the opening of the reaction chamber in the groove, slightly overlapping at the end. The top of the reaction chamber is then placed carefully on top, fixed to the chamber by the Allen bolts, and

^{*} Indium metal forms a protective oxide layer over time and can be safely and easily handled. However, bare elemental indium metal exposed after treating with HCl will readily ‘dry weld’ to itself. This is useful for creating indium O-rings, but users should take care when handling the freshly etched metal so that it does not need to be redrawn into wire.

gently tightened as indicated in Figure 4-7. The bolts need to be tightened only ‘two finger’ tight initially, and progressively tighter over several ‘cycles’. Slow, even tightening ensures the indium wire melts into the cap properly to form a cryogenic seal. Several rounds of retightening should be applied over the next few days as the indium reshapes into a cryogenic seal.

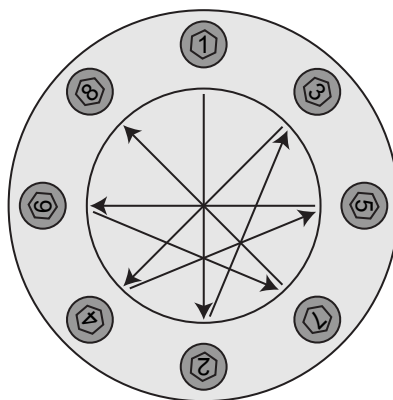


Figure 4-7 Order of tightening of Allen bolts on the reaction chamber. Gentle, evenly distributed pressure is important for a proper seal to be established.

5. All impurities that reduce $p\text{H}_2$ formation, including oxygen, nitrogen and water, must be removed from the catalyst. This is done by closing the system and heating the reaction chamber to between 100 °C and 145 °C* under vacuum for a minimum of 4 hours. An insulated lab heating tape can be used† with a thermocouple or thermometer attached to the copper reaction chamber. A liquid nitrogen cold trap is used to protect the vacuum pump at this stage, and a stream of nitrogen gas or compressed air is applied to the copper tube wrapped around the outside top of the reaction chamber to reduce the temperature at the indium seal. A heat gun may be used to heat the rest of the copper tubing in the rig to assist removal of contaminants from these parts. (1 2 3 4 5 6 7 8 9 10 11)
6. After 4 hours, the pressure should be measured on the vacustat. Pressures near 20 pa (0.003 psi) should be achievable when the vacuum is only open to the high-pressure side. Pressures of 100 pa (0.015 psi) or higher indicate a

* The melting point of indium is 156.6 °C

† Care needs to be taken to ensure the electrical safety of the heating tape. Many laboratory heating-tapes are designed for use on glass or ceramic tubes or columns and so may not be sufficiently insulated for use on a conductive surface such as copper. Best practice would also include attaching a ground line from the apparatus to the power supply or fume hood. A residual current device (RCD) protected circuit is also recommended.

significant leak somewhere in the rig or that the vacuum pump needs servicing. This issue needs to be resolved before going further. (1 2 3 4^{5 6 7 8 9 10} 11)

7. The apparatus is then taken off vacuum and the cold trap is removed from the liquid N₂ bath (1 2 3 4^{5 6 7 8 9 10 11}). The vacustat is disconnected from the vacuum line and a gas bubbler is attached. The apparatus, still under heating, is then filled with argon gas, and then purged for a minimum of 1 hour with a slight flow. This is achievable by opening tap 8 and setting pressure regulator B to just above atmospheric pressure or until a slow steady stream of bubbles is present in the gas bubbler (1 2 3 4 5^{6 7 8 9 10 11}).
8. After one hour, the apparatus is then evacuated again as per step 5 for a minimum of one hour, with the exception that: a) the liquid N₂ bath must be replaced with a dry ice/ethanol bath, as argon solidifies at liquid N₂ temperatures, and b) the glass side is also evacuated (1 2 3 4 5 6 7 8^{9 10 11}). Checking with the vacustat again is advisable, although pressure tightness is less important for the low-pressure side, so a measurement of 50 to 100 Pa (0.0075 to 0.015 psi) is acceptable.
9. The apparatus is then taken off vacuum, and the heating tape removed. The system is then filled with high purity H₂ gas and purged as in step 7 for a minimum of 1 hour (1 2 3 4 5^{6 7 8 9 10 11}).
10. From now, a positive pressure of about 275 kPa (40 psi) must be maintained on the high-pressure side of the apparatus. This ensures that any minor leaks do not let moisture or oxygen into the reaction chamber. If the pressure drops to close to atmospheric pressure, reconditioning is likely to be necessary.

Generating pH₂

To generate pH₂, the following steps are taken

11. Ensure tap 1 is open and tap 2 is closed, then attach an ultra-pure hydrogen cylinder and set regulator A to 500 kPa (75 psi). Keep the cylinder open to the reaction chamber for cooling (1^{2 3 4 5 6 7 8 9 10 11}).
12. Place a pre-cooled 5 L liquid N₂ Dewar with about 250 mL of liquid nitrogen onto a laboratory jack and raise it around the reaction chamber. This minimises liquid nitrogen boil off to just that required to cool the reaction

chamber. Half-fill the Dewar with liquid nitrogen *in situ* using another vessel and wait for the rapid boiling to cease. Continue to incrementally add liquid nitrogen to the Dewar until full, waiting for the rapid boil off to end after each top up. Once the Dewar is full, and not vigorously boiling, the apparatus can be left for up to 30 minutes without significant warming occurring. Gas will flow into the reaction chamber as it cools due to thermal contraction of the gas and absorption into the activated charcoal.

13. After 30 minutes, evacuate the storage vessel and the low-pressure side of the rig (**1** ² **3** **4** **5** **6** **7** **8** ⁹ ¹⁰ ¹¹). Close off the vacuum and close off the cylinder from the reaction chamber (¹ ² **3** ⁴ ⁵ ⁶ ⁷ ⁸ ⁹ ¹⁰ ¹¹), then open the reaction chamber to the storage vessel to store some $p\text{H}_2$ gas for purging (¹ ² **3** ⁴ ⁵ ⁶ ⁷ ⁸ ⁹ ¹⁰ ¹¹). Next, close off the storage vessel and the reaction chamber and then reopen the cylinder to the reaction chamber (**1** ² ³ ⁴ ⁵ ⁶ ⁷ ⁸ ⁹ ¹⁰ ¹¹).
14. After 30 to 60 minutes $p\text{H}_2$ will have formed in the reaction chamber. Close regulator B. Purge the system with the gas stored in the storage vessel by venting it into the system and then evacuating once more (**1** ² **3** **4** **5** ⁶ **7** ⁸ ⁹ ¹⁰ ¹¹) At this stage set regulator B to the pressure desired for the NMR sample and leave it set for the entire run. Then evacuate again (**1** ² ³ **4** **5** **6** **7** **8** ⁹ ¹⁰ ¹¹) and then close off the vacuum (**1** ² ³ ⁴ ⁵ ⁶ ⁷ ⁸ ⁹ ¹⁰ ¹¹).
15. Freeze an NMR sample inside the tube in liquid nitrogen and then evacuate the tube by attaching it to the low-pressure side and opening up the tube to vacuum (**1** ² ³ ⁴ ⁵ ⁶ ⁷ **8** **9** **10** ¹¹). Close tap 9 and 10, thaw the sample, and repeat several times to de-gas the NMR solvent of any oxygen or nitrogen.
16. After de-gassing the sample, freeze the NMR tube again. While frozen, purge the area in the tube above the sample a few times by evacuating (**1** ² ³ **4** **5** ⁶ ⁷ **8** **9** **10** ¹¹) then adding $p\text{H}_2$ (**1** ² ³ **4** **5** ⁶ ⁷ ⁸ **9** **10** ¹¹), before finally closing tap 10 on the NMR tube with a dose of $p\text{H}_2$ present.

Warm-up and Preparation for Next Use

Significant expansion occurs when the system warms to room temperature and, as a safety precaution, a pressure relief valve has been fitted and set to 689 MPa (100 psi). This safety measure is only available to sections of the rig open to the reaction chamber. Care should be taken that no high-pressure gas will form as the system warms.

17. Set gas tap to (¹ **2 3 4 5** ^{6 7 8} **9** ^{10 11}). Ensure the pressure regulator B is still open. Turn off the hydrogen gas cylinder at regulator A, and on the cylinder. Disconnect the hydrogen gas cylinder. It is important to remove the NMR tube from the rig at this point, as the NMR tube attachment site is where excess gas will be vented if something goes wrong later.
18. Slowly lower the liquid nitrogen Dewar from the reaction chamber until it can be removed completely.
19. The pressure will increase steadily up to 689 MPa (100 psi) until the pressure relief valve opens and vents the hydrogen gas into the fume hood. If the pressure relief valve does not open (the pressure measured on the storage vessel goes higher than 100 psi), immediately vent the system by opening tap 7 (¹ **2 3 4 5** ^{6 7 8} **9** ^{10 11}), which will vent out the NMR tube slot. Do not leave the rig unattended before confirming that the valve has opened and the gas is venting. If the pressure relief valve is slow to open, do not use the rig until a qualified technician has serviced or replaced it.
20. Once the valve has opened, set the taps to (¹ **2 3** ^{4 5 6 7 8 9 10 11}). Place an absorbent cloth or paper towel under the reaction chamber to minimize water spillage due to melting ice around the reaction chamber. The rig is safe to leave while it warms to room temperature.
21. Check the rig at least every 2 weeks to ensure the H₂ gas pressure remains above 275 kPa (40 psi).

4.2.4 Assessment of pH₂ Yield After Optimisation

A simple 1D ¹H NMR spectrum was acquired to determine pH₂ yield similar to the experiment described by Bhattacharya *et al.*³¹⁰ The spectrum is first set up using 300 kPa of H₂ gas at thermal equilibrium.

The test sample is then compared at exactly the same pressure (by not adjusting the pressure regulator B) for a sample converted to pH₂. The result for yield is shown in Figure 4-8.

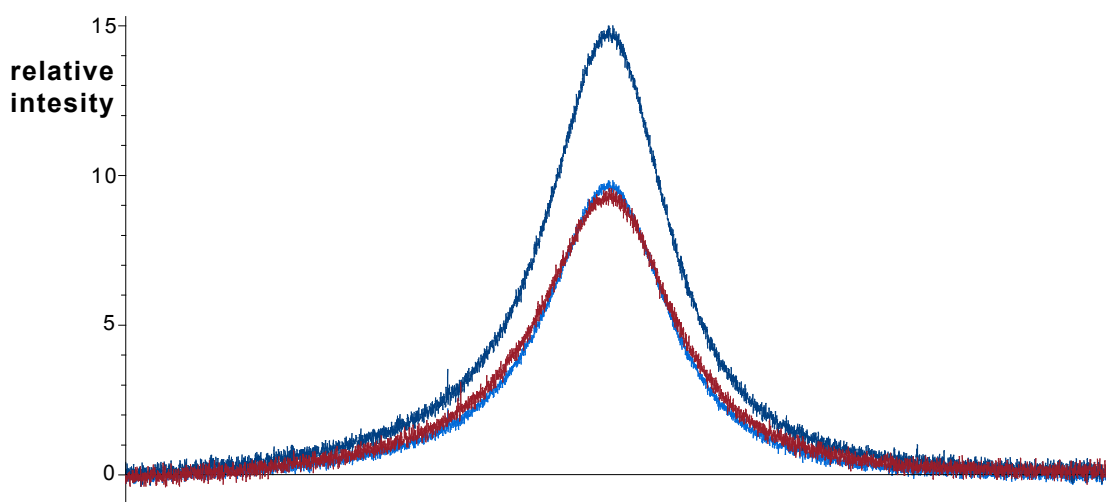


Figure 4-8 ^1H NMR gas spectrum of detectible $o\text{H}_2$ in thermal H_2 gas (blue) and $p\text{H}_2$ enriched H_2 gas (red). The thermal peak almost exactly overlays with the $p\text{H}_2$ enriched sample peak when multiplied by 0.67 (light blue). This indicates an increase in non-detectible $p\text{H}_2$ concentration (with a concurrent decrease in concentration of detectible $o\text{H}_2$) consistent with theoretical expectations for liquid nitrogen temperatures (Figure 4-1).

The content of $p\text{H}_2$ gas at liquid nitrogen temperature is close to 50% (Figure 4-1). Hydrogen gas at room temperature contains 25% $p\text{H}_2$, so a decrease of the $o\text{H}_2$ signal by 1/3 is expected. This is in excellent agreement with the integral of the curves in Figure 4-8, indicating that the $p\text{H}_2$ rig, when operated following the procedure above, is generating optimal yields.

4.3 Discussion

4.3.1 Future Design Recommendations

The design of the $p\text{H}_2$ rig was optimised to produce close to theoretically obtainable yields of $p\text{H}_2$ gas; nonetheless, recommendations can be made for subsequent improvements of the system, which would make it more flexible for experimental work.

1. Most of the gas leak issues were due to joints developing leaks during multiple thermal cycles through temperatures between $-196\text{ }^\circ\text{C}$ to $100\text{ }^\circ\text{C}$. Any future design should avoid joints near the reaction area that is cooled by using continuous copper tubing or welded joints. In order to minimise differences in thermal conductivity and expansion, the use of different metals in the construction of the reaction chamber and adjoining regions should be avoided.

2. The current reaction chamber is large and useful only for batch processing. A continuous feed system could be achieved by changing the large open reaction chamber for a long, thin copper tube filled with a fine activated charcoal powder and packed with glass wool. This tube could then be immersed in a liquid nitrogen Dewar (like the current system) with only minimal nitrogen loss as a lid could be added to the Dewar to reduce boil off. This could then be modified at a later point to be immersed in solid nitrogen (obtainable by placing liquid nitrogen under vacuum) or imbedded into a copper block attached to a liquid helium refrigeration system for higher $p\text{H}_2$ yields (up to 75% and 99% $p\text{H}_2$ enrichment respectively – Figure 4-9).

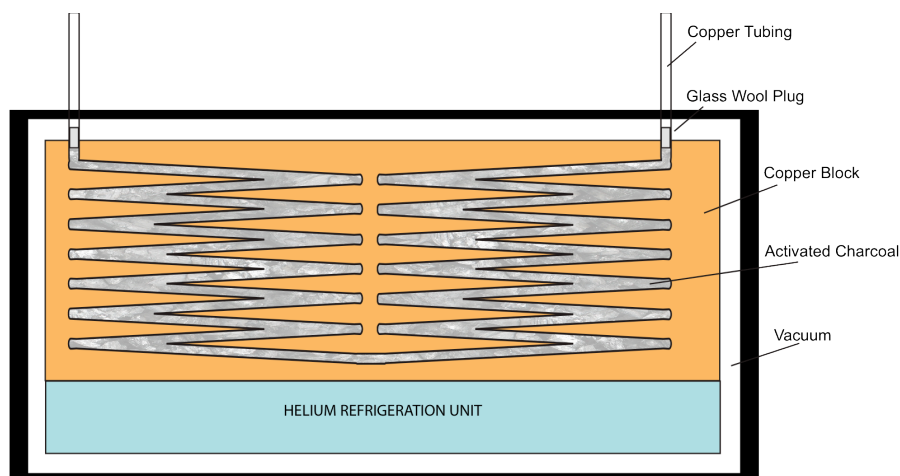


Figure 4-9 Potential helium cooled system to generate 99% $p\text{H}_2$ samples. A long reaction tube packed with catalyst rather than a short large-diameter reaction chamber would facilitate continuous $p\text{H}_2$ generation.

3. To reduce the loss of usable pressure between the reaction chamber and the NMR tube, the tube diameter and length should be minimised between the reaction chamber and the outlet.
4. The filters prior to and after the reaction chamber are made from stainless steel. The stainless steel filter seemed to have a minimal effect on $p\text{H}_2$ yield, which is likely due to cooling of the filters by thermal conductivity (Figure 4-10). For future designs where these filters may not be so close to the liquid nitrogen Dewar, these filters should be replaced by either copper or glass filters, as the iron in the stainless steel will provide a mechanism for back conversion to thermal H_2 .

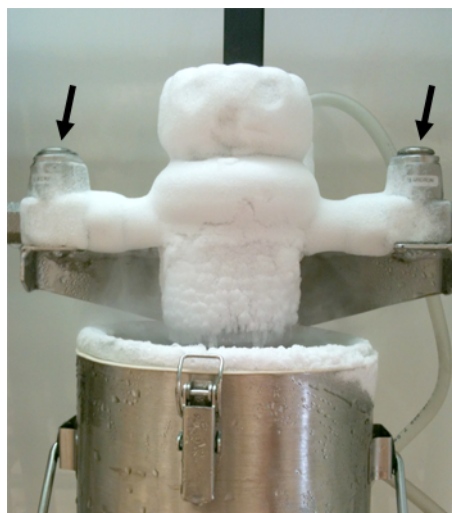


Figure 4-10 Evidence of liquid nitrogen cooling the reaction chamber and the two filters (seen on either side of the centre column highlighted by arrows). The fact that the two filters are also cooled may explain why the stainless steel did not have a detrimental effect on the $p\text{H}_2$ yield as expected initially. The same filter further downstream from the reaction chamber could have a detrimental effect if it were not cooled.

5. A bypass tube between tap 5 and regulator B would be beneficial, as it would enable the user to purge the glass section and perform control experiments with thermal H_2 .
6. With a highly efficient $p\text{H}_2$ gas generation system, ‘gas fed’ NMR experiments become feasible, where $p\text{H}_2$ is constantly generated and fed directly into the sample tube via a gas permeable membrane while it is in the NMR magnet. Therefore, an ideal design would ensure no magnetic parts are present to hinder the placement of the rig close to the NMR magnet. It should also be small and not sensitive to vibration from movement on a trolley. If this is not feasible, a supplementary, non-magnetic rig that can hold several storage vessels may be a useful alternative.
7. As the generation of $p\text{H}_2$ is somewhat time consuming and wasteful of liquid nitrogen and hydrogen gas (due to purging), a verified method of storing $p\text{H}_2$ gas at suitably high pressure would be beneficial. This would require one of the following:
 - a. the high-pressure side to be pressure tested to higher pressures, combined with a larger ‘ $p\text{H}_2$ friendly’ storage cylinder with no exposed steel parts;
 - b. several smaller storage vessels like the one already used to be acquired and used either sequentially or in parallel with an appropriate pressure regulator and attachments;

- c. a compressor with no metal parts exposed to the gas to recompress the $p\text{H}_2$ into a cylinder with no exposed metal parts.

These methods would need to be verified and a ‘shelf life’ determined for the stored gas.

4.4 Conclusions and Future Work

The $p\text{H}_2$ rig has been optimised to work at close to theoretical yields for a liquid nitrogen system. This now paves the way for future experiments utilising hyperpolarisation with $p\text{H}_2$ incorporation via hydrogenation reactions or systems like SABRE.^{304,305} Even though signal improvements of 3.5×10^3 may not be achievable in an aqueous environment, even a fraction of this gain would be greatly beneficial to biological NMR experimentation.

Future work should investigate the stability of $p\text{H}_2$ in aqueous environments and in the presence of water-soluble metal complexes that bind H_2 reversibly at room temperature. These complexes may be able to transfer a portion of their hyperpolarised signal via NOE and other interactions to a protein molecule and give signal improvements for the solvent exposed surface. A continuous gas feed system akin to that described by Roth *et al.*³¹⁵ and Baumer *et al.*³¹⁴ would also be advantageous to enable longer multidimensional experiments to be acquired. Several gas exchange membrane samples from Membrana (Germany) have already been acquired for such a project. These membranes are usually used for blood dialysis and degassing solutions. They are expected to be suitable for constant-feed $p\text{H}_2$ experiments.

4.5 Experimental Methodology

Simple single pulse-acquire 1D ^1H NMR experiments were performed on a Bruker 600 MHz spectrometer at 298 K using 12 μs pulse length. No lock was used and the sample was not shimmed. Without a lock or internal calibrant, the ppm value of the broad hydrogen gas peak is uncertain. The $p\text{H}_2$ gas sample was ensured to have the same pressure as the thermal H_2 gas sample by not adjusting regulator B between experiments.

5 Promotion of Mammalian Angiogenesis by Neolignans Derived from Soybean Extracellular Fluids – NMR Elucidation of Natural Products

5.1 Introduction

Natural product extraction can lead to the identification of novel compounds with biological activity. An essential part of the natural product discovery process is the structural elucidation of sometimes rather complex molecules. This elucidation is often hampered by limited product yields, however, sensitive techniques like mass spectrometry fragmentation analysis and comparison to known fragmentation libraries make it possible to identify many previously characterised natural products. When these methods fail, other techniques are required to determine the chemical structure of the isolated compound.

This chapter describes the NMR structure elucidation of two naturally derived diastereomeric products extracted from soybean extracellular fluids that were found to exhibit pro-angiogenic properties.

5.2 Results

Three fractions separated via ultrafiltration and reverse phase HPLC from xylem sap (soybean) were found to have pro-angiogenic activity when tested using a modified rat aortic ring assay^{317,318}. * One of the fractions was disregarded as it was found to lose pro-angiogenic activity after storage, indicating instability of the active compound. The other two fractions maintained activity even after long-term storage, and were designated *FK1* and *FK2*. These compounds demonstrated bioactivity at micro to nanomolar concentrations. *FK1* and *FK2* both induced tube formation in the rat aorta

* All natural product isolation, purification, mass spectral analysis and biological testing were performed by Dr F. Kordbacheh (RSB, ANU), Mrs A. Bezos (JCSMR, ANU), Prof. C. Parish (JCSMR, ANU), Dr C. Hocart (RSB, ANU) and Dr M. Djordjevic (RSB, ANU).

ring assay, however, *FK2* also partially stimulated HUVEC* proliferation in the absence of bFGF†.

FK1 and *FK2* displayed identical mass spectra and UV absorbance spectra, implying that the two fractions were very similar compounds, possibly diastereomers. Large-scale extraction of 2000 mL of xylem sap was performed on 300 plants and yielded 458 µg of *FK1* and 387 µg of *FK2*.

The two purified isolates were presented to our group as lyophilised products with the hope of structural elucidation after identification via mass spectrometry fragmentation analysis at the Research School of Biology (ANU) proved unsuccessful. Initial mass data (Agilent 6530 Accurate Mass LC-MS Q-TOF) implied a chemical formula of C₂₀H₂₂O₆ (*m/z* 359), however, through the NMR structure elucidation process an extra proton signal belonging to the molecule of interest was found. It was proposed that the mass observed was in fact the [M-OH]⁺ peak, implying a formula of C₂₀H₂₄O₇. Further MS studies in both positive and negative modes with a reduced nebulizer spray temperature finally detected the molecular mass peak (M⁺, *m/z* 376) along with fragmentation patterns consistent with previously reported data^{319,320} for the solved NMR structure (Figure 5-1).

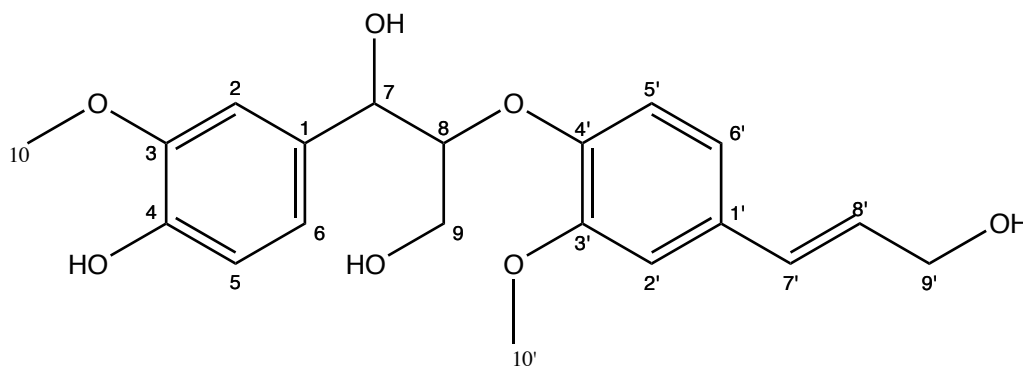


Figure 5-1 Structure of the natural product, guaiacylglycerol-8-*O*-4'-(coniferyl alcohol) ether, with numbering as used in the text. Note the chirality of C-7 and C-8 is undefined, however the double bond C-7'-C-8' was determined to be *trans*.

Initial 1D ¹H NMR spectra were recorded for both *FK1* and *FK2* products. *FK1* was determined to be more pure and of higher concentration, so initial structure determination was performed on this product. ¹³C-HSQC, ¹³C-HMBC, ¹H-¹H

* Human umbilical vein endothelial cells (HUVEC) are used as a model of endothelial cells.

† Basic fibroblast growth factor (bFGF) promotes angiogenesis

DQF-COSY, ^1H - ^1H TOCSY and ^1H - ^1H NOESY NMR spectra were then measured of *FK1* and structural fragments were constructed as follows. Two methoxy resonances were identified in the ^1H NMR spectrum at δ 3.68 (3H, s, **H-10**) and δ 3.70 (3H, s, **H-10'**). Two protons at δ 6.56 (1H, dt, $J = 16.0, 1.0$ Hz, **H-8'**) and δ 6.30 (1H, dt, $J = 15.9, 6.0$ Hz, **H-7'**) were identified in a *trans* double bond arrangement due to their 3J coupling of 16.0 Hz, and were linked to a degenerate methylene group at δ 4.25 (2H, dd, $J = 6.0, 0.9$ Hz, **H₂-9'**) via their 3J and 4J couplings, respectively. Proton signals at δ 4.07 (dd, $^2J = 12.3$ Hz, $^3J = 2.8$ Hz, 1H, **H-9a**) and δ 3.94 (dd, $^2J = 12.3$ Hz, $^3J = 6.7$ Hz, 1H, **H-9b**) were linked through their 2J coupling and their shared carbon shift in the ^{13}C -HSQC spectrum, and were linked to a multiplet at δ 4.66 (m, 1H, **H-8**) via the DQF-COSY. An ABX aromatic coupling system was identified, and positioned the aromatic proton at δ 6.86 (dd, $^3J = 8.1$ Hz, $^4J = 1.9$ Hz, 1H, **H-6**) *meta* from δ 6.88 (d, $^4J = 2.0$ Hz, 1H, **H-2**) and *ortho* to δ 6.74 (d, $^3J = 8.1$ Hz, 1H, **H-5**). Three further aromatic protons were identified and linked via the TOCSY cross-peaks, but needed correlations from the HSQC and HMBC spectra to resolve δ 6.97, (overlapped s, 1H, **H-6'**) as *ortho* to δ 6.97, (overlapped s, 1H, **H-5'**), and *para* to δ 6.98 (bs, 1H, **H-2'**). The HSQC and HMBC spectra were also used to resolve a solvent overlapped peak, $\text{H}\delta$ 4.7 C δ 72.54 (overlapped m, 2H, **H-7**, **C-7**) and link this resonance to C δ 61.52 (**C-9**). The methoxy group **H₃-10** was linked to **H-2** via the NOESY spectrum and to C δ 147.72 (**C-3**) via the HMBC spectrum, which was also linked to **H-6** and **H-5**. Methoxy **H₃-10** was linked to **H-2'** via the NOESY spectrum and to C δ 149.22 (**C-3'**) via the HMBC spectrum, which was further linked to **H-5'** and **H-6'**. NOEs were observed between **H-2'**, **H-5'** and **H-6'** to **H-7'** and **H-8'**, linking these fragments, and was positioned by the HMBC correlation from **H-7'** to C δ 119.45 (**C-6'**) and C δ 109.78 (**C-2'**) as was **H-8'** to C δ 131.13 (**C-1'**). Finally, HMBC correlations between **6-H**, **2-H** and **C-7** and further correlations between **H-8** and C δ 146.94 (**C-4'**) constructed the final compound.

Assignments could easily be made for *FK2* due to the similarity of the ^{13}C -HSQC cross-peaks to those of *FK1* and ^1H - ^1H couplings constants (Figure 5-2). It was then proposed that *FK1* and *FK2* were diastereomers, with undefined chirality of **C-7** and **C-8**. The compound identified (Figure 5-1) was proposed to be the previously described natural product guaiacylglycerol-8-*O*-4'(coniferyl alcohol) ether, of which there are four possible stereoisomers. The NMR spectra were found to be in agreement with previously reported chemical shifts and couplings.³²¹

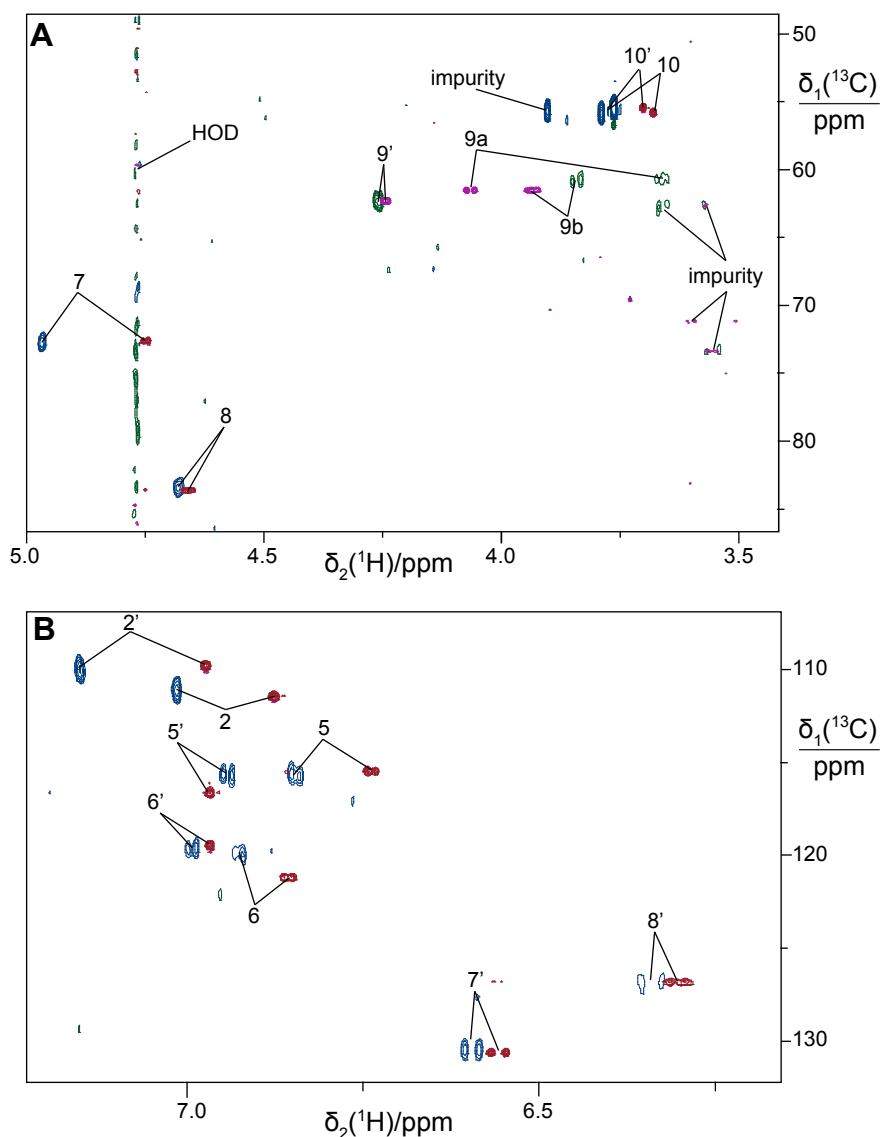


Figure 5-2 Overlay of ^{13}C -HSQC spectra for the **A)** aliphatic and **B)** aromatic region, highlighting the similarity of spectra between FK1 (red/pink) and FK2 (blue/green). Along with coupling constants measured from 1D ^1H NMR spectra, assignments were easily transferred from FK1 to FK2. Negative peaks (green and pink) indicate CH_2 resonances.

A commercial sample of *erythro*-guaiacylglycerol-8-*O*-4'(coniferyl alcohol) ether* and an independently derived sample of *threo*-guaiacylglycerol-8-*O*-4'(coniferyl alcohol) ether (isolated from *Bretshneidera sinensis*)† were obtained. These were found to have almost identical spectroscopic and chromatographic properties to FK1 and FK2.

* BOC Sciences, NY, USA

† Kindly provided by Prof. Wei-Dong Zhang and Dr Shan Lei (Second Military Medical University, Shanghai, China)

Finally, *erythro*- and *threo*-guaiacylglycerol-8-*O*-4'-(coniferyl alcohol) ether were chemically synthesized and assayed for bioactivity.* The synthesised compounds gave similar results to *FK1* and *FK2* in the bioassays, which confirmed the identification of *FK1* and *FK2* as the *erythro*- and *threo*-isomers of guaiacylglycerol-8-*O*-4'-(coniferyl alcohol) ether respectively.

5.2.1 *FK1* Chemical Shifts

$\delta(^1\text{H}, \text{D}_2\text{O}, 800 \text{ MHz})$ 6.88 (d, $^4J=2.0 \text{ Hz}$, 1H, **H-2**), 6.74 (d, $^3J=8.1 \text{ Hz}$, 1H, **H-5**), 6.86 (dd, $^3J=8.1 \text{ Hz}$, $^4J=1.9 \text{ Hz}$, 1H, **H-6**), 4.7 (overlapped m, 2H, **H-7**), 4.66 (m, 1H, **H-8**), 4.07 (dd, $^2J=12.3 \text{ Hz}$, $^3J=2.8 \text{ Hz}$, 1H, **H-9a**), 3.94 (dd, $^2J=12.3 \text{ Hz}$, $^3J=6.7 \text{ Hz}$, 1H, **H-9b**), 3.6824 (s, 3H, **H₃-10**), 6.98 (bs, 1H, **H-2'**), 6.97 (overlapped s, 1H, **H-5'**), 6.97 (overlapped s, 1H, **H-6'**), 6.56 (dt, $^3J=16.0 \text{ Hz}$, $^4J=1 \text{ Hz}$, 1H, **H-7'**), 6.31 (dt, $^3J=15.9 \text{ Hz}$, $^3J=6.0 \text{ Hz}$, 1H, **H-8'**), 4.25 (dd, $^3J=6.0 \text{ Hz}$, $^4J=1.0 \text{ Hz}$, 2H, **H₂-9'**), 3.7041 (s, 3H, **H₃-10'**)

$\delta(^{13}\text{C}, \text{D}_2\text{O}, 201 \text{ MHz})$ 130.60 (**C-1**), 111.38 (**C-2**), 147.72 (**C-3**), 147.2 (**C-4**), 115.42 (**C-5**), 121.13 (**C-6**), 72.54 (**C-7**), 83.56 (**C-8**), 61.52 (**C-9**), 55.69 (**C-10**), 131.13 (**C-1'**), 109.78 (**C-2'**), 149.22 (**C-3'**), 146.94 (**C-4'**), 116.56 (**C-5'**), 119.45 (**C-6'**), 130.61 (**C-7'**), 126.76 (**C-8'**), 62.29 (**C-9'**), 55.46 (**C-10'**)

5.2.2 *FK2* Chemical Shifts

$\delta(^1\text{H}, \text{D}_2\text{O}, 800 \text{ MHz})$ 6.94 (d, $^4J=1.9 \text{ Hz}$, 1H, **H-2**), 6.85 (d, $^3J=8.1 \text{ Hz}$, 1H, **H-5**), 6.85 (overlapped dd, $^3J=8.1 \text{ Hz}$, $^4J=1.7 \text{ Hz}$, 1H, **H-6**), 4.89 (d, $^3J=5.5 \text{ Hz}$, 2H, **H-7**), 4.61 (m, 1H, **H-8**), 3.59 (dd, $^2J=12.2 \text{ Hz}$, $^3J=6.0 \text{ Hz}$, 1H, **H-9a**), 3.77 (dd, $^2J=12.9 \text{ Hz}$, $^3J=3.7 \text{ Hz}$, 1H, **H-9b**), 3.69 (s, 3H, **H₃-10** or **10'**), 7.08 (d, $^4J=1.8 \text{ Hz}$, 1H, **H-2'**), 6.87 (d, $^3J=8.64 \text{ Hz}$, 1H, **H-5'**), 6.92 (dd, $^3J=8.46 \text{ Hz}$, $^4J=1.8 \text{ Hz}$, 1H, **H-6'**), 6.59 (dt, $^3J=15.9 \text{ Hz}$, $^4J=1.0 \text{ Hz}$, 1H, **H-7'**), 6.34 (dt, $^3J=15.8 \text{ Hz}$, $^3J=6.0 \text{ Hz}$, 1H, **H-8'**), 4.18 (dd, $^3J=6.1 \text{ Hz}$, $^4J=1.2 \text{ Hz}$, 2H, **H₂-9'**), 3.71 (s, 3H, **H₃-10'** or **10**)

$\delta(^{13}\text{C}, \text{D}_2\text{O}, 201 \text{ MHz})$ 110.75 (**C-2**), 115.48 (**C-5**), 119.59 (**C-6**), 72.43 (**C-7**), 83.21 (**C-8**), 60.49 (**C-9**), 55.43 (**C-10**), 109.81 (**C-2'**), 115.42 (**C-5'**), 119.48 (**C-6'**), 130.09 (**C-7'**), 126.70 (**C-8'**), 61.95 (**C-9'**), 55.43 (**C-10'**)

* Chemical synthesis performed by J. Buckler (RSC, ANU) and Prof. M. Banwell (RSC, ANU)

5.3 Publication

A journal article describing the complete project is currently in the late stages of drafting prior to submission hopefully in mid 2014.

Kordbacheh, F.; **Carruthers, T.**; Buckler, J.; Bezos, A.; Hocart, C.; Banwell, M.; Parish, C.; Djordjevic, M. (*in drafting – submission planned mid 2014*) Promotion of Mammalian Angiogenesis by Neolignans Derived from Soybean Extracellular Fluids.

5.4 Experimental Methodology

NMR spectroscopy experiments were recorded on either a Bruker AVANCE 800 or 600 MHz NMR spectrometer with TCI cryoprobe using D₂O as the solvent at 298 K. Spectra were analysed using Bruker TopSpin 2.1 software.

¹H NMR chemical shifts in parts per million (ppm) are reported using the HOD signal as an internal chemical shift reference (4.72 ppm at 298 K). ¹³C chemical shifts in ppm are referenced indirectly to the proton shift.

¹H. 1D proton NMR spectra were performed using a standard Bruker pulse program, *zgpr*, which included solvent suppression via pre-saturation. A total experiment time of 5 min was used with a *t*_{1max} of 1.25 sec.

¹H-¹H DQF-COSY.³²² A phase-sensitive DQF-COSY spectrum was also measured using the standard Bruker sequence *cosydfphpr*, which includes a double-quantum filter and pre-saturation. A total experiment time of 38 min was used with a *t*_{1max} of 26 msec and a *t*_{2max} of 104 msec.

¹H-¹H TOCSY.³²³ A TOCSY spectrum was measured using the Bruker pulse program *mlevphpp* that was modified to include pre-saturation. A total experiment time of 19 min was used with a *t*_{1max} of 13 ms, a *t*_{2max} of 250 ms and a TOCSY mixing time of 60 ms.

¹H-¹H NOESY.^{324,325} A NOESY spectrum was recorded using the Bruker pulse program *noesygpshpp* modified to include pre-saturation. A total experiment time of 14.2 hours was used with a *t*_{1max} of 39 ms, a *t*_{2max} of 1.62 sec and a 500 msec NOE mixing time.

^{13}C - ^1H HSQC.³²⁶⁻³²⁸ A ^{13}C -HSQC spectrum was recorded using the standard Bruker pulse sequence hsqcedetgpsisp2.2. A $t_{1\text{max}}$ of 15.3 ms, a $t_{2\text{max}}$ of 152 ms and a total experiment time of 2.3 hrs was used.

^{13}C - ^1H HMBC.³²⁹ A ^{13}C -HMBC spectrum was recorded using the standard Bruker pulse sequence hmbcetgpl2nd, which includes a two-fold low-pass J -filter to suppress one-bond correlations. A $t_{1\text{max}}$ of 10.1 ms, a $t_{2\text{max}}$ of 304 ms and a total experiment time of 8 hrs was used.

6 Cited Literature

1. Mohr, P. J., Taylor, B. N. & Newell, D. B. The 2010 CODATA recommended values of the fundamental physical constants. at <http://physics.nist.gov/constants>
2. Bertini, I., Kowalewski, J., Luchinat, C. & Parigi, G. Cross correlation between the dipole-dipole interaction and the Curie spin relaxation: the effect of anisotropic magnetic susceptibility. *J. Magn. Reson.* **152**, 103–108 (2001).
3. Otting, G. Protein NMR using paramagnetic ions. *Annu. Rev. Biophys.* **39**, 387–405 (2010).
4. Bertini, I., Luchinat, C. & Parigi, G. Paramagnetic constraints: an aid for quick solution structure determination of paramagnetic metalloproteins. *Concepts Magn. Res.* **14**, 259–286 (2002).
5. Iwahara, J., Schwieters, C. D. & Clore, G. M. Ensemble approach for NMR structure refinement against ^1H paramagnetic relaxation enhancement data arising from a flexible paramagnetic group attached to a macromolecule. *J. Am. Chem. Soc.* **126**, 5879–5896 (2004).
6. Kowalewski, J., Kruk, D. & Parigi, G. in *Advances in Inorganic Chemistry* **57**, 41–104 (Elsevier, 2005).
7. Clore, G. M. & Iwahara, J. Theory, practice, and applications of paramagnetic relaxation enhancement for the characterization of transient low-population states of biological macromolecules and their complexes. *Chem. Rev.* **109**, 4108–4139 (2009).
8. Solomon, I. Relaxation processes in a system of two spins. *Phys. Rev.* **99**, 559–565 (1955).
9. Solomon, I. & Bloembergen, N. Nuclear magnetic interactions in the HF molecule. *J. Chem. Phys.* **25**, 261–266 (1956).
10. Bloembergen, N. Spin relaxation processes in a two-proton system. *Phys. Rev.* **104**, 1542–1547 (1956).
11. Ma, L., Jørgensen, A.-M. M., Sørensen, G. O., Ulstrup, J. & Led, J. J. Elucidation of the paramagnetic R_1 relaxation of heteronuclei and protons in Cu(II) plastocyanin from *Anabaena variabilis*. *J. Am. Chem. Soc.* **122**, 9473–9485 (2000).
12. Lauffer, R. B. Paramagnetic metal complexes as water proton relaxation agents for NMR imaging: theory and design. *Chem. Rev.* **87**, 901–927 (1987).
13. Otting, G. Prospects for lanthanides in structural biology by NMR. *J. Biomol. NMR* **42**, 1–9 (2008).
14. Kervern, G., Steuernagel, S., Engelke, F., Pintacuda, G. & Emsley, L. Absence of Curie relaxation in paramagnetic solids yields long ^1H coherence lifetimes. *J. Am. Chem. Soc.* **129**, 14118–14119 (2007).
15. John, M. & Otting, G. Strategies for measurements of pseudocontact shifts in protein NMR spectroscopy. *ChemPhysChem* **8**, 2309–2313 (2007).
16. John, M., Park, A. Y., Dixon, N. E. & Otting, G. NMR detection of protein ^{15}N spins near paramagnetic lanthanide ions. *J. Am. Chem. Soc.* **129**, 462–463 (2007).

17. Bax, A., Kontaxis, G. & Tjandra, N. Dipolar couplings in macromolecular structure determination. *Methods Enzymol.* **339**, 127–174 (2001).
18. Bax, A. Weak alignment offers new NMR opportunities to study protein structure and dynamics. *Protein Sci.* **12**, 1–16 (2003).
19. Bax, A. & Grishaev, A. Weak alignment NMR: a hawk-eyed view of biomolecular structure. *Curr. Opin. Struct. Biol.* **15**, 563–570 (2005).
20. Chen, K. & Tjandra, N. The use of residual dipolar coupling in studying proteins by NMR. *Top. Curr. Chem.* **326**, 47–67 (2012).
21. Pervushin, K., Riek, R., Wider, G. & Wüthrich, K. Attenuated T_2 relaxation by mutual cancellation of dipole-dipole coupling and chemical shift anisotropy indicates an avenue to NMR structures of very large biological macromolecules in solution. *Proc. Natl. Acad. Sci. U.S.A.* **94**, 12366–12371 (1997).
22. Pintacuda, G., Hohenthanner, K., Otting, G. & Müller, N. Angular dependence of dipole-dipole-Curie-spin cross-correlation effects in high-spin and low-spin paramagnetic myoglobin. *J. Biomol. NMR* **27**, 115–132 (2003).
23. Bertini, I., Cavallaro, G., Cosenza, M., Kümmerle, R., Luchinat, C., Piccioli, M. & Poggi, L. Cross correlation rates between Curie spin and dipole-dipole relaxation in paramagnetic proteins: the case of cerium substituted calbindin D_{9k} . *J. Biomol. NMR* **23**, 115–125 (2002).
24. Bertini, I., Luchinat, C., Parigi, G. & Pierattelli, R. NMR spectroscopy of paramagnetic metalloproteins. *ChemBioChem* **6**, 1536–1549 (2005).
25. Bertini, I., Luchinat, C. & Parigi, G. Hyperfine shifts in low-spin iron(III) hemes: A ligand field analysis. *Eur. J. Inorg. Chem.* **2000**, 2473–2480 (2000).
26. Liu, W.-M., Overhand, M. & Ubbink, M. The application of paramagnetic lanthanoid ions in NMR spectroscopy on proteins. *Coord. Chem. Rev.* **273-274**, 2-12 (2014).
27. Keizers, P. H. J., Mersinli, B., Reinle, W., Donauer, J., Hiruma, Y., Hannemann, F., Overhand, M., Bernhardt, R. & Ubbink, M. A solution model of the complex formed by adrenodoxin and adrenodoxin reductase determined by paramagnetic NMR spectroscopy. *Biochemistry* **49**, 6846–6855 (2010).
28. Bertini, I., Luchinat, C. & Parigi, G. *Solution NMR of paramagnetic molecules*. Elsevier, 2001.
29. John, M., Park, A. Y., Pintacuda, G., Dixon, N. E. & Otting, G. Weak alignment of paramagnetic proteins warrants correction for residual CSA effects in measurements of pseudocontact shifts. *J. Am. Chem. Soc.* **127**, 17190–17191 (2005).
30. Schmitz, C., Stanton-Cook, M. J., Su, X.-C., Otting, G. & Huber, T. Numbat: an interactive software tool for fitting $\Delta\chi$ -tensors to molecular coordinates using pseudocontact shifts. *J. Biomol. NMR* **41**, 179–189 (2008).
31. Cornilescu, G. & Bax, A. Measurement of proton, nitrogen, and carbonyl chemical shielding anisotropies in a protein dissolved in a dilute liquid crystalline phase. *J. Am. Chem. Soc.* **122**, 10143–10154 (2000).
32. Li, Q.-F., Yang, Y., Maleckis, A., Otting, G. & Su, X.-C. Thiol-ene reaction: a versatile tool in site-specific labelling of proteins with chemically inert tags for paramagnetic NMR. *Chem. Commun.* **48**, 2704–2706 (2012).
33. Allegrozzi, M., Bertini, I., Janik, M. B. L., Lee, Y.-M., Liu, G. & Luchinat, C. Lanthanide-induced pseudocontact shifts for solution structure refinements of macromolecules in shells up to 40 Å from the metal ion. *J. Am. Chem. Soc.* **122**, 4154–4161 (2000).
34. Stanton-Cook, M., Su, X.-C., Otting, G. & Huber, T. PyParaTools — Software for working with paramagnetic NMR data. at

<<http://comp-bio.anu.edu.au/mscook/PPT/>>

35. Di Pietro, S., Piano, S. L. & Di Bari, L. Pseudocontact shifts in lanthanide complexes with variable crystal field parameters. *Coord. Chem. Rev.* **255**, 2810–2820 (2011).
36. Berardozzi, R. & Di Bari, L. A simple and general method to determine reliable pseudocontact shifts in lanthanide complexes. *Inorg. Chem.* **52**, 11514–11518 (2013).
37. Schmitz, C., Vernon, R., Otting, G., Baker, D. & Huber, T. Protein structure determination from pseudocontact shifts using ROSETTA. *J. Mol. Biol.* **416**, 668–677 (2012).
38. Yagi, H., Pilla, K. B., Maleckis, A., Graham, B., Huber, T. & Otting, G. Three-dimensional protein fold determination from backbone amide pseudocontact shifts generated by lanthanide tags at multiple sites. *Structure* **21**, 883–890 (2013).
39. Simons, K. T., Kooperberg, C., Huang, E. & Baker, D. Assembly of protein tertiary structures from fragments with similar local sequences using simulated annealing and Bayesian scoring functions. *J. Mol. Biol.* **268**, 209–225 (1997).
40. Pintacuda, G., Keniry, M. A., Huber, T., Park, A. Y., Dixon, N. E. & Otting, G. Fast structure-based assignment of ^{15}N HSQC spectra of selectively ^{15}N -labeled paramagnetic proteins. *J. Am. Chem. Soc.* **126**, 2963–2970 (2004).
41. Schmitz, C., John, M., Park, A. Y., Dixon, N. E., Otting, G., Pintacuda, G. & Huber, T. Efficient χ -tensor determination and NH assignment of paramagnetic proteins. *J. Biomol. NMR* **35**, 79–87 (2006).
42. Pintacuda, G., John, M., Su, X.-C. & Otting, G. NMR structure determination of protein-ligand complexes by lanthanide labeling. *Acc. Chem. Res.* **40**, 206–212 (2007).
43. Skinner, S. P., Moshev, M., Hass, M. A. S., Keizers, P. H. J. & Ubbink, M. PARAssign-paramagnetic NMR assignments of protein nuclei on the basis of pseudocontact shifts. *J. Biomol. NMR* **55**, 379–389 (2013).
44. Shishmarev, D. & Otting, G. How reliable are pseudocontact shifts induced in proteins and ligands by mobile paramagnetic metal tags? A modelling study. *J. Biomol. NMR* **56**, 203–216 (2013).
45. Bertini, I., Kursula, P., Luchinat, C., Parigi, G., Vahokoski, J., Wilmanns, M. & Yuan, J. Accurate solution structures of proteins from X-ray data and a minimal set of NMR data: calmodulin-peptide complexes as examples. *J. Am. Chem. Soc.* **131**, 5134–5144 (2009).
46. de la Cruz, L., Nguyen, T. H. D., Ozawa, K., Shin, J., Graham, B., Huber, T. & Otting, G. Binding of low molecular weight inhibitors promotes large conformational changes in the dengue virus NS2B-NS3 protease: fold analysis by pseudocontact shifts. *J. Am. Chem. Soc.* **133**, 19205–19215 (2011).
47. John, M., Pintacuda, G., Park, A. Y., Dixon, N. E. & Otting, G. Structure determination of protein-ligand complexes by transferred paramagnetic shifts. *J. Am. Chem. Soc.* **128**, 12910–12916 (2006).
48. Guan, J.-Y., Keizers, P. H. J., Liu, W.-M., Löhr, F., Skinner, S. P., Heeneman, E. A., Schwalbe, H., Ubbink, M. & Siegal, G. Small-molecule binding sites on proteins established by paramagnetic NMR spectroscopy. *J. Am. Chem. Soc.* **135**, 5859–5868 (2013).
49. Saio, T., Yokochi, M., Kumeta, H. & Inagaki, F. PCS-based structure determination of protein-protein complexes. *J. Biomol. NMR* **46**, 271–280 (2010).
50. Saio, T., Ogura, K., Shimizu, K., Yokochi, M., Burke, T. R. & Inagaki, F. An

- NMR strategy for fragment-based ligand screening utilizing a paramagnetic lanthanide probe. *J. Biomol. NMR* **51**, 395–408 (2011).
51. Hall, B. G. & Barlow, M. Evolution of the serine β -lactamases: past, present and future. *Drug Resist. Updat.* **7**, 111–123 (2004).
 52. Drawz, S. M. & Bonomo, R. A. Three decades of β -lactamase inhibitors. *Clin. Microbiol. Rev.* **23**, 160–201 (2010).
 53. Palzkill, T. Metallo- β -lactamase structure and function. *Ann. N.Y. Acad. Sci.* **1277**, 91–104 (2013).
 54. Sigma-Aldrich Co. LLC. Australia | Sigma-Aldrich. *Sigma-Aldrich* (2014). at <<http://sigmaaldrich.com>>
 55. Szabo, D., Silveira, F., Hujer, A. M., Bonomo, R. A., Hujer, K. M., Marsh, J. W., Bethel, C. R., Doi, Y., Deeley, K. & Paterson, D. L. Outer membrane protein changes and efflux pump expression together may confer resistance to ertapenem in *Enterobacter cloacae*. *Antimicrob. Agents Chemother.* **50**, 2833–2835 (2006).
 56. Mammeri, H., Nordmann, P., Berkani, A. & Eb, F. Contribution of extended-spectrum AmpC (ESAC) β -lactamases to carbapenem resistance in *Escherichia coli*. *FEMS Microbiol. Lett.* **282**, 238–240 (2008).
 57. Bebrone, C. Metallo- β -lactamases (classification, activity, genetic organization, structure, zinc coordination) and their superfamily. *Biochem. Pharmacol.* **74**, 1686–1701 (2007).
 58. Abraham, E. P. & Chain, E. An enzyme from bacteria able to destroy penicillin. *Nature* **146**, 837–837 (1940).
 59. Jacoby, G. A. & Bush, K. β -lactamase classification and amino acid sequences for TEM, SHV and OXA extended-spectrum and inhibitor resistant enzymes. *Lahey Clinic* at <<http://www.lahey.org/Studies/>>
 60. Ambler, R. P. The structure of β -lactamases. *Philos. T. R. Soc. Lon. B* **289**, 321–331 (1980).
 61. Jaurin, B. & Grundström, T. *ampC* cephalosporinase of *Escherichia coli* K-12 has a different evolutionary origin from that of β -lactamases of the penicillinase type. *Proc. Natl. Acad. Sci. U.S.A.* **78**, 4897–4901 (1981).
 62. Ouellette, M., Bissonnette, L. & Roy, P. H. Precise insertion of antibiotic resistance determinants into Tn21-like transposons: nucleotide sequence of the OXA-1 beta-lactamase gene. *Proc. Natl. Acad. Sci. U.S.A.* **84**, 7378–7382 (1987).
 63. Massova, I. & Mobashery, S. Kinship and diversification of bacterial penicillin-binding proteins and β -lactamases. *Antimicrob. Agents Chemother.* **42**, 1–17 (1998).
 64. Walther-Rasmussen, J. & Høiby, N. OXA-type carbapenemases. *J. Antimicrob. Chemother.* **57**, 373–383 (2006).
 65. Ambler, R. P., Coulson, A. F., Frère, J.-M., Ghuysen, J. M., Joris, B., Forsman, M., Levesque, R. C., Tiraby, G. & Waley, S. G. A standard numbering scheme for the class A β -lactamases. *Biochem. J.* **276**, 269–270 (1991).
 66. Couture, F., Lachapelle, J. & Levesque, R. C. Phylogeny of LCR-1 and OXA-5 with class A and class D β -lactamases. *Mol. Microbiol.* **6**, 1693–1705 (1992).
 67. Garau, G., García-Sáez, I., Bebrone, C., Anne, C., Mercuri, P., Galleni, M., Frère, J.-M. & Dideberg, O. Update of the standard numbering scheme for class B β -lactamases. *Antimicrob. Agents Chemother.* **48**, 2347–2349 (2004).
 68. Jacoby, G. A. AmpC β -lactamases. *Clin. Microbiol. Rev.* **22**, 161–182 (2009).
 69. Hall, B. G., Salipante, S. J. & Barlow, M. The metallo- β -lactamases fall into two distinct phylogenetic groups. *J. Mol. Evol.* **57**, 249–254 (2003).

70. Hall, B. G. & Barlow, M. Revised Ambler classification of β -lactamases. *J. Antimicrob. Chemother.* **55**, 1050–1051 (2005).
71. Frère, J.-M., Galleni, M., Bush, K. & Dideberg, O. Is it necessary to change the classification of β -lactamases? *J. Antimicrob. Chemother.* **55**, 1051–1053 (2005).
72. Bush, K. Characterization of β -lactamases. *Antimicrob. Agents Chemother.* **33**, 259–263 (1989).
73. Bush, K. Classification of β -lactamases: groups 1, 2a, 2b, and 2b'. *Antimicrob. Agents Chemother.* **33**, 264–270 (1989).
74. Bush, K. Classification of β -lactamases: groups 2c, 2d, 2e, 3, and 4. *Antimicrob. Agents Chemother.* **33**, 271–276 (1989).
75. Bush, K., Jacoby, G. A. & Medeiros, A. A. A functional classification scheme for β -lactamases and its correlation with molecular structure. *Antimicrob. Agents Chemother.* **39**, 1211–1233 (1995).
76. Bush, K. & Jacoby, G. A. Updated Functional Classification of β -Lactamases. *Antimicrob. Agents Chemother.* **54**, 969–976 (2010).
77. Woodford, N., Tierno, P. M., Young, K., Tysall, L., Palepou, M.-F. I., Ward, E., Painter, R. E., Suber, D. F., Shungu, D., Silver, L. L., Inglis, K., Kornblum, J. & Livermore, D. M. Outbreak of *Klebsiella pneumoniae* producing a new carbapenem-hydrolyzing class A β -lactamase, KPC-3, in a New York Medical Center. *Antimicrob. Agents Chemother.* **48**, 4793–4799 (2004).
78. Samra, Z., Ofir, O., Lishtzinsky, Y., Madar-Shapiro, L. & Bishara, J. Outbreak of carbapenem-resistant *Klebsiella pneumoniae* producing KPC-3 in a tertiary medical centre in Israel. *Int. J. Antimicrob. Ag.* **30**, 525–529 (2007).
79. Laraki, N., Franceschini, N., Rossolini, G. M., Santucci, P., Meunier, C., de Pauw, E., Amicosante, G., Frère, J.-M. & Galleni, M. Biochemical characterization of the *Pseudomonas aeruginosa* 101/1477 metallo- β -lactamase IMP-1 produced by *Escherichia coli*. *Antimicrob. Agents Chemother.* **43**, 902–906 (1999).
80. Marchiaro, P., Ballerini, V., Spalding, T., Cera, G., Mussi, M. A., Morán-Barrio, J., Vila, A. J., Viale, A. M. & Limansky, A. S. A convenient microbiological assay employing cell-free extracts for the rapid characterization of Gram-negative carbapenemase producers. *J. Antimicrob. Chemother.* **62**, 336–344 (2008).
81. Costello, A. L., Sharma, N. P., Yang, K.-W., Crowder, M. W. & Tierney, D. L. X-ray absorption spectroscopy of the zinc-binding sites in the class B2 metallo- β -lactamase ImiS from *Aeromonas veronii* bv. *sobria*. *Biochemistry* **45**, 13650–13658 (2006).
82. Xu, D., Xie, D. & Guo, H. Catalytic mechanism of class B2 metallo- β -lactamase. *J. Biol. Chem.* **281**, 8740–8747 (2006).
83. Brown, A. G., Butterworth, D., Cole, M., Hanscomb, G., Hood, J. D., Reading, C. & Rolinson, G. N. Naturally-occurring β -lactamase inhibitors with antibacterial activity. *J. Antibiot.* **29**, 668–669 (1976).
84. Reading, C. & Cole, M. Clavulanic acid: a beta-lactamase-inhibiting beta-lactam from *Streptomyces clavuligerus*. *Antimicrob. Agents Chemother.* **11**, 852–857 (1977).
85. Neu, H. C. & Fu, K. P. Clavulanic acid, a novel inhibitor of β -lactamases. *Antimicrob. Agents Chemother.* **14**, 650–655 (1978).
86. Howarth, T. T., Brown, A. G. & King, T. J. Clavulanic acid, a novel β -lactam isolated from *Streptomyces clavuligerus*; X-ray crystal structure analysis.

- Chem. Commun.* 266–267 (1976).
87. English, A. R., Retsema, J. A., Girard, A. E., Lynch, J. E. & Barth, W. E. CP-45,899, a beta-lactamase inhibitor that extends the antibacterial spectrum of beta-lactams: initial bacteriological characterization. *Antimicrob. Agents Chemother.* **14**, 414–419 (1978).
 88. Fisher, J., Belasco, J. G., Charnas, R. L., Khosla, S. & Knowles, J. R. β -lactamase inactivation by mechanism-based reagents. *Philos. Trans. R. Soc. Lond. B* **289**, 309–319 (1980).
 89. Aronoff, S. C., Jacobs, M. R., Johenning, S. & Yamabe, S. Comparative activities of the β -lactamase inhibitors YTR 830, sodium clavulanate, and sulbactam combined with amoxicillin or ampicillin. *Antimicrob. Agents Chemother.* **26**, 580–582 (1984).
 90. Lim, H. M., Pène, J. J. & Shaw, R. W. Cloning, nucleotide sequence, and expression of the *Bacillus cereus* 5/B/6 β -lactamase II structural gene. *J. Bacteriol.* **170**, 2873–2878 (1988).
 91. Walsh, T. R., Hall, L., Assinder, S. J., Nichols, W. W., Cartwright, S. J., MacGowan, A. P. & Bennett, P. M. Sequence analysis of the L1 metallo- β -lactamase from *Xanthomonas maltophilia*. *Biochim. Biophys. Acta* **1218**, 199–201 (1994).
 92. Rossolini, G. M. Acquired metallo- β -lactamases: An increasing clinical threat. *Clin. Infect. Dis.* **41**, 1557–1558 (2005).
 93. Stoczko, M., Frère, J.-M., Rossolini, G. M. & Docquier, J. D. Functional diversity among metallo- β -lactamases: Characterization of the CAR-1 enzyme of *Erwinia carotovora*. *Antimicrob. Agents Chemother.* **52**, 2473–2479 (2008).
 94. Pfeifer, Y., Cullik, A. & Witte, W. Resistance to cephalosporins and carbapenems in Gram-negative bacterial pathogens. *Int. J. Med. Microbiol.* **300**, 371–379 (2010).
 95. Cornaglia, G., Mazzariol, A., Lauretti, L., Rossolini, G. M. & Fontana, R. Hospital outbreak of carbapenem-resistant *Pseudomonas aeruginosa* producing VIM-1, a novel transferable metallo- β -lactamase. *Clin. Infect. Dis.* **31**, 1119–1125 (2000).
 96. Hirakata, Y., Yamaguchi, T., Nakano, M., Izumikawa, K., Mine, M., Aoki, S., Kondoh, A., Matsuda, J., Hirayama, M., Yanagihara, K., Miyazaki, Y., Tomono, K., Yamada, Y., Kamihira, S. & Kohno, S. Clinical and bacteriological characteristics of IMP-type metallo- β -lactamase-producing *Pseudomonas aeruginosa*. *Clin. Infect. Dis.* **37**, 26–32 (2003).
 97. Cornaglia, G., Akova, M., Amicosante, G., Cantón, R., Cauda, R., Docquier, J.-D., Edelstein, M., Frère, J.-M., Fuzi, M., Galleni, M., Giamarellou, H., Gniadkowski, M., Koncan, R., Libisch, B., Luzzaro, F., Miriagou, V., Navarro, F., Nordmann, P., Pagani, L., Peixe, L., Poirel, L., Souli, M., Tacconelli, E., Vatopoulos, A. & Rossolini, G. M. Metallo- β -lactamases as emerging resistance determinants in Gram-negative pathogens: open issues. *Int. J. Antimicrob. Ag.* **29**, 380–388 (2007).
 98. Herbert, S., Halvorsen, D. S., Leong, T., Franklin, C., Harrington, G. & Spelman, D. Large outbreak of infection and colonization with Gram-negative pathogens carrying the metallo- β -lactamase gene *bla*_{IMP-4} at a 320-bed tertiary hospital in Australia. *Infect. Cont. Hosp. Ep.* **28**, 98–101 (2007).
 99. Yong, D., Toleman, M. A., Giske, C. G., Cho, H. S., Sundman, K., Lee, K. & Walsh, T. R. Characterization of a new metallo- β -lactamase gene, *bla*_{NDM-1}, and a novel erythromycin esterase gene carried on a unique genetic structure in *Klebsiella pneumoniae* sequence type 14 from India. *Antimicrob. Agents*

- Chemother.* **53**, 5046–5054 (2009).
100. Oelschlaeger, P., Schmid, R. D. & Pleiss, J. Insight into the mechanism of the IMP-1 metallo- β -lactamase by molecular dynamics simulations. *Protein Eng.* **16**, 341–350 (2003).
 101. Kaase, M., Nordmann, P., Wichelhaus, T. A., Gatermann, S. G., Bonnin, R. A. & Poirel, L. NDM-2 carbapenemase in *Acinetobacter baumannii* from Egypt. *J. Antimicrob. Chemother.* **66**, 1260–1262 (2011).
 102. Nordmann, P., Boulanger, A. E. & Poirel, L. NDM-4 metallo- β -lactamase with increased carbapenemase activity from *Escherichia coli*. *Antimicrob. Agents Chemother.* **56**, 2184–2186 (2012).
 103. Göttig, S., Hamprecht, A. G., Christ, S., Kempf, V. A. J. & Wichelhaus, T. A. Detection of NDM-7 in Germany, a new variant of the New Delhi metallo- β -lactamase with increased carbapenemase activity. *J. Antimicrob. Chemother.* **68**, 1737–1740 (2013).
 104. Hornsey, M., Phee, L. & Wareham, D. W. A novel variant, NDM-5, of the New Delhi metallo- β -lactamase in a multidrug-resistant *Escherichia coli* ST648 isolate recovered from a patient in the United Kingdom. *Antimicrob. Agents Chemother.* **55**, 5952–5954 (2011).
 105. Rogers, B. A., Sidjabat, H. E., Silvey, A., Anderson, T. L., Perera, S., Li, J. & Paterson, D. L. Treatment options for New Delhi metallo-beta-lactamase-harboring *Enterobacteriaceae*. *Microb. Drug Resist.* **19**, 100–103 (2013).
 106. Poirel, L., Lagrutta, E., Taylor, P., Pham, J. & Nordmann, P. Emergence of metallo- β -lactamase NDM-1-producing multidrug-resistant *Escherichia coli* in Australia. *Antimicrob. Agents Chemother.* **54**, 4914–4916 (2010).
 107. Shoma, S., Kamruzzaman, M., Ginn, A. N., Iredell, J. R. & Partridge, S. R. Characterization of multidrug-resistant *Klebsiella pneumoniae* from Australia carrying *bla*_{NDM-1}. *Diagn. Microbiol. Infect. Dis.* **78**, 93–97 (2014).
 108. Pollini, S., Maradei, S., Pecile, P., Olivo, G., Luzzaro, F., Docquier, J.-D. & Rossolini, G. M. FIM-1, a new acquired metallo- β -lactamase from a *Pseudomonas aeruginosa* clinical isolate from Italy. *Antimicrob. Agents Chemother.* **57**, 410–416 (2013).
 109. Horton, L. B., Shanker, S., Mikulski, R., Brown, N. G., Phillips, K. J., Lykissa, E., Venkataram Prasad, B. V. & Palzkill, T. Mutagenesis of zinc ligand residue Cys221 reveals plasticity in the IMP-1 metallo- β -lactamase active site. *Antimicrob. Agents Chemother.* **56**, 5667–5677 (2012).
 110. Walsh, T. R., Toleman, M. A., Poirel, L. & Nordmann, P. Metallo- β -lactamases: the quiet before the storm? *Clin. Microbiol. Rev.* **18**, 306–325 (2005).
 111. Zhang, H. & Hao, Q. Crystal structure of NDM-1 reveals a common β -lactam hydrolysis mechanism. *FASEB J.* **25**, 2574–2582 (2011).
 112. King, D. T., Worrall, L. J., Gruninger, R. & Strynadka, N. C. J. New Delhi metallo- β -lactamase: structural insights into β -lactam recognition and inhibition. *J. Am. Chem. Soc.* **134**, 11362–11365 (2012).
 113. Yuan, Q., He, L. & Ke, H. A potential substrate binding conformation of β -lactams and insight into the broad spectrum of NDM-1 activity. *Antimicrob. Agents Chemother.* **56**, 5157–5163 (2012).
 114. Notake, S., Matsuda, M., Tamai, K., Yanagisawa, H., Hiramatsu, K. & Kikuchi, K. Detection of IMP metallo- β -lactamase in carbapenem-nonsusceptible *Enterobacteriaceae* and non-glucose-fermenting Gram-negative rods by immunochromatography assay. *J. Clin. Microbiol.* **51**, 1762–1768 (2013).
 115. Nagano, R., Adachi, Y., Imamura, H., Yamada, K., Hashizume, T. &

- Morishima, H. Carbapenem derivatives as potential inhibitors of various β -lactamases, including class B metallo- β -lactamases. *Antimicrob. Agents Chemother.* **43**, 2497–2503 (1999).
116. Siemann, S., Clarke, A. J., Viswanatha, T. & Dmitrienko, G. I. Thiols as classical and slow-binding inhibitors of IMP-1 and other binuclear metallo- β -lactamases. *Biochemistry* **42**, 1673–1683 (2003).
 117. Kurosaki, H., Yasuzawa, H., Yamaguchi, Y., Jin, W., Arakawa, Y. & Goto, M. Detection of a metallo- β -lactamase (IMP-1) by fluorescent probes having dansyl and thiol groups. *Org. Biomol. Chem.* **1**, 17–20 (2003).
 118. Kurosaki, H., Yamaguchi, Y., Higashi, T., Soga, K., Matsueda, S., Yumoto, H., Misumi, S., Yamagata, Y., Arakawa, Y. & Goto, M. Irreversible inhibition of metallo- β -lactamase (IMP-1) by 3-(3-mercaptopropionylsulfanyl)propionic acid pentafluorophenyl ester. *Angew. Chem. Int. Ed.* **44**, 3861–3864 (2005).
 119. Hammond, G. G., Huber, J. L., Greenlee, M. L., Laub, J. B., Young, K., Silver, L. L., Balkovec, J. M., Pryor, K. D., Wu, J. K., Leiting, B., Pompliano, D. L. & Toney, J. H. Inhibition of IMP-1 metallo- β -lactamase and sensitization of IMP-1-producing bacteria by thioester derivatives. *FEMS Microbiol. Lett.* **179**, 289–296 (1999).
 120. Toney, J. H., Hammond, G. G., Fitzgerald, P. M. D., Sharma, N. P., Balkovec, J. M., Rouen, G. P., Olson, S. H., Hammond, M. L., Greenlee, M. L. & Gao, Y.-D. Succinic acids as potent inhibitors of plasmid-borne IMP-1 metallo- β -lactamase. *J. Biol. Chem.* **276**, 31913–31918 (2001).
 121. Siemann, S., Evanoff, D. P., Marrone, L. & Clarke, A. J. *N*-arylsulfonyl hydrazones as inhibitors of IMP-1 metallo- β -lactamase. *Antimicrob. Agents Chemother.* **46**, 2450–2457 (2002).
 122. Payne, D. J., Hueso-Rodríguez, J. A., Boyd, H., Concha, N. O., Janson, C. A., Gilpin, M., Bateson, J. H., Cheever, C., Niconovich, N. L., Pearson, S., Rittenhouse, S., Tew, D., Díez, E., Pérez, P., La Fuente, De, J., Rees, M. & Rivera-Sagredo, A. Identification of a series of tricyclic natural products as potent broad-spectrum inhibitors of metallo- β -lactamases. *Antimicrob. Agents Chemother.* **46**, 1880–1886 (2002).
 123. Heinz, U., Bauer, R., Wommer, S., Meyer-Klaucke, W., Papamichaels, C., Bateson, J. H. & Adolph, H.-W. Coordination Geometries of Metal Ions in D- or L-captopril-inhibited metallo- β -lactamases. *J. Biol. Chem.* **278**, 20659–20666 (2003).
 124. Antony, J., Gresh, N., Olsen, L., Hemmingsen, L., Schofield, C. J. & Bauer, R. Binding of D- or L-captopril inhibitors to metallo- β -lactamase studied by polarizable molecular mechanics and quantum mechanics. *J. Comput. Chem.* **23**, 1281–1296 (2002).
 125. Antony, J., Piquemal, J.-P. & Gresh, N. Complexes of thiomandelate and captopril mercaptocarboxylate inhibitors to metallo- β -lactamase by polarizable molecular mechanics. Validation on model binding sites by quantum chemistry. *J. Comput. Chem.* **26**, 1131–1147 (2005).
 126. Fast, W. & Sutton, L. D. Metallo- β -lactamase: Inhibitors and reporter substrates. *BBA-Proteins Proteom.* **1834**, 1648–1659 (2013).
 127. Morán-Barrio, J., Limansky, A. S. & Viale, A. M. Secretion of GOB metallo- β -lactamase in *Escherichia coli* depends strictly on the cooperation between the cytoplasmic DnaK chaperone system and the Sec machinery: completion of folding and Zn(II) ion acquisition occur in the bacterial periplasm. *Antimicrob. Agents Chemother.* **53**, 2908–2917 (2009).
 128. Wang, Z. & Benkovic, S. J. Purification, characterization, and kinetic studies of

- a soluble *Bacteroides fragilis* metallo- β -lactamase that provides multiple antibiotic resistance. *J. Biol. Chem.* **273**, 22402–22408 (1998).
129. Neuwald, A. F., Liu, J. S., Lipman, D. J. & Lawrence, C. E. Extracting protein alignment models from the sequence database. *Nucleic Acids Res.* **25**, 1665–1677 (1997).
 130. Campos-Bermudez, V. A., González, J. M., Tierney, D. L. & Vila, A. J. Spectroscopic signature of a ubiquitous metal binding site in the metallo- β -lactamase superfamily. *J. Biol. Inorg. Chem.* **15**, 1209–1218 (2010).
 131. Daiyasu, H., Osaka, K., Ishino, Y. & Toh, H. Expansion of the zinc metallo-hydrolase family of the β -lactamase fold. *FEBS Lett.* **503**, 1–6 (2001).
 132. Jacoby, G. A. β -lactamase nomenclature. *Antimicrob. Agents Chemother.* **50**, 1123–1129 (2006).
 133. Watanabe, M., Iyobe, S., Inoue, M. & Mitsuhashi, S. Transferable imipenem resistance in *Pseudomonas aeruginosa*. *Antimicrob. Agents Chemother.* **35**, 147–151 (1991).
 134. Zhao, W.-H. & Hu, Z.-Q. IMP-type metallo- β -lactamases in Gram-negative bacilli: distribution, phylogeny, and association with integrons. *Crit. Rev. Microbiol.* **37**, 214–226 (2011).
 135. Hanson, N. D., Thomson, K. S. & Moulds, N. M. *Proteus mirabilis* strain PmCB1 metallo- β -lactamase IMP-27 gene, complete cds. *GenBank Direct Submission* (2011). at <<http://www.ncbi.nlm.nih.gov/nucore/JF894248>>
 136. Pérez-Llarena, F. J., Fernández, A., Zamorano, L., Kerff, F., Beceiro, A., Aracil, B., Cercenado, E., Miro, E., Oliver, A., Oteo, J., Navarro, F. & Bou, G. Characterization of a novel IMP-28 metallo- β -lactamase from a Spanish *Klebsiella oxytoca* clinical isolate. *Antimicrob. Agents Chemother.* **56**, 4540–4543 (2012).
 137. Jeannot, K., Poirel, L., Robert-Nicoud, M., Cholley, P., Nordmann, P. & Plésiat, P. IMP-29, a novel IMP-type metallo- β -lactamase in *Pseudomonas aeruginosa*. *Antimicrob. Agents Chemother.* **56**, 2187–2190 (2012).
 138. Osano, E., Arakawa, Y., Wacharotayankun, R., Ohta, M., Horii, T., Ito, H., Yoshimura, F. & Kato, N. Molecular characterization of an enterobacterial metallo β -lactamase found in a clinical isolate of *Serratia marcescens* that shows imipenem resistance. *Antimicrob. Agents Chemother.* **38**, 71–78 (1994).
 139. Liu, E. M., Pegg, K. M. & Oelschlaeger, P. The sequence-activity relationship between metallo- β -lactamases IMP-1, IMP-6, and IMP-25 suggests an evolutionary adaptation to meropenem exposure. *Antimicrob. Agents Chemother.* **56**, 6403–6406 (2012).
 140. Riccio, M. L., Franceschini, N., Boschi, L., Caravelli, B., Cornaglia, G., Fontana, R., Amicosante, G. & Rossolini, G. M. Characterization of the metallo- β -lactamase determinant of *Acinetobacter baumannii* AC-54/97 reveals the existence of *bla*_{IMP} allelic variants carried by gene cassettes of different phylogeny. *Antimicrob. Agents Chemother.* **44**, 1229–1235 (2000).
 141. Koh, T. H., Khoo, C. T., Tan, T. T., Arshad, M. A. B. M., Ang, L. P., Lau, L. J., Hsu, L.-Y. & Ooi, E. E. Multilocus sequence types of carbapenem-resistant *Pseudomonas aeruginosa* in Singapore carrying metallo- β -lactamase genes, including the novel *bla*_{IMP-26} gene. *J. Clin. Microbiol.* **48**, 2563–2564 (2010).
 142. Iyobe, S., Kusadokoro, H., Ozaki, J., Matsumura, N., Minami, S., Haruta, S., Sawai, T. & O'Hara, K. Amino acid substitutions in a variant of IMP-1 metallo- β -lactamase. *Antimicrob. Agents Chemother.* **44**, 2023–2027 (2000).
 143. Chu, Y.-W., Afzal-Shah, M., Houang, E. T. S., Palepou, M.-F. I., Lyon, D. J., Woodford, N. & Livermore, D. M. IMP-4, a novel metallo- β -lactamase from

- nosocomial *Acinetobacter* spp. collected in Hong Kong between 1994 and 1998. *Antimicrob. Agents Chemother.* **45**, 710–714 (2001).
144. Da Silva, G. J., Correia, M., Vital, C., Ribeiro, G., Sousa, J. C., Leitão, R., Peixe, L. & Duarte, A. Molecular characterization of *bla*_{IMP-5}, a new integron-borne metallo- β -lactamase gene from an *Acinetobacter baumannii* nosocomial isolate in Portugal. *FEMS Microbiol. Lett.* **215**, 33–39 (2002).
 145. Yano, H., Kuga, A., Okamoto, R., Kitasato, H., Kobayashi, T. & Inoue, M. Plasmid-encoded metallo- β -lactamase (IMP-6) conferring resistance to carbapenems, especially meropenem. *Antimicrob. Agents Chemother.* **45**, 1343–1348 (2001).
 146. Pegg, K. M., Liu, E. M., Lacuran, A. E. & Oelschlaeger, P. Biochemical characterization of IMP-30, a metallo- β -lactamase with enhanced activity toward ceftazidime. *Antimicrob. Agents Chemother.* **57**, 5122–5126 (2013).
 147. Ho, S. E., Subramaniam, G., Palasubramaniam, S. & Navaratnam, P. Carbapenem-resistant *Pseudomonas aeruginosa* in Malaysia producing IMP-7 β -lactamase. *Antimicrob. Agents Chemother.* **46**, 3286–3287 (2002).
 148. Pfennigwerth, N., Gatermann, S. G. & Kaase, M. Description of IMP-31, a novel metallo- β -lactamase found in a ST235 *Pseudomonas aeruginosa* in Western Germany. *GenBank Direct Submission* (2013). at <<http://www.ncbi.nlm.nih.gov/nuccore/KF148593>>
 149. Yan, J. J., Ko, W. C. & Wu, J. J. Identification of a plasmid encoding SHV-12, TEM-1, and a variant of IMP-2 metallo- β -lactamase, IMP-8, from a clinical isolate of *Klebsiella pneumoniae*. *Antimicrob. Agents Chemother.* **45**, 2368–2371 (2001).
 150. Tribuddharat, C., Prombhul, S., Tulanont, D., Aranya, C., Bamrungsri, N. & Mekviwattanawong, S. Fatal pneumonia by *Klebsiella pneumoniae* producing new variant of *bla*_{IMP} allele, *bla*_{IMP-32}. *GenBank Direct Submission* (2012). at <<http://www.ncbi.nlm.nih.gov/nuccore/JQ002629>>
 151. Xiong, J., Hynes, M. F., Ye, H., Chen, H., Yang, Y., M'zali, F. & Hawkey, P. M. *bla*_{IMP-9} and its association with large plasmids carried by *Pseudomonas aeruginosa* isolates from the People's Republic of China. *Antimicrob. Agents Chemother.* **50**, 355–358 (2006).
 152. Deshpande, L. M., Davies, T. A., Blandino, G., Nicoletti, G., Jones, R. N. & Castanheira, M. IMP-33, a New IMP variant detected in *Pseudomonas aeruginosa* from Sicily. *Antimicrob. Agents Chemother.* **57**, 6401–6403 (2013).
 153. Iyobe, S., Kusadokoro, H., Takahashi, A., Yomoda, S., Okubo, T., Nakamura, A. & O'Hara, K. Detection of a variant metallo- β -lactamase, IMP-10, from two unrelated strains of *Pseudomonas aeruginosa* and an *Alcaligenes xylosoxidans* strain. *Antimicrob. Agents Chemother.* **46**, 2014–2016 (2002).
 154. Shigemoto, N., Kayama, S., Kuwahara, R., Hisatsune, J., Kato, F., Nishio, H., Yamasaki, K., Wada, Y., Sueda, T., Ohge, H. & Sugai, M. A novel metallo- β -lactamase, IMP-34, in *Klebsiella* isolates with decreased resistance to imipenem. *Diagn. Microbiol. Infect. Dis.* **76**, 119–121 (2013).
 155. Iyobe, S., Murayama, S., Takahashi, A., Yomoda, S., Okubo, T. & Nakamura, A. A novel gene encoding variant metallo- β -lactamase IMP-11 derived from *Acinetobacter baumannii* and *Pseudomonas aeruginosa* strains. *GenBank Direct Submission* (2001). at <<http://www.ncbi.nlm.nih.gov/nuccore/AB074436>>
 156. Pournaras, S., Köck, R., Mossialos, D., Mellmann, A., Sakellaris, V., Stathopoulos, C., Friedrich, A. W. & Tsakris, A. Detection of a phylogenetically distinct IMP-type metallo- β -lactamase, IMP-35, in a CC235

- Pseudomonas aeruginosa* from the Dutch-German border region (Euregio). *J. Antimicrob. Chemother.* **68**, 1271–1276 (2013).
157. Docquier, J.-D., Riccio, M. L., Mugnaioli, C., Luzzaro, F., Endimiani, A., Toniolo, A., Amicosante, G. & Rossolini, G. M. IMP-12, a new plasmid-encoded metallo- β -lactamase from a *Pseudomonas putida* clinical isolate. *Antimicrob. Agents Chemother.* **47**, 1522–1528 (2003).
 158. Toleman, M. A., Biedenbach, D., Bennett, D., Jones, R. N. & Walsh, T. R. Genetic characterization of a novel metallo- β -lactamase gene, *bla*_{IMP-13}, harboured by a novel Tn5051-type transposon disseminating carbapenemase genes in Europe: report from the SENTRY worldwide antimicrobial surveillance programme. *J. Antimicrob. Chemother.* **52**, 583–590 (2003).
 159. Fournier, D., Jeannot, K., Robert-Nicoud, M., Muller, E., Cholley, P., van der Mee-Marquet, N. & Plésiat, P. Spread of the *bla*_{IMP-13} gene in French *Pseudomonas aeruginosa* through sequence types ST621, ST308 and ST111. *Int. J. Antimicrob. Ag.* **40**, 571–573 (2012).
 160. Tribuddharat, C., Wilailuckana, C., Tiensasitorn, C., Techachaiwiwat, W., Rugdeekha, S., Naenna, P., Pongpech, P., Srifuengfung, S., Dhiraputra, C. & Danchaivijitr, S. New variants of class B β -lactamases, IMP-14 and IMP-15, in *Pseudomonas aeruginosa* clinical isolates from Thailand. *GenBank Direct Submission* (2005). at <<http://www.ncbi.nlm.nih.gov/nucleotide/AY553332>>
 161. Liu, W. & Jian, Z. A new IMP-type metallo- β -lactamase in *Klebsiella pneumoniae* isolates in China. *GenBank Direct Submission* (2012). at <<http://www.ncbi.nlm.nih.gov/nucleotide/HQ875573>>
 162. Garza-Ramos, U., Morfin-Otero, R., Sader, H. S., Jones, R. N., Hernández, E., Rodriguez-Noriega, E., Sanchez, A., Carrillo, B., Esparza-Ahumada, S. & Silva-Sanchez, J. Metallo- β -lactamase gene *bla*_{IMP-15} in a class 1 integron, In95, from *Pseudomonas aeruginosa* clinical isolates from a hospital in Mexico. *Antimicrob. Agents Chemother.* **52**, 2943–2946 (2008).
 163. Mendes, R. E., Toleman, M. A., Ribeiro, J., Sader, H. S., Jones, R. N. & Walsh, T. R. Integron carrying a novel metallo- β -lactamase gene, *bla*_{IMP-16}, and a fused form of aminoglycoside-resistant gene *aac(6')-30/aac(6'')-Ib*: report from the SENTRY Antimicrobial Surveillance Program. *Antimicrob. Agents Chemother.* **48**, 4693–4702 (2004).
 164. Kikuchi, K., Notake, S., Matsuda, M., Tamai, K., Yanagisawa, H. & Hiramatsu, K. Detection of IMP-type metallo- β -lactamase in *Enterobacteriaceae* and glucose non-fermenting Gram-negative rods by immunochromatography. *GenBank Direct Submission* (2012). at <<http://www.ncbi.nlm.nih.gov/nucleotide/AB753457>>
 165. Hanson, N. D., Hossain, A., Buck, L., Moland, E. S. & Thomson, K. S. First occurrence of a *Pseudomonas aeruginosa* isolate in the United States producing an IMP metallo- β -lactamase, IMP-18. *Antimicrob. Agents Chemother.* **50**, 2272–2273 (2006).
 166. Neuwirth, C., Siebor, E., Robin, F. & Bonnet, R. First occurrence of an IMP metallo- β -lactamase in *Aeromonas caviae*: IMP-19 in an isolate from France. *Antimicrob. Agents Chemother.* **51**, 4486–4488 (2007).
 167. Tada, T., Miyoshi-Akiyama, T., Shimada, K., Shimojima, M. & Kirikae, T. IMP-43 and IMP-44 metallo- β -lactamases with increased carbapenemase activities in multidrug-resistant *Pseudomonas aeruginosa*. *Antimicrob. Agents Chemother.* **57**, 4427–4432 (2013).
 168. Shibata, N. & Arakawa, Y. A new IMP-2 variant metallo- β -lactamase in *Pseudomonas aeruginosa* isolated in Japan. *GenBank Direct Submission*

- (2004). at <<http://www.ncbi.nlm.nih.gov/nucore/AB196988>>
169. Shibata, N. & Arakawa, Y. A new IMP-type metallo- β -lactamase in *Pseudomonas aeruginosa* isolated in Japan. *GenBank Direct Submission* (2005). at <<http://www.ncbi.nlm.nih.gov/nucore/AB204557>>
 170. Wang, Y., Wang, X., Schwarz, S., Zhang, R., Lei, L., Liu, X., Lin, D. & Shen, J. IMP-45-producing multidrug-resistant *Pseudomonas aeruginosa* of canine origin. *J. Antimicrob. Chemother.* **69**, 2579–2581 (2014).
 171. Pellegrini, C., Mercuri, P. S., Celenza, G., Galleni, M., Segatore, B., Sacchetti, E., Volpe, R., Amicosante, G. & Perilli, M. Identification of *bla*_{IMP-22} in *Pseudomonas* spp. in urban wastewater and nosocomial environments: biochemical characterization of a new IMP metallo-enzyme variant and its genetic location. *J. Antimicrob. Chemother.* **63**, 901–908 (2009).
 172. Lee, M.-F., Peng, C.-F., Hsu, H.-J. & Chen, Y.-H. Molecular characterisation of the metallo- β -lactamase genes in imipenem-resistant Gram-negative bacteria from a university hospital in southern Taiwan. *Int. J. Antimicrob. Ag.* **32**, 475–480 (2008).
 173. Petersen, T. N., Brunak, S., Heijne, von, G. & Nielsen, H. SignalP 4.0: discriminating signal peptides from transmembrane regions. *Nat. Methods* **8**, 785–786 (2011).
 174. Sievers, F., Wilm, A., Dineen, D., Gibson, T. J., Karplus, K., Li, W., Lopez, R., McWilliam, H., Remmert, M., Söding, J., Thompson, J. D. & Higgins, D. G. Fast, scalable generation of high-quality protein multiple sequence alignments using Clustal Omega. *Mol. Syst. Biol.* **7**, 1–6 (2011).
 175. Sievers, F. & Higgins, D. G. Clustal Omega, accurate alignment of very large numbers of sequences. *Method. Mol. Biol.* **1079**, 105–116 (2014).
 176. European Molecular Biology Laboratory, Clustal Omega. *EMBL-EBI* (2014). at <<http://www.ebi.ac.uk/Tools/msa/clustalo/>>
 177. Thompson, J. D., Higgins, D. G. & Gibson, T. J. CLUSTAL W: improving the sensitivity of progressive multiple sequence alignment through sequence weighting, position-specific gap penalties and weight matrix choice. *Nucleic Acids Res.* **22**, 4673–4680 (1994).
 178. Larkin, M. A., Blackshields, G., Brown, N. P., Chenna, R., McGettigan, P. A., McWilliam, H., Valentin, F., Wallace, I. M., Wilm, A., Lopez, R., Thompson, J. D., Gibson, T. J. & Higgins, D. G. Clustal W and Clustal X version 2.0. *Bioinformatics* **23**, 2947–2948 (2007).
 179. European Molecular Biology Laboratory, ClustalW2 Phylogenetic Tree. *EMBL-EBI* (2014). at <http://www.ebi.ac.uk/Tools/phylogeny/clustalw2_phylogeny/>
 180. Rambaut, A. FigTree. *Molecular Evolution, Phylogenetics and Epidemiology, Institute of Evolutionary Biology, University of Edinburgh* at <<http://tree.bio.ed.ac.uk/software/figtree/>>
 181. Chen, L.-R., Zhou, H.-W., Cai, J.-C., Zhang, R. & Chen, G.-X. Detection of plasmid-mediated IMP-1 metallo- β -lactamase and quinolone resistance determinants in an ertapenem-resistant *Enterobacter cloacae* isolate. *J. Zhejiang Univ.-Sci. B* **10**, 348–354 (2009).
 182. Concha, N. O., Janson, C. A., Rowling, P., Pearson, S., Cheever, C. A., Clarke, B. P., Lewis, C., Galleni, M., Frère, J.-M., Payne, D. J., Bateson, J. H. & Abdel-Meguid, S. S. Crystal structure of the IMP-1 metallo β -lactamase from *Pseudomonas aeruginosa* and its complex with a mercaptocarboxylate inhibitor: binding determinants of a potent, broad-spectrum inhibitor. *Biochemistry* **39**, 4288–4298 (2000).

183. Kurosaki, H., Yamaguchi, Y., Yasuzawa, H., Jin, W., Yamagata, Y. & Arakawa, Y. Probing, inhibition, and crystallographic characterization of metallo- β -lactamase (IMP-1) with fluorescent agents containing dansyl and thiol groups. *ChemMedChem* **1**, 969–972 (2006).
184. Yamaguchi, Y., Kuroki, T., Yasuzawa, H., Higashi, T., Jin, W., Kawanami, A., Yamagata, Y., Arakawa, Y., Goto, M. & Kurosaki, H. Probing the role of Asp-120(81) of metallo- β -lactamase (IMP-1) by site-directed mutagenesis, kinetic studies, and X-ray crystallography. *J. Biol. Chem.* **280**, 20824–20832 (2005).
185. Leung, G. H., Gray, T. J., Cheong, E. Y., Haertsch, P. & Gottlieb, T. Persistence of related bla-IMP-4 metallo-beta-lactamase producing Enterobacteriaceae from clinical and environmental specimens within a burns unit in Australia - a six-year retrospective study. *Antimicrob. Resist. Infect. Control* **2**, 1–8 (2013).
186. Poirel, L., Pham, J. N., Cabanne, L., Gatus, B. J., Bell, S. M. & Nordmann, P. Carbapenem-hydrolysing metallo- β -lactamases from *Klebsiella pneumoniae* and *Escherichia coli* isolated in Australia. *Pathology* **36**, 366–367 (2004).
187. Peleg, A. Y., Franklin, C., Bell, J. M. & Spelman, D. W. Dissemination of the metallo- β -lactamase gene bla_{IMP-4} among Gram-negative pathogens in a clinical setting in Australia. *Clin. Infect. Dis.* **41**, 1549–1556 (2005).
188. Merritt, E. A. X-ray anomalous scattering. *Skuld* (2012). at <<http://skuld.bmsc.washington.edu/scatter/>>
189. Cromer, D. T. & Liberman, D. Relativistic calculation of anomalous scattering factors for X rays. *J. Chem. Phys.* **53**, 1891–1898 (1970).
190. Jackson, C. J., Carr, P. D., Kim, H.-K., Liu, J.-W., Herrald, P., Mitić, N., Schenk, G., Smith, C. A. & Ollis, D. L. Anomalous scattering analysis of *Agrobacterium radiobacter* phosphotriesterase: the prominent role of iron in the heterobinuclear active site. *Biochemistry J.* **397**, 501–508 (2006).
191. Brennan, S. & Cowan, P. L. A suite of programs for calculating x-ray absorption, reflection, and diffraction performance for a variety of materials at arbitrary wavelengths. *Rev. Sci. Instrum.* **63**, 850–853 (1992).
192. Sivashanmugam, A., Murray, V., Cui, C., Zhang, Y., Wang, J. & Li, Q. Practical protocols for production of very high yields of recombinant proteins using *Escherichia coli*. *Protein Sci.* **18**, 936–948 (2009).
193. Goto, M., Yasuzawa, H., Higashi, T., Yamaguchi, Y., Kawanami, A., Mifune, S., Mori, H., Nakayama, H., Harada, K. & Arakawa, Y. Dependence of hydrolysis of β -lactams with a zinc(II)- β -lactamase produced from *Serratia marcescens* (IMP-1) on pH and concentration of zinc(II) ion: dissociation of Zn(II) from IMP-1 in acidic medium. *Biol. Pharm. Bull.* **26**, 589–594 (2003).
194. Griffin, D. H., Richmond, T. K., Sanchez, C., Moller, A. J., Breece, R. M., Tierney, D. L., Bennett, B. & Crowder, M. W. Structural and kinetic studies on metallo- β -lactamase IMP-1. *Biochemistry* **50**, 9125–9134 (2011).
195. Sklenář, V. & Bax, A. Spin-echo water suppression for the generation of pure-phase two-dimensional NMR spectra. *J. Magn. Reson.* **74**, 469–479 (1987).
196. Anglister, J., Grzesiek, S., Ren, H., Klee, C. B. & Bax, A. Isotope-edited multidimensional NMR of calcineurin B in the presence of the non-deuterated detergent CHAPS. *J. Biomol. NMR* **3**, 121–126 (1993).
197. Moali, C., Anne, C., Lamotte-Brasseur, J., Gros Lambert, S., Devreese, B., Van Beeumen, J., Galleni, M. & Frère, J.-M. Analysis of the importance of the metallo- β -lactamase active site loop in substrate binding and catalysis. *Chem. Biol.* **10**, 319–329 (2003).
198. Studier, F. W. Protein production by auto-induction in high density shaking

- cultures. *Protein Expr. Purif.* **41**, 207–234 (2005).
199. Schenk, G., Mitić, N., Hanson, G. R. & Comba, P. Purple acid phosphatase: A journey into the function and mechanism of a colorful enzyme. *Coord. Chem. Rev.* **257**, 473–482 (2013).
 200. Strohalm, M., Kavan, D., Novák, P., Volný, M. & Havlíček, V. *mMass 3*: A cross-platform software environment for precise analysis of mass spectrometric data. *Anal. Chem.* **82**, 4648–4651 (2010).
 201. Waldo, G. S., Ling, J., Sanders-Loehr, J. & Theil, E. C. Formation of an Fe(III)-tyrosinate complex during biomineralization of H-subunit ferritin. *Science* **259**, 796–798 (1993).
 202. Bertani, G. Studies on lysogenesis I. *J. Bacteriol.* **62**, 293–300 (1951).
 203. Siemann, S., Badiei, H. R., Karanassios, V., Viswanatha, T. & Dmitrienko, G. I. ^{68}Zn isotope exchange experiments reveal an unusual kinetic lability of the metal ions in the di-zinc form of IMP-1 metallo- β -lactamase. *Chem. Commun.* 532–534 (2006).
 204. Gardonio, D. & Siemann, S. Chelator-facilitated chemical modification of IMP-1 metallo- β -lactamase and its consequences on metal binding. *Biochem. Biophys. Res. Commun.* **381**, 107–111 (2009).
 205. Yamaguchi, Y., Ding, S., Murakami, E., Imamura, K., Fuchigami, S., Hashiguchi, R., Yutani, K., Mori, H., Suzuki, S., Arakawa, Y. & Kurosaki, H. A demetallation method for IMP-1 metallo- β -lactamase with restored enzymatic activity upon addition of metal ion(s). *ChemBioChem* **12**, 1979–1983 (2011).
 206. Kelly, S. M., Jess, T. J. & Price, N. C. How to study proteins by circular dichroism. *BBA-Proteins Proteom.* **1751**, 119–139 (2005).
 207. Gill, S. C. & Hoppel, von, P. H. Calculation of protein extinction coefficients from amino acid sequence data. *Anal. Biochem.* **182**, 319–326 (1989).
 208. Pace, C. N., Vajdos, F., Fee, L., Grimsley, G. & Gray, T. How to measure and predict the molar absorption coefficient of a protein. *Protein Sci.* **4**, 2411–2423 (1995).
 209. Katz, B. A., Mackman, R., Luong, C., Radika, K., Martelli, A., Sprengeler, P. A., Wang, J., Chan, H. & Wong, L. Structural basis for selectivity of a small molecule, S1-binding, submicromolar inhibitor of urokinase-type plasminogen activator. *Chem. Biol.* **7**, 299–312 (2000).
 210. Cruickshank, D. W. J. Remarks about protein structure precision. *Acta. Cryst. D* **55**, 583–601 (1999).
 211. Emsley, P. & Cowtan, K. Coot: model-building tools for molecular graphics. *Acta. Cryst. D* **60**, 2126–2132 (2004).
 212. Rother, K., Hildebrand, P. W., Goede, A., Gruening, B. & Preissner, R. Voronoia: analyzing packing in protein structures. *Nucleic Acids Res.* **37**, D393–D395 (2009).
 213. Wu, P. S., Ozawa, K., Jergic, S., Su, X.-C., Dixon, N. E. & Otting, G. Amino-acid type identification in ^{15}N -HSQC spectra by combinatorial selective ^{15}N -labelling. *J. Biomol. NMR* **34**, 13–21 (2006).
 214. Ozawa, K., Wu, P. S. C., Dixon, N. E. & Otting, G. ^{15}N -Labelled proteins by cell-free protein synthesis. *FEBS J.* **273**, 4154–4159 (2006).
 215. Jia, X., Ozawa, K., Loscha, K. & Otting, G. Glutarate and *N*-acetyl-L-glutamate buffers for cell-free synthesis of selectively ^{15}N -labelled proteins. *J. Biomol. NMR* **44**, 59–67 (2009).
 216. Kazanis, S., Pochapsky, T. C., Barnhart, T. M., Penner-Hahn, J. E., Mirza, U. A. & Chait, B. T. Conversion of a Fe_2S_2 ferredoxin into a Ga^{3+} rubredoxin. *J.*

- Am. Chem. Soc.* **117**, 6625–6626 (1995).
217. Arasasingham, R. D., Balch, A. L., Olmstead, M. M. & Phillips, S. L. Paramagnetic iron(III) and diamagnetic gallium(III) porphyrin complexes with axial allyl and vinyl ligands. *Inorg. Chim. Acta* **263**, 161–170 (1997).
 218. Caillet-Saguy, C., Delepiepierre, M., Lecroisey, A., Bertini, I., Piccioli, M. & Turano, P. Direct-detected ^{13}C NMR to investigate the iron(III) hemophore HasA. *J. Am. Chem. Soc.* **128**, 150–158 (2006).
 219. Baret, P., Beaujolais, V., Bougault, C., Gaude, D. & Pierre, J. L. ^1H NMR studies of the diamagnetic gallium (III) and paramagnetic iron (III) complexes of a chiral macrobicyclic ligand of bicapped tris (binaphthol) type. *J. Chim. Phys.* **95**, 112–121 (1998).
 220. Merks, M. & Averill, B. A. Ga^{3+} as a functional substitute for Fe^{3+} : Preparation and characterization of the $\text{Ga}^{3+}\text{Fe}^{2+}$ and $\text{Ga}^{3+}\text{Zn}^{2+}$ forms of bovine spleen purple acid phosphatase. *Biochemistry* **37**, 8490–8497 (1998).
 221. Vo, E., Wang, H. C. & Germanas, J. P. Preparation and characterization of [2Ga-2S] *Anabaena* 7120 ferredoxin, the first gallium-sulfur cluster-containing protein. *J. Am. Chem. Soc.* **119**, 1934–1940 (1997).
 222. Xu, X., Kim, S.-K., Schürmann, P., Hirasawa, M., Tripathy, J. N., Smith, J., Knaff, D. B. & Ubbink, M. Ferredoxin/ferredoxin–thioredoxin reductase complex: Complete NMR mapping of the interaction site on ferredoxin by gallium substitution. *FEBS Lett.* **580**, 6714–6720 (2006).
 223. Kazanis, S. & Pochapsky, T. C. Structural features of the metal binding site and dynamics of gallium putidaredoxin, a diamagnetic derivative of a $\text{Cys}_4\text{Fe}_2\text{S}_2$ ferredoxin. *J. Biomol. NMR* **9**, 337–346 (1997).
 224. Guignard, L., Ozawa, K., Pursglove, S. E., Otting, G. & Dixon, N. E. NMR analysis of in vitro-synthesized proteins without purification: a high-throughput approach. *FEBS Lett.* **524**, 159–162 (2002).
 225. Lassaux, P., Traoré, D. A. K., Loisel, E., Favier, A., Docquier, J.-D., Sohier, J. S., Laurent, C., Bebrone, C., Frère, J.-M., Ferrer, J.-L. & Galleni, M. Biochemical and structural characterization of the subclass B1 metallo- β -lactamase VIM-4. *Antimicrob. Agents Chemother.* **55**, 1248–1255 (2011).
 226. Valappil, S. P., Ready, D., Neel, E. A. A., Pickup, D. M., Chrzanowski, W., O'Dell, L. A., Newport, R. J., Smith, M. E., Wilson, M. & Knowles, J. C. Antimicrobial gallium-doped phosphate-based glasses. *Adv. Funct. Mater.* **18**, 732–741 (2008).
 227. Lessa, J. A., Parrilha, G. L. & Beraldo, H. Gallium complexes as new promising metallodrug candidates. *Inorg. Chim. Acta* **393**, 53–63 (2012).
 228. Bonchi, C., Imperi, F., Minandri, F., Visca, P. & Frangipani, E. Repurposing of gallium-based drugs for antibacterial therapy. *BioFactors* **40**, 303–312 (2014).
 229. Banin, E., Lozinski, A., Brady, K. M., Berenshtein, E., Butterfield, P. W., Moshe, M., Chevion, M., Greenberg, E. P. & Banin, E. The potential of desferrioxamine-gallium as an anti-*Pseudomonas* therapeutic agent. *Proc. Natl. Acad. Sci. U.S.A.* **105**, 16761–16766 (2008).
 230. Kaneko, Y., Thoendel, M., Olakanmi, O., Britigan, B. E. & Singh, P. K. The transition metal gallium disrupts *Pseudomonas aeruginosa* iron metabolism and has antimicrobial and antibiofilm activity. *J. Clin. Invest.* **117**, 877–888 (2007).
 231. Waldron, K. J. & Robinson, N. J. How do bacterial cells ensure that metalloproteins get the correct metal? *Nat. Rev. Microbiol.* **7**, 25–35 (2009).
 232. Pekel, N., Savaş, H. & Güven, O. Complex formation and adsorption of V^{3+} , Cr^{3+} and Fe^{3+} ions with poly(*N*-vinylimidazole). *Colloid Polym. Sci.* **280**, 46–51 (2002).

233. Schilling, O., Wenzel, N., Naylor, M., Vogel, A., Crowder, M., Makaroff, C. & Meyer-Klaucke, W. Flexible metal binding of the metallo- β -lactamase domain: Glyoxalase II incorporates iron, manganese, and zinc *in vivo*. *Biochemistry* **42**, 11777–11786 (2003).
234. Shriver, D. F. & Atkins, P. W. *Inorganic Chemistry*. Oxford University Press, (1999).
235. Tsan, P., Caffrey, M., Daku, M. L., Cusanovich, M., Marion, D. & Gans, P. Unusual contact shifts and magnetic tensor orientation in *Rhodobacter capsulatus* ferrocycytochrome *c'*: NMR, magnetic susceptibility, and EPR studies. *J. Am. Chem. Soc.* **121**, 1795–1805 (1999).
236. Turano, P., Battaini, G. & Casella, L. Validation of paramagnetic cross correlation rates for solution structure determination of high spin iron(III) heme proteins. *Chem. Phys. Lett.* **373**, 460–463 (2003).
237. Banci, L., Bertini, I., Rosato, A. & Scacchieri, S. Solution structure of oxidized microsomal rabbit cytochrome b5. Factors determining the heterogeneous binding of the heme. *Eur. J. Biochem.* **267**, 755–766 (2000).
238. Wlodawer, A., Minor, W., Dauter, Z. & Jaskolski, M. Protein crystallography for non-crystallographers, or how to get the best (but not more) from published macromolecular structures. *FEBS J.* **275**, 1–21 (2007).
239. Yamaguchi, Y., Imamura, K., Sasao, A., Murakami, E., Arakawa, Y. & Kurosaki, H. Metal preference of Zn(II) and Co(II) for the dinuclear metal binding site of IMP-1 metallo- β -lactamase and spectroscopic properties of Co(II)-substituted IMP-1 with mercaptoacetic acid. *MedChemComm* **2**, 720–725 (2011).
240. Siemann, S., Brewer, D., Clarke, A. J. & Lajoie, G. IMP-1 metallo- β -lactamase: effect of chelators and assessment of metal requirement by electrospray mass spectrometry. *Biochim. Biophys. Acta* **1571**, 190–200 (2002).
241. Heinz, U. & Adolph, H.-W. Metallo- β -lactamases: two binding sites for one catalytic metal ion? *Cell. Mol. Life Sci.* **61**, 2827–2839 (2004).
242. Morán-Barrio, J., González, J. M., Lisa, M. N., Costello, A. L., Peraro, M. D., Carloni, P., Bennett, B., Tierney, D. L., Limansky, A. S., Viale, A. M. & Vila, A. J. The metallo- β -lactamase GOB is a mono-Zn(II) enzyme with a novel active site. *J. Biol. Chem.* **282**, 18286–18293 (2007).
243. Hu, Z., Gunasekera, T. S., Spadafora, L., Bennett, B. & Crowder, M. W. Metal content of metallo- β -lactamase L1 is determined by the bioavailability of metal ions. *Biochemistry* **47**, 7947–7953 (2008).
244. Outten, C. E. & O'Halloran, A. T. V. Femtomolar sensitivity of metalloregulatory proteins controlling zinc homeostasis. *Science* **292**, 2488–2492 (2001).
245. Ma, Z., Jacobsen, F. E. & Giedroc, D. P. Coordination chemistry of bacterial metal transport and sensing. *Chem. Rev.* **109**, 4644–4681 (2009).
246. Meini, M.-R., González, L. J. & Vila, A. J. Antibiotic resistance in Zn(II)-deficient environments: metallo- β -lactamase activation in the periplasm. *Future Microbiol.* **8**, 947–979 (2013).
247. Pfeiffer, P., Thielert, H. & Glaser, H. Gegenseitiger Austausch von Metallen in inneren Komplexsalzen. *J. Prakt. Chem.* **152**, 145–156 (1939).
248. Irving, H. & Williams, R. J. P. Order of Stability of Metal Complexes. *Nature* **162**, 746–747 (1948).
249. Irving, H. & Williams, R. J. P. 637. The stability of transition-metal complexes. *J. Chem. Soc.* 3192–3210 (1953).
250. Cameron, A. D., Ridderström, M., Olin, B. & Mannervik, B. Crystal structure

- of human glyoxalase II and its complex with a glutathione thiolester substrate analogue. *Structure* **7**, 1067–1078 (1999).
251. Huang, L.-S. & Lin, K.-C. Detection of iron species using inductively coupled plasma mass spectrometry under cold plasma temperature conditions. *Spectrochim. Acta B* **56**, 123–128 (2001).
 252. Thomas, R. *Practical Guide to ICP-MS*. (CRC Press, 2013).
 253. Segura, M., Madrid, Y. & Cámara, C. Elimination of calcium and argon interferences in iron determination by ICP-MS using desferrioxamine chelating agent immobilized in sol-gel and cold plasma conditions. *J. Anal. Atom. Spectrom.* **18**, 1103–1108 (2003).
 254. McCall, K. A., Huang, C.-C. & Fierke, C. A. Function and mechanism of zinc metalloenzymes. *J. Nutr.* **130**, 1437S–1446S (2000).
 255. Vela, P. & Schenk, G. Personal Communication (2011).
 256. Maret, W. Metalloproteomics, metalloproteomes, and the annotation of metalloproteins. *Metallomics* **2**, 117–125 (2010).
 257. Marcy, H. Metalloenzymes: Native co-factor or experimental artifact? *Biochem. Anal. Biochem.* **1**, 1–2 (2012).
 258. Hu, Z., Periyannan, G., Bennett, B. & Crowder, M. W. Role of the Zn₁ and Zn₂ sites in metallo-β-lactamase L1. *J. Am. Chem. Soc.* **130**, 14207–14216 (2008).
 259. Sgrignani, J., Magistrato, A., Dal Peraro, M., Vila, A. J., Carloni, P. & Pierattelli, R. On the active site of mononuclear B1 metallo β-lactamases: a computational study. *J. Comput. Aided Mol. Des.* **26**, 425–435 (2012).
 260. Jacquin, O., Balbeur, D., Damblon, C., Marchot, P., De Pauw, E., Roberts, G. C. K., Frère, J.-M. & Matagne, A. Positively cooperative binding of zinc ions to *Bacillus cereus* 569/H/9 β-lactamase II suggests that the binuclear enzyme is the only relevant form for catalysis. *J. Mol. Biol.* **392**, 1278–1291 (2009).
 261. Hernick, M., Gattis, S. G., Penner-Hahn, J. E. & Fierke, C. A. Activation of *Escherichia coli* UDP-3-O-[(R)-3-hydroxymyristoyl]-N-acetylglucosamine deacetylase by Fe²⁺ yields a more efficient enzyme with altered ligand affinity. *Biochemistry* **49**, 2246–2255 (2010).
 262. Gattis, S. G., Hernick, M. & Fierke, C. A. Active site metal ion in UDP-3-O-((R)-3-hydroxymyristoyl)-N-acetylglucosamine deacetylase (LpxC) switches between Fe(II) and Zn(II) depending on cellular conditions. *J. Biol. Chem.* **285**, 33788–33796 (2010).
 263. Neylon, C., Brown, S. E., Kralicek, A. V., Miles, C. S., Love, C. A. & Dixon, N. E. Interaction of the *Escherichia coli* replication terminator protein (Tus) with DNA: a model derived from DNA-binding studies of mutant proteins by surface plasmon resonance. *Biochemistry* **39**, 11989–11999 (2000).
 264. Loscha, K. V., Herlt, A. J., Qi, R., Huber, T., Ozawa, K. & Otting, G. Multiple-site labeling of proteins with unnatural amino acids. *Angew. Chem. Int. Ed.* **51**, 2243–2246 (2012).
 265. Perez, F. Serial Cloner. at <http://serialbasics.free.fr/Serial_Cloner.html>
 266. SnapGene. SnapGene Viewer. at <<http://www.snapgene.com/>>
 267. Apponyi, M. A., Ozawa, K., Dixon, N. E. & Otting, G. Cell-free protein synthesis for analysis by NMR spectroscopy. *Methods Mol. Biol.* **426**, 257–268 (2008).
 268. Su, X.-C., Loh, C. T., Qi, R. & Otting, G. Suppression of isotope scrambling in cell-free protein synthesis by broadband inhibition of PLP enzymes for selective ¹⁵N-labelling and production of perdeuterated proteins in H₂O. *J. Biomol. NMR* **50**, 35–42 (2011).
 269. Beynon, R. A recipe calculator for thermodynamically correct buffers for pH

- control. at <<http://www.liv.ac.uk/buffers/>>
270. Kirsch, P. D., Ekerdt, J. G. KaleidaGraph: Graphing and data analysis. Version 3.5 for Windows. *J. Am. Chem. Soc.* **122**, 11755–11755 (2000).
 271. Winn, M. D., Ballard, C. C., Cowtan, K. D., Dodson, E. J., Emsley, P., Evans, P. R., Keegan, R. M., Krissinel, E. B., Leslie, A. G. W., McCoy, A., McNicholas, S. J., Murshudov, G. N., Pannu, N. S., Potterton, E. A., Powell, H. R., Read, R. J., Vagin, A. & Wilson, K. S. Overview of the CCP4 suite and current developments. *Acta. Cryst. D* **67**, 235–242 (2011).
 272. McCoy, A. J., Grosse-Kunstleve, R. W., Adams, P. D., Winn, M. D., Storoni, L. C. & Read, R. J. *Phaser* crystallographic software. *J. Appl. Crystallogr.* **40**, 658–674 (2007).
 273. Vagin, A. A., Steiner, R. A., Lebedev, A. A., Potterton, L., McNicholas, S., Long, F. & Murshudov, G. N. *REFMAC5* dictionary: organization of prior chemical knowledge and guidelines for its use. *Acta. Cryst. D* **60**, 2184–2195 (2004).
 274. Strahs, G. & Kraut, J. Low-resolution electron-density and anomalous-scattering-density maps of *Chromatium* high-potential iron protein. *J. Mol. Biol.* **35**, 503–512 (1968).
 275. Read, R. J. & Schierbeek, A. J. A phased translation function. *J. Appl. Crystallogr.* **21**, 490–495 (1988).
 276. DeLano, W. L. PyMOL: An open-source molecular graphics tool. *CCP4 Newsletter On Protein Crystallography* **40**, (2002).
 277. Schrödinger LLC. The PyMOL molecular graphics system. *PyMOL* (2010).
 278. Campbell, R., Holder, T. & Asai, S. data2bfactor.py. (2003).
 279. Tsai, J., Taylor, R., Chothia, C. & Gerstein, M. The packing density in proteins: standard radii and volumes. *J. Mol. Biol.* **290**, 253–266 (1999).
 280. Wishart, D. S., Bigam, C. G., Yao, J., Abildgaard, F., Dyson, H. J., Oldfield, E., Markley, J. L. & Sykes, B. D. ^1H , ^{13}C and ^{15}N chemical shift referencing in biomolecular NMR. *J. Biomol. NMR* **6**, 135–140 (1995).
 281. Delaglio, F., Grzesiek, S., Vuister, G. W., Zhu, G., Pfeifer, J. & Bax, A. NMRPipe: a multidimensional spectral processing system based on UNIX pipes. *J. Biomol. NMR* **6**, 277–293 (1995).
 282. Fogh, R. H., Boucher, W., Vranken, W. F., Pajon, A., Stevens, T. J., Bhat, T. N., Westbrook, J., Ionides, J. M. C. & Laue, E. D. A framework for scientific data modeling and automated software development. *Bioinformatics* **21**, 1678–1684 (2005).
 283. Vranken, W. F., Boucher, W., Stevens, T. J., Fogh, R. H., Pajon, A., Llinas, M., Ulrich, E. L., Markley, J. L., Ionides, J. & Laue, E. D. The CCPN data model for NMR spectroscopy: development of a software pipeline. *Proteins* **59**, 687–696 (2005).
 284. Tonelli, M., Singarapu, K. K., Makino, S.-I., Sahu, S. C., Matsubara, Y., Endo, Y., Kainosho, M. & Markley, J. L. Hydrogen exchange during cell-free incorporation of deuterated amino acids and an approach to its inhibition. *J. Biomol. NMR* **51**, 467–476 (2011).
 285. Etezady-Esfarjani, T., Hiller, S., Villalba, C. & Wüthrich, K. Cell-free protein synthesis of perdeuterated proteins for NMR studies. *J. Biomol. NMR* **39**, 229–238 (2007).
 286. Tong, K. I., Yamamoto, M. & Tanaka, T. A simple method for amino acid selective isotope labeling of recombinant proteins in *E. coli*. *J. Biomol. NMR* **42**, 59–67 (2008).
 287. McIntosh, L. P. & Dahlquist, F. W. Biosynthetic incorporation of ^{15}N and ^{13}C

- for assignment and interpretation of nuclear magnetic resonance spectra of proteins. *Q. Rev. Biophys.* **23**, 1–38 (1990).
288. Morino, Y. & Nagashima, F. [10] Pyridoxal phosphate-binding site in enzymes: Reduction and comparison of sequences. in *Methods Enzymol.* **106**, 116–137 (1984).
 289. Cambridge Isotope Laboratories. CIL. *Cambridge Isotope Laboratories, Inc.* (2014). at <<http://www.isotope.com>>
 290. Yokoyama, J., Matsuda, T., Koshiba, S. & Kigawa, T. An economical method for producing stable-isotope labeled proteins by the *E. coli* cell-free system. *J. Biomol. NMR* **48**, 193–201 (2010).
 291. Su, X.-C., McAndrew, K., Huber, T. & Otting, G. Lanthanide-binding peptides for NMR measurements of residual dipolar couplings and paramagnetic effects from multiple angles. *J. Am. Chem. Soc.* **130**, 1681–1687 (2008).
 292. Duckett, S. B. & Wood, N. J. Parahydrogen-based NMR methods as a mechanistic probe in inorganic chemistry. *Coord. Chem. Rev.* **252**, 2278–2291 (2008).
 293. Ashmead, D. R., Eley, D. D. & Rudham, R. The parahydrogen conversion on neodymium oxide. *J. Chem. Soc. Faraday Trans.* **59**, 207–215 (1963).
 294. Schmauch, G. E. & Singleton, A. H. Technical aspects of ortho-parahydrogen conversion. *Ind. Eng. Chem.* **56**, 20–31 (1964).
 295. Kummer, J. T. Ortho-para-hydrogen conversion by metal surfaces at 21°K. *J. Phys. Chem.* **66**, 1715–1719 (1962).
 296. Dennison, D. M. A note on the specific heat of the hydrogen molecule. *Proc. R. Soc. Lon. Ser. A* **115**, 483–486 (1927).
 297. Bowers, C. & Weitekamp, D. Transformation of symmetrization order to nuclear-spin magnetization by chemical reaction and nuclear magnetic resonance. *Phys. Rev. Lett.* **57**, 2645–2648 (1986).
 298. Bowers, C. R. & Weitekamp, D. P. Parahydrogen and synthesis allow dramatically enhanced nuclear alignment. *J. Am. Chem. Soc.* **109**, 5541–5542 (1987).
 299. Blazina, D., Duckett, S. B., Dunne, J. P. & Godard, C. Applications of the parahydrogen phenomenon in inorganic chemistry. *J. Chem. Soc. Dalton Trans.* 2601–2609 (2004).
 300. Harkness, R. W. & Deming, W. E. The equilibrium of para and ortho hydrogen. *J. Am. Chem. Soc.* **54**, 2850–2852 (1932).
 301. Eisenschmid, T. C., Kirss, R. U., Deutsch, P. P., Hommeltoft, S. I., Eisenberg, R., Bargon, J., Lawler, R. G. & Balch, A. L. Para hydrogen induced polarization in hydrogenation reactions. *J. Am. Chem. Soc.* **109**, 8089–8091 (1987).
 302. Kovtunov, K. V., Beck, I. E., Bukhtiyarov, V. I. & Koptug, I. V. Observation of parahydrogen-induced polarization in heterogeneous hydrogenation on supported metal catalysts. *Angew. Chem. Int. Ed.* **47**, 1492–1495 (2008).
 303. Balu, A. M., Duckett, S. B. & Luque, R. Para-hydrogen induced polarisation effects in liquid phase hydrogenations catalysed by supported metal nanoparticles. *J. Chem. Soc. Dalton Trans.* 5074–5076 (2009).
 304. Atkinson, K. D., Cowley, M. J., Elliott, P. I. P., Duckett, S. B., Green, G. G. R., López-Serrano, J. & Whitwood, A. C. Spontaneous transfer of parahydrogen derived spin order to pyridine at low magnetic field. *J. Am. Chem. Soc.* **131**, 13362–13368 (2009).
 305. Adams, R. W., Aguilar, J. A., Atkinson, K. D., Cowley, M. J., Elliott, P. I. P., Duckett, S. B., Green, G. G. R., Khazal, I. G., López-Serrano, J. & Williamson,

- D. C. Reversible interactions with para-hydrogen enhance NMR sensitivity by polarization transfer. *Science* **323**, 1708–1711 (2009).
306. Zeng, H., Xu, J., Gillen, J., McMahon, M. T., Artemov, D., Tyburn, J.-M., Lohman, J. A. B., Mewis, R. E., Atkinson, K. D., Green, G. G. R., Duckett, S. B. & van Zijl, P. C. M. Optimization of SABRE for polarization of the tuberculosis drugs pyrazinamide and isoniazid. *J. Magn. Reson.* **237**, 73–78 (2013).
 307. Lloyd, L. S., Adams, R. W., Bernstein, M., Coombes, S., Duckett, S. B., Green, G. G. R., Lewis, R. J., Mewis, R. E. & Sleight, C. J. Utilization of SABRE-derived hyperpolarization to detect low-concentration analytes via 1D and 2D NMR methods. *J. Am. Chem. Soc.* **134**, 12904–12907 (2012).
 308. van Weerdenburg, B. J. A., Glöggler, S., Eshuis, N., Engwerda, A. H. J. T., Smits, J. M. M., de Gelder, R., Appelt, S., Wymenga, S. S., Tessari, M., Feiters, M. C., Blümich, B. & Rutjes, F. P. J. T. Ligand effects of NHC-iridium catalysts for signal amplification by reversible exchange (SABRE). *Chem. Commun.* **49**, 7388–7390 (2013).
 309. Pravica, M. G. & Weitekamp, D. P. Net NMR alignment by adiabatic transport of parahydrogen addition products to high magnetic field. *Chem. Phys. Lett.* **145**, 255–258 (1988).
 310. Bhattacharya, P., Harris, K., Lin, A. P., Mansson, M., Norton, V. A., Perman, W. H., Weitekamp, D. P. & Ross, B. D. Ultra-fast three dimensional imaging of hyperpolarized ^{13}C *in vivo*. *Magn. Reson. Mater. Phys. Biol. Med.* **18**, 245–256 (2005).
 311. Hövener, J.-B., Chekmenev, E. Y., Harris, K. C., Perman, W. H., Tran, T. T., Ross, B. D. & Bhattacharya, P. Quality assurance of PASADENA hyperpolarization for ^{13}C biomolecules. *Magn. Reson. Mater. Phys. Biol. Med.* **22**, 123–134 (2009).
 312. Bhattacharya, P., Chekmenev, E. Y., Perman, W. H., Harris, K. C., Lin, A. P., Norton, V. A., Tan, C. T., Ross, B. D. & Weitekamp, D. P. Towards hyperpolarized ^{13}C -succinate imaging of brain cancer. *J. Magn. Reson.* **186**, 150–155 (2007).
 313. Warren, W. S., Jenista, E., Branca, R. T. & Chen, X. Increasing hyperpolarized spin lifetimes through true singlet eigenstates. *Science* **323**, 1711–1714 (2009).
 314. Baumer, D., Brunner, E., Blümmler, P., Zänker, P. P. & Spiess, H. W. NMR spectroscopy of laser-polarized ^{129}Xe under continuous flow: a method to study aqueous solutions of biomolecules. *Angew. Chem. Int. Ed.* **45**, 7282–7284 (2006).
 315. Roth, M., Kindervater, P., Raich, H.-P., Bargon, J., Spiess, H. W. & Münnemann, K. Continuous ^1H and ^{13}C signal enhancement in NMR spectroscopy and MRI using parahydrogen and hollow-fiber membranes. *Angew. Chem. Int. Ed.* **122**, 8536–8540 (2010).
 316. Glöggler, S., Müller, R., Colell, J., Emondts, M., Dabrowski, M., Blümich, B. & Appelt, S. Para-hydrogen induced polarization of amino acids, peptides and deuterium–hydrogen gas. *Phys. Chem. Chem. Phys.* **13**, 13759–13764 (2011).
 317. Nicosia, R. F. & Ottinetti, A. Growth of microvessels in serum-free matrix culture of rat aorta. A quantitative assay of angiogenesis *in vitro*. *Lab. Invest.* **63**, 115–122 (1990).
 318. Auerbach, R., Lewis, R., Shinnars, B., Kubai, L. & Akhtar, N. Angiogenesis assays: a critical overview. *Clin. Chem.* **49**, 32–40 (2003).
 319. Morreel, K., Kim, H., Lu, F., Dima, O., Akiyama, T., Vanholme, R., Niculaes, C., Goeminne, G., Inzé, D., Messens, E., Ralph, J. & Boerjan, W. Mass

- spectrometry-based fragmentation as an identification tool in lignomics. *Anal. Chem.* **82**, 8095–8105 (2010).
320. Morreel, K., Dima, O., Kim, H., Lu, F., Niculaes, C., Vanholme, R., Dauwe, R., Goeminne, G., Inzé, D., Messens, E., Ralph, J. & Boerjan, W. Mass spectrometry-based sequencing of lignin oligomers. *Plant Physiol.* **153**, 1464–1478 (2010).
 321. Lourith, N., Katayama, T. & Suzuki, T. Stereochemistry and biosynthesis of 8-*O*-4' neolignans in *Eucommia ulmoides*: diastereoselective formation of guaiacylglycerol-8-*O*-4'-(sinapyl alcohol) ether. *J. Wood Sci.* **51**, 370–378 (2005).
 322. Derome, A. E. & Williamson, M. P. Rapid-pulsing artifacts in double-quantum-filtered COSY. *J. Magn. Reson.* **88**, 177–185 (1990).
 323. Bax, A. & Davis, D. G. MLEV-17-based two-dimensional homonuclear magnetization transfer spectroscopy. *J. Magn. Reson.* **65**, 355–360 (1985).
 324. Wagner, R. & Berger, S. Gradient-selected NOESY - a fourfold reduction of the measurement time for the NOESY experiment. *J. Magn. Reson. Ser. A* **123**, 119–121 (1996).
 325. Jeener, J., Meier, B. H., Bachmann, P. & Ernst, R. R. Investigation of exchange processes by two-dimensional NMR spectroscopy. *J. Chem. Phys.* **71**, 4546–4553 (1979).
 326. Palmer, A. G., III, Cavanagh, J., Wright, P. E. & Rance, M. Sensitivity improvement in proton-detected two-dimensional heteronuclear correlation NMR spectroscopy. *J. Magn. Reson.* **93**, 151–170 (1991).
 327. Kay, L., Keifer, P. & Saarinen, T. Pure absorption gradient enhanced heteronuclear single quantum correlation spectroscopy with improved sensitivity. *J. Am. Chem. Soc.* **114**, 10663–10665 (1992).
 328. Schleucher, J., Schwendinger, M., Sattler, M., Schmidt, P., Schedletsky, O., Glaser, S. J., Sørensen, O. W. & Griesinger, C. A general enhancement scheme in heteronuclear multidimensional NMR employing pulsed field gradients. *J. Biomol. NMR* **4**, 301–306 (1994).
 329. Cicero, D. O., Barbato, G. & Bazzo, R. Sensitivity enhancement of a two-dimensional experiment for the measurement of heteronuclear long-range coupling constants, by a new scheme of coherence selection by gradients. *J. Magn. Reson.* **148**, 209–213 (2001).